NOVEL CARBON NANOMATERIALS: SYNTHESIS AND APPLICATIONS

by

Brett Lee Allen

B. S., Bethany College, 2006

Submitted to the Graduate Faculty of

Arts and Sciences in partial fulfillment

of the requirements for the degree of

Doctor of Philosophy

University of Pittsburgh

2010

UNIVERSITY OF PITTSBURGH

GRADUATE ARTS AND SCIENCES

This dissertation was presented

by

Brett Lee Allen

It was defended on

July 21, 2010

and approved by

Dr. Adrian C. Michael, Professor, Department of Chemistry

Dr. Stephen G. Weber, Professor, Department of Chemistry

Dr. Valerian Kagan, Professor, Department of Environmental and Occupation Health,

Dissertation Advisor: Dr. Alexander Star, Assistant Professor, Department of Chemistry

Copyright © by Brett Lee Allen

2010

Reproduced with permission from:

Kuzmych, O.; Allen, B. L.; Star, A., *Nanotechnology*, **2007**, *18*, 375502-0 –7 (homepage: www.iop.org/journals/nano); Allen, B. L.; Kichambare, P. D.; Star, A., *ACS Nano*, **2008**, *2*, 1914-1920; Allen, B. L.; Kichambare, P. D.; Gou, P.; Vlasova, I. I.; Kapralov, A. A.; Konduru, N.; Kagan, V. E.; Star, A., *Nano Lett.*, **2008**, *8*, 3899-3903; Allen, B. L.; Kotchey, G. P.; Chen, Y.; Yanamala, N. V. K.; Klein-Seetharaman, J.; Kagan, V. E.; Star, A., *J. Am. Chem. Soc.*, **2009**, *131*, 17194-17205; Tang, Y.; Allen, B. L.; Kauffman, D. R.; Star, A., *J. Am. Chem. Soc.*, **2009**, *131*, 13200-13201; Kauffman, D. R.; Sorescu, D. C.; Schofield, D. P.; Allen, B. L.; Jordan, K. D.; Star, A., *Nano Lett.*, **2010**, *10*, 958-963; Allen, B. L.; Shade, C. M.; Yingling, A. M.; Petoud, S.; Star, A., *Adv. Mater.*, **2009**, *21*, 4692-4695 (Copyright Wiley-VCH Verlag GmbH & Co. KGaA); Allen, B. L.; Keddie, M. B.; Star, A., Nanoscale **2010**, *2*, 1105-1108 (Reproduced with permission from The Royal Chemistry Society); and Kagan, V. E.; Konduru, N. V.; Feng, W.; Allen, B. L.; Conroy, J. *et al.*, *Nature Nano.*, **2010**, *5*, 354-359.

NOVEL CARBON NANOMATERIALS: SYNTHESIS AND APPLICATIONS

Brett Lee Allen, PhD

University of Pittsburgh, 2010

Carbon nanotubes (CNTs) hold exceptional promise for an array of applications in numerous disciplines. Discovered in 1991 by Sumio Iijima, CNTs have been synthesized in a myriad of varieties including single-walled (SWNTs), multiwalled (MWNTs), and chemically doped, resulting in unique electronic and physical properties, as well as an innate biocompatibility towards biological organisms. Such attractive properties have been demonstrated in CNTs' implementation in applications such as electronic sensors, drug delivery vehicles, and reinforcements in composite materials. Moreover, by chemical doping, carbon nanomaterial hybrids have been formed with intrinsic morphological and physical properties differing from their un-doped counterparts.

Despite successful execution in these areas, reports have been generated indicating degrees of cytotoxicity induced by carbon nanotubes. Specifically, CNTs have demonstrated asbestos-like pathogenicity, resulting in pro-inflammatory response and granuloma formation. Additionally, because CNTs are composed of sp^2 hybridized carbon atoms, they possess an inherent resiliency toward degradation.

In my Ph.D. studies, we have addressed multiple facets of the growing field of carbon nanomaterials. We have synthesized a nitrogen-doped carbon nanomaterial using the process of chemical vapor deposition, which we called nitrogen-doped carbon nanotube cups. These doped nanostructures can be conceptualized as stacked cups, which can be separated into individual

cups through mechanical grinding. Characterized through a variety of microscopic and spectroscopic methods, we observed that the presence of nitrogen functionalities on the cups' open basal rims allows for cross-linkage, forming nanocapsules capable of encapsulating a desired cargo. We also hypothesize that the presence of nitrogen functionalities will increase their biocompatibility for drug delivery and imaging applications.

To address the realm of "nanotoxicity", we have performed investigations of benign degradation methods, specifically enzymatic catalysis, to oxidize carbon nanomaterials. We have observed that incubation of carbon nanomaterials with a peroxidase-based enzyme (such as horseradish peroxidase) with low levels of H_2O_2 (40 μM) results in the oxidation of carbon nanomaterials to CO_2 gas over ten days at room temperature. Subsequent research has elucidated the nature of interactions between carbon nanotubes and enzymatic cofactors. These studies, thus, elucidate a benign approach to degrade carbon nanomaterials, typically oxidized under harsh acidic conditions or thermal oxidation in air.

TABLE OF CONTENTS

LIST OF TABLES

LIST OF FIGURES

PREFACE

I would first like to express my deepest gratitude to my research advisor Dr. Alexander Star, who has continued to challenge me to push my limits. He has always granted me the permission to pursue my curiosity in lieu of the established direction of the research group. We may not have always known the way we were going, but the journey was one of immense intellectual stimulation and jubilation. He has truly influenced the way I perceive the world, and I hold him personally accountable for my transition into independent scientific thought. As a mentor, I appreciate all the insight he has been able to provide, the frustrations we have faced together, and the excitement of ground-breaking results. As a colleague, I have always been grateful for his faith in my abilities and an unwavering confidence in what could be achieved.

I would also like to thank all past and present members of the group and collaborators for their help and friendship throughout this process. In particular, I would like to thank Gregg P. Kotchey for bearing with me in my daily stresses and providing an atmosphere that is genuinely lighthearted, Matthew B. Keddie, and Katherine Durgin for their assistance in data collection. At times, I needed all the hands I could get, and you both were beyond reliable. To Yifan, Yanan, Ding, Yong, Pingping, Ian, Brian, and Harindra, I wish you all the very best and many future successes. And to Doug, thank you for getting me established and setting the bar so high.

Additionally, I would also like to thank the members of my committee, Dr. Stephen Weber, Dr. Adrian Michael, and Dr. Valerian Kagan, for their insight over the past four years, not only in the direction of my research, but also in my future aspirations as a scientist.

I would also like to thank my parents, Richard and Kay Allen, who spent countless hours making me the man I am today, for encouraging me to pursue my ever-changing dreams, allowing me to make my own mistakes, and giving me the strength and support to endeavor this process. To my grandfather, who I believe has always been with me, facing challenges head on, and who I am proud to be compared to. To my in-laws, Richard and Theresa Coopie, my home away from home. You have been as supportive as anyone could be, and have always provided an atmosphere where I could unwind. It's an honor to be able to call you mom and dad. To Becca, my partner in crime, I thank you for being the little sister I never got to have (or wanted…just kidding). It will be a sad day if you separate from the rest of us to start your life. To my friends, Ben, Joey, David, and Justin, thank you for your words of encouragement and support throughout this process.

And finally, to the love of my life…Kristen, this has been the most exhausting process I have ever had the privilege to experience. Thank you for guiding me through it. Without your love, honesty, and faith, I could not have pushed as far as I have. For being snowed in with me and suffering through my workaholic nature, for forcing me out of my shell when I didn't know what I was missing, for being my best friend, I am forever indebted.

1.0 INTRODUCTION

An allotrope of carbon, carbon nanotubes (CNTs) are elongated members of the fullerene[1] family comprised of carbon atoms arranged in cylindrical fashion. Typically these structures can range on the order of 1 - 3 nanometers in diameter for the single-walled variety or tens to hundreds of nanometers in diameter for the multi-walled variety. In addition, typical lengths average from a few microns to centimeters long, giving them an extraordinarily high aspect ratio (length to width). It is this aspect ratio that gives rise to interesting applications in a multitude of disciplines. Because CNTs are electrically conductive, they have been utilized as one-dimensional wires in electronics applications. Composed entirely of surface atoms, CNTs are afforded the unique opportunity to sense changes in a local chemical environment. Indeed, by implementing such a material in electronics applications, resistors and transistors have been made to act as sensors for chemical[2] and biological species.[3] Furthermore, their small size and all-carbon composition offer the ability to integrate these 1-D structures, not only as sensing elements, but also into biological environments as composite materials.[4] It is these fundamental aspects of carbon nanotubes that allow for probing of chemical species, gases, and biologically significant environments, thus aiding in the basic understanding of complex interactions in a variety of systems.

1.1 PHYSICAL AND ELECTRONIC STRUCTURE

In 1991, Sumio Iijima discovered carbon nanotubes in the multiwalled variety while studying the surface of carbon electrodes used in an electric-arc discharge apparatus employed to make fullerenes.[5] These needle-like carbon fibers had diameters of 4-30 nm and a length of 1 μm. Later, in 1993 Iijima[6] and D. S. Bethune[7] simultaneously published the discovery of a single-walled variety with diameters of ~ 1 nm. These discovered carbon nanotubes can best be conceptualized by considering a 2-dimensional sheet of graphene, an atomically thin layer of sp^2 hybridized carbon, rolled up into a cylindrical shape[8] as shown in **Figure 1**. Multiwalled carbon nanotubes (MWNTs), as shown in **Figure 1**, consist of many concentrically nestled tubes separated by a distance of 3.4 Å between adjacent walls. The other common variety of nanotubes, single-walled carbon nanotubes (SWNTs), contains only one graphitic wall, as shown by the inner most concentric CNT in **Figure 1** (colored blue).

The intrinsic properties of carbon nanotubes, in terms of electronic structure, can be derived from their chirality, or in a more conceptual sense, how the single graphene sheet is rolled to form a cylinder. As such, there is a variety of ways that this sheet can roll upon itself, such as direct overlap or at a particular angle. Typically, this "roll-up" geometry is described by two specific vectors, termed roll-up vectors and labeled as (n, m)[9] as shown in **Figure 1, C**. Again, based upon a graphene model, each carbon atom within the graphitic lattice has three sp^2 electrons bonded to each nearest neighbor and one $2p_z$ electron, which projects normal from the axial surface, thus creating a delocalized π-electron system.[10] The roll up vectors describe the relative overlap of these orbitals and indicate whether the system is metallic, satisfying the conditions n-m values equal 3k or 0 where k is any integer value, or semiconducting for all other values not satisfying this condition.

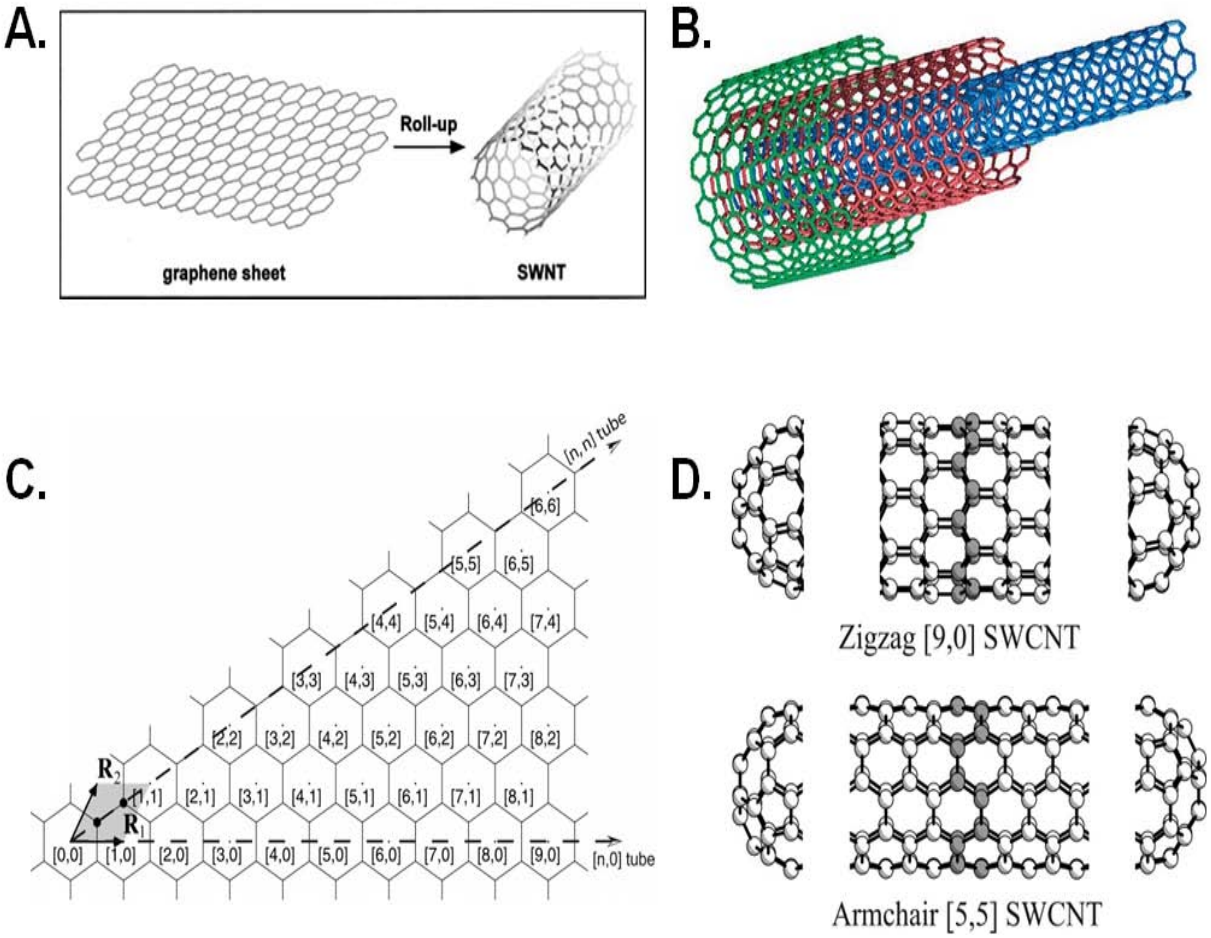

Figure 1. A) Conceptual analogy of carbon nanotube (CNT) formation by "rolling up" of a single sheet of graphene. B) Representation of multiwalled carbon nanotube (MWNT) where concentric walls are spaced 3.4 Å apart. Innermost blue region represents a single-walled carbon nanotube (SWNT). C) Graphene sheet depicting roll up vectors (n, m). Vector pairs designate roll up notation. D) Schematic of zigzag and armchair nanotube formation.

To give a more thorough explanation to this phenomenon, metallic CNTs have a finite density of electronic states (no band gap) at their Fermi level – the position between valence and conduction bands. For our purposes, we can loosely define the top of the valence band and the bottom of the conduction band as the CNT highest occupied molecular orbital, HOMO, and lowest unoccupied molecular orbital, LUMO, respectively. In contrast to metallic CNTs, semiconducting CNTs have a region of forbidden electronic states between the HOMO and LUMO, and therefore possess a band gap. Specific classifications of carbon nanotubes with varying roll up vectors have also been given: armchair nanotubes have roll-up vectors such that n = m, also denoted (n, n). Zigzag CNTs satisfy the condition such that the roll up vectors are (n, 0) as demonstrated in **Figure 1, D**. Lastly, chiral nanotubes must satisfy the condition ($n \neq m$).

1.2 CARBON NANOTUBE SYNTHESIS

Currently, there are three predominant techniques employed for the synthesis of carbon nanotubes: (i) arc discharge,[5] (ii) laser ablation,[11] and (iii) chemical vapor deposition.[12] While there are other methods including flame synthesis,[13] liquid hydrocarbon synthesis,[14] and plastic pyrolysis,[15] these methods are not currently developed to the capacity of those previously mentioned. As such, we will briefly describe the process of arc discharge and laser ablation, with a more lengthy discussion of chemical vapor deposition, since this is the technique we currently employ.

Highly crystalline MWNTs were first discovered by Iijima, as previously mentioned,[5] in soot formed by the direct current (dc) arc discharge method. The principle of this technique is the generation of an electric arc between two closely spaced (<1 mm), graphite electrodes under

an inert atmosphere of helium or argon.[16] Additionally, this process (shown in **Figure 2, A**) is typically carried out at reduced pressures of 50 – 700 mbar.[16] To synthesize carbon nanotubes using this technique, a direct current, between 50 and 120 A carried by a driving potential of ~30 V creates a high-temperature plasma (3000 °C) between the two electrodes.[16] During the arcing, a deposit forms on the cathode while the anode is consumed.[17] In the interelectrode plasma region, the carbon electrodes sublime and condense rapidly to form CNTs and other carbon by-products. This deposit presents a cigar-like structure in which a gray shell is forned around the periphery (**Figure 2, B**). The inner core of this electrode, however, is where carbon nanotubes are formed, as well as polyhedral graphene particles. Single-walled carbon nanotubes can additionally be produced by this method by the simple modification of changing to Fe-graphite electrodes.[6] It is here that the first "hints" of requiring a metal catalyst for SWNT growth are shown, as will be discussed later.

The premise of a second synthesis technique, laser ablation, is very similar to that of electric arc discharge. The use of high-powered lasers in conjunction with high temperature furnaces offers another alternative to the arc discharge approach in producing both SWNTs and MWNTs. In this technique, laser vaporization of a graphite target in a silica tube with inert argon atmosphere takes place. This whole system (**Figure 2, C**) is confined to a high temperature furnace at ~1200 °C, thus generating MWNTs.[18] As is shown, an NdYAG laser is typically used to vaporize the graphitic target, and subsequent condensing and collection occurs on a cooled water trap. Also similar to the arc discharge technique is the process to produce SWNTs from laser ablation. In order to produce SWNTs using this technique, it is necessary to use metal particles, which catalyze the reaction. In this sense, *Thess et al.*[19] were the first to produce SWNT bundles (**Figure 2, D**) by using a graphite-Co-Ni target. These bundles mainly

contained (10,10) nanotubes packed in crystalline form, however when other groups tried to repeat this procedure less than 20% exhibited this type of chirality, indicating the difficulty of reproducibility using this technique.[20] It is mainly important to mention the disadvantages of this technique. In particular, laser ablation is not economically advantageous, as the process involves high purity graphite targets, the additional expense of the high powered lasers, and the yield of nanotubes is not nearly as high as the last technique we will discuss.

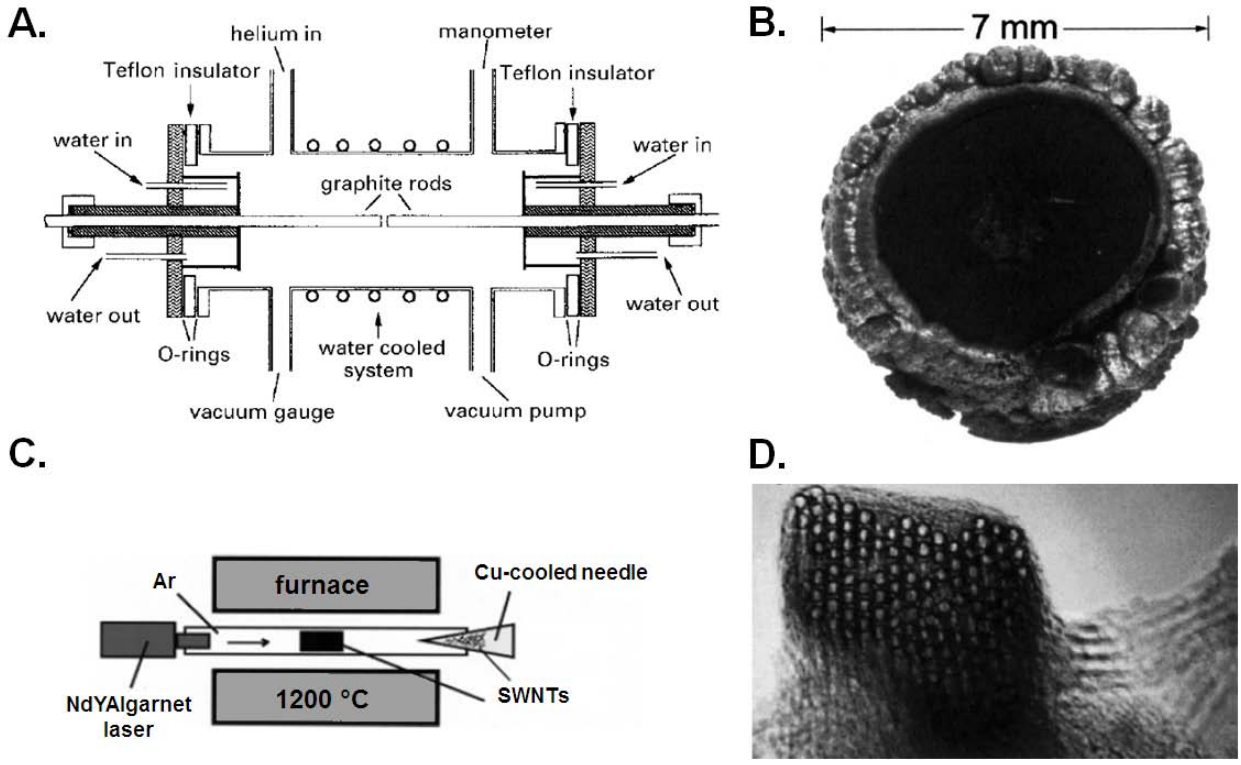

Figure 2. A) Illustrative schematic of electric-arc discharge apparatus. Helium provides the inert atmosphere, while a vacuum pump reduces the internal pressure in the chamber containing high-purity graphite electrodes. B) Optical image of a graphite electrode used in electric arc discharge. Cigar-like structure is clearly evident with nanotube growth being predominantly contained to the soft, dark interior portion. C) Illustrative schematic of laser ablation apparatus. An NdYAG (Neodymium-doped yttrium aluminum garnet) laser vaporizes a graphite-Co-Ni target to produce SWNTs. D) Transmission electron microscope (TEM) image of SWNT bundle produced by laser ablation technique.

Chemical vapor deposition (CVD) is currently one of the most common techniques for growing CNTs of both multi- and single-walled varieties. The technique is essentially a thermal dehydrogenation reaction in which transition metal catalysts lower the temperature required to decompose a hydrocarbon feedstock into component carbon and hydrogen. Because of its inherent operational simplicity, many variant techniques have been reported including, (i) floating catalysts,[21] (ii) fluidized beds,[22] (iii) fixed beds,[23] (iv) aerosols,[24] and (v) combination methods[25] such as laser- and microwave-assisted CVD.

To cover this method from a basic perspective, there are two main aspects involved in the CVD process: catalyst preparation and type, and the actual reaction itself. Catalysts are commonly prepared using one of four specific methods: (i) impregnation,[26] (ii) sol-gel,[27] (iii) metallo-organic CVD,[28] or (iv) co-precipitation.[29] In addition to these techniques, catalyst preparation may be formed *in situ* via the decomposition of volatile metallo-organic compounds within the reactor and without the use of a substrate. This type of preparation method is known as the floating catalyst method.[30] Reaction methods, though they vary slightly, are typically initiated by the introduction of a gaseous or liquid carbon feedstock, at moderate temperatures between 500 and 1000 °C. **Figure 3** shows both a schematic view of a typical CVD apparatus and a photograph of our own house-built CVD reactor for illustrative purposes. In this arrangement, typically used for a fixed-bed mechanism, a cross-flow set up is used inside a horizontal furnace where hydrocarbon vapors decompose onto the solid catalyst bed to form CNTs.

CVD offers excellent versatility in synthesizing nanotubes directly on to useable substrates. By growing nanotubes on a solid substrate such as a silicon wafer, these nanotubes can be immediately incorporated into electronic devices such as field-effect transistors, chemresistors, and field-emission devices.[31] This is a significant advantage over both laser ablation and electric arc discharge techniques, as no immediate applications can be realized without the further processing of nanotubes from the starting material, graphite electrodes.

While all these techniques offer some simplicity in operation, carbon nanotube growth has been at the forefront of serious conjecture among researchers. Despite this scrutiny, the exact mechanism of CNT growth is still not fully understood. However, even if this specified growth technique has yet to be completely analyzed, several factors remain constant for CNT formation: 1) a carbon source, 2) a heat energy source to achieve sufficient decomposition of the carbon source, and 3) especially in the case of SWNTs, the presence of a transition metal catalyst.

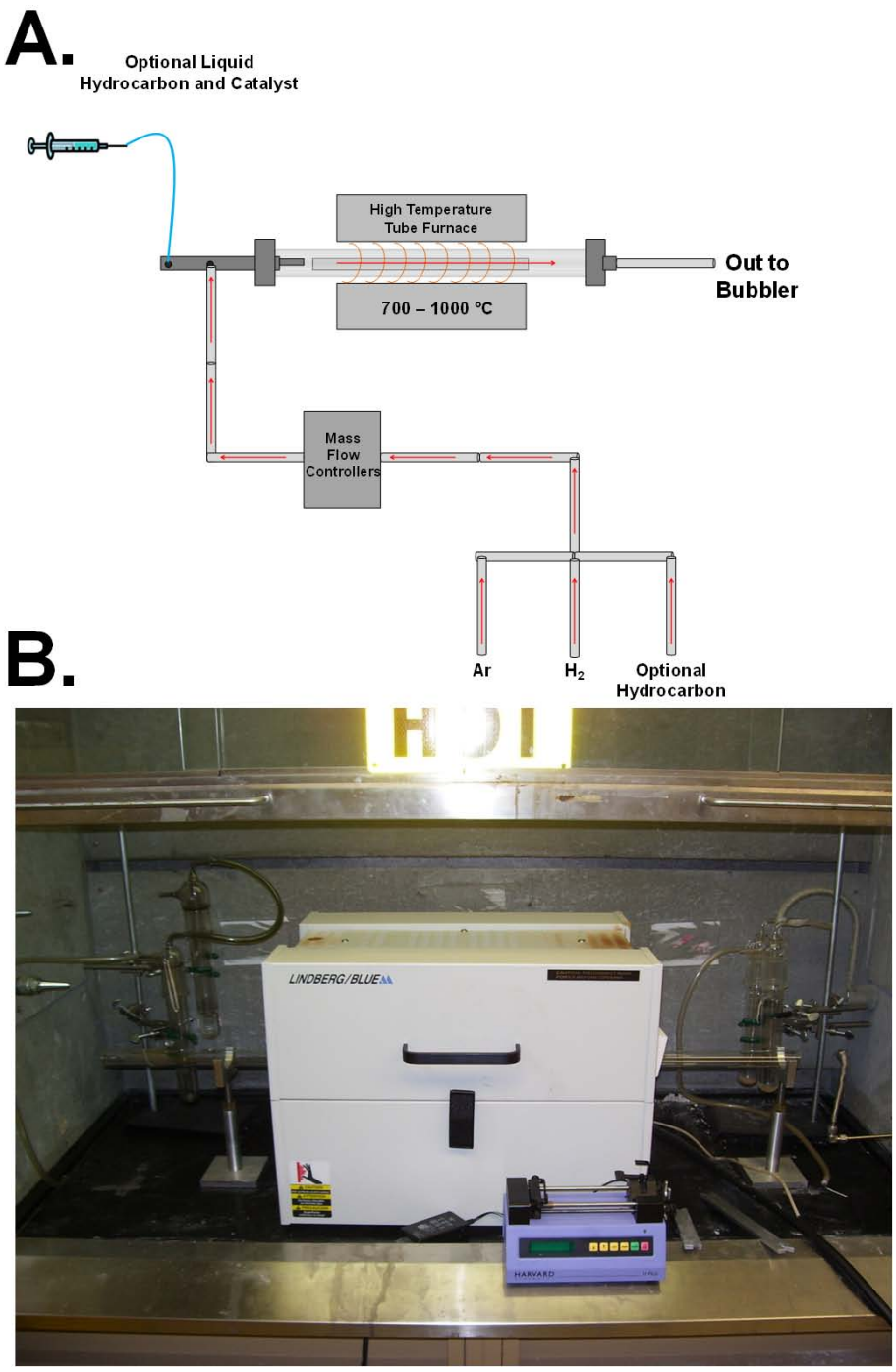

Figure 3. A) Schematic illustration of a typical chemical vapor deposition (CVD) reactor with optional gas and liquid feedstock ports. B) Photograph of our current CVD reactor.

1.3 CARBON NANOTUBE TOXICITY

While carbon nanotubes have been garnishing more applications in commercialized products, as well as biological applications, an intrinsic drawback has yet to be discussed: they have shown a variety of toxic and cytotoxic effects. Of some disconcertment, carbon nanotubes (needle-like in shape) have been compared to asbestos.[32] Exposure and the industrial use of asbestos has led to a global pandemic of lung diseases. Studies of exposed populations showed that the main body of the lung was a target for fibrous asbestos, resulting in granuloma formation and scarring.[33] Toxicologists have, thus, derived a benchmark in which a hazardous asbestos fiber is thinner than 3 μm, and longer than ~20 μm, without breaking into shorter fibers.[34] Additionally, concentrations must be reached to cause chronic activation of inflammatory cells, leading to fibrosis and cancer in the target tissue.[35]

An analogous comparison between asbestos and carbon nanotubes has led researchers to assess the inherent health risk of such fiber-like nanoparticles. It has been recently shown that certain modifications of multiwalled carbon nanotubes can induce mesothelioma in mice following intraperitoneal injection.[36] However, these findings (specific for long, unfunctionalized MWNTs) are exceptionally difficult to extrapolate to other carbon nanotube types.[37,38] Moreover, MWNTs have been excluded from those with carcinogenic potential according to a recent two-year bioassay study, which utilized intraperitoneal injection.[39] Such studies have demonstrated that fiber-length and bio-persistence are the key physical properties that may be relevant for potential toxicity, suggesting that short (functionalized) carbon nanotubes will be preferred for future biomedical product development.

Regarding single-walled carbon nanotubes, available toxicological data are still fragmentary and subject to criticism as no definitive consensus has been established. For instance, *in vivo* studies demonstrated strong inflammatory response from carbon nanotubes that reach the lungs in animal models.[40] In a second study, cytotoxic responses and apoptosis during *in vitro* cellular studies were observed as a result of incubation with SWNTs and MWNTs.[41] However, in spite of this work, other *in vivo*[42] and *in vitro*[43] studies have demonstrated low or no toxicity associated with carbon nanotubes. This discrepancy may be due to a lack of appropriate methods of characterization of nanomaterials prior to and after exposure to living cells or animals, as well as inadequate exposure protocols.[44] Furthermore, the inherent inhomogeneous nature of CNT samples may be responsible for contradictory results. Researchers have, thus, started investigations into certain aspects of CNTs for their potential role in toxicity. These have included (1) the length of carbon nanotubes, (2) the role of residual catalytic material, (3) and the degree of hydrophilicity.

1.3.1 Role of CNT Length

Several studies have attempted to elucidate the influence of CNT length on overall toxicity. Subcutaneous injection of chemically "cut" MWNTs of two length regimes, 220 nm and 825 nm, resulted in a pro-inflammatory response from both lengths.[45] However, the inflammatory response lessened for those CNTs at 220 nm length due to the ability of macrophages to readily engulf the fibers of smaller length. A second investigation studied the toxicity effects of MWNT exposure within the mesothelial lining, or lung lining, of mice. Poland *et al*. demonstrated that MWNTs with lengths greater than 20 μm promoted a pro-inflammatory response and the formation of granuloma lesions in the mesothelial lining, an analogous behavior to asbestos

exposure.[46] Short, tangled MWNTs, on the other hand, elicited only a minor inflammatory response. Such minimization of inflammation was once again attributed to the ability of macrophages to engulf CNTs, quelling their toxic effects. These studies demonstrate the influence of carbon nanotube length, albeit other factors such as surface functionality must still be considered.

1.3.2 Role of Residual Catalytic Material

As previously mentioned, transition metal catalysts are often used for the synthesis of carbon nanotubes, resulting in their encapsulation within a graphitic lattice or surface adsorption on a graphitic lattice.[47] It is possible to remove these transition metal particles; however, this generally requires treatment by harsh acids[48] or heating at high temperatures.[49] Studies have shown that the presence of residual metal catalyst in commercial CNT samples resulted in an increased cellular concentration of reactive oxygen species (ROS).[43] Conversely, CNTs that had been acid-treated to remove residual catalytic material demonstrated little to no ROS formation. This was similarly confirmed in studies where Fe-containing CNTs promoted oxidative stress and antioxidant concentration reduction for macrophages relative to CNTs stripped of iron by thermal and acid treatment.[50] Based on these preliminary results, the presence of transition metal catalysts promotes the formation of ROS that causes oxidative stress. The production mechanism is highly analogous to the process of Fenton catalysis,[51] known to produce hydroxyl radicals (•OH) through the homolytic cleavage of hydrogen peroxide (H_2O_2).

1.3.3 Degree of Hydrophilicity

Not so surprisingly, carbon nanotubes (utilized in both hydrophobic, pristine form and oxidized, hydrophilic form) contribute differently to overall toxicity. Thus far, it appears that more hydrophilic CNTs demonstrated enhanced cytotoxicity, relative to pristine, as-prepared CNTs. For example, Bottini *et al.* showed that oxidized CNTs (dose: 400 μg/mL) induced apoptosis in T cells.[52] Contrary to this, pristine CNTs elicited minimal inflammatory response, presumably stemming from aggregation in an aqueous environment and possibly increasing the ease of macrophage isolation. As imparted hydrophilicity to oxidized CNTs results in their increased dispersivity and difficulty in isolation by macrophages, there is a higher probably of increased cellular dispersion, which may be responsible for their pro-inflammatory responses and even apoptosis.

1.4 OVERVIEW OF RESEARCH PROGRAM

The work reported herein discusses a multifaceted approach to the field of nanotechnology, specifically from a carbon nanomaterials viewpoint. We consider new nanomaterials development, impending toxicities and methodologies to mitigate these effects, and useful applications derived from carbon nanomaterials.

Chapter 2.0 details the synthesis of novel carbon nanomaterials known as nitrogen-doped carbon nanotube cups (NCNCs). Utilizing the synthetic process of chemical vapor deposition, NCNCs are formed by the addition of a nitrogen precursor (such as acetonitrile) with a hydrocarbon precursor of ethanol (EtOH) and iron catalyst (ferrocene) to form carbon fibers that

are inherently segmented, analogous to the stacking of Styrofoam cups. Such fibers were characterized by a variety of methodologies including scanning electron microscopy (SEM), transmission electron microscopy (TEM), and atomic force microscopy (AFM). Characterization revealed the ability to separate the "stacked-cup" fibers into individualized cups, possessing an open basal rim and closed conical top. Further AFM analysis revealed the presence of functionalities on the open basal rim, capable of hydrogen bonding to a hydrophilic surface. These groups were subsequently manipulated utilizing bioconjugation schemes through biotinylation and incubation with streptavidin-coated gold nanoparticles (GNPs). Using force volume measurements, it was possible to monitor the relative adhesion forces between modified and unmodified-cups participating in hydrogen bonding. Such studies provided indirect results alluding to the presence of nitrogen functionalities, primarily concentrated on the open basal plane.

Chapter 3.0 extends the study of nanocups by further exploiting the primary concentration of nitrogen functionalities on the open basal rim. We demonstrated that by the simple addition of a fixing agent, such as glutaraldehyde, nanocups can be cross-linked to form nanocapsules. Furthermore, these capsules are capable of encapsulating a wide variety of cargo, presumably through a capillary action-like effect. In our studies, we have encapsulated commercially-available gold nanoparticles (mean diameter: 5 nm, sodium citrate capped) by their addition to separated nanocups *prior* to cross-linkage. Internalization was monitored by tracking the surface plasmon resonance peak exhibited by GNPs, as well as characterization by AFM. The general applicability of this approach was further demonstrated by the encapsulation of fluorescent quantum dots, specifically ZnS nanoparticles doped by Tb^{3+}.

In Chapter 4.0, we focus on controlling the volumetric parameters of nanocapsules by first controlling the physical parameters of the starting fibrous material. As it has been previously demonstrated that the diameters of carbon nanotubes can be controlled by implementation of monodispersed catalyst particles, we investigated the diameter control of NCNCs by synthesizing a variety of monodispersed iron catalyst particles in the following size regimes: 1-5 nm, 5-10 nm, and 10-20 nm. Using a thermal decomposition reaction involving iron pentacarbonyl ($Fe(CO)_5$), all three size regimes were synthesized by adjusting the carbon chain length of our capping agent (fatty acids). CVD synthesis was then performed with a fixed-bed growth mechanism. Results demonstrated diameter distributions proportional to catalyst particle size. We further controlled the segment lengths of NCNCs by adjusting the concentration of N-precursor relative to hydrocarbon precursor. Concentrations of 1%, 5%, and 9% NH_3 in EtOH were used to alter segment length. As expected, increasing the concentration of N-precursor resulted in smaller segment lengths. Furthermore, after forming capsules with the synthesized material, interior loading capacity diminished proportionally to diameter and segment length.

Chapter 5.0 focuses on toxicity mitigation of carbon nanomaterials. Single-walled carbon nanotubes (as well as MWNTs) possess intriguing physical properties, as well as intrinsic resilience/stability as a result of their sp^2 hybridized carbon structure. As CNTs have been compared to asbestos, our contribution investigated a benign way to remove or oxidize carbon nanotubes without harsh oxidizing agents or high temperature thermal decomposition. In our work, horseradish peroxidase (HRP) was incubated with carboxylated SWNTs at 4°C. The addition of 40 μM H_2O_2 initiated the enzymatic degradation of SWNTs over the course of 16 weeks. Transmission electron micrographs demonstrated the shape deformation of the

nanomaterial as a function of time. Degradation was further confirmed with techniques such as dynamic light scattering (DLS), gel electrophoresis, thermogravimetric analysis (TGA), and absorbance spectroscopy. Initial results also demonstrated a preference for large diameter SWNTs over that of smaller diameter SWNTs present in a commercially available sample (Carbon Solutions, Inc.).

In Chapter 6.0, a fundamental investigation of the mechanism of enzymatic degradation is detailed. In this work, we examined the preferential degradation of carboxylated SWNTs over hydrophobic, pristine SWNTs. With the implementation of HRP, H_2O_2 is heterolytically cleaved to form Compound I and H_2O. Because of this mechanism proximity between the active enzymatic cofactor and SWNT must be established for oxidation to occur. Thus, we observe hydrophilic SWNTs that presumably bind close to this cofactor are degraded, while pristine SWNTs (which bind at a distal site) remain intact. We further investigated this mechanism by "deconstructing" the HRP enzyme into progressively smaller units such as a heme porphyrin and iron (III) chloride salt. Both the porphyrin and iron salt promoted the degradation of both carboxylated and pristine SWNTs, alluding to a homolytic cleavage of H_2O_2 that produces scavenging hydroxyl (•OH) and hydroperoxyl radicals (•OOH), non-specific in their oxidation of substrates.

In Chapter 7.0, additional publications in which I had a contributing role are described. Such research includes fundamental investigations of stacked carbon nanotube cups as catalytic material in oxygen reduction reactions, understanding the sensor response of metal decorated single-walled carbon nanotubes towards carbon monoxide adsorption, utilization of a human myeloperoxidase enzyme for the degradation of carboxylated single-walled carbon nanotubes,

and implementation of single-walled carbon nanotube networks in resistor architectures for gas detection.

Finally, Chapter 8.0 summarizes the work and suggests future direction for each of the projects, including nanocapsule development and extensions of enzymatic degradation. Chapter 8.0 also discusses the importance of each of these projects separately, and presents an overarching outlook on the future of carbon nanomaterials and nanotechnology.

2.0 SYNTHESIS, CHARACTERIZATION, AND MANIPULATION OF NITROGEN-DOPED CARBON NANOTUBE CUPS

Abstract

Isolated, carbon nanotube cups with diameters of 12-40 nm have been synthesized by chemical vapor deposition through incorporation of nitrogen atoms into graphitic carbon structure and subsequent mechanical separation. Incorporation of nitrogen affords carbon nanotube cups with a unique composition comprising multiwalled, graphitic lattice with nitrogen groups on the exterior rim and hollow interior cavities. These nanostructures demonstrate the ability to participate in hydrogen bonding because of nitrogen functionalities on their open edges. Furthermore, reaction with these nitrogen functionalities results in the coupling of gold nanoparticles (GNPs) to the open rim of carbon nanotube cups. Through atomic force microscopy manipulation and adhesion force measurements, we compare the mobility of these structures on a hydrophilic surface before and after GNP coupling. Understanding of these forces will aid in useful nanostructure assembly for energy and medical applications.

For this work (published in *ACS Nano* **2008**, *2*, 1914), I contributed by performing electron microscopy (both SEM and TEM). AFM characterization and manipulation was performed in tandem with Padmakar Kichambare and me. All conceptualization and planning of the experiments was performed by all authors.

2.1 INTRODUCTION

Recent development of carbon nanostructures has drawn much attention in a multitude of fields due to their intrinsic structure, mechanical and electrical properties, and compatibility with biologically significant systems. Interest in such systems has branched out from carbon fullerenes[53] and carbon nanotubes[54] towards other novel carbon nanomaterials such as graphitic onions,[55] cones,[56] nanohorns,[57] nanohelices,[58] nanobarrels,[59] and graphene.[60] All of these unique carbon nanomaterials show promising capabilities for applications in electronic sensors, as catalyst support, energy storage, and drug delivery.[61]

Of particular interest is the design and implementation of hollow nanostructures for utilization of their inherent cavities. For instance, it has been highly desirable to tailor nanostructures for the specific task of drug delivery and biomedical applications.[62,63] Initial studies have thus utilized the interior cavities of multiwalled carbon nanotubes for biomedical applications through ferromagnetic filling.[64] Such structures are promising for medical treatments including magnetically guided hypothermia.[64] Furthermore, nitrogen-doped cup-like structures have been proposed for applications as electrodes for probing DNA nucleotides.[65] These types of structures are also valuable for energy applications.[66] Inherent cavities create an ideal medium for hydrogen[67,68] and lithium storage,[69] and utilization for field emission.[70]

To pursue the continuing progress of such materials, we have synthesized and probed hollow, graphitic nanomaterials, nitrogen-doped carbon nanotube cups, otherwise known as carbon nanobells.[71] These structures are synthesized and then characterized by a variety of microscopy techniques. In these structures, nitrogen atoms are incorporated into graphitic structure on the edges as pyridine-like nitrogen and in the interior, where nitrogen substitutes carbon atoms.[72-74] In this study, we test the reactivity of the nitrogen functionalities in terms of their interactions with functionalized surfaces and by their conjugation with gold nanoparticles (GNPs). AFM manipulation and adhesion measurements reveal strong hydrogen bonding between hydrophilic surfaces and unmodified cups that can be alleviated by GNP coupling, thus enhancing their mobility on the surfaces

2.2 EXPERIMENTAL

2.2.1 Chemical Vapor Deposition Growth and Separation of Carbon Nanotube Cups

Cups were grown using the technique of CVD with a liquid precursor. Briefly, a Lindberg/Blue tube furnace was utilized at 950 °C. Using a three-foot long, sealed quartz tube (2.5 cm inner diameter), cups were made by passing a liquid precursor consisting 5.0 g MeCN, 1.25 g ferrocene, and 93.75 g of EtOH at a rate of 5 mL/ hr for one hour. Carrier gases included Ar at 422 sccm and H_2 at 125 sccm. After one hour, the furnace, liquid injector, and H_2 gas were terminated, allowing for a 1-hour cool down time in an argon atmosphere. The cup film was then collected off a quartz plate using a one-sided razor blade.

Separation of the stacked, as-prepared cups was done following the previously reported procedure.[71] The cup film was placed in a mortar and grinded with a pestle along with a drop-wise addition of EtOH. This grinding motion allowed for the physical separation of cups by breaking the van der Waals attraction between them. The solvent was then allowed to evaporate and the solid product collected for future use.

2.2.2 Decoration of Cups with Gold Nanoparticles

Approximately 1 mg of separated cups was suspended in N, N-dimethylformamide (DMF) (Sigma Aldrich) via ultrasonication for approximately 20 minutes. After a stable suspension was formed this was allowed to react with an excess of 5mM (+)-Biotin N-hydroxy-succinimide ester (Sigma Aldrich) in DMF for 24 hours at room temperature. The suspension was then centrifuged at 3400 rpm for 20 minutes. Supernatant was discarded and the cup-biotin complex was re-suspended in 10% ethanol via ultransonication.

Streptavidin (*from Streptomyces avidinii*) coated gold nanoparticles (~10 nm nominal) in buffered aqueous glycerol solution were purchased from Sigma Aldrich. This concentrated sample was then diluted 100X with deionized water. The reaction between the streptavidin coated nanoparticles and cup-biotin complex was allowed to occur by mixing them at a ratio of 1:100 (cups to GNPs). We found best results occurred when incubation occurred at room temperature.

2.2.3 Characterization Methods

The SEM images were obtained with a Philips XL-30 FEG microscope. The electron beam accelerating voltage of the SEM was held at 10.0 keV for all images. The cup samples, both as-prepared and separated, were probed as a powder fixated on to carbon tape without any heavy metal coating.

Low-resolution TEM images were obtained with a Philips/FEI Morgagni microscope. The electron beam accelerating voltage of the TEM was held at 80.0 keV for all imaging. All cup samples were prepared by suspension in DMF or EtOH and drop casting on a lacey carbon TEM grid (Pacific Grid-Tech) and allowing the solvent to evaporate completely. For imaging of streptavidin/cup bioconjugates, samples were stained with 2% uranyl acetate for improved contrast. Stain was dropped on the sample and grid, and allowed to dry for ten minutes before excess stain was blotted away with filter paper.

High-resolution TEM images were obtained with a JEOL JEM-2100F field-emission microscope. The electron beam accelerating voltage of the HRTEM was held at 200 keV for all imaging. Energy filtering was performed for zero point energy loss. All sample preparation remained the same as with the low-resolution microscope.

AFM characterization was carried out on a Multimode scanning probe microscope (Veeco). Tapping mode with super sharp tips (AppNano ACL-SS) allowed for intricate manipulation and characterization.

Characterization of separated cups was carried out by freshly cleaving mica with double-sided tape. An aqueous solution of 0.01% poly-L-lysine (20µL) was spin-coated on the mica at 100,000 rpm for one minute, followed by washing with an equal amount of deionized water. This was then allowed to dry for 45 minutes before spin coating one drop of cups suspended in DMF or, in the case of decorated cups, suspended in 10% EtOH. After all solvent evaporated, this was then characterized via tapping mode at a scan rate of 2.98 Hz and a drive frequency of 187.630 kHz.

2.3 RESULTS AND DISCUSSION

2.3.1 Nanocups: Synthesis and Characterization

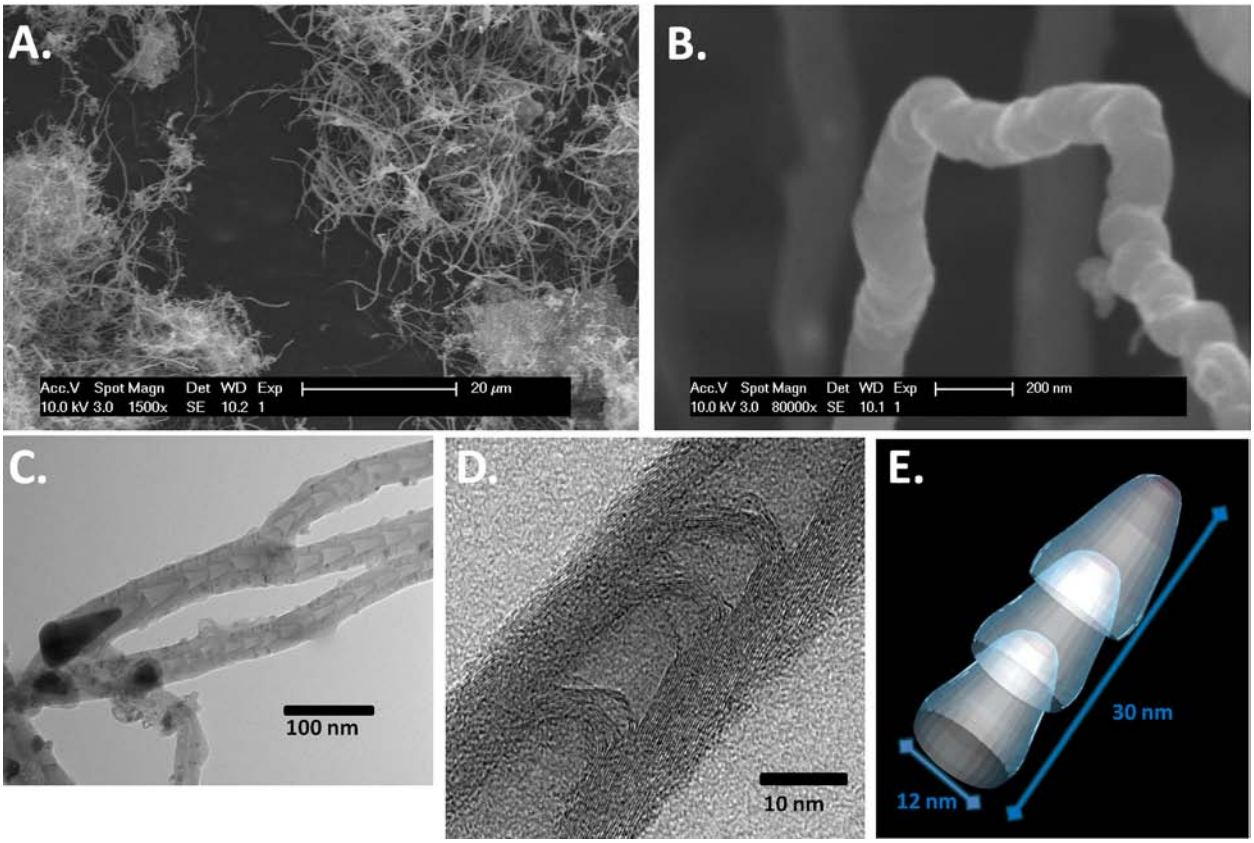

Figure 4. Synthesis of stacked nitrogen-doped carbon nanotube cups. (A,B) SEM images of as-prepared cups. C) TEM image reveals that fibers consist of stacked cups. D) High resolution energy-filtered TEM image of stacked, multiwalled cups. E) Translucent schematic cartoon illustrating orientation of cups with respect to nearest neighbor.

Nanotube cups were synthesized using chemical vapor deposition (CVD) from liquid carbon/nitrogen precursors. Specifically, a mixture of EtOH, ferrocene, and MeCN was injected at a rate of 5 ml/hr, using H_2 and Ar carrier gases into a CVD furnace at 950°C for one hour. Thermal decomposition of this mixture of nitrogen and hydrocarbon precursors over an *in situ* generated iron catalyst results in carbon nanotube cup growth on a quartz plate inside the reactor. Approximately 2-3 mg (~50% yield) of the as-prepared graphitic product was isolated as a black film layered on the quartz plate, which was peeled off with the aid of a razor blade. Scanning electron microscopy (SEM) reveals that this material is fibrous (**Figure 4, A**). The fibers, typically 1-4 microns long and diameters ranging from 12-40 nm, appear as a thick carpet under low magnification. At higher magnification, an individual fiber appears with inherent "kinks" and twists along the tubular axis (**Figure 4, B**). We used Transmission Electron Microscopy (TEM) to make a closer examination of the fibers and elucidate their growth process. A TEM image (**Figure 4, C**) reveals that fibers are composed of stacked cups with diameters which are defined by the size of iron catalyst nanoparticles (dark spots in the image) as seen in the case of two nanoparticles merging into one. The Fe catalyst particle is shown undergoing compression strain, which also contributes to the stacked nature of the cups, as the catalyst is ejected to form a new cup. Individual nanotube cups thus grow as conical, self-contained stacks to create an individual fiber. Their conical structure, caused by nitrogen doping at the open-edge of the nanotube cup, has been theoretically and spectroscopically examined and found to be highly dependent on the nitrogen concentration during the growth process.[75,76] This growth mechanism and structure[77] is similar to what has already been shown previously with the growth of bamboo-like carbon nanotubes.[78] High- resolution transmission electron microscopy (HRTEM) reveals the intricate lattice structure (**Figure 4, D**). Additionally, N-doping of the carbon nanotube cup

lattice was determined at 2-7% by electron energy loss spectroscopy (EELS) (see supporting information). As with multiwalled carbon nanotubes where all lattice walls are parallel along the longitudinal axis, carbon nanotube cups deviate from this general schematic. The walls of the cups extend from the curvature of the individual structures diagonally outward, but never running in parallel along the long axis. Due to this growth formation, nanotube cups are intrinsically isolated from each other in a "stacked" conformation. This allows for the inherent separation of cups held together by van der Waals forces and an outer layer of amorphous carbon.

Mechanical separation, performed by grinding with a mortar and pestle, results in a black carbon powder of single nanotube cups. **Figure 5** illustrates these separated cups and the structure they possess. As can be seen in **Figure 5, A**, even though the cups are physically separated from one another, they tend to aggregate together, presumably due to hydrogen bonding between each other through varying types of nitrogen functionalities located on their open rim. **Figure 5, B** and **C** further highlight the features of the cups, i.e. the hollow interior and multiple walls (c.a. 30 walls) encompassing the structure.

Individual nanotube cups, isolated as a black powder, are opened to further investigations using Atomic Force Microscopy (AFM). Utilizing this technique provides valuable characterization, manipulation, and adhesion information.

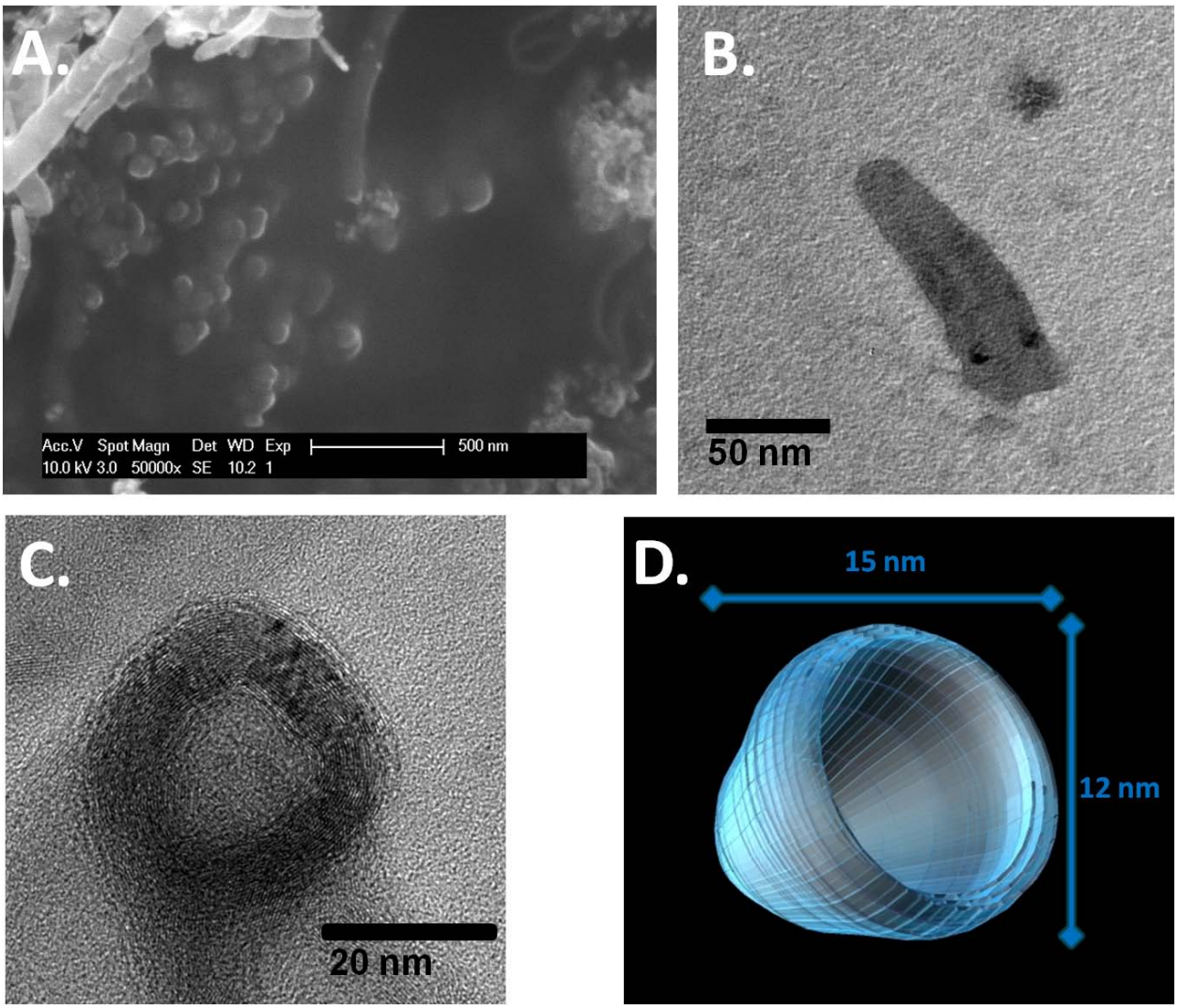

Figure 5. Separation of stacked cups. A) SEM image of separated cups fixated to carbon tape. B) Low-resolution TEM image of a separated cup. C) High-resolution energy-filtered TEM image of a single, separated cup. D) Translucent cartoon of a single, separated cup illustrating its multiple walls and hollow interior.

2.3.2 AFM Characterization and Manipulation

Using AFM on a piece of freshly cleaved mica coated with 0.01% poly-L-lysine,[79] we could clearly distinguish cups as having a uniform height distribution narrowed to the range of 12-40 nm in height. Use of a sharp AFM probe (2-3 nm) is sufficient to map out the topology of the cups in terms of orientation on the treated mica surface. **Figure 6, A** shows this conical orientation via a 3-D topographical image. Furthermore, the phase image of **Figure 6, B** depicts lighter portions in the center of the nanotube cup structure, indicative of a peak rather than a depression that would be seen if we were observing the open side of the cup. Presumably, amine and amide groups of poly-L-lysine, which can form hydrogen bonds with the nitrogen functionalities of nanotube cups, give this specific "open-side-down" orientation (**Figure 6, C**). This orientation implies the presence of nitrogen atoms on the open edge of the cups, as was implicated in their growth mechanism.

Using the force of the tapping mode probe, we manipulated the cups across the mica surface by varying the force modulation. By increasing or decreasing the amplitude set point of the AFM, we can effectively extend or retract the tip to the mica surface.[80] This extension, therefore, acts as a means to mechanically manipulate the structures. We have observed that while nanotube cups easily move on an untreated mica surface (Supporting Information), they are strongly fixated to the poly-L-lysine treated mica surface (**Figure 6, D**). As can be seen from the figure, the cups could be moved, however only with excessive damage. In addition to the proposed hydrogen bonding, another source deterring nanotube cup movement in this orientation could be tribological processes occurring between the mica surface and the open side of the carbon nanotube cups.[81] Optimum adhesion forces, i.e. friction, occurs when then the contacting surfaces perfectly conform to each other during the critical moment of pull-off, or when the tip

forces movement to occur.[82] That being stated, we must assume that while there may not be perfect conformity between these two surfaces, even partial conformity must contribute to the determent of movement. Additionally, it also must be included that nitrogen doping within the interior lattice structure causes inherent defects, thus weakening the overall mechanical stability of the nanotube cup.[83,84]

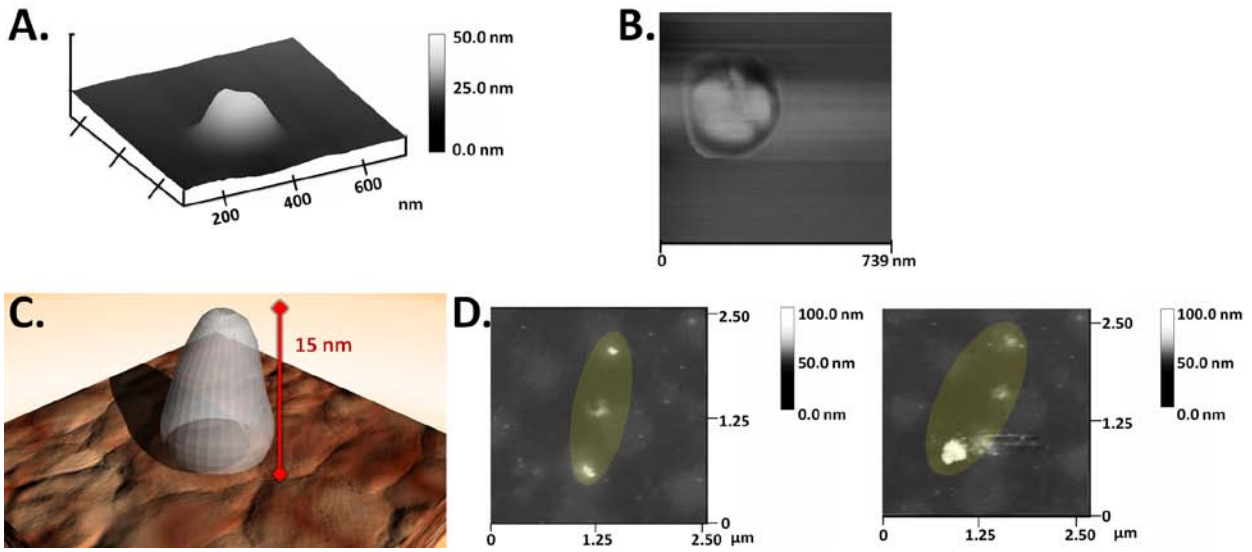

Figure 6. AFM characterization and manipulation of unmodified cups. A) 3D AFM rendering of carbon nanotube cup oriented "open side" against a mica surface treated with poly – L – lysine (0.01%). B) AFM phase image of carbon nanotube cup orientation. White color indicates peaks. C) Translucent cartoon of a single nanotube cup oriented on a treated mica surface. D) Mechanical manipulation of unmodified cup on treated mica surface.

2.3.3 Bioconjugation of Nanocups with Gold Nanoparticles

To defer this fixation through hydrogen bonding on a hydrophilic surface, we sought to modify these basal nitrogen groups with gold nanoparticles. Through biotinylation of carbon nanotube cups and the corresponding reaction with streptavidin-coated GNPs, we were able covalently decorate the open edge of the cups. Cups were reacted with (+)-Biotin N-hydroxy-succinimide ester in DMF at room temperature. After re-suspending this complex into a 10% ethanol solution, we were able to combine streptavidin-coated GNPs in buffered solution to incubate. Following complete incubation (typically 24 hours), we further characterized and manipulated the hybrid product via AFM in tapping mode. **Figure 7, A** and **B** show the topology of GNP-decorated cups. We can see the general structure is maintained by a single cup in the center surrounded by GNPs decorating the exterior, open-edge. We further visualize this by a low-resolution TEM image shown in **Figure 7, D**. It is evident that the GNPs only decorate this open edge of the carbon nanotube cup, as approximately five GNPs of 10 nm or less are visible.

Additionally, as this sample was negatively stained with 2% uranyl acetate for improved contrast,[85] we can still see the streptavidin surrounding the materials. Incomplete biotinylation may have been responsible for the non-uniform distribution of GNPs around the exterior edge. Further section analysis of this self-complexed structure can be found in the Supporting Information. Incubation of unmodified cups with streptavidin-coated GNPs results in a lesser degree of attachment, presumably due to hydrogen bonding between streptavidin and the cups' nitrogen functionalities (Supporting Information). Therefore, biotinylation of cups is essential for GNP attachment.

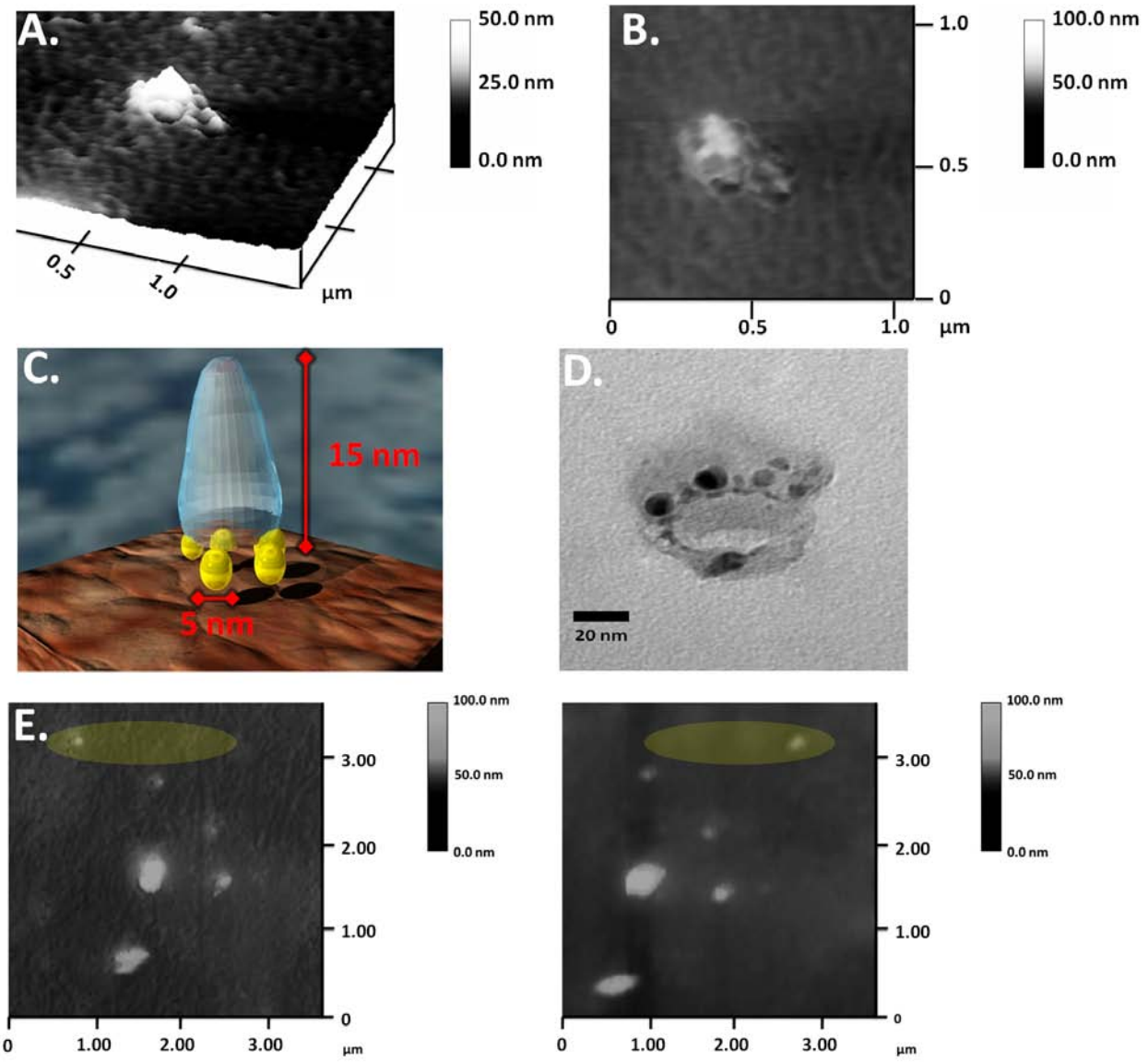

Figure 7. AFM characterization and manipulation of GNP-decorated cups. A) 3D AFM rendering of a GNP-decorated, carbon cup on a treated mica surface. B) AFM height image of GNP-decorated, carbon cup. Lighter portions indicate peaks. C) Translucent cartoon indicating the decoration preference of GNPs on the open side of the cup structure. D) Low-resolution TEM image of a GNP-decorated carbon nanotube cup. E) Mechanical manipulation of GNP-decorated cup on treated mica surface.

Using the aforementioned parameters for tapping mode manipulation, we proceeded to determine whether we had deterred the fixation of cups through hydrogen bonding to a treated mica surface by the simple covalent attachment of GNPs. **Figure 7, E** illustrates the manipulation of GNP-decorated cups using the same conditions as listed above. As observed from this image, it is quite evident that the modified cup is now free to be manipulated through probe force. In addition, it is seen that there is no structural deformation upon manipulation, indicating that the hydrogen bonding and tribological effects between sample and substrate have indeed been minimized.

2.3.4 Quantitative Adhesion Force Measurements

To quantitatively measure the impact of adhesion through hydrogen bonding and subsequent determent through modification, force plots[86] in contact mode on the AFM were performed. The spring constant of our contact mode probe was first calculated using reference cantilevers (See Supporting Information). Surface images were then resolved in contact mode, prior to switching over to "force calibrate" mode to acquire a deflection sensitivity. It is important to note that the deflection sensitivity measurement was accurate as long as the laser spot position was not changed, i.e. for the current sample. After acquiring this value (typically ~ 240 nm/V), the AFM was set to force volume mode where ten force measurements were made on cups both unmodified and decorated each (See Supporting Information). Adhesion forces could thus be calculated using values obtained from force volume plots, as well as the deflection sensitivity, and spring constant. **Figure 8, A** correlates adhesion forces for both unmodified and decorated cups. As can been seen there is no correlation between cup size and adhesion forces. Furthermore, it is evident that far less adhesion forces are involved in GNP-decorated cups.

While force plots typically measure interactions between the sample and tip, we have already shown that cups have the same orientation regardless of modification. In these instances, a silicon probe is interacting with the graphitic, conical shell of the cup (**Figure 8, B**). Only basal modification is imparted to these structures, indicating any variations in adhesion forces must be a result of sample/substrate interactions. Due to the presence of GNPs, there is a decrease in tribological effects as well as hydrogen bonding through passivated nitrogen groups of the cups.

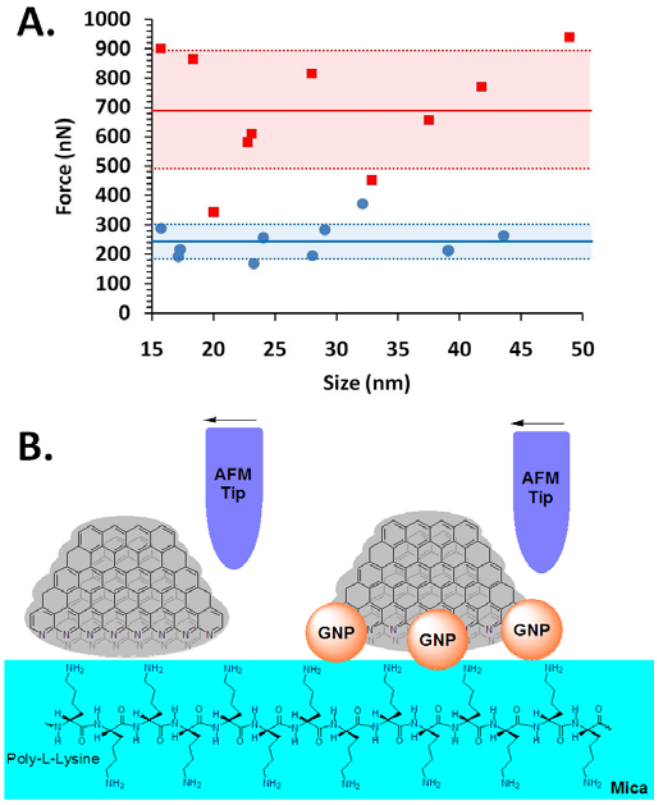

Figure 8. AFM experiment. A) Comparison of adhesion forces versus cup's size for unmodified (■) and GNP-decorated (●) cups. Solid lines indicating average force and corresponding shaded areas (standard deviations) show statistically significant differences in adhesion of unmodified cups as compared to GNP-decorated cups. B) Scheme demonstrating AFM manipulation experiment, where (left) mobility of unmodified cup is affected by hydrogen bonding between pyridine-like nitrogen functionalities on cup's edges and poly – L – lysine, and (right) improved by attachment of GNPs.

2.4 CONCLUSIONS

To conclude, we have shown the synthesis of a versatile material and subsequent characterization and AFM manipulation. By showing that these structures have nitrogen atoms and can indeed be utilized for assembly, opens up venues for many alternatives for this material. Decoration of cups with GNPs in this manner exploits the nitrogen groups on the exterior of these structures, a versatile point for "capping". By using the hollow interior for drugs and capping the structures through amide linkage, it may be possible to create a nanoscopic delivery platform. Additionally, because of their "cup-like" shape, these structures can be used for nanocontainers, isolating reactions within their interior. With further exploration into this structure and "bottom-up" assembly, we can truly realize the full potential of these nanostructures in electronics, energy, biomedical, and chemical applications.

2.5 ACKNOWLEDGMENTS

The microscopy work was performed using the resources of the NanoScale Fabrication and Characterization Facility (NFCF) and the Department of Materials Science and Engineering, University of Pittsburgh.

2.6 SUPPORTING INFORMATION

Supporting information for Chapter 2.0 ‘Synthesis, Characterization, and Manipulation of Nitrogen-doped Carbon Nanotube Cups’ can be found in **Appendix A**. The data available includes electron energy loss spectroscopy (EELS) of nitrogen-doped carbon nanotube cups (**Figure 29**) as well as AFM manipulation of unmodified nanocups (**Figure 30**), section analysis of GNP-decorated cups (**Figure 31**), 3D topographical AFM imaging of cups decorated with GNPs without biotinylation (**Figure 32**), AFM imaging of free GNPs (**Figure 33**), spring constant calculations, force volume plots **(Figure 34 and Figure 35**), adhesion force calculations and statistical data.

3.0 GRAPHITIC NANOCAPSULES

Abstract

Nitrogen-containing carbon nanotube cups are crosslinked with glutaraldehyde to form capsule-shaped nanostructures. Introduction of commercially available gold nanoparticles prior to the crosslinkage process results in their encapsulation within the interior cavity of the linked structures. A similar encapsulation of ZnS:Tb nanoparticles shows the general applicability of the encapsulation system. Such a facile protocol alludes to drug-delivery and energy-storage applications.

For this work (published in *Adv. Mater.* **2009**, *21*, 4692), my contribution involved the synthesis of nanocups, crosslinking with glutaraldehyde, and encapsulating cargo including commercially available gold nanoparticles. I also performed electron microscopy, atomic force microscopy, and absorbance spectroscopy analysis. Chad Shade performed time-resolved luminescence studies on ZnS:Tb nanoparticles and encapsulated nanoparticles. Adrienne Yingling synthesized the ZnS:Tb nanoparticles. All authors contributed to the designing of experiments and interpretation of data.

3.1 INTRODUCTION

Carbon nanomaterials have made vast strides in a variety of fields including biological and materials sciences.[87] Synthesis of hollow carbon nanomaterials such as fullerenes[1] and carbon nanotubes[5] are particularly useful for their inherent capacity to contain materials. This containment has been demonstrated by encapsulation of metal nanoparticles and C_{60} within the hollow interior of CNTs,[88] alluding to applications in drug delivery, which are typically dominated by the field of polymer nanocapsules.[89,90] Although the wetting and capillarity of CNTs is an active area of research,[91,92] such encapsulation into hollow carbon nanomaterials is typically performed at high temperatures during their synthesis[93] or by their opening under oxidative conditions,[94] limiting the ability to encapsulate a wide range of organic molecules. Here we demonstrate cross-linkage of nitrogen-doped carbon nanotube cups (NCNCs) via incubation in 4% glutaraldehyde for the formation of graphitic nanocapsules with hollow interiors. We found that the use of basal nitrogen functionalities on adjacent NCNCs leads to a crosslinkage through this common fixing agent. Moreover, we demonstrate the encapsulation of gold nanoparticles (GNPs) or lanthanide-containing ZnS:Tb nanoparticles into NCNCs, where they are subsequently trapped through the linkage process. In addition to being chemically inert, this system affords a facile encapsulation process with the capacity to hold varying cargo within the interior cavity. We anticipate our encapsulation method to be the starting point of more sophisticated drug delivery or storage systems.

The desire for creating hollow nanostructures and utilizing inherent cavities is becoming more predominant, as applications for drug delivery and medical diagnostics become increasingly popular.[95,96] For instance, it has been demonstrated that CNTs can be filled with a chemotherapeutic agent that inhibits the growth of tumour cells.[97] Furthermore, it has been

shown that such hollow nanomaterials may encapsulate fluorescent molecules for potential application in diagnostic imaging.[98] In the realm of energy applications, hollow nanomaterials have found use primarily as storage media for lithium and hydrogen.[99,100] While these applications demonstrate novelty and practicality, facilitating such work is difficult. In our study, we utilize synthesized NCNCs for the encapsulation of commercially available GNPs as well as ZnS:Tb nanoparticles through simple glutaraldehyde crosslinking, thus taking advantage of inherent nitrogen functionalities on the basal rim of these structures.

3.2 EXPERIMENTAL

3.2.1 Crosslinkage of NCNCs

Approximately 0.1 mg of NCNC powder[101] was suspended in pure ethanol (EtOH; 10 mL) through ultrasonication for 5 min. Following the appearance of a stable suspension, 4% glutaraldehyde in EtOH (500 µL) was added to the suspension and allowed to incubate for 24 h before characterization.

3.2.2 Synthesis of ZnS:Tb Nanoparticles

A reaction mixture of zinc stearate (0.4801 g), tetracosane (4.1180 g), and octadecene (5 mL) was heated to 360 °C for 2 h, while stirring under nitrogen. After dissolution of the cation precursor within the reaction mixture, the dopant lanthanide (Tb) mixture consisting of $Tb(NO_3)_3$ (0.0601 g), toluene (0.5 mL), octadecene (2.5 mL), and trioctylphosphine (TOP) (2

mL) was injected rapidly and left to stir for 1 h at a reduced temperature of 300 °C. Subsequently, a solution consisting of sulfur (0.0090 g), toluene (0.5 mL), and octadecene (2.5 mL) was injected to initiate the nucleation of nanoparticles. Aliquots were withdrawn at various times (1-120 min), and particle sizes of ~2-4 nm further purified by dissolution in butanol followed by precipitation in methanol. Precipitated nanocrystals were re-dissolved in octanol to remove excess solvent (octadecene/tetracosane), and precipitated once more with methanol.

3.2.3 Encapsulation of GNPs or ZnS:Tb Nanoparticles into NCNCs

Similarly to crosslinkage, approximately 0.1 mg of NCNC powder was suspended in EtOH through ultrasonication for 5 min. Concurrently, commercially available GNPs (Sigma-Aldrich) were diluted in pure EtOH at a 16:1 ratio (EtOH to stock solution). Following the appearance of a stable suspension of NCNCs, the diluted GNPs (or ZnS:Tb) were added at a volume of 500 µL. This suspension was then re-sonicated for another 5 min before 4% glutaraldehyde was added and incubated for 24 h.

3.2.4 Characterization Methods

Low-resolution TEM images were obtained with a Philips/FEI Morgagni microscope. The electron-beam accelerating voltage of the TEM was held constant at 80 keV for all imaging. All samples were suspended in EtOH, dropcasted onto a lacey-carbon TEM grid (Pacific Grid-Tech), and allowed for the solvent to evaporate completely.

AFM characterization was carried out on a Multimode scanning-probe microscope (Veeco). Samples were prepared by spin-coating NCNCs and their variations (suspended in EtOH) onto a freshly cleaved sheet of mica. After 45 min of drying in ambient conditions, the images were taken. Tapping-mode experiments using Supersharp tips (AppNano ACL-SS) (~2 nm) allowed for the intricate characterization of all samples.

Time-resolved emission and excitation spectra were collected on a Varian Cary Eclipse fluorimeter, coupled to a personal computer with software supplied by Varian. Scans were collected with 10 flashes, a 5.0 ms gate time, a 0.5 ms delay time (if no other value is stated), and a 20.0 ms total decay time. Excitation and emission slits of 20 nm were used. An automated filter set was used for all excitation and emission scans. Samples were placed in 1-mm quartz fluorescence cells purchased from NSG Precision Cells, Inc. (Farmingdale NY). Spectra were smoothed using OriginPro (version 7.0).

3.3 RESULTS AND DISCUSSION

3.3.1 Growth, Characterization, and Separation of NCNCs

NCNCs were prepared as mentioned previously.[101] **Figure 9** shows a schematic representation of the initial synthesis process. Thermal decomposition of hydrocarbons over the *in situ* generated catalyst perpetuates the growth of graphitic fibers. These fibers, typically 1 – 4 μm in length and 12-40 nm in diameter, appear as stacked, conical segments under transmission electron microscopy (TEM) images (**Figure 9**, right). In addition to the induction of multiple nitrogen functionalities, unique to this hybrid material is the nitrogen doping within the graphitic

lattice that forces the lattice walls to run in parallel, diagonally outward from the main long axis, thus isolating each segment from its nearest neighbor.[101] Mechanical grinding of stacked NCNCs with a mortar and pestle breaks the van der Waals attraction between them and exposes various possible nitrogen functionalities on the open basal plane. With this methodology, individualized NCNCs are removed from their "stacked" conformation and are further opened to subsequent manipulation by cross-linkage with 4% glutaraldehyde in EtOH.

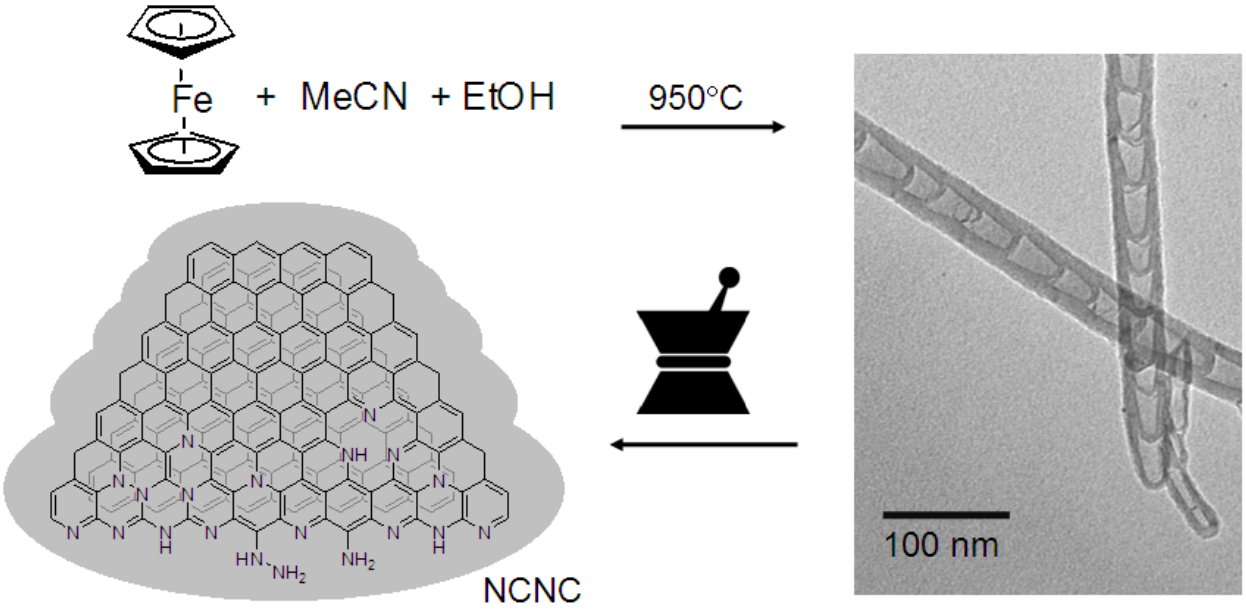

Figure 9. Schematic representation of the preparation of NCNCs. Chemical vapor deposition (CVD) from ferrocene, acetonitrile (MeCN), and ethanol (EtOH) creates stacked NCNCs. Mechanical separation with a mortar and pestle separates the stacks into isolated structures with varying plausible nitrogen functionalities including aniline- and hydrazine-type functionalities that can react with glutaraldehyde to form aromatic hemi-aminal, imine, and hydrazone compounds. The rightmost image displays the TEM image of the stacked-cup formation of NCNCs.

3.3.2 Capsule Formation

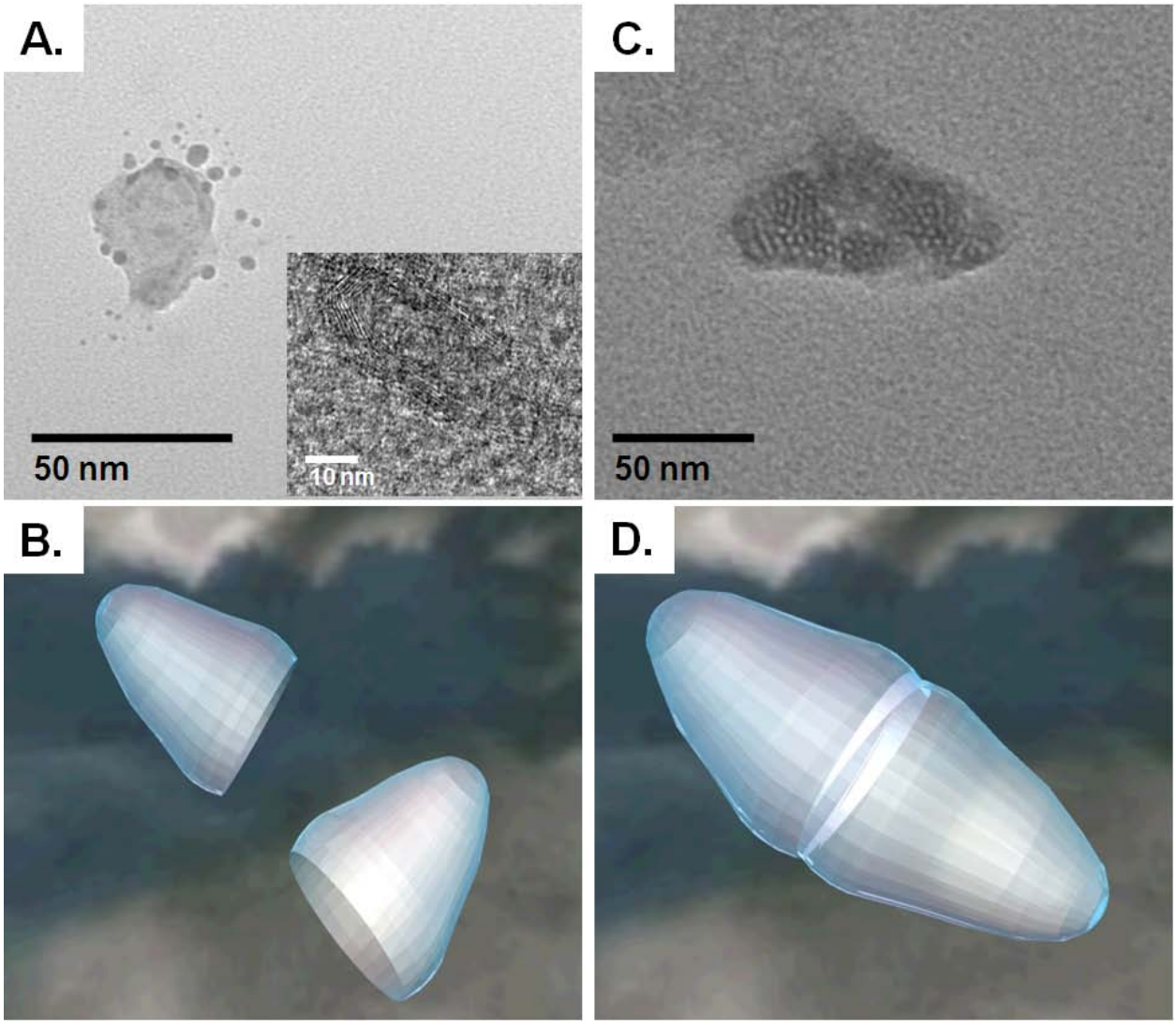

Figure 10. A) TEM image of a single separated NCNC. The graphitic lattice structure is clear from the high-resolution TEM image (inset). B) Cartoon illustration depicting adjacent, separated NCNCs. C) TEM image of crosslinked NCNCs. D) Cartoon illustration depicting the crosslinkage of NCNCs.

Figure 10, A shows the TEM image of a single, separated NCNC. As can be seen, the single, NCNC is approximately 40 nm in length with an "open" end and a curved cap as reported previously.[101] High-resolution TEM imaging (inset) shows that these cup-like structures consist of multiple walls (~10 walls shown). A cartoon image, as shown in **Figure 10, B**, further illustrates the separated NCNCs. Due to the presence of nitrogen functionalities on the basal "open" plane of these structures, we are able to crosslink two neighboring NCNCs of similar diameter, as will be explained further. **Figure 10, C** shows the TEM image of such crosslinked NCNCs. The linked structure is approximately 80 nm in length and exhibits a "capsule" shape, in contrast to the separated structures. A cartoon image shown in **Figure 10, D** further illustrates the crosslinking between proximal structures. Presumably, the reaction of the nitrogen groups on the base of NCNCs with glutaraldehyde leads to the formation of covalent bonding between the "linker" molecules and the NCNCs.

3.3.3 Nanoparticle Encapsulation

Progressing further with the utilization of this system, it is desirable to establish the capability for encapsulation during the crosslinkage process as a step towards functional nanocapsules. Thus, we investigated the capture of commercially available GNPs of an approximately 5 nm (mean) diameter. The basal openings of NCNCs are 20-30 nm in diameter, accommodating for such small particles to penetrate the inner cavity. As such, the addition of GNPs in solution to a suspension of NCNCs prior to the addition of 4% glutaraldehyde should allow for the encapsulation of particles within the inner cavities of the crosslinked structure.

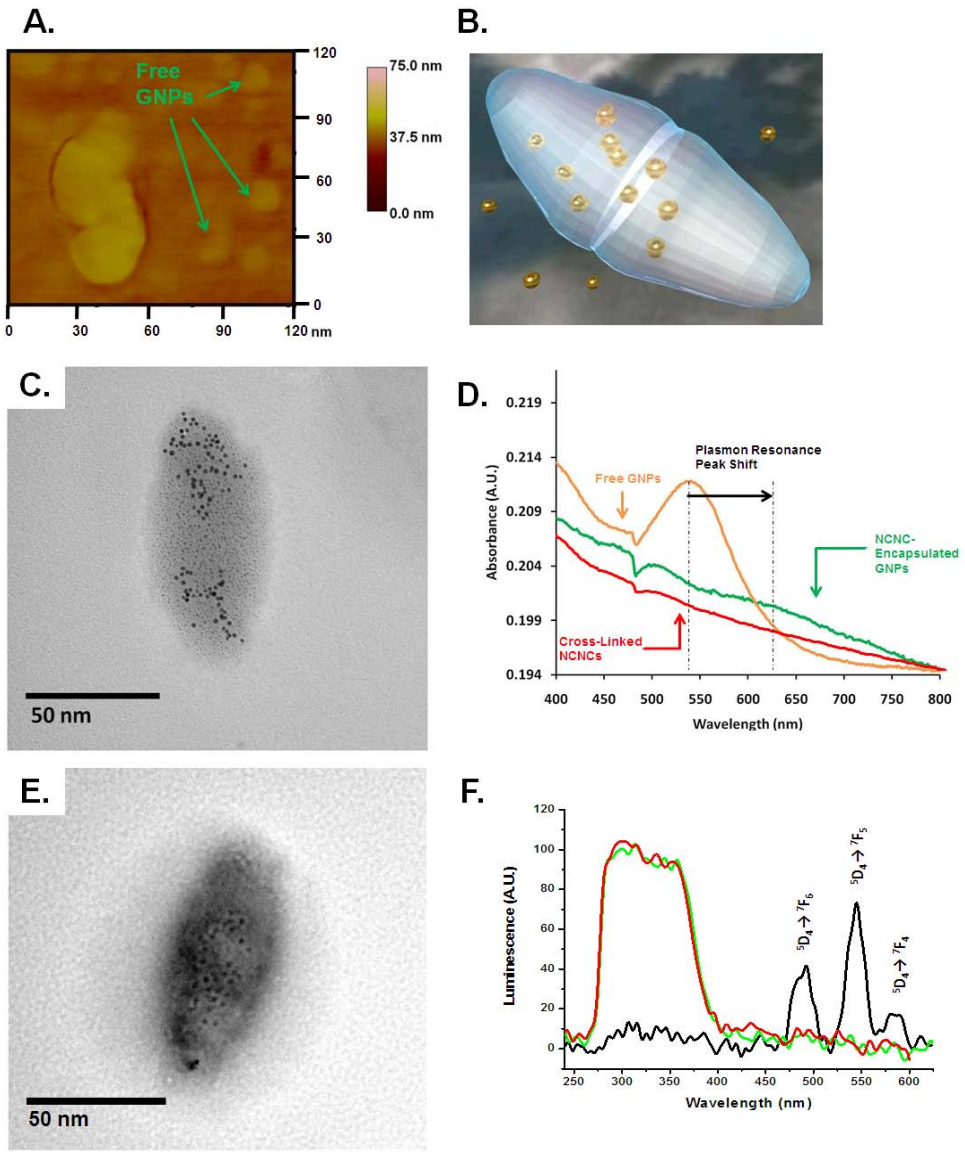

Figure 11. A) AFM image of crosslinked NCNCs with GNPs. Free GNPs are seen sporadically in the field of view as indicated. B) Cartoon illustration of the crosslinkage of adjoining NCNCs with interior confinement of GNPs. C) TEM image of crosslinked NCNCs encapsulating GNPs (~5 nm in diameter) in the interior cavities. D) UV/Vis spectra of free GNPs, vacant crosslinked NCNCs, and GNPs after encapsulation in crosslinked NCNCs. All spectra are taken in EtOH. E) TEM image of ZnS:Tb nanoparticles encapsulated in crosslinked NCNCs. Encapsulation was performed under identical conditions as GNP encapsulation. F) Time-resolved emission spectrum at an excitation wavelength of λ_{ex} = 225 nm with a 0.5 ms delay of ZnS:Tb (black), crosslinked NCNCs (red), and ZnS:Tb encapsulated in NCNCs (green).

Figure 11, A depicts an atomic force microscopy image (AFM) image of the resultant incubation. Initial observations from a height image captured in tapping mode demonstrate the successful linkage of two adjacent NCNCs, with free GNPs positioned sporadically in the surrounding field. It is worth mentioning here that minute size distortions are common in tapping mode imaging. Therefore, NCNCs and GNPs sizes were confirmed by section analysis (Supporting Information). No predominant features confirm exterior adsorption; however, because of the method of imaging, AFM did not elucidate interior confinement of GNPs. **Figure 11, B** further illustrates the results of such GNP encapsulation. TEM was utilized to prove spatial interior confinement. The GNPs appear to be confined to the interior cavity of the crosslinked NCNCs, as illustrated in **Figure 11, C**. In majority, this confinement of GNPs is centralized within two specific areas of the crosslinked structures. Both distributions appear at the topmost conical portion of each structure. Additionally, the lack of sporadic distribution of GNPs alludes to interior confinement, as opposed to exterior adsorption.

We investigated optical properties of the resulting functional system using UV/Vis spectroscopy (**Figure 11, D**). At approximately 540 nm, the surface-plasmon resonance band for free GNPs (with a mean diameter of 5 nm) is evident.[102] After incubation with NCNCs during crosslinking, the band for GNPs is greatly suppressed and appears at approximately 625 nm, significantly red shifted, as is expected according to literature for GNP aggregation.[103] These spectra are different from those of separated NCNCs and crosslinked NCNCs without GNPs (Supporting Information). In addition, control experiments, where NCNCs were crosslinked prior to the addition of GNPs, demonstrate a majority of vacant NCNCs, with rare cases of exterior adsorption of GNPs as indicated by TEM and AFM imaging. No shift of the surface-plasmon resonance band was observed by UV/Vis spectroscopy (Supporting Information). Furthermore, control experiments with 4% glutaraldehyde and GNPs incubated in EtOH show no shift of the surface-plasmon resonance band (Supporting Information).

In addition to the ease of facilitation, this encapsulation system exhibits interesting mechanistic components, resulting in larger linkage success rates. Because the linkage of two adjacent structures occurs on the open basal planes of NCNCs, there is intrinsic diameter compatibility between them. We have observed that only similar diameter NCNCs will participate in the successful crosslinkage with glutaraldehyde to make a nanocapsule. Essentially, it is thought that crosslinkage of smaller-diameter NCNCs to larger-diameter NCNCs will be less stable due to incomplete crosslinkage of the nitrogen functionalities. To satisfy this bonding scheme, structures with similar diameters must be in close proximity for capsule formation to occur. Incompatible-diameter species have been observed but are a rarity (~2%), as shown in the Supporting Information.

Presumably due to capillary action, GNPs are taken into the interior cavity of NCNCs. NCNCs are comparable to CNTs in graphitic composition and their hollow interior, and previously, it has been observed that CNTs exhibit capillary forces, resulting in entrapped species.[104] Furthermore, GNPs are able to migrate through the confines of the joint interior cavity with adjoining NCNCs (Supporting Information). Because of this simplistic uptake mechanism, other nanoparticles or molecular species should be encapsulated without significantly manipulating external conditions. Additionally, once encapsulation occurs, aggregation may ensue due to a change in the chemical environment. Commercially available GNPs are initially suspended in aqueous solution by electrostatic stabilization[105] with a variety of salts. Upon encapsulation, GNPs are surrounded by a hydrophobic shell, possibly without the presence of stabilizing salts. However, we cannot completely rule out the possibility of aggregation due to spatial confinement. In either case, such aggregation is responsible for the red shift of the plasmon resonance band discussed above and in accordance with the literature.[106]

For confirmation of capillary uptake and for a demonstration of the general applicability of this system, a control sample of ZnS nanoparticles doped with Tb^{3+} (ZnS:Tb)[107,108] (~2-4 nm in size) was used in an identical procedure. ZnS:Tb nanoparticles are encapsulated within crosslinked NCNCs as viewed by TEM imaging in **Figure 11, E**. Because of the presence of luminescent lanthanide cations within the ZnS shell, it is also possible to track the luminescence emission related to the Tb^{3+} species. Free ZnS:Tb nanoparticles (in ethanol) are shown in a time-resolved emission spectrum (recorded with a 0.5 ms delay), as demonstrated in **Figure 11, F**. Three narrow emission bands are present corresponding to the slow relaxation from the $^5D_4$ state to $^7F_1$ levels of Tb^{3+}. More importantly, once encapsulated by NCNCs through the same crosslinkage procedure ascribed for GNPs, a major change in the optical properties is observed

and the Tb^{3+} luminescence is strongly suppressed, as demonstrated in **Figure 11, F**. Such encapsulation and change in the luminescence properties further demonstrates the broad applicability of this system, including the design of photonic materials.

It is also worth mentioning here that it should be possible to tailor specific interior volumes based upon the control of the growth process of NCNCs. Previous theoretical studies have demonstrated growth dependence on the presence of the nitrogen abundance from the stock precursor.[109] The current synthesis affords NCNCs with 2-7% N-doping of the graphitic lattice.[101] However, increasing this doping effect directly by increasing the relative abundance in the liquid precursor will tailor shorter NCNCs and, thus, smaller interior cavities. Furthermore, precise control over the diameter distributions of catalytic particles should allow for a direct determination of the diameter distributions of NCNCs.

3.4 CONCLUSIONS

In conclusion, by imparting NCNCs with basal nitrogen functionalities, we were able to utilize a common fixing agent, glutaraldehyde, for the crosslinkage of two adjacent nanostructures, creating a "nanocapsule". Further to this process, we have demonstrated a capillary-uptake encapsulation method for the confinement of nanoparticles within the interior cavities of adjoining NCNCs. The results allude to applications in drug delivery and energy storage. Through the utilization of the hollow cavities for drugs or chemotherapeutic agents, followed by this crosslinkage for encapsulation, it may be possible to perpetuate a delivery platform, where simple bond cleavage releases the cargo, while leaving the carbon shell open for functionalization, thus directing the NCNCs to specific areas of the body. Moreover, it may be

possible to use the interior of these structures for catalysis or storage. Further investigations of encapsulation and subsequent "releasing" mechanisms will increase the potential applicability for such materials.

3.5 ACKNOWLEDGMENTS

Funding was provided through the University of Pittsburgh and partially through the National Science Foundation (Grant DBI-0352346).

3.6 SUPPORTING INFORMATION

Supporting information for Chapter 3.0 ‘Graphitic Nanocapsules’ can be found in **Appendix B**. The data available includes UV/Vis spectra of separated and crosslinked NCNCs (**Figure 36**), section analysis of crosslinked NCNCs encapsulating GNPs (**Figure 37**), 3D AFM profile of separated NCNC and GNP **(Figure 38**), section analysis of separated NCNCs and GNPs (**Figure 39**), TEM imaging of crosslinked NCNCs followed by GNP incubation (**Figure 40**), AFM phase imaging of crosslinked NCNCs followed by GNP incubation (**Figure 41**), UV/Vis spectra of free GNPs and GNPs added after crosslinkage of NCNCs (**Figure 42**), TEM imaging of mismatched, crosslinked NCNCs with GNPs (**Figure 43**), TEM imaging of free GNPs with 4% glutaraldehyde (**Figure 44**), UV/Vis spectra of free GNPs and GNPs with 4% glutaraldehyde (**Figure 45**), UV/Vis spectra of free GNPs, encapsulated GNPs, and separated NCNCs with GNPs (**Figure 46**), TEM imaging showing particle migration (**Figure 47**), TEM imaging of non-encapsulated GNPs (**Figure 48**), and time-resolved emission and excitation spectra of ZnS:Tb nanoparticles (**Figure 49**).

4.0 CONTROLLING THE VOLUMETRIC PARAMETERS OF NITROGEN-DOPED CARBON NANOTUBE CUPS

Abstract

Analogous to multiwalled carbon nanotubes, nitrogen-doped carbon nanotube cups (NCNCs) have been synthesized with defined volumetric parameters (diameter and segment lengths) by controlling the catalyst particle size and the concentration of nitrogen precursor utilized in the chemical vapor deposition (CVD) reaction, allowing for tailored interior cavity space of cross-linked NCNCs, *i. e.* nanocapsules.

This work, published in *Nanoscale* **2010**, *2*, 1105-1108, was a collaborative effort between undergraduate researcher Matthew B. Keddie and me. Matthew contributed by performing the thermal decomposition reaction required for varying diameter iron nanoparticle synthesis. Additionally, he performed CVD synthesis of NCNCs on varying diameter catalyst particles, as well as prepared and utilized multiple nitrogen concentrations of feedstock solution. In this work, I contributed electron microscopy characterization, atomic force microscopy characterization, dynamic light scattering analysis, and performed statistical analysis on encapsulated GNPs. All authors discussed and contributed to the experimental work plan.

4.1 INTRODUCTION

Chemical doping of carbon nanomaterials, especially carbon nanotubes (CNTs), has attracted much interest because of the ability to modify their electronic properties.[110] For instance, such modification has been performed by B and N doping.[111] It has been theoretically modeled and experimentally confirmed that N-doped single-walled carbon nanotubes exhibit metallic behavior.[112] Furthermore, the incorporation of nitrogen atoms induces structural defects resulting in novel bamboo-like fibers.[113] Essentially, induction of nitrogen during the synthesis of graphitic CNTs results in the formation of pentagons (as opposed to hexagons) increasing the curvature of the lattice,[114] observed as defects and bamboo-like morphology. If this concentration is further increased, it is possible to synthesize stacked cup-like fibers comprised of individual conical segments.[115]

Previously, we have demonstrated the synthesis of multiwalled, stacked cup-like carbon nanotubes, known as nitrogen-doped carbon nanotube cups (NCNCs), through the incorporation of nitrogen precursor during the CVD reaction.[101] These fibers, presumably because of the presence of nitrogen functionalities, exhibited electrocatalytic activity towards oxygen reduction.[116] Furthermore, treatment through mechanical grinding allowed for the separation of individual segments or "cups" from the fiber. Studies by atomic force microscopy (AFM) revealed the presence of a large concentration of nitrogen functionalities decorating the open basal plane of individual cups, allowing for the possibility of bioconjugation.[101] By the addition of glutaraldehyde, a suspension of hollow, separated cups can be cross-linked to form nanocapsules capable of encapsulating a variety of cargo such as gold nanoparticles (GNPs) or quantum dots.[117] Such studies demonstrate the versatility of synthesized nanostructures in terms of both morphology and electronic properties; however, the ability to control the volumetric

parameters of synthesized NCNCs and, in turn, the interior cavity space of nanocapsules has yet to be demonstrated. In this paper, the volumetric parameters (diameter and segment length) of NCNCs were controlled by the use of monodispersed iron nanoparticles and varying the N-precursor (NH_3) concentration. We demonstrate that the diameter of individual cups can be tuned by the use of defined diameter catalyst particles. Moreover, segment length is demonstrated to be inversely related to N-precursor concentration.

4.2 EXPERIMENTAL

4.2.1 Iron Nanoparticle Synthesis

Iron nanoparticles (FeNPs) were synthesized by the thermal decomposition of iron pentacarbonyl ($Fe(CO)_5$) as reported previously.[118] Briefly, approximately 2 mmol of $Fe(CO)_5$ was mixed with 5 mmol of a fatty acid consisting of either oleic, lauric, or octanoic acid in 10 mL of dioctyl ether. The solution was then refluxed at 286 °C under an N_2 atmosphere for 1 hour (**Figure 12**). Particles were precipitated by the addition of 20 mL of isopropyl alcohol (IPA) and centrifuged at 3400 rpm. This was followed by several washings with IPA and subsequent resuspension in hexane for further use in CVD reaction

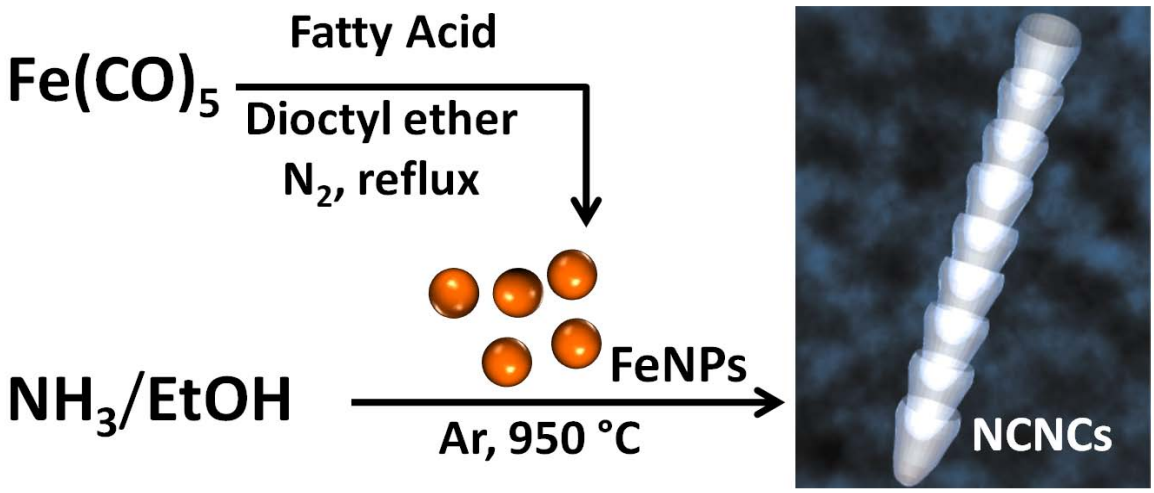

Figure 12. Synthesis of nitrogen-doped carbon nanotube cups (NCNCs) by chemical vapor deposition (CVD) reaction from NH_3 and EtOH using monodispersed Fe nanoparticles (FeNPs) as a catalyst.

4.2.2 NCNC Synthesis from Monodispersed FeNPs

Synthesized particles were further spin-coated at 1400 rpm on to a bare quartz plate (2.5 cm × 2.5 cm) and placed in a sealed quartz tube for CVD reaction. As illustrated in **Figure 12**, NCNCs were synthesized from a liquid precursor of 1%, 5%, or 9% NH_3 (wt/wt) in EtOH. Specifically, a three-foot long, sealed quartz tube (2.5 cm i.d.) was placed in a Lindberg/Blue tube furnace and heated to 950 °C. Carrier gases of Ar and H_2 with flow rates of 422 sccm and 125 sccm, respectively, were used to remove O_2 from the system. The liquid precursor of 5% NH_3 was injected at 5 mL/h for 1 h, followed by termination of the reaction by stopping the precursor. H_2 was then shut off and the system was allowed to cool in an Ar atmosphere for 1 h prior to collection of the synthesized product by sonicating the quartz plate in 15 mL of N, N-dimethylformamide (DMF).

4.3 RESULTS AND DISCUSSION

4.3.1 Diameter Control

Transmission electron microscopy (TEM) was used to characterize as-synthesized FeNPs and the resultant NCNCs. As shown in **Figure 13**, NCNCs' diameter distributions appear to be directly proportional to FeNP diameter. Using octanoic acid in the thermal decomposition of $Fe(CO)_5$, FeNPs of 12 ± 1.8 nm are produced yielding NCNCs of 33 ± 5 nm in diameter. Likewise, FeNPs synthesized with lauric acid result in an average diameter of 7.1 ± 0.8 nm, with an average NCNC diameter of 26 ± 5 nm. Synthesized FeNPs from oleic acid have an average diameter of 3.1 ± 0.6 nm with NCNCs' average diameter of 16 ± 4 nm; however, it is important to note the shape of NCNCs utilizing oleic acid-synthesized FeNPs. As shown in the top inset of **Figure 13, C**, NCNCs deviate from their typical conical morphology in exchange for a "tear-drop" shape. Presumably, a result of the high radius of curvature from oleic acid-synthesized catalyst particles, the resulting tear-drop morphology is observed. Such divergence from a conical segment structure alludes to a size threshold for radius of curvature in FeNPs in NCNC synthesis.

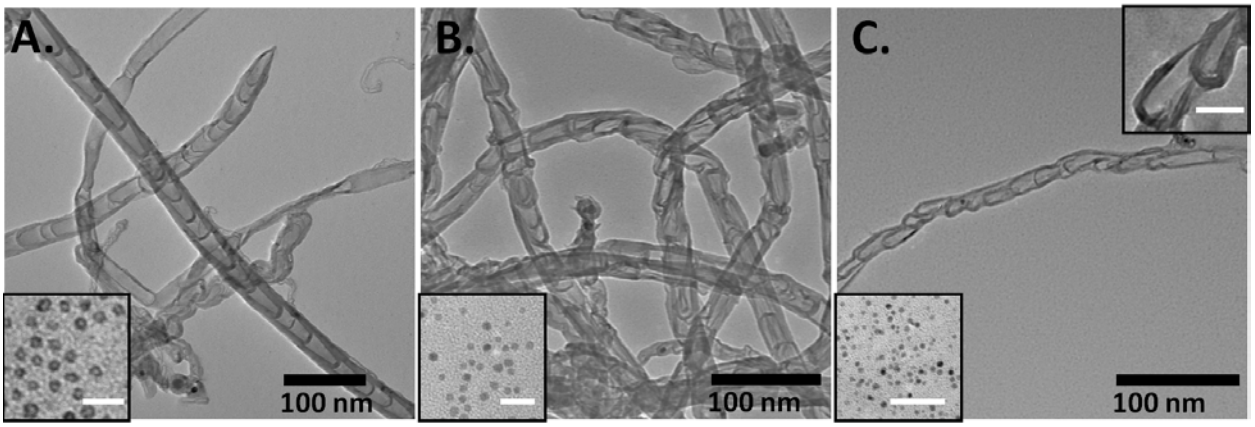

Figure 13. TEM micrograph of NCNCs synthesized from (A) octanoic acid capped iron nanoparticles (FeNPs, ~15 nm), (B) lauric acid capped FeNPs (~ 10 nm), and (C) oleic acid capped FeNPs (~5 nm). Diameter distributions of NCNCs are observed to depend on catalyst particle size (shown lower left insets, scale bar 50 nm). Inset in (C) illustrates shape deformation from a conical "cuplike" structure (Scale bar 20 nm).

Table 1 provides the resulting statistical measurements for synthesized FeNPs and corresponding NCNC diameter distributions. Moreover, dynamic light scattering (DLS) was performed to assess size discriminations in FeNP diameter distributions inherently witnessed by TEM (Supporting Information). As listed, slight variance between TEM and DLS measurements of FeNPs are observed. Because NCNCs are fibrous 1-D structures, DLS measurements were not performed as spherical estimations would prove disingenuous. Shown in the Electronic Supplementary Information, AFM was also used to assess the size of synthesized FeNPs of varying diameter. Briefly, particles were spin-coated from hexane on a bare piece of mica. Tapping mode imaging was then implemented to visualize particles, followed by cross-sectional height analysis to measure 20.8 nm, 12.4 nm, and 2.7 nm for FeNPs synthesized using octanoic, lauric, and oleic acids, respectively.

Table 1. FeNP Diameter Distributions

Fatty acid	Diameter of FeNPs	Diameter of NCNCs
Octanoic acid	16 ± 3 nm[a] (12.5 ± 1.8 nm)[b]	33 ± 5 nm
Lauric acid	8 ± 2 nm[a] (7.1 ± 0.8 nm)[b]	26 ± 5 nm
Oleic acid	5 ± 2 nm[a] (3.1 ± 0.6 nm)[b]	16 ± 4 nm

[a] TEM data. [b] DLS data.

4.3.2 Effect of N-Doping on Segment Length

We further controlled the volumetric parameters of NCNCs and experimentally elucidated the role of N-doping on structural morphology by altering the nitrogen concentration in the liquid precursor at a "fixed" monodispersed nanoparticle distribution. For our studies, octanoic acid-synthesized particles were used for CVD reaction possessing a diameter distribution listed above (12.5 ± 1.8 nm). Additionally, stock solutions of 1%, 5%, and 9% NH_3 in EtOH were prepared as liquid precursors for NCNC growth.

As described previously, CVD was performed using octanoic acid-synthesized FeNPs spin-coated from hexane on a bare quartz plate. The NH_3-containing precursor was injected at a rate of 5 ml/h for 1 h under an inert atmosphere at 950 °C, followed by termination of the reaction and sonication of the product into DMF. TEM analysis was then used to examine the structural morphology due to the variation of NH_3 concentrations in the feedstock. **Figure 14** illustrates the corresponding low and high resolution TEM micrographs of NCNCs synthesized with 1%, 5%, and 9% NH_3, respectively. Additionally, electron energy loss spectroscopy

(EELS) was performed and confirmed a range of 2-7 atomic % N in each sample (Supporting Information). It is also important to note that since the same FeNPs were used for each variance in N concentration, all three runs resulted in NCNCs with similar diameters (38 ± 9 nm) but different segment lengths. As can be observed from the micrograph indicating 1% NH_3, an individual segment length is approximately 750 nm. Of interesting note, some structures exhibited no segments at all, but were represented by the morphology of a multiwalled carbon nanotube. As the concentration of NH_3 in the feedstock increased to 5%, however, conical segments of the type illustrated previously were observed. Using 9% NH_3 as the liquid precursor, increasingly smaller segment lengths were observed in the range of 31 ± 8 nm, as indicated in the corresponding table.

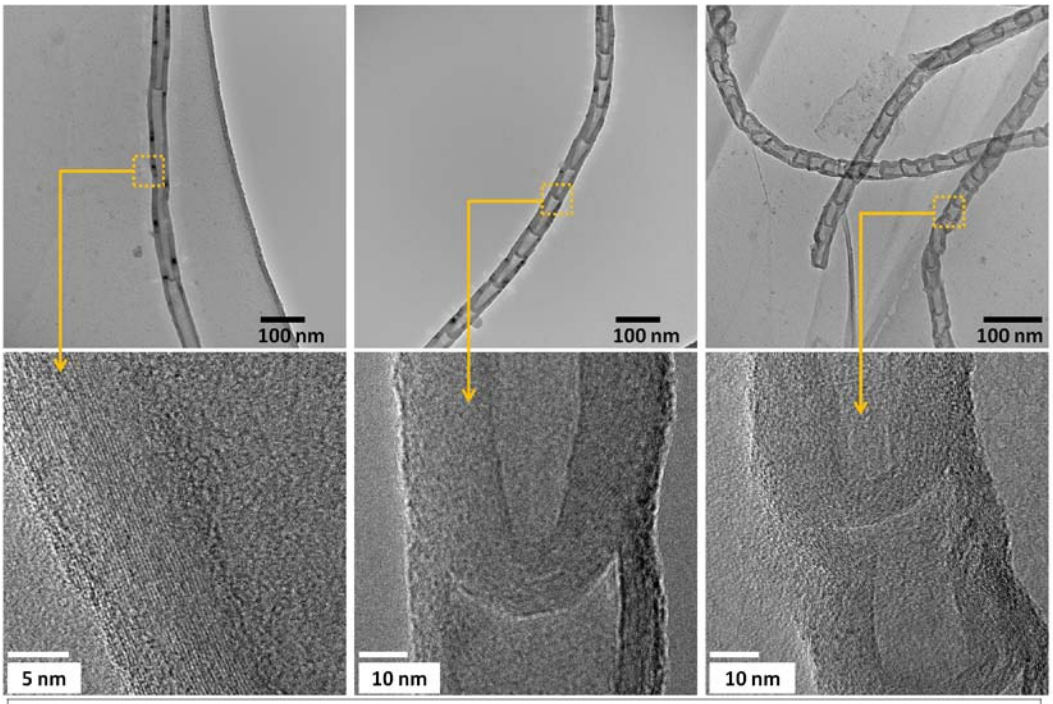

CVD Conditions		
1% NH_3	5% NH_3	9% NH_3
Length of NCNCs		
760 ± 80 nm	130 ± 80 nm	31 ± 8 nm

Figure 14. Varying the NH_3 concentration during the CVD reaction (uniform particle size, 16 ± 3 nm) resulted in alteration of the segment lengths of NCNCs. Nominal length values and ranges are listed under each concentration 1%, 5%, and 9% respectively.

Such control of segment length has been theoretically predicted.[119.109] Two models were studied in which (1) carbon atoms in the wall of the NCNCs were substituted or (2) nitrogen atoms were adsorbed at the open edge of the NCNCs. Results from this study concluded that dopant nitrogen atoms exhibit a preference for edge adsorption, as opposed to side wall incorporation. Thus, once enough N atoms are present on the open edge of the NCNC, carbon atoms will not attach to this site, effectively acting as a "stopper" for further growth of longer nanotubes. Our experimental results support this hypothesis. As NH_3 concentration in the liquid precursor is increased, available N atoms are also increased resulting in faster saturation of open edge planes and shorter segment lengths. The converse holds true as well, as indicated by longer segment lengths using 1% NH_3.

4.3.3 Tailored Encapsulation of GNPs

Defining these parameters (segment length and diameter) enables for the tailored volumetric capacity of individual NCNCs. As we have previously demonstrated,[117] separated NCNCs can be cross-linked by the addition of glutaraldehyde. Moreover, cargo such as gold nanoparticles (GNPs) and quantum dots can be encapsulated by their addition prior to crosslinkage, presumably through a capillary action effect. However, in facilitating this work, polydispersed structures were often found, each with its own intrinsic loading capacity. Utilizing NCNCs of controlled diameter and segment length should provide uniform and tailored interior volume for encapsulation of a variety of cargo. Indeed, it was observed that variation in these parameters effectively increased or decreased the loading capacity. Briefly, 0.1 mg of NCNCs doped by 1%, 5%, or 9% NH_3 were mechanically separated through grinding with a mortar and pestle and resuspended through sonication in EtOH for 5 min (**Figure 15**). Approximately 2 mL of the

separated NCNC suspension was mixed with 500 µL of commercially available GNPs (Sigma Aldrich, 5 nm nominal diameter, diluted 16:1 with EtOH) and further sonicated for an additional 5 min. Subsequently, 500 µL of 4% glutaraldehyde (GA) was added, and the suspension was incubated for 24 h. **Figure 15** shows the TEM micrographs from encapsulated GNPs. Using TEM, the morphology of the resultant nanocapsules, as well as the number of GNPs encapsulated within their interior cavity was examined. For 5% NH_3-synthesized nanocapsules, 9 ± 4 GNPs were found within the interior of 25 measured structures. In contrast, 9% NH_3-synthesized nanocapsules revealed the encapsulation of 3 ± 1 particles within the interior cavity. Moreover, an increased distribution of particles was found for the former. This suggests that while 5% NH_3-synthesized nanocapsules can posses tens of particles, a critical value of ~4 GNPs can be encapsulated within the small interior cavity of 9% NH_3-synthesized nanocapsules, confirming a direct correlation between segment length and interior loading capacity. Results from 1% NH_3-synthesized nanocapsules deviated from this trend, however. We expected that increased segment length would result in an increased number of particles encapsulated. On average, no GNPs were found within the interior of formed nanocapsules. Additionally, capsule formation was not observed in many cases, presumably the result of non-covalent π-π interactions dominating that of covalent bond formation. Therefore, with the exception of NCNCs made using 1% NH_3 precursor, interior cavity space can be estimated based upon the number of encapsulated GNPs. GNPs of 5 nm diameter occupy a volume of 65 nm^3. Thus, for 5% NH_3-synthesized nanocapsules, the average interior volume is approximately 600 nm^3, while that of 9% NH_3 is 200 nm^3.

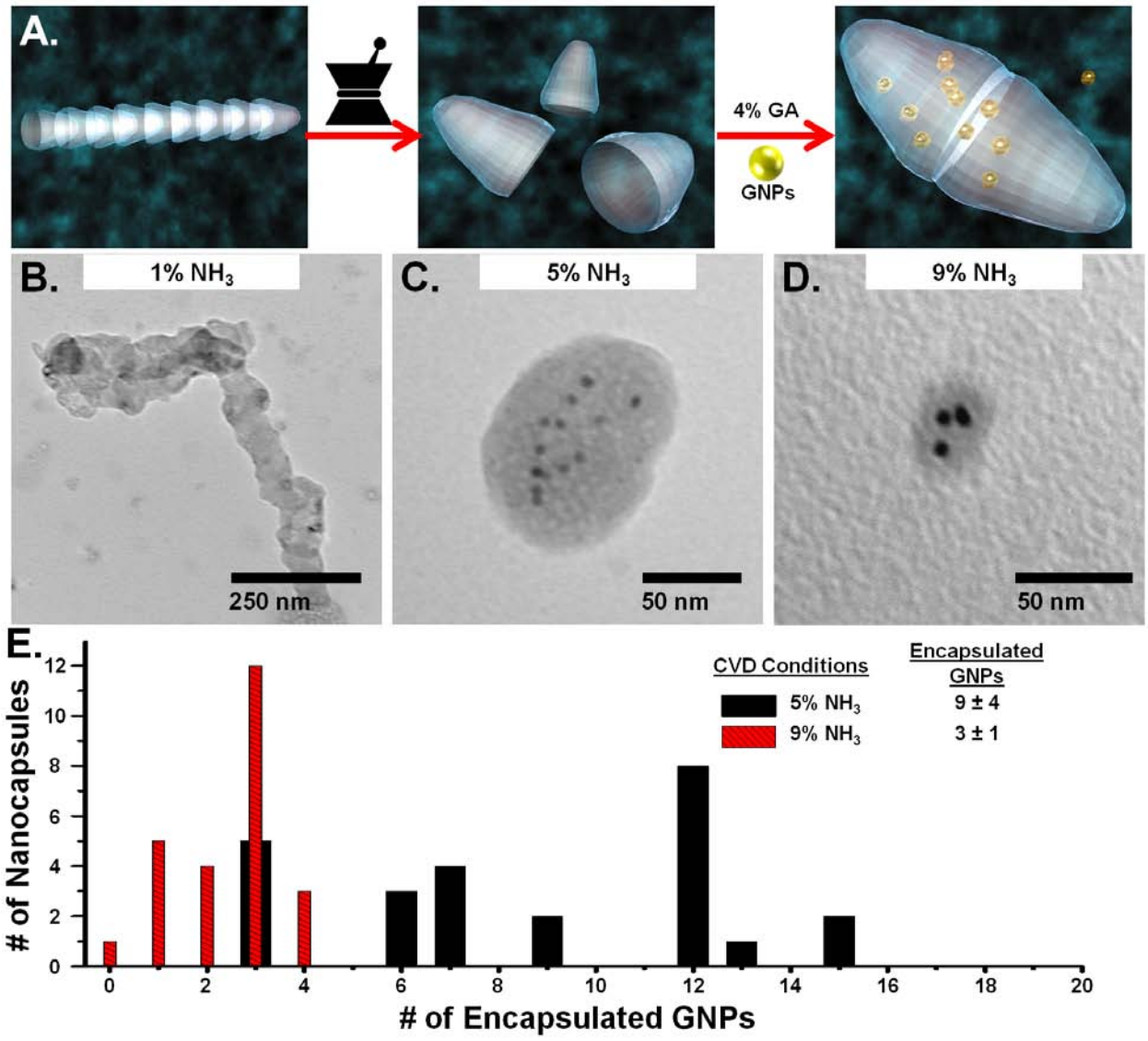

Figure 15. A) Schematic illustration of stacked NCNC segment separation by mechanical grinding, followed by cross-linkage with 4% glutaraldehyde (GA) in the presence of gold nanoparticles (GNPs), resulting in encapsulated GNPs. TEM micrographs demonstrate the encapsulation of GNPs with cross-linked NCNCs for (B) 1%, (C) 5%, and (D) 9% NH_3-synthesized NCNCs. E) Corresponding bar graph shows the statistical distribution of encapsulated GNPs. 1% NH_3-synthesized nanocapsules did not contain a significant contribution of encapsulated GNPs.

While we demonstrate the successful control of NCNCs by CVD using monodispersed FeNPs, similar types of nanostructures can be synthesized by other methods. For instance, Chun *et al.* utilized an anodized aluminum oxide (AAO) template and performed CVD reactions using acetylene to deposit graphitic carbon within the template wells.[120] The resultant product was a film of carbon nanocups that could be separated through the use of Ar milling. With this methodology, a higher degree of control of physical dimensions can be attained; however, there are no intrinsic N-functionalities with which to perform subsequent reactions. Our protocol, in lieu of an exact degree of dimensional tailoring, incorporates a variety of N-functionalities for chemical reactions. As a result, we have demonstrated the successful cross-linkage of NCNCs to form nanocapsules, a task not easily accomplished without the inherent presence of N-functionalities.

The ease of encapsulating cargo such as GNPs in graphitic nanocapsules offers significant advantages over current nano-encapsulation methods. Typically, alternative systems utilize layer-by-layer adsorption of oppositely charged macromolecules to a colloidal template.[121] Polymer nanocapsules have been able to encapsulate species such as quantum dots and magnetic nanoparticles; however, these systems suffer from complexity of compositional processes or limited stability in external chemical environments as varying pH may make such capsules more or less permeable.[121] In contrast, NCNC-formed nanocapsules encapsulated cargo presumably through capillary action, followed by chemical crosslinking reaction. Once encapsulated, the multiwalled graphitic shell provides an inert barrier between external environments and interior cargo, offering high stability and versatility for a variety of applications.

4.4 CONCLUSIONS

Finite control over structural and morphological properties of nanomaterials through chemical doping is essential for their engineered properties. We have demonstrated the novel utility of nitrogen-doping to achieve desired volumetric parameters of a hybrid carbon nanomaterial. Furthermore, imparted functionality is observed in the fabrication of nanocapsules of defined interior capacity for the encapsulation of cargo. Such immediate applications of this type of material may include their use in drug delivery where inherent nitrogen functionalities permit biocompatibility, and tailored cavity space may be utilized for medicinal cargo.

4.5 ACKNOWLEDGMENTS

The authors would like to thank the Nanoscale Fabrication and Characterization Facility of the Petersen Institute of Nanoscience and Engineering for access to characterization instrumentation. This work was supported by an NSF CAREER Award No. 0954345.

4.6 SUPPORTING INFORMATION

Supporting information for Chapter 4.0 ‘Controlling the Volumetric Parameters of Nitrogen-Doped Carbon Nanotube Cups’ can be found in **Appendix C**. The data available includes AFM height profiles of synthesized FeNPs (**Figure 50**), DLS measurements of synthesized FeNPs (**Figure 51**), high-resolution TEM and EELS analysis of synthesized NCNCs (**Figure 52**), and low-resolution TEM image of encapsulated GNPs (**Figure 53**).

5.0 BIODEGRADATION OF SINGLE-WALLED CARBON NANOTUBES THROUGH ENZYMATIC CATALYSIS

Abstract

We show here the biodegradation of single-walled carbon nanotubes through natural, enzymatic catalysis. By incubating nanotubes with a natural horseradish peroxidase (HRP) and low concentrations of H_2O_2 (~40 μM) at 4 °C over 12 weeks under static conditions, we show the increased degradation of nanotube structure. This reaction was monitored via multiple characterization methods, including transmission electron microscopy (TEM), dynamic light scattering (DLS), gel electrophoresis, mass spectrometry, and ultraviolet – visible – near-infrared (UV-vis-NIR) spectroscopy. These results mark a promising possibility for carbon nanotubes to be degraded by HRP in environmentally relevant settings. This is also tempting for future studies involving biotechnological and natural (plant peroxidases) ways for degradation of carbon nanotubes in the environment.

This work, published in *Nano Lett.* **2008**, *8*, 3899-3903, was the collaborative work of the Star Research Group and the Kagan Research Group (Environmental and Occupational Health) at the University of Pittsburgh. Contributing roles included initial observations reported by Padmakar D. Kichambare and Pingping Gou, electron paramagnetic resonance studies performed and analyzed by Irina I. Vlasova, and gel electrophoresis performed and analyzed by

Alexander A. Kapralov and Nagarjun Konduru. My contribution to this work was the execution of incubation studies over a 16 week period, including TEM and DLS analysis, thermogravimetric analysis, and absorbance spectroscopy. Dr. John Williams of the University of Pittsburgh performed and interpreted MALDI-TOF mass spectrometry data. Professors Alexander Star and Valerian Kagan aided in experimental design and discussion.

5.1 INTRODUCTION

Single-walled carbon nanotubes represent an emerging realm between nanomaterials and biological systems, specifically for that of biosensing[3,122] and drug delivery.[123-125] These progressions towards biological systems have subsequently spawned necessary research into toxicity of carbon nanotubes as varying functionalities and carbon nanotube types become incorporated into experimental parameters and introduced by altering media.[126-128] While it has been shown that carbon nanotubes can indeed act as a means for drug delivery, negative effects such as unusual and robust inflammatory response,[129] oxidative stress and formation of free radicals, and accumulation of peroxidative products have also been found as a result of carbon nanotubes and their accumulated aggregates.[130-136] Here we report the catalytic biodegradation of carbon nanotubes in vitro by oxidative activity of horseradish peroxidase and low concentrations of hydrogen peroxide (40 μM). This indicates possible biotechnological and natural (plant peroxidases) ways for degradation of carbon nanotubes in the environment.

5.2 EXPERIMENTAL

Experimental work was carried out using electric arc discharge single-walled carbon nanotubes purchased from Carbon Solutions Inc. (P2-SWNTs) and further purified by oxidative treatment with H_2SO_4/H_2O_2 to remove residual metal catalyst.[137] This treatment is known to impart carboxylic acid groups, thus improving solubility in aqueous media. After rigorous filtration with copious amounts of water, approximately 0.1 mg of nanotubes was suspended in 4.5 ml of phosphate buffered saline (PBS) at pH 7.0 using an ultrasonic bath for one minute (Branson 1510, Frequency 40kHz). These suspended nanotubes typically remained well dispersed for one week at room temperature prior to precipitation, allowing for greater surface area exposure, and possibly greater degradation. Lyophilized horseradish peroxidase (HRP) Type VI (Sigma Aldrich) was solubilized in PBS at 0.385 mg/mL, and then added to the carboxylated nanotube suspension at a volume of 4.0 mL. The entire suspension was then statically incubated over 24 hours at 4 °C in the dark. We believe these temperature conditions correspond with possible applications of the biocatalytic system for environmental biodegradation of carbon nanotubes in different seasons. An excess of 10.0 mL of 80 μM H_2O_2 was added to the bulk sample to start the catalytic biodegradation of carbon nanotubes in the presence HRP. Static incubation with H_2O_2 (resulting concentration ~40 μM) was also performed in refrigerated conditions and kept in the dark to avoid enzyme denaturation and photolysis of H_2O_2.[138] Furthermore, assessments of HRP activity incubated with carbon nanotubes were performed. To avoid complications of spectrophotometric assays in the presence of strongly-light scattering suspensions, we used electron spin-resonance measurements of the activity based on detection of radicals formed during one electron oxidation of ascorbate,[139] or a phenolic compound, etoposide.[140,141] Both assays revealed strong signals from the respective peroxidase substrates, thus demonstrating that

carbon nanotubes did not cause inactivation of the enzyme (see Supporting Information), in agreement with the data in the literature.[142,143] Careful control of pH and temperature conditions was maintained to ensure the enzyme's prolonged survival over the incubation period.

5.3 RESULTS AND DISCUSSION

Throughout the course of 16 weeks, aliquots (250 μL) of the incubating suspension were removed bi-weekly after gentle shaking of the bulk sample to evenly distribute material without denaturation of HRP. An equal volume of 80 μM H_2O_2 was then added to replace the volume of aliquot removed. **Figure 16** presents visual evidence of biodegradation of the suspended carbon nanotubes over the full range of incubation time. As can be seen, there is a steady progression of fading color intensity and turbidity from the control sample through week 16, where the solution of incubated nanotubes appears to be clear. This decline of light scattering and absorbance from nanotubes cannot be the result of simple dilution, as even though 250 μL aliquots were replaced with an equal volume of H_2O_2, this is hardly a significant volume for a mass dilution of the 20 mL bulk sample. A simple explanation involves oxidation of already carboxylated nanotubes through a highly reactive intermediate (Compound I) produced via the interaction of H_2O_2 and HRP.

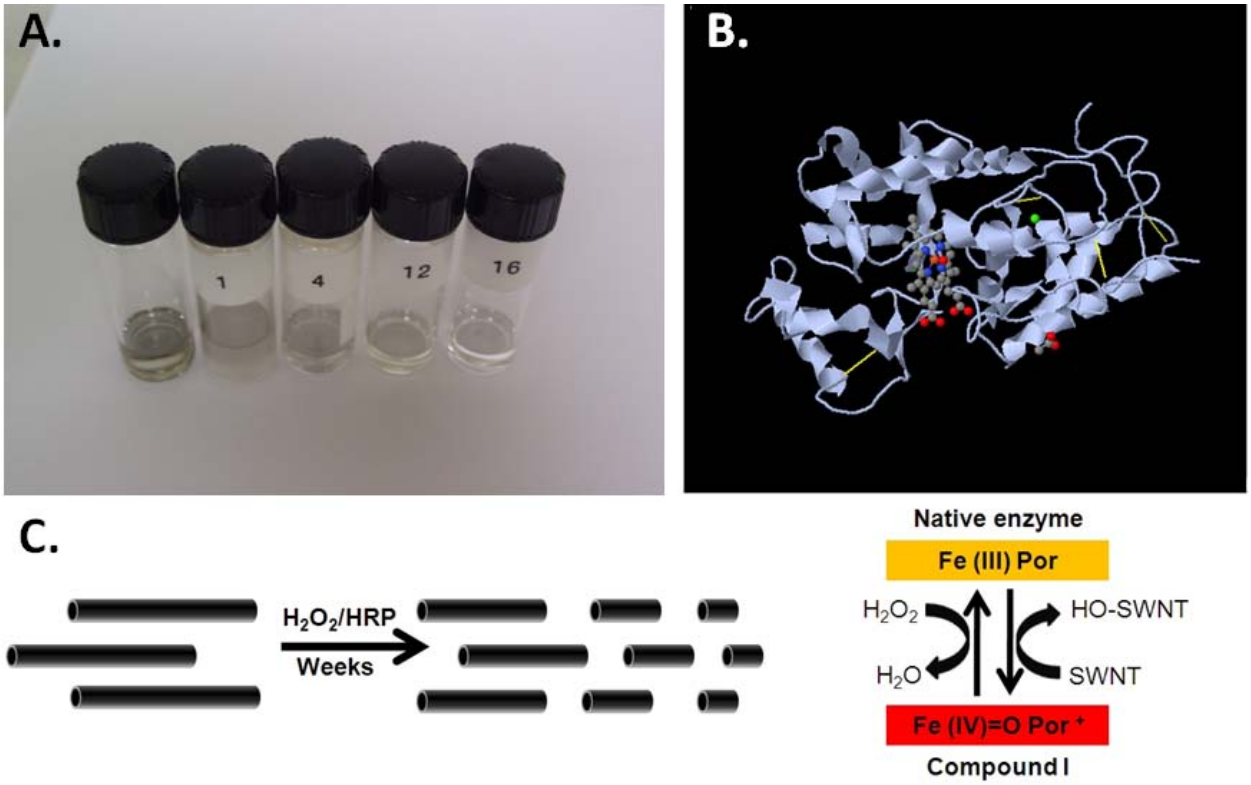

Figure 16. Aliquots of carbon samples are displayed by increasing HRP/H_2O_2 incubation time in weeks (left to right). A) A control of carboxylated nanotubes is shown (far left) in comparison to a gradient decay of light scattering and absorbance as incubation time continues. B) HRP is shown as a cartoon image of tertiary structure, while the active heme center is illustrated. C) Interaction of H_2O_2 with the HRP active center produces highly oxidizing species, a ferryl oxo (+4) iron, and porphyrin (Por) π radical cation, resulting in length decrease of carbon nanotubes.

A highly oxidizing redox potential (about 950 mV) for HRP Compound I/Compound II[144,145] defines its broad spectrum of applications as a potent biotechnological oxidant (particularly in the immobilized form) in the environmental and health care sectors, and in pharmaceutical and chemical industries.[146] These features represent a poignant characteristic of HRP, and reason why intrinsic catalytic iron is insufficient to degrade nanotubes in the presence of low, local levels of H_2O_2 as evidenced by our controls consisting of carboxylated nanotubes incubated with HRP, and carboxylated nanotubes incubated with H_2O_2 at the same concentrations listed above (see Supporting Information).

To add to the visual confirmation of biodegradation of HRP-incubated nanotubes, transmission electron microscopy (TEM) was used to examine each aliquot removed from the incubating bulk sample. Initially, atomic force microscopy (AFM) was used to characterize these aliquots, but visualization at later weeks became impossible because biodegraded material obscured the images (see Supporting Information). In order to effectively, terminate the oxidative reaction of HRP/H_2O_2 and to effectively remove PBS salts, which were found to obstruct the imaging, centrifugation (3400 rpm) was used to decant off the PBS solution, followed by suspension into approximately 1 mL of *N*, *N*-dimethylformamide (DMF) through sonication. As DMF has typically shown excellent dispersion of carbon nanotubes, while denaturing HRP, this acted as an effective solvent for imaging without the development of any noticeable residue. One drop of the aliquot in DMF was then placed on a lacey carbon grid (Pacific-Grid Tech) and allowed to dry in ambient for 2 hours prior to TEM imaging (FEI Morgagni, 80 keV). **Figure 17** shows a time-lapsed series of nanotubes throughout the incubation period in HRP/H_2O_2. As can be seen in the first panel, carboxylated carbon nanotubes were approximately 517 ± 372 nm (see Supporting Information), based on point-to-

point measurements, indicative of the 24 hour cutting procedure as previously mentioned.[137] As incubation time progressed to 8 weeks, we observed a substantial decrease in average nanotube length (231 ± 94 nm) and the appearance of globular material, as demonstrated by the second panel. By the end of concurrent incubation period (16 weeks), it had become difficult to account for any nanotube structure. Examination of the samples at 12 weeks, revealed that the bulk of nanotubes were no longer present, and globular material had amassed, contributing to the predominant species imaged. In agreement with these data, dynamic light scattering (Particle Technology Labs, Malvern Zetasizer Nano) (**Figure 17, D**) showed a sharp contrast in size distributions through progressive weeks. Particle sizes were determined based off the refractive index of carbon as the particle and DMF as the carrier fluid. Smaller size distributions at progressive weeks may be attributed to decreased bundling in nanotube structures, however other data point to degradation of material. To further examine the ability of HRP/H_2O_2 to biodegrade nanotubes, we additionally analyzed their mobility profile using electrophoresis in a 0.5% agarose gel (**Figure 17, E**). To reveal the location of nanotubes in the gel, we utilized a complex of albumin with bromophenol blue stain. In the absence of nanotubes, albumin/bromophenol blue complex gave a distinctive band (1). Control (non-treated) nanotubes, due to their relatively large size, did not enter the gel (arrow) and caused retardation in the migration of the albumin/bromophenol blue complex (asterisk) (2). When the suspension incubated for 16 weeks with HRP/H_2O_2 was loaded on the gel, no distinctive band of nanotubes was detectable at the loading site and the albumin/bromophenol blue complex migrated as a free complex similar to the control (3).

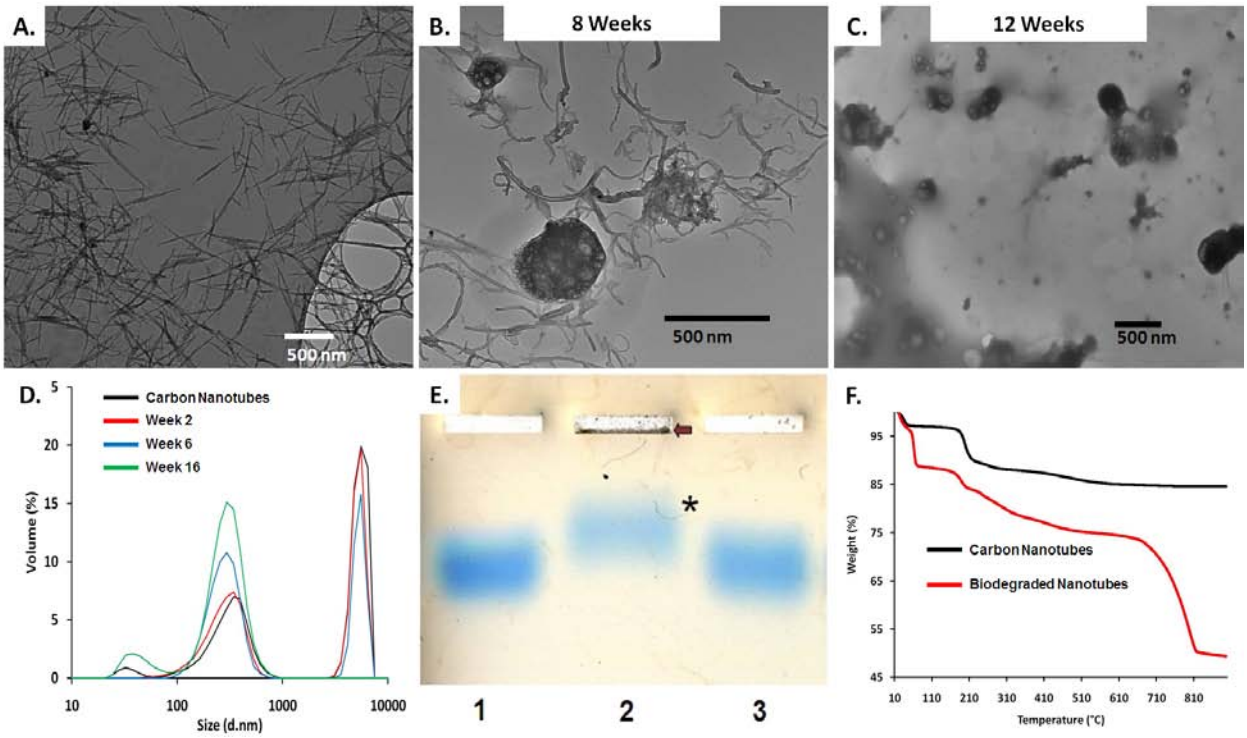

Figure 17. TEM tracks the biodegradation of carbon nanotubes as incubation time increases (A-C) Length decrease is seen at week 8 with some globular material present, while at week 12 mostly globular material is present. This change is attributed to nanotube biodegradation. D) DLS shows size distribution between select weeks. Larger material present in week 2 is not present in week 16, while additional smaller material is found to be present at week 16. E) Agarose gel electrophoresis reveals that HRP/H_2O_2 functionalization results in the disappearance of nanotubes capable of binding albumin/bromophenol blue complex. Electrophoresis was performed in TAE buffer (40 mM Tris acetate and 1mM EDTA). Prior to loading, nanotubes were incubated with bovine serum albumin fraction V (100 mkg per sample) and bromophenol blue (0.05%) for 30 min at room temperature. F) TGA of carbon nanotubes prior to incubation (black) and after degradation (red).

In addition, thermogravimetric analysis (TGA) was performed on a larger sample with more frequent H_2O_2 additions. Approximately 5 mg of carboxylated nanotubes were incubated with HRP at 37 °C with hourly additions of 1 mM H_2O_2 for 5 days. Examining the mass of this sample after solvent removal, we have found that approximately 40% by weight of nanotube material was lost. TGA shows a marked contrast in profiles (**Figure 17, F**). Carboxylated carbon nanotubes, as shown in black, start to lose weight around 200 °C as opposed to pristine SWNTs (900 °C), in agreement with the literature.[147] However, nanotubes incubated with HRP/H_2O_2 were less stable and demonstrated larger overall weight loss with the most significant losses at 100 °C and 670 °C. This indicates a higher level of induced defects in good agreement with TEM observations.

To further characterize species present in the incubation aliquots, matrix assisted laser desorption/ionization time of flight (MALDI-TOF) mass spectrometry was used to analyze varying samples. We employed Applied Biosystems Voyager 6174 in a positive ionization mode whereby all samples were analyzed using α-cyano-4-hydroxycinnamic acid as a calibration matrix. All samples (carbon nanotubes, nanotubes with HRP, and nanotubes incubated in HRP/H_2O_2 for t = 16 weeks) were suspended in DMF and prepared as previously mentioned. **Figure 18** shows the overlay of significant signals for each sample. As can be seen, carbon nanotubes (blue) and our control of nanotubes with HRP but without H_2O_2 (red), share similar mass to charge (m/z) peaks, specifically at approximately 12,000. This evidence supports that HRP alone (43,000 m/z)[148] is not responsible for any decrease in m/z of carboxylated nanotubes. In contrast, nanotubes incubated for 16 weeks with HRP/H_2O_2 (green) had sharply differing characteristics. Shown in **Figure 18**, only the lower end of the spectrum produced any relevant signal, with no peaks present at m/z of 12,000. Focusing on the m/z ratio from 500 to 2500,

multiple peaks were found in high intensity (>50%), specifically between 600 and 1000. The presence of these lower m/z peaks and the lack of signal at 12,000 may be indicative of oxidative fragmentation and possibly a shortening of nanotube material throughout the incubation period.

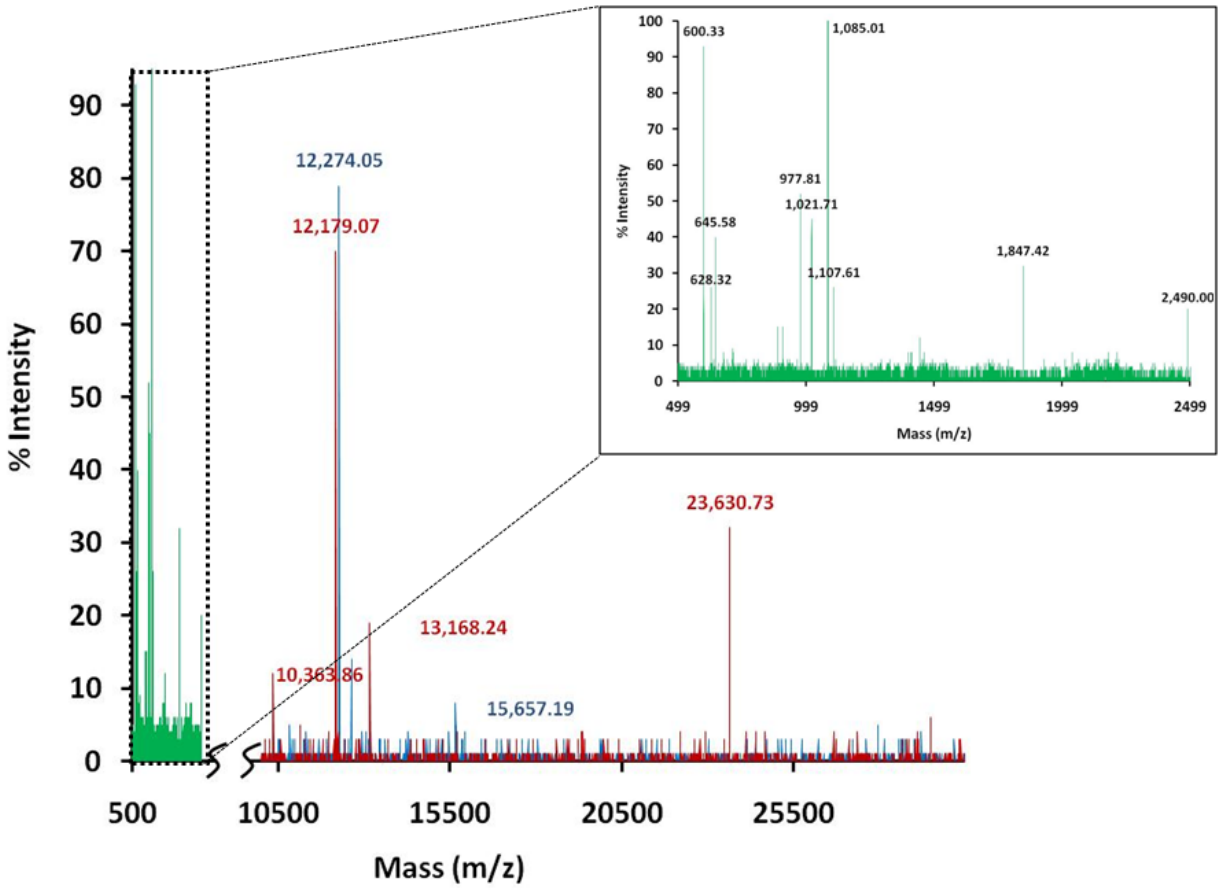

Figure 18. MALDI-TOF Mass spectrometry results of carboxylated nanotubes (blue), control sample of nanotubes with HRP only (red), and nanotubes after 16 weeks of incubation with HRP and 80 µM H_2O_2 (green). Inset shows expanded view of incubated sample.

Furthermore, HRP/H_2O_2 mediated oxidative modification of carbon nanotubes was investigated using UV-Vis-NIR spectroscopy (Perkin Elmer). Aliquots (500 µL) were sonicated briefly in DMF before being analyzed. **Figure 19** shows the resulting UV-Vis-NIR spectra from 600 – 1200 nm. This wavelength range was chosen to avoid spectral interference from solvent and water molecules. It should be recalled here that carbon nanotubes are mixtures of different diameters and helicities; the resultant spectrum includes electronic transitions for both metallic and semiconducting nanotubes (**Figure 19, A**). The broad S_2 semiconducting band of the carbon nanotubes is evident between 1000 and 1100 nm, as well as the M_1 metallic band between 650-750 nm. By monitoring the S_2 band over the incubation period, we could see notably two distinct features: 1) The S_2 band blue shifted as time progressed and 2) by week 16, most band structure in terms of the S_2 and M_1 bands was lost. Both the blue shifting of the S_2 band and loss of structure by week 16 can be attributed to the degradation of carbon nanotubes. Because blue shifting is not significant upon enzyme addition, we can postulate that only smaller diameter nanotubes are present in later weeks of incubation. Since nanotubes have an energy-induced band gap inversely proportional to nanotube diameter,[149] it is possible that only smaller diameter material is present; while at week 16, loss of band structure is indicative of most nanotube material being oxidized.

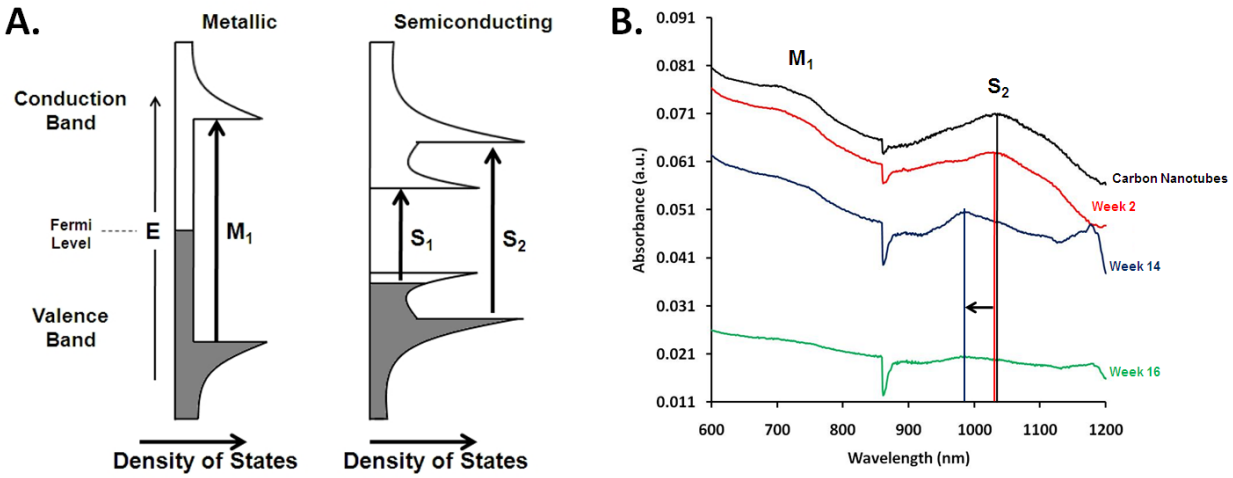

Figure 19. Nanotube density of states band diagram and UV-vis-NIR spectroscopic measurements tracking the biodegradation of nanotubes as HRP/H_2O_2 incubation time increases. A) Nanotubes are synthesized with varying helicities and diameters giving rise to both metallic and semiconducting tubes with respective energetic transitions. B) Blue shifting is seen in the S_2 semiconducting band as incubation time increases. This shift correlates to the presence of smaller diameter nanotubes. Week 16 subsequently shows a loss in band structure as nanotubes biodegrade.

5.4 CONCLUSIONS

In conclusion, we provided here compelling evidence of the biodegradation of carbon nanotubes by HRP/H_2O_2 over the period of several weeks. This marks a promising possibility for nanotubes to be degraded by HRP in environmentally relevant settings. It is tempting to speculate that other peroxidases in plants and animals (e.g. myloperoxidase) may be effective in oxidative degradation of carbon nanotubes. If so, enhancement of these catalytic biodegradation pathways may be instrumental in avoiding cytotoxicity in drug delivery,[150] gene silencing,[151] and tumor imaging.[152] With further insight into this type of biodegradation process, it will be possible to engineer better, more efficient drug delivery platforms, where the patient need not worry about the injection of materials that could possibly accumulate causing cytotoxic effects. While we demonstrate this initial biodegradation, more studies are necessitated to ascertain the by-products of the biodegradation, as well as cellular studies for practical application.

5.5 ACKNOWLEDGMENTS

The authors thank Thomas Harper for the provision of access to the transmission electron microscope and John Williams for assistance and consultation of mass spectrometry.

5.6 SUPPORTING INFORMATION

Supporting information for Chapter 5.0 ‘Biodegradation of Single-Walled Carbon Nanotubes through Enzymatic Catalysis’ can be found in **Appendix D**. The data available includes statistical data correlating nanotube length as a function of time (**Table 2**), TEM imaging of H_2O_2 (**Figure 54**) and HRP **(Figure 55**) controls, AFM imaging of carbon nanotubes prior to incubation (**Figure 56**) and after 8 weeks of incubation with HRP/H_2O_2 (**Figure 57**), EPR spectra (**Figure 58**), and EPR methodology.

6.0 MECHANISTIC INVESTIGATIONS OF HORSERADISH PEROXIDASE-CATALYZED DEGRADATION OF SINGLE-WALLED CARBON NANOTUBES

Abstract

Single-walled carbon nanotubes (SWNTs) have been investigated for a variety of applications including composite materials, electronics, and drug delivery. However, these applications may be compromised depending on the negative effects of SWNTs to living systems. While reports of toxicity induced by SWNTs vary, means to alleviate or quell these effects are in small abundance. We have reported recently the degradation of carboxylated SWNTs through enzymatic catalysis with horseradish peroxidase (HRP). In this full Article, we investigated the degradation of both carboxylated and pristine SWNTs with HRP and compared these results with chemical degradation by hemin and $FeCl_3$. The interaction between pristine and carboxylated SWNTs with HRP was further studied by computer modeling, and the products of the enzymatic degradation were identified. By examining these factors with both pristine and carboxylated SWNTs through a variety of techniques including atomic force microscopy (AFM), transmission electron microscopy (TEM), Raman spectroscopy, ultraviolet-visible-near-infrared (UV−vis−NIR) spectroscopy, gas chromatography−mass spectrometry (GC-MS), high-performance liquid chromatography (HPLC), and liquid chromatography-mass spectrometry (LC−MS), degradation pathways were elucidated. It was observed that pristine SWNTs

demonstrate no degradation with HRP incubation but display significant degradation when incubated with either hemin or $FeCl_3$. Such data signify a heterolytic cleavage of H_2O_2 with HRP as pristine nanotubes do not degrade, whereas Fenton catalysis results in the homolytic cleavage of H_2O_2 producing free radicals that oxidize pristine SWNTs. Product analysis shows complete degradation produces CO_2 gas. Conversely, incomplete degradation results in the formation of different oxidized aromatic hydrocarbons.

This work, published in *J. Am. Chem. Soc.* **2009**, *131*, 17194-17205, was once again a collaboration between the Star Research Group and the Kagan Research group. Contributing roles included gas chromatography-mass spectrometry, high-performance liquid chromatography, liquid chromatography-mass spectrometry, and Amplex Red measurements performed and analyzed by Gregg P. Kotchey and Dr. John Williams, enzyme immobilization and absorbance measurements by Yanan Chen, and molecular modeling by Naveena Yanamala and Dr. Judith Klein-Seetharaman. I contributed by initiation of enzymatic and non-enzymatic degradation reactions (hemin and iron chloride), TEM analysis, UV-vis-NIR analysis, Raman spectroscopic analysis, and AFM imaging. Profs. Valerian Kagan and Alexander Star directed experimentation and discussion.

6.1 INTRODUCTION

Single-walled carbon nanotubes (SWNTs) have been at the forefront of nanoscience research for a variety of applications including gas sensing,[153,154] composite materials,[155,156] biosensing,[157] and drug delivery.[158-160] While the latter two applications have been successful, there are reports

of cellular toxicity induced by SWNTs. Specifically, oxidative stress and the formation of free radicals,[161] robust inflammatory response,[162] and even asbestos-like pathogenicity[163] have been found as a result of the inception of SWNTs into biological systems. As a means to diminish these effects, various bioconjugation schemes have been used to functionalize SWNTs including DNA[164] and peptides,[165] as well as supramolecular approaches such as functionalization with poly(ethylene glycol) (PEG).[166] These methods do, indeed, subdue the initial toxicity typically induced by this variety of carbon nanomaterials; however, the issue of long-term circulation without the possibility of physiological or even environmental degradation remains.

Recently, we have demonstrated the enzymatic degradation of carboxylated SWNTs using horseradish peroxidase (HRP) and low, localized concentrations of H_2O_2 (~40 μM).[167] Degradation of SWNTs with HRP was shown to proceed over the course of several weeks at 4 °C in the dark. The interaction between HRP and H_2O_2 has been extensively studied.[168] In essence, HRP, as a heme peroxidase, contains a single protoporphyrin IX heme group. While in an inactive form, the heme peroxidase is of a ferric (Fe^{3+}) oxidation state. Hydrogen peroxide then binds to the ferric species, and a transient intermediate forms, in which peroxide is bound to the heme iron as a ligand. It is then thought to undergo a protein-assisted conversion to an oxywater complex specifically through the His 42 and Arg 38 residues, leading to what is known as Compound I, comprised of a ferryl oxo iron (Fe^{4+}=O) and a porphyrin π cation radical. We hypothesize that the generation of Compound I (redox potential of 950 mV)[169] through the heterolytic cleavage of H_2O_2 would result in the degradation of carboxylated SWNTs located in close proximity to the HRP catalytic site. On the other hand, $FeCl_3$ would affect Fenton catalysis, where homolytic radical generation from H_2O_2 would demonstrate no selectivity, and pristine SWNTs would be degraded as well as carboxylated SWNTs.

To elucidate the mechanism of enzymatic degradation of SWNTs, we focus on the HRP preferential oxidation of carboxylated SWNTs over pristine SWNTs and the identification of the degradation products. From the perspective of the enzymatic substrate (SWNTs), it is tempting to speculate that, as a result of complete degradation, SWNTs will be completely oxidized to CO_2,[170] via formation of various intermediate species in the degradation solution. Additionally, from the perspective of HRP, it is unknown whether degradation is contingent upon proximity of the enzyme's heme site to the surface of SWNTs.

In this Article, the interaction between HRP and SWNTs is examined through a variety of methods including transmission electron microscopy (TEM), atomic force microscopy (AFM), ultraviolet-visible-near-infrared (UV-vis-NIR) spectroscopy, Raman spectroscopy, gas chromatography-mass spectrometry (GC-MS), high-performance liquid chromatography (HPLC), and liquid chromatography-mass spectrometry (LC-MS). As compared to our previous work, SWNTs were incubated with HRP and varying concentrations of H_2O_2 at higher temperature. Evaluation of these conditions shows significant acceleration of reaction kinetics at room temperature with little influence by an excess of H_2O_2 in the tested regime. These findings do not apply to pristine SWNTs, however, as no degradation was observed, alluding to hydrophobic interactions preventing proximity of the HRP heme site to the substrate (pristine SWNTs). Molecular modeling was additionally implemented to investigate possible binding sites for carboxylated and pristine SWNTs to HRP, resulting in varying proximity to this active site. Incubation with other ferric iron species including hemin and $FeCl_3$ with H_2O_2 resulted in the degradation of both carboxylated and pristine SWNTs, consistent with a homolytic cleavage of H_2O_2 and the formation of free radicals. Further characterization with GC-MS and HPLC of carboxylated SWNT samples (incubated with either HRP or ferric iron species) elucidated CO_2

production as expected, as well as multiple products in solution identified by LC-MS. Product analysis reveals the formation of CO_2 and intermediate oxidized aromatic hydrocarbons. These findings are important for better understanding the exact mechanism of enzymatic degradation of SWNTs.

6.2 EXPERIMENTAL

6.2.1 Materials

SWNTs prepared by the arc-discharge process[171] were purchased from Carbon Solutions, Inc. (P2-SWNT). Lyophilized HRP type VI, PBS, reagent grade MeOH, hemin (chloride), $FeCl_3$ (hexahydrate), and 30% H_2O_2 were purchased from Sigma Aldrich. Amplex Red was purchased from Molecular Probes, Invitrogen.

6.2.2 Carboxylation of SWNTs

SWNTs were carboxylated as reported previously.[137] Briefly, approximately 25 mg of SWNTs was sonicated (Branson 1510, frequency 40 kHz) in 200 mL of H_2SO_4/H_2O_2 (30%) at a ratio of 3:1 for 24 h at 0 °C. It is important to note that this solution is highly oxidizing. Caution must be taken when handling this system. After 10 and 15 h, 2.0 mL of H_2O_2 was supplemented into the reaction to compensate for H_2O_2 decomposition. The final dispersion was heated at 70 °C for 10 min, and subsequently diluted 10-fold, filtered on a 0.22 μm Teflon membrane filter, and washed with copious amounts of water to a neutral pH.

6.2.3 Incubation with HRP and H_2O_2

Two vials were prepared by sonicating for 1 min approximately 1 mg of carboxylated SWNTs into 4.0 mL of 1× (11.9 mM phosphates, 137 mM NaCl, and 2.7 mM KCl) phosphate buffered saline (PBS) per each vial. Lyophilized HRP type VI was solubilized in PBS at 0.385 mg/mL and added to the carboxylated SWNTs suspension at a volume of 4.0 mL, creating a total volume of 8.0 mL. All vials were then sealed with a septum and wrapped with parafilm to create an airtight seal. Following one full day of incubation, an initial 8 mL of either 80 or 800 μM H_2O_2 was added by needle through the septum to start the degradation reaction, followed by daily additions of 250 μL of either 80 or 800 μM H_2O_2 added to one of the two vials. This was continued on a daily basis for 10 days.

6.2.4 Monitoring HRP Activity with Amplex Red

Two vials were prepared by sonicating for 1 min approximately 1 mg of pristine SWNTs into 4.0 mL of PBS per each vial. Lyophilized HRP type VI was solubilized in PBS at 0.385 mg/mL, and then added to the two pristine vials at a volume of 4.0 mL, for a total volume of 8.0 mL per vial. An additional 8.0 mL of 80 μM H_2O_2 or 800 μM H_2O_2 was added to vials containing pristine SWNTs and HRP to start the degradation reaction. On a daily basis, 250 μL of either 80 or 800 μM H_2O_2 was injected into one of the two vials for 10 days. As a control, two vials consisting of 4.0 mL of HRP and 4.0 mL PBS were prepared, and the reaction was initiated by 8.0 mL of H_2O_2 (80 or 800 μM). Daily additions of 250 μL of either 80 or 800 μM H_2O_2 was performed for 10 days. All samples were then analyzed at days 1 and 10.

Amplex Red (Molecular Probes, Invitrogen) was employed to test HRP activity. A 10 mM stock solution of Amplex Red was prepared by dissolving the reagent in dimethyl sulfoxide (DMSO). To a 250 μL aliquot of sample being tested for enzymatic activity were added 234 μL of double-distilled water, 15 μL of 800 μM H_2O_2, and 1 μL of 10 mM Amplex Red. After gentle mixing, the UV-vis spectrum of the sample was taken with double-distilled water used as the background.

6.2.5 Incubation with Hemin and H_2O_2

Two vials were prepared by sonicating for 1 min approximately 1 mg of carboxylated or pristine SWNTs into 4.0 mL of dimethylformamide (DMF). Hemin (1×10^{-4} M in DMF) was then added in excess at a volume of 16.0 mL. Following 24 h of incubation, samples were centrifuged for 1 h and decanted of nonphysisorbed hemin,[172] followed by washing with double-distilled H_2O. The washed precipitates were then sonicated for approximately 1 min into 4.0 mL of double-distilled water followed by the addition of 4.0 mL of 800 μM H_2O_2 to initiate the reaction. Approximately 250 μL of 800 μM H_2O_2 was thereafter added on a daily basis.

6.2.6 Incubation with $FeCl_3$ and H_2O_2

Two vials were prepared by sonicating for 1 min approximately 1 mg of carboxylated or pristine SWNTs into 4.0 mL of double-distilled water. $FeCl_3$ (1×10^{-4} M aqueous) was then added at a volume of 500 μL and left to incubate for 24 h. Following incubation, 4.0 mL of 800 μM H_2O_2 was added to initiate the reaction. Approximately 250 μL of 800 μM H_2O_2 was then added on a daily basis.

6.2.7 Transmission Electron Microscopy

Samples in PBS solution were first centrifuged at 3400 rpm for 3 h and decanted of supernatant to effectively remove salts from the buffer. Resuspension into approximately 1 mL of DMF was performed by sonication for 1 min. One drop of the suspended sample was placed on a lacey carbon grid (Pacific-Grid Tech) and allowed to dry in ambient conditions for 2 h prior to TEM imaging (FEI Morgagni, 80 keV or JEOL 2100F, 200 keV). Samples in double-distilled water were used without any further preparation.

6.2.8 UV−vis−NIR Spectroscopy

Aqueous samples (150 μL) were analyzed using a Lambda 900 spectrophotometer (Perkin-Elmer) and 0.20 mL quartz cuvettes (path length: 1 cm, World Precision Instruments, Inc.). SWNTs were scanned from 600 to 1300 nm, while studies involving Amplex Red were scanned from 300 to 800 nm. All samples were used without any further treatment or purification.

6.2.9 Raman Spectroscopy

Samples were centrifuged at 3400 rpm for 3 h and decanted of supernatant to remove salts from the buffer, then resuspended in MeOH through sonication for approximately 1 min. Samples suspended in MeOH were prepared by drop-casting approximately 20 μL on a quartz microscope slide and drying. All spectra were collected on a Renishaw inVia Raman microscope using an excitation wavelength of 633 nm. Samples were scanned from 1000 to 1800 cm^{-1} to visualize D and G band intensity changes from the degradation process. Spectra were collected with a 15 s exposure time and averaged across 5 scans per sample.

6.2.10 Gas Chromatography−Mass Spectrometry (GC−MS)

Approximately 2 μL of sample headspace (total headspace volume: 5 mL) was injected into a Shimadzu QP5050A GC-MS unit with an XTI-F capillary column by sampling through the septum of one of the two previously mentioned vials. A basic temperature program was performed, starting at 100 °C held for 1 min, followed by temperature ramping at a rate of 10 °C/min until a maximum temperature of 325 °C was achieved and held for an additional 10 min.

6.2.11 High-Performance Liquid Chromatography (HPLC)

Samples in PBS solution or double-distilled water were first subjected to gentle heating (40 °C) under vacuum to remove water. Resuspension into approximately 200 μL of MeOH was performed by gentle shaking for 1 min, to concentrate the sample. A Waters 600 analytical HPLC system equipped with both a 996 photodiode array detector and 2410 refractive index

detector was utilized for separation, and this device was outfitted with a reversed phase C18 column consisting of either a Waters Nova C18 or a Waters Symmetry 300 C18 column (Supporting Information). An isocratic solvent system consisting of 30% water and 70% MeCN was selected. Both the water and the MeCN were sparged with He (Valley Gas) for 30 min, and the C18 column was equilibrated for 30 min with the solvent prior to use. Twenty microliters of sample was analyzed over a period of 30 min with a solvent flow rate of 1 mL/min. Empower Pro software was utilized to complete all postprocess data analysis.

6.2.12 Liquid Chromatography−Mass Spectrometry (LC−MS)

Approximately 3 mL of aqueous samples was acidified by the addition of 500 μL of 0.1 M HCl and extracted with dichloromethane (3 mL). After removal of dichloromethane, products were then redispersed in pure MeOH (500 μL). Approximately 10 μL of concentrated sample was injected into an Agilent/HP 1100 LC/MSD unit with an isocratic mobile phase of H_2O:MeCN (30:70) using an Xterra C18 column. Samples were analyzed for positive ions using electrospray mass spectrometry.

6.2.13 Atomic Force Microscopy (AFM)

A Multimode scanning probe microscope (Veeco) was utilized in tapping mode for height, phase, and sectional analysis. Sample preparation was performed on freshly cleaved mica treated with approximately 20 μL of 0.1% (w/w) poly-l-lysine (aq) through spin-coating at 1400 rpm. Approximately 10 μL of sample (aq) was spin-coated at 1400 rpm and allowed to dry in ambient for 45 min prior to imaging. Using a "Supersharp" Si probe (tip radius <5 nm, AppNano), tapping mode at a drive frequency of 182.316 Hz, an amplitude set point of 0.2465 V, and a drive amplitude of 216 mV was performed. Images were initially scanned in a 13.1 μm area prior to magnification of relevant areas. Post imaging processing included section analysis for quantifying cross-sectional heights of samples.

6.2.14 Molecular Modeling, Docking of SWNTs to HRP

The 3-D structure of SWNTs was generated using Nanotube Modeler software[173] to have a diameter of 1.3 nm using the chiral indices (*m*, *n*) as (8, 8) and (14, 4) to model metallic and semiconducting SWNTs, respectively. SWNTs were modified to contain carboxyl and hydroxyl groups using the Builder Tool, provided by Pymol visualization software.[173] Docking of the modified (carboxylated and hydroxylated) and pristine SWNT to the HRP X-ray crystal structure (PDB ID: 1H5A, chain A) was performed using the iterated Local Search Global Optimization algorithm provided by AutoDock Vina.[174] The pdbqt format files (required as input) of both the receptor and the SWNT were generated using the ADT tools package provided by AutoDock4.0.[175] The entire surface of the target was searched for possible binding sites without bias. The grid maps representing the protein were calculated automatically by the AutoDock Vina software.[174] A cubic box was built around the protein with 126 × 126 × 126 points as *x*, *y*, and *z* sizes. A spacing of 0.4 Å between the grid points was used, making the center of the protein to be the center of the cube, that is, *x*, *y*, and *z* centers at 5.766, 5.952, and 13.735, respectively. A total of two CPUs were used to perform the docking. All other parameters were set as default as defined by AutoDock Vina. We further analyzed these conformations to find the most preferred binding site (clusters with a maximum number of conformations and minimum energy) in each case. Although both binding sites were predicted as potential interaction sites for modified (carboxylated and hydroxylated) SWNTs, the preference for each site differed.

6.3 RESULTS AND DISCUSSION

6.3.1 Enzymatic Degradation of SWNTs at Room Temperature

In our previous communication, we presented evidence of enzymatic degradation of carboxylated SWNTs over the course of 12−16 weeks at refrigerated conditions (~4 °C).[167] It is known that rates of chemical reactions are generally increased by a factor of 2-4 for every 10 °C.[176] Thus, for a temperature increase from 4 to 25 °C, an increase in the kinetic rate by a factor of 4−8 should be observed. Such an increase in temperature would result in the same degradation in approximately 2 weeks, provided that enzyme denaturation does not occur.

HRP and carboxylated SWNTs were statically incubated for 24 h at room temperature prior to the addition of 8.0 mL of 80 μM H_2O_2 to begin the reaction. H_2O_2 was then subsequently added to the reaction on a daily basis at 250 μL volume for 10 days, and the sample vials were kept in the dark to avoid photolysis of H_2O_2.[177] As evidence of degradation after 10 days of incubation, **Figure 20, A** shows a photograph of an initial vial of carboxylated nanotubes (left) versus day 10 of incubation with HRP and daily additions of 80 μM H_2O_2 (right). There is a noticeable decrease in light scattering and absorbance from the sample at day 10 of incubation, alluding to degradation as witnessed previously over the course of 16 weeks.

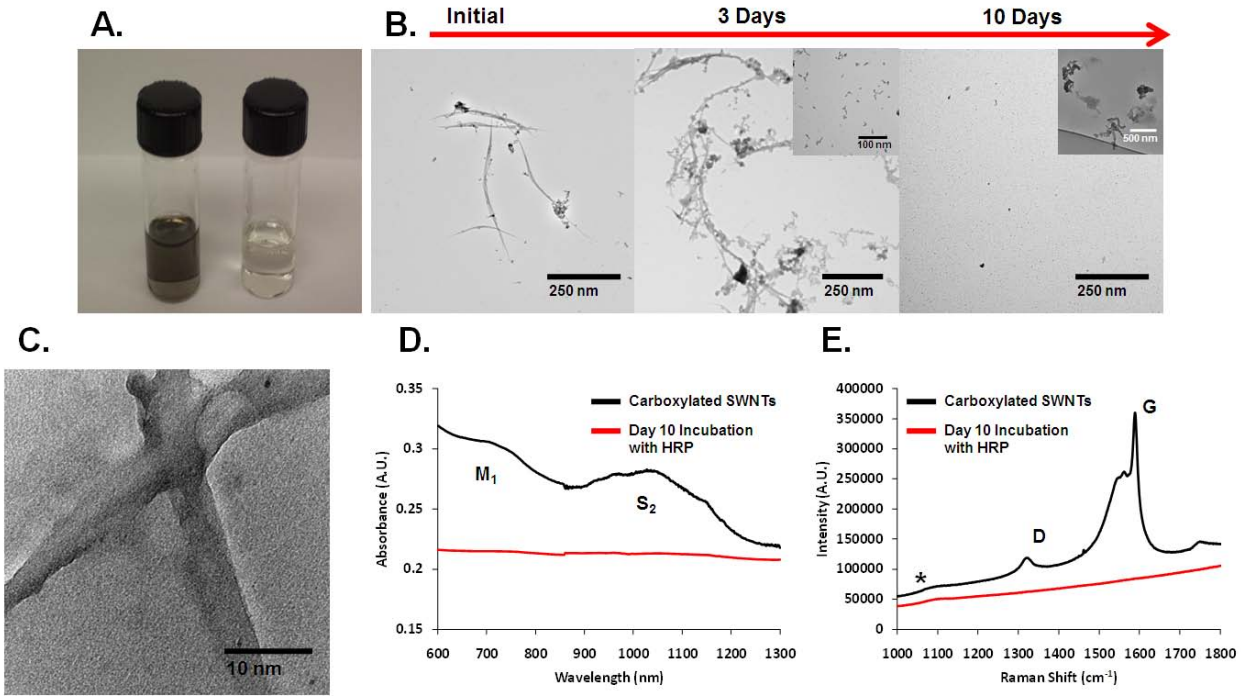

Figure 20. A) Photograph demonstrating enzymatic degradation of carboxylated SWNTs (left) and after 10 days of incubation with HRP and H_2O_2 (right). B) TEM micrograph confirming degradation of carboxylated SWNTs. (Insets) Approximately 2% of fields displayed carbonaceous intermediates. C) High-resolution TEM micrograph of carboxylated SWNTs after 3 days of degradation with HRP and 80 µM H_2O_2. No crystal lattice structure is observed. D) Vis-NIR spectra of carboxylated SWNTs (black) and HRP-degraded SWNTs (red). E) Raman spectra of carboxylated SWNTs (black) and HRP-degraded SWNTs (red) (asterisk indicates contribution from quartz substrate).

To confirm that this decrease in light scattering was the result of degradation, transmission electron microscopy (TEM) was performed on samples prior to and after 10 days of incubation with HRP and H_2O_2. **Figure 20, B** shows tracking of non-degraded, carboxylated SWNTs (left) and carboxylated SWNTs degraded by HRP and H_2O_2 at room temperature over the course of 10 days. As can be seen, carboxylated SWNTs display lengths of approximately 400 nm prior to incubation. After 3 days, some carbonaceous material is present resembling that of SWNTs. Additionally, **Figure 20, C** shows a high-resolution TEM image of SWNTs after 3 days of degradation. As observed, while a one-dimensional structure is still evident, no tubular structure is present, indicating the oxidation of graphitic material. However, after 10 days, no noticeable carbon nanotube material is apparent, presumably due to the oxidation of the graphitic carbon lattice to CO_2 gas. While most fields on a lacey carbon TEM grid appeared to be unoccupied, ~2% (1 field in 50) had carbonaceous products, not resembling SWNTs (inset) and presumably represent an intermediate of incomplete oxidation.

Degradation was additionally confirmed spectroscopically. Visible-near-infrared (vis-NIR) absorption spectroscopy measurements were taken on carboxylated SWNTs (aq) and those degraded after 10 days of incubation with HRP and 80 μM H_2O_2 (aq). It should be noted that SWNTs are synthesized as mixtures of varying diameters and chiralities, exhibiting metallic and semiconducting electronic properties, as well as corresponding spectral features. **Figure 20, D** shows the spectral features of carboxylated SWNTs, evident from the broad S_2 second semiconducting transition absorbing between 1000 and 1100 nm, and the M_1 metallic transition absorbing between 650 and 750 nm.[178] These bands appear to be subdued upon incubation with HRP and H_2O_2 (red trace). As graphitic structure becomes oxidized, transitions associated with sp^2 carbon framework of pristine SWNTs would diminish and completely disappear as a result of

enzymatic degradation. Further examination with Raman spectroscopy reveals similar results. **Figure 20, E** displays the tangential G-band and disorder-induced D-band of carboxylated SWNTs, as previously reported.[179] After enzymatic degradation for 10 days, these bands are no longer present, and only the signal for the quartz substrate (denoted by *) is present. These data again confirm the degradation of carboxylated SWNTs over the span of 10 days when incubating at room temperature (25 °C).

To examine further the mechanism of degradation between HRP and SWNTs, studies were performed investigating the role of carboxylated versus pristine graphitic lattices. As such, pristine SWNTs (Carbon Solutions, Inc.) were incubated under the same conditions as mentioned for carboxylated SWNTs. Briefly, pristine SWNTs were sonicated for approximately 5 min in DMF. Subsequently, samples were centrifuged at 3400 rpm, and the supernatant was decanted. The precipitated pristine SWNTs were then washed with double-distilled H_2O and resuspended in 4.0 mL of PBS through additional sonication. Pristine SWNTs treated in this manner retained some solubility (suspension stable for up to 2 days), but not to the extent of carboxylated SWNTs. Periodic shaking was then necessary to re-suspend pristine SWNTs. To this suspension was added 4.0 mL of 0.385 mg/mL HRP (aq), and it was allowed to incubate for 24 h prior to H_2O_2 additions as previously performed. Over the course of the 10 day incubation with HRP and H_2O_2, there was no noticeable decrease in scattering or absorbance but increased aggregation, suggesting a lack of degradation of carbon material. To confirm this phenomenon, TEM imaging was performed on an aliquot taken 10 days after incubation with HRP and 80 μM H_2O_2. **Figure 21, A** shows that pristine SWNTs are still intact (≥ 2 μm in length) and do not appear to be deformed or degraded in any manner. Because pristine SWNTs did not degrade, two factors were of immediate importance to investigate: (1) the role of H_2O_2 concentration and (2) the viability of HRP with pristine SWNTs.

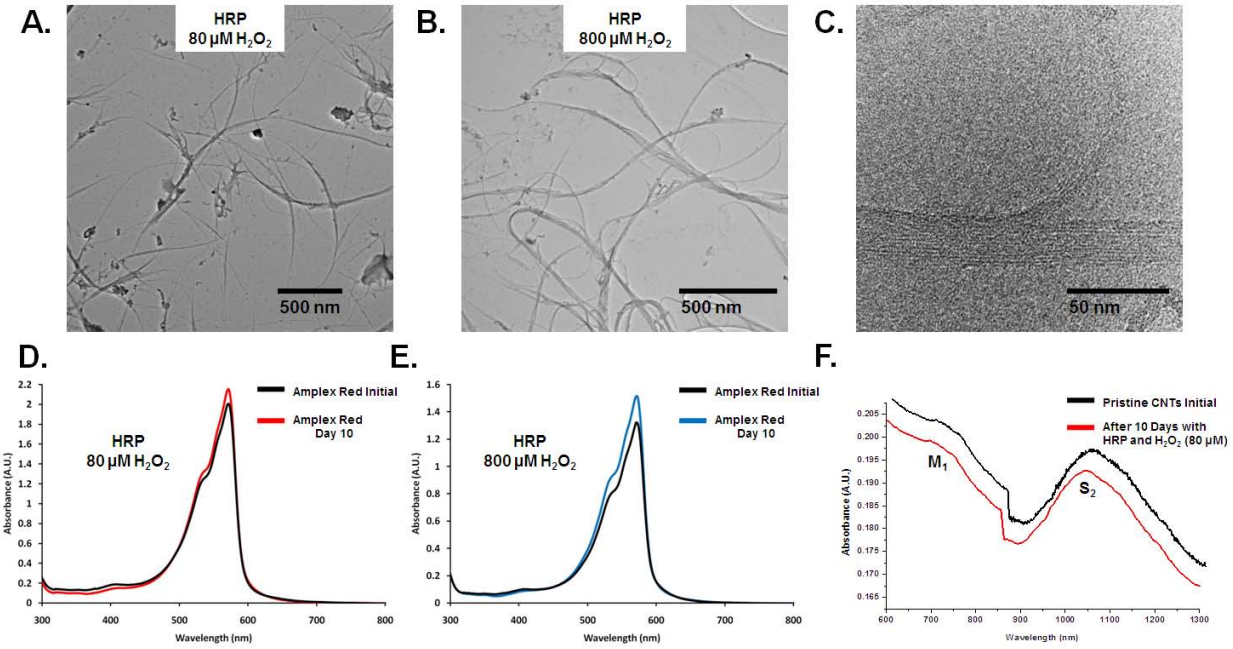

Figure 21. A) TEM micrograph of pristine SWNTs after 10 days of incubation with HRP and 80 μM H_2O_2 and (B) 800 μM H_2O_2. C) High-resolution TEM micrograph of pristine SWNTs after 10 days of degradation with HRP and 800 μM H_2O_2. Crystal lattice structure is observable as SWNTs appear bundled, with exfoliation of smaller bundles present at the immediate ends of larger bundles. D) UV-vis spectra of Amplex Red activity with HRP and 80 μM H_2O_2 or (E) 800 μM H_2O_2. F) Vis-NIR spectra of pristine SWNTs (black) and after 10 days of incubation with HRP and 80 μM H_2O_2.

Pristine SWNTs were then subjected to conditions identical to those mentioned with the exception of initiating degradation with an excess of 800 μM H_2O_2 (K_M: 0.11 mM).[180] It was interesting to see whether changing the concentration by an order of magnitude would affect the degradation of pristine SWNTs in a significant manner. As indicated by the TEM micrograph in **Figure 21, B**, no significant degradation was found with the addition of 800 μM H_2O_2. Closer examination using high-resolution TEM revealed bundled SWNTs that retained their crystal lattice structure after 10 days of incubation with HRP and 800 μM H_2O_2 (**Figure 21, C**). Such data, however, may point to the denaturation or inactivation of HRP by pristine SWNTs. It is then advantageous to investigate whether the enzyme retains activity in solution with pristine SWNTs and if this activity is affected by the 10-fold increase in H_2O_2 concentration.

To test the viability of HRP in the presence of pristine SWNTs, Amplex Red was used. Amplex Red (10-acetyl-3,7-dihydroxyphenoxazine) is a reagent commonly employed to measure trace H_2O_2 concentrations in biological systems.[181] In the presence of H_2O_2, Amplex Red undergoes HRP-catalyzed oxidation to form radical intermediates. The radical intermediates then proceed via a dismutation reaction to form resorufin, which has distinct fluorescence and absorbance spectra. Because the conversion of Amplex Red to resorufin depends on an active enzyme, the spectral features of resorufin can be used to monitor HRP activity. Thus, by monitoring an absorbance peak present at 570 nm, a result of resorufin produced from active enzyme and Amplex Red, it is possible to validate enzyme viability. **Figure 21, D,E** depicts the results for the Amplex Red assay; three major trends can be ascertained from this data. First, initially, the UV-vis spectroscopic data displayed a peak around 570 nm, which indicated that HRP was originally active. Second, there was no decrease in absorbance at day 10; therefore, a sufficient quantity of HRP remained active to catalyze the conversion of Amplex Red into

resorufin. While it may be possible that HRP is deactivated by auto-oxidation, a significant contribution from active HRP is still present. Third, HRP remained viable after additions of both 80 and 800 μM H_2O_2. These observations logically lead one to conclude that while HRP remains active (or active in part) in the presence of pristine SWNTs, it cannot catalyze their degradation in the tested time frame and given HRP concentration. Further spectroscopic confirmation of this phenomenon was observed using vis-NIR spectroscopy. **Figure 21, F** shows a spectroscopic comparison between pristine SWNTs and those subjected to HRP and 800 μM H_2O_2. As indicated by the spectral features, characteristic S_2 and M_1 bands are present after 10 days of incubation, demonstrating a lack of degradation. One plausible explanation for this observation involves interactions between SWNTs and HRP, to be discussed below.

6.3.2 Oxidation of SWNTs by Fenton's Reagents

Data thus far allude to heterolytic cleavage of H_2O_2 to form Compound I and H_2O. As pristine SWNTs do not degrade in the presence of HRP and H_2O_2, this lends credibility to a proximity effect between the active site of Compound I and SWNTs. In contrast to this mechanism, homolytic cleavage of H_2O_2 results in the production of hydroxyl radicals ($^{\bullet}OH$) via Fenton's chemistry.[182] In essence, H_2O_2 oxidizes Fe^{2+} to Fe^{3+} and produces OH^- and $^{\bullet}OH$. Ferric iron is then reduced back to ferrous iron by additional peroxide, producing H^+ and $^{\bullet}OOH$.

$$Fe^{2+} + H_2O_2 \rightarrow Fe^{3+} + {\bullet}OH + OH^- \quad (1)$$

$$Fe^{3+} + H_2O_2 \rightarrow Fe^{2+} + {\bullet}OOH + H^+ \quad (2)$$

While both Compound I and hydroxyl/hydroperoxyl radicals are highly oxidizing species, the ability of Compound I to degrade SWNTs may be contingent upon spatial proximity to the heme active site, whereas the reactivity of hydroxyl and hydroperoxyl radicals is limited only by the rate of diffusion and their half-lives.[183]

To compare the HRP oxidation mechanisms involving Compound I formation and hydroxyl and hydroperoxyl radicals formed via Fenton chemistry to degrade SWNTs, we chose hemin (chloride), a ferric iron chloroprotoporphyrin, and a ferric iron salt ($FeCl_3$). It is important to note that while Fenton catalysis is typically initiated with ferrous iron, we chose ferric iron species to be consistent among all iron forms tested. Most importantly, because $FeCl_3$ lacks the protein structure of HRP, homolytic cleavage of H_2O_2 to form hydroperoxyl and hydroxyl radicals is the predominant pathway for oxidation to occur, whereas hemin may act under either a homo- or a heterolytic cleavage mechanism.

For the examination of hemin, approximately 1 mg of pristine or carboxylated SWNTs was sonicated in 4.0 mL of DMF. Hemin (1×10^{-4} M, in DMF) was then added in excess at a volume of 16.0 mL. After 24 h of incubation, samples were centrifuged, decanted of excess hemin and DMF, and sonicated into 4.0 mL of double-distilled water. Typically, hemin forms an inactive dimer when free in solution.[184] However, it has been previously shown that porphyrins physisorb onto SWNTs, providing close proximal contact to the iron site.[172] Such proximity may result in increased activity, generating oxidizing species close to carboxylated and pristine SWNTs, promoting degradation. The degradation reaction was initiated by the addition of 4.0 mL of 800 μM H_2O_2, followed by daily additions of 250 μL of 800 μM H_2O_2 for a total of 10 days.

Over the 10 day incubation period, carboxylated SWNTs were degraded by hemin and 800 μM H_2O_2 (Supporting Information). In contrast to incubation with HRP and 800 μM H_2O_2, pristine SWNTs have also showed significant degradation. **Figure 22, A** shows TEM images of the products of this degradation reaction over the course of 10 days. As demonstrated, after 2 days of incubation, pristine SWNTs appeared to "swell" and aggregated together. After day 4, however, pristine SWNTs broke down with significant noticeable deformation. By day 8, only small carbonaceous products and residual iron (catalyst from nanotube synthesis) were present (Supporting Information).

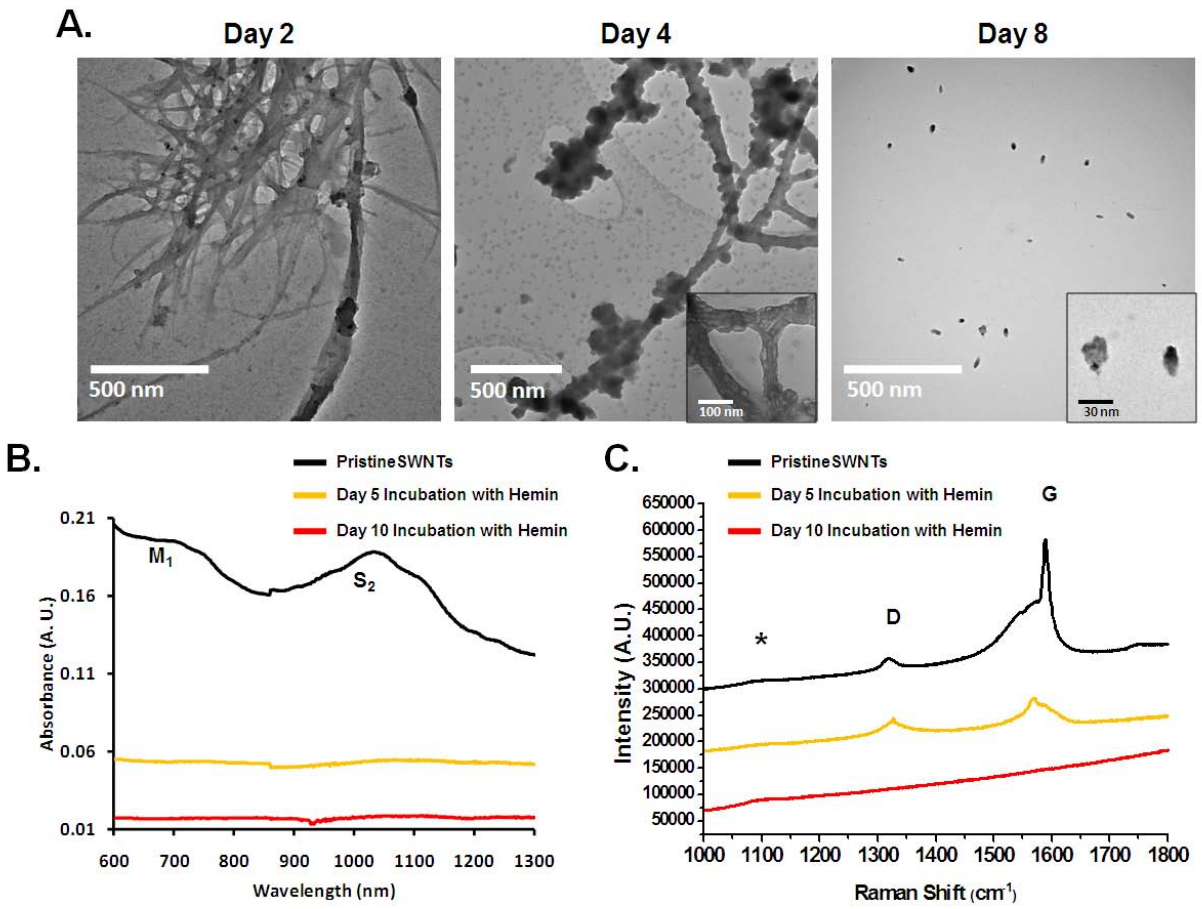

Figure 22. A) TEM micrographs displaying degradation of pristine SWNTs with hemin and 800 µM H_2O_2 over 10 days. Inset at day 4 shows deformation of individual fibers, while inset at day 8 shows residual iron. B) Vis-NIR spectra of pristine SWNTs after incubation with hemin and H_2O_2. C) Raman spectra of pristine SWNTs degraded by hemin and H_2O_2. (Asterisk indicates quartz substrate contribution.)

Spectroscopic data further support these observations. **Figure 22, B** shows the vis-NIR spectra of pristine SWNTs degraded with hemin and H_2O_2 over 10 days. A loss of intensity and changes in band shape for the M_1 and S_2 metallic and semiconducting transitions of pristine SWNTs are quite evident and comparable to results seen with carboxylated SWNT degraded by HRP and H_2O_2. These spectral changes suggest degradation of the pristine graphitic material. Raman characterization further supports this degradation as demonstrated in **Figure 22, C**. Pristine SWNTs display prominent D and G band contributions initially. After 5 days of degradation, the D:G band ratio increases, indicating modification of the pristine SWNT structure, accompanied by an increase in the number of defect sites. By day 10 of incubation, only the residual peak for the quartz substrate is present, as indicated by an asterisk. Therefore, the degradation of pristine SWNTs by hemin is likely to proceed by increased proximity to the active iron site, whereas HRP limits this proximity as a result of distal site binding, as will be further explained.

To compare these degradation methods to that of a Fenton catalyst, where only free radicals are generated, $FeCl_3$ was used. Briefly, 1 mg of carboxylated (Supporting Information) or pristine SWNTs was sonicated for 1 min into 4.0 mL of double-distilled water. Next, 500 μL of $FeCl_3$ (1×10^{-4} M, aqueous) was added to all samples, and they were incubated for 24 h before 4.0 mL of 800 μM H_2O_2 was added to initiate the reaction. Daily additions of 250 μL of 800 μM H_2O_2 were continued for 10 days. **Figure 23, A** shows the TEM images of pristine SWNTs incubated with $FeCl_3$ and H_2O_2. Evidently, even after 2 days of incubation, long pristine SWNTs oxidized into individual flakes, an observation similar to that reported by Kosynkin *et al.* whereby unzipping was facilitated by chemical treatment with H_2SO_4 and $KMnO_4$.[185] By day 4, flakes were approximately 40 nm in length, while at day 8, it appeared that mostly residual iron was present. Upon closer examination with high-resolution TEM, flakes (~3 nm wide) displayed a crystalline structure, indicating the presence of graphitic material (**Figure 23, B**).

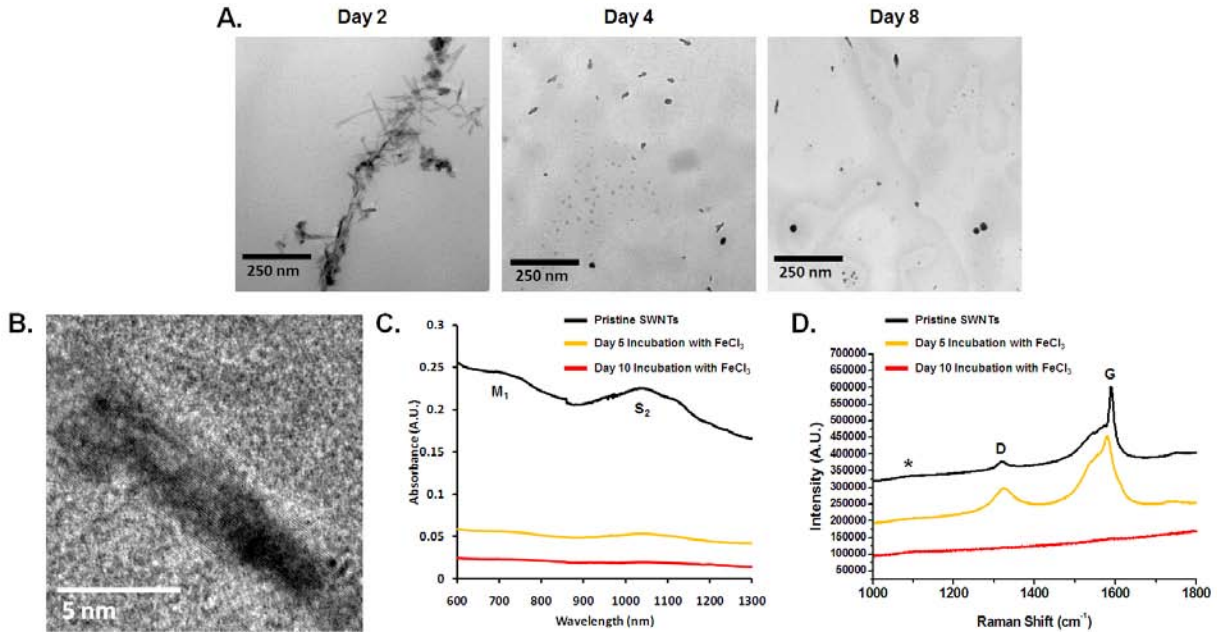

Figure 23. A) TEM micrographs of $FeCl_3$-catalyzed degradation of pristine SWNTs. SWNTs are shown to "flake" at day 2, followed by progressive shortening through day 8. B) High-resolution TEM micrograph of "flake" produced after degradation (day 5) with $FeCl_3$ and 800 µM H_2O_2. Crystal lattice structure is still observable for the individual flake. Further elemental analysis shows the presence of carbon, oxygen, and iron (Supporting Information). C) Vis–NIR spectra of pristine SWNTs degraded by $FeCl_3$ and 800 µM H_2O_2. D) Raman spectra of pristine SWNTs degraded by $FeCl_3$ and 800 µM H_2O_2. (Asterisk indicates quartz substrate contribution.)

Similar results were obtained spectroscopically, as well. **Figure 23, C** shows the vis−NIR spectra of pristine SWNT degradation. Initially, pristine SWNTs displayed pronounced semiconducting and metallic transition bands (S_2 and M_1, respectively). Following 5 days of incubation, these bands were greatly suppressed, and finally all band structure was lost at day 10. Raman data conformed to these results as shown in **Figure 23, D**. Pristine SWNTs were observed to have defined D and G band peaks contributed by the defect sites and the pristine graphitic lattice of the SWNTs, respectively. The ratio of the D to G bands then increased after 5 days, indicating progressive oxidation of the material. By day 10, however, only the peak for the quartz substrate was observed, indicating a complete loss of nanomaterial.

Results of both hemin and $FeCl_3$ demonstrate that by increasing the proximity of active iron sites and generating radical oxygen species, pristine SWNTs will degrade. Conversely, no degradation is evident with pristine SWNTs and HRP, indicating an alternate degradation mechanism, presumably because of the heterolytic cleavage of H_2O_2 to form Compound I. The role of SWNTs in the homolytic degradation reaction is even more significant as Fenton catalysis is typically generated from ferrous iron, although it is ferric prior to addition with pristine SWNTs. Because the degradation reaction does progress, it may be that carbon nanotubes are acting as a reducing agent to reduce ferric iron to ferrous iron because of their unique redox properties[186] and possible reducing character of the inherent polyphenol functionalities located within the SWNT lattice of both pristine and carboxylated varieties.[187]

6.3.3 Degradation Product Analysis

Identification of intermediate products of the HRP-catalyzed degradation reaction was performed using HPLC, LC–MS, and GC–MS. While the formation of CO_2 gas will be shown as a likely final product of the degradation process, classes of intermediate species resulting from incomplete degradation have yet to be identified or enumerated. It may be possible that multiple intermediate products may form and reside in the aqueous media, including various oxidized aromatic hydrocarbons. To begin evaluating the variety of species present within aqueous media, reversed-phase HPLC was implemented. Briefly, aqueous samples were dried by heating under vacuum at 40 °C for 2 h, thus retaining carbonaceous products and buffer salts contained therein. It is important to note that during this procedure it is possible that low boiling point molecules were lost in the process. However, in PBS solution prior to concentration, they are in low abundance and not detected by an HPLC chromatogram (Supporting Information). Reagent grade MeOH was then added to re-suspend the dehydrated product through gentle shaking. Samples consisting of HRP-degraded, hemin-degraded, and $FeCl_3$-degraded, carboxylated nanotubes at day 8 of incubation were injected into a reversed phase HPLC column. An isocratic program consisting of a 30:70 mixture of H_2O:MeCN ran for 30 min at a flow rate of 1 mL/min.

Figure 24, A shows the resulting chromatogram from HRP-degraded SWNTs. Beginning at 4.5 min and terminating at 10.5 min, a series of peaks are eluted with a 1 min elution delay. This series of peaks may be due to the presence of oxidized aromatic hydrocarbons, while elution peaks at 20 and 25 min may be due to larger oxidized aromatic species with higher affinity to the C18 column. As a comparison, mellitic acid and *trans*-cinnamaldehyde were injected as standards (Supporting Information). They were observed to elute in the same retention time as peaks presented in the HRP-degraded sample. Additionally, pure HRP in MeOH was injected to verify that observed peaks from HRP-degraded samples did not belong to fragmented enzyme (Supporting Information).

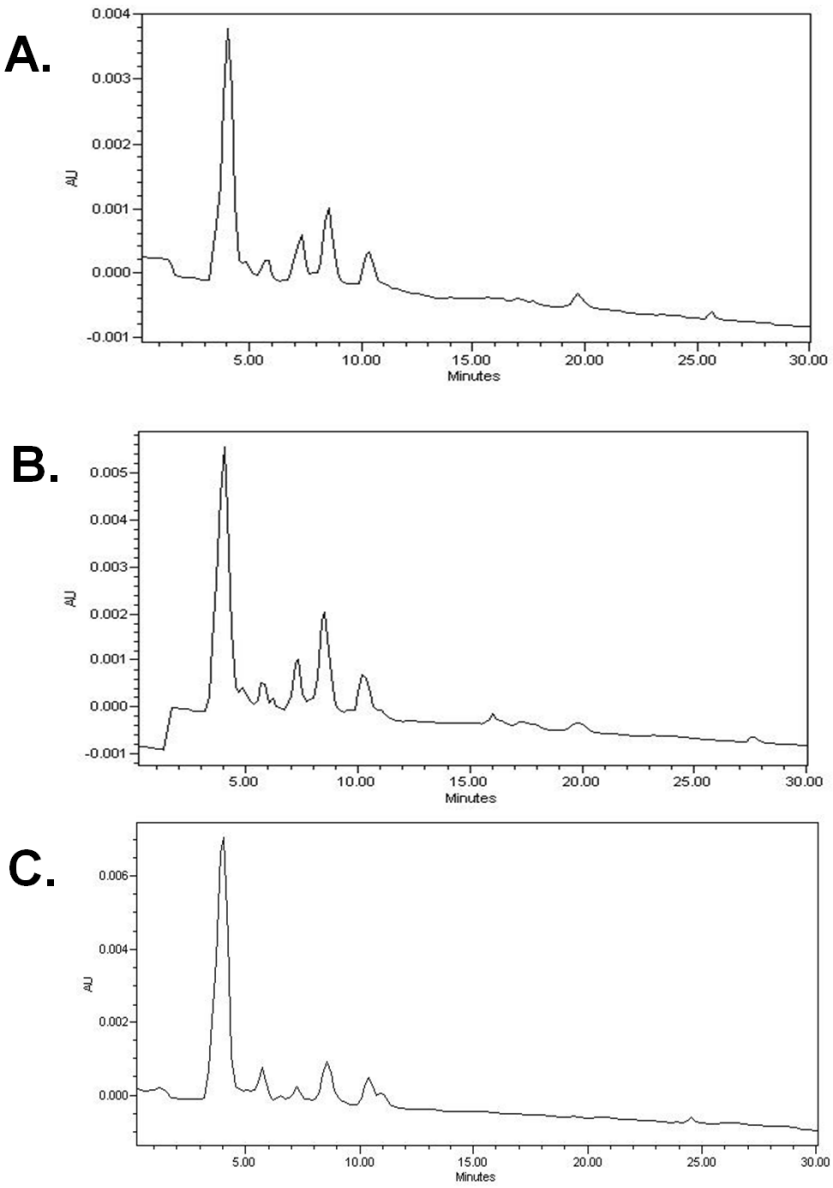

Figure 24. A) HPLC (Nova C18 column) chromatogram of HRP-degraded, carboxylated SWNTs after 8 days of incubation. B) Hemin-degraded and (C) $FeCl_3$-degraded, carboxylated SWNTs after 8 days of incubation.

Products resulting from hemin and $FeCl_3$ degradation by free radical oxidation were analyzed by HPLC. **Figure 24, B** shows the resulting chromatogram for hemin degraded products. As is evident with hemin degradation, a series of peaks is observed immediately after 4.5 min, at elution times previously demonstrated for HRP products, and identified as possible oxidized aromatic hydrocarbons. Only past elution times of 15 min are any differences noted in the chromatograms (areas indicative of larger oxidized aromatic hydrocarbons). Similar results are shown for $FeCl_3$-degraded carboxylated SWNTs (**Figure 24, C**). A series of peaks corresponding presumably to oxidized 2–5 membered rings is seen, although with less intensity. These results demonstrate that products formed are strikingly similar regardless of heterolytic or homolytic reaction pathways for SWNT degradation. However, differences present at elution times past 15 min, where larger oxidized polycyclic aromatic hydrocarbons (PAHs) may be found, suggest the nonspecific oxidation of SWNTs (by hemin and $FeCl_3$) into larger flakes through an "unzipping" effect as opposed to that of HRP degradation, where oxidation is mediated on site-specific areas consistent with TEM observations. Additional structure elucidation of the intermediate degradation products would require their isolation on a preparative scale HPLC and characterization by NMR and mass spectrometry methods, as we are examining a mixture of intermediate products without finite separation.

To identify types of products resulting from the degradation of SWNTs by HRP, hemin, or $FeCl_3$, LC–MS was performed. Briefly, samples were prepared by removing 3 mL aliquots from bulk aqueous solutions, acidifying with 0.1 M HCl, and extracting with dichloromethane (3 mL). After solvent removal, the products were re-dispersed into 500 μL of MeOH and separated/analyzed using a reversed-phase C18 column and mass spectrometer with conditions identical to those mentioned previously for HPLC. By analyzing positive ions, multiple products

were identified from HRP-degraded, carboxylated SWNTs. Shown in **Figure 25, A**, mass to charge (*m*/*z*) values of 106.1, 110.1, 132.1, and 212.1 were observed for HRP-degraded SWNTs, indicative of benzaldehyde (**1**), 1,2-benzenediol (**2**), cinnamaldehyde (**3**), and diphenylacetic acid (**4**). Of significance, $FeCl_3$-degraded pristine SWNTs exhibited similar degradation products (**Figure 25, B**). In addition to those molecules attributed to HRP degradation, benzyl alcohol (**5**), 1,3,5-benzenetriol (**6**), cinnamic acid (**7**), and 4-benzyloxybenzoic acid (**8**) were also identified. This again confirms the presence of similar classes of compounds for both heterolytic and homolytic degradation mechanisms; however, it is important to note that mass spectrometry cannot distinguish between molecular ions and fragments, and preparative scale experiments involving product separation still need to be performed. Moreover, the identified products were similar to those observed in studies of the bioremediation of polycyclic aromatic hydrocarbons (PAHs).[188] In that work, degradation was observed by the addition of cytochrome P_{450} monoxygenase enzyme; PAHs were first oxidized to arene oxides followed by the formation of dyhydrodiols and phenols, as well as aromatic carboxylic acids.[189] Complete oxidation in that case resulted in the formation of CO_2.

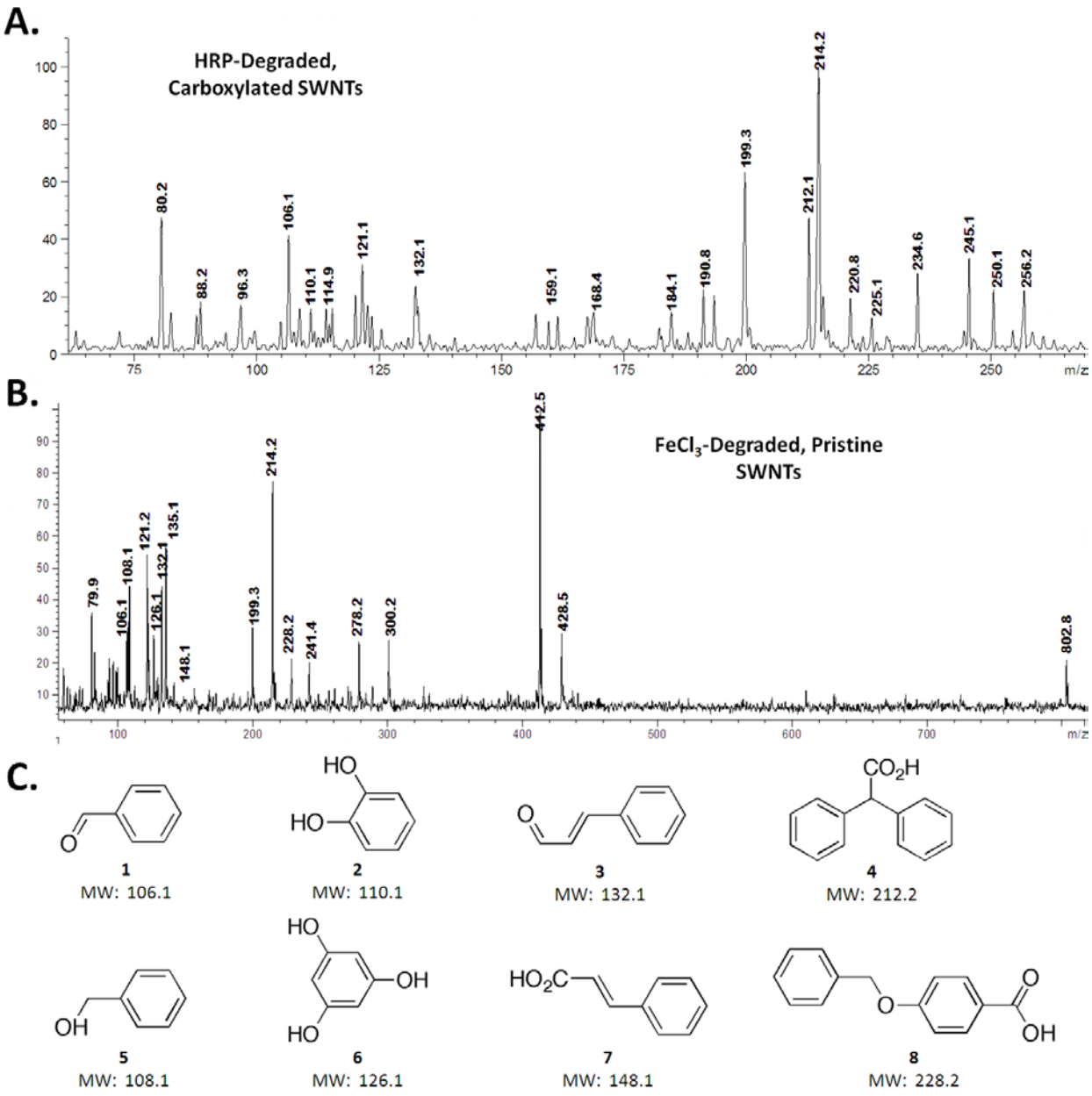

Figure 25. A) LC-MS spectrum of HRP -degraded, carboxylated SWNTs and (B) $FeCl_3$-degraded pristine SWNTs. C) Products identified and present in the HRP degradation method included oxidized PAHs such as benzaldehyde (1), 1,2-benzenediol (2), cinnamaldehyde (3), and diphenylacetic acid (4). $FeCl_3$-degraded pristine SWNTs produced benzyl alcohol (5), 1,3,5-benzenetriol (6), cinnamic acid (7), and 4-benzyloxybenzoic acid (8), as well as products common to both methods (1 and 3).

As a result of complete oxidative degradation of SWNTs, however, one would expect the final product to be carbon dioxide, a gas. To verify the production of CO_2 as a product of complete degradation, G∈MS was used to analyze the headspace of the sample. As was previously noted, sample vials were prepared by capping with a septum and parafilm, thus allowing for the sampling of headspace using a gastight needle. Approximately 2 μL of sample headspace was injected at two discrete times: (i) prior to the introduction of H_2O_2 to initiate the reaction and (ii) after 10 days of incubation with HRP and H_2O_2. CO_2 concentrations were evaluated relative to ambient N_2 concentrations present in the headspace. Further, a control of double-distilled water and H_2O_2 (no HRP) was treated and analyzed under the same conditions to verify contributions from any possible ambient CO_2 (Supporting Information). **Figure 26, A** demonstrates the increase in CO_2 (*m*/*z*: 44) contributions after 10 days of incubation. Apparently, the abundance of CO_2 doubled over the course of 10 days. Further examination of CO_2 production with hemin and $FeCl_3$-mediated degradation was also performed. The change in the CO_2 abundance after 10 days of SWNT degradation relative to the original value is shown in **Figure 26, B**. As can be seen, the CO_2 concentration became approximately 100% higher with carboxylated SWNTs degraded in the presence HRP, hemin, or $FeCl_3$. Conversely, pristine SWNTs incubated with HRP had a minimal evolution of CO_2, comparable to the control of H_2O. Pristine SWNTs incubated with hemin or $FeCl_3$, however, displayed a marked increase in CO_2 (Supporting Information).

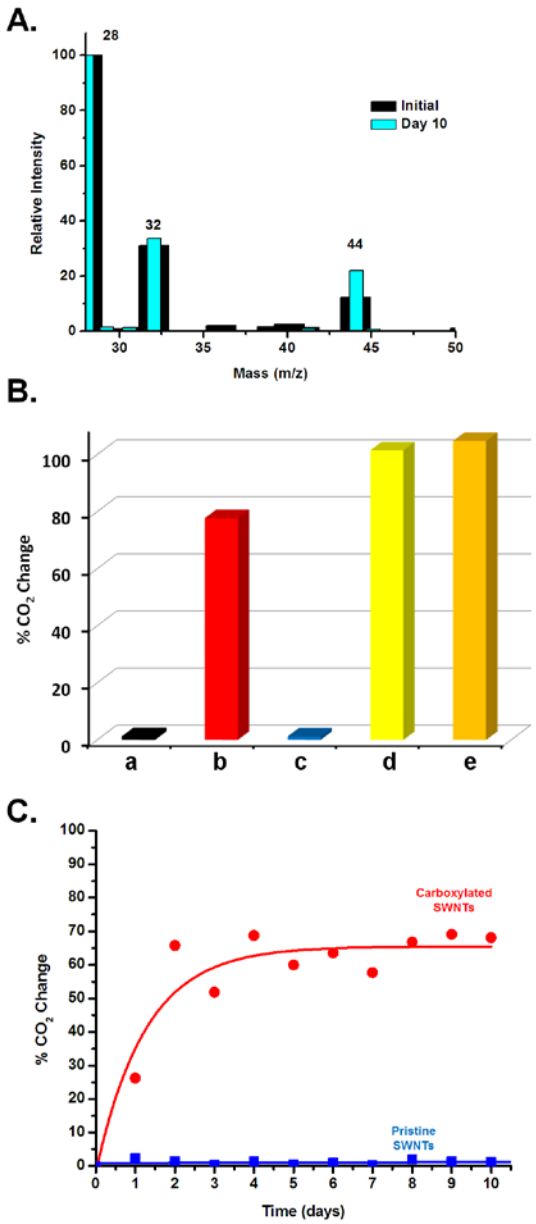

Figure 26. A) Relative intensity versus mass (*m*/*z*) for CO_2 headspace concentration relative to N_2 for HRP-degraded SWNTs. Enzymatic degradation results in an approximate doubling of the CO_2 concentration. B) Percent (%) change in the headspace CO_2 concentration after 10 days of incubation of (b) carboxylated SWNTs, HRP, and H_2O_2, (c) pristine SWNTs, HRP, and H_2O_2, (d) carboxylated SWNTs, hemin, and H_2O_2, and (e) carboxylated SWNTs, $FeCl_3$, and H_2O_2. A control of H_2O with daily additions of H_2O_2 (without HRP) is shown in black (a). C) Kinetics tracking of CO_2 evolution by GC–MS over a 10 day period for carboxylated and pristine SWNTs incubated with HRP and H_2O_2 (800 µM).

Furthermore, we have monitored the evolution of CO_2 gas in sample headspace on a daily basis to compare the kinetics of the degradation process between carboxylated and pristine SWNTs incubated with HRP and H_2O_2 (800 μM). As shown in **Figure 26, C**, CO_2 evolution was followed for 10 days and measured relative to N_2. As evident from this figure, pristine SWNTs incubated with HRP and H_2O_2 did not produce any significant concentrations of CO_2 in the sample headspace over the course of 10 days, further indicating a lack of degradation of the pristine material. Conversely, when carboxylated SWNTs were incubated with HRP and H_2O_2, CO_2 was measured in the sample headspace and found to follow pseudo first-order kinetics (**Figure 26, C**).

6.3.4 AFM Characterization

Atomic force microscopy (AFM) was used to probe the interaction between HRP and carboxylated SWNTs. Previously, AFM has been implemented to monitor interactions between biological species and SWNTs.[190-193] As such, multiple samples including HRP, carboxylated SWNTs, and HRP incubated with carboxylated SWNTs were imaged in tapping mode using a super sharp silicon probe (<5 nm radius, AppNano). **Figure 27, A** illustrates the height profile of a single HRP unit. Of important note, because tapping mode was used for imaging, distortions arose in the sample in the form of exaggerated size features.[194] Thus, it was important to perform a cross-section analysis on all samples to verify true height profiles. HRP then demonstrated a height of approximately 5 nm as shown by the section analysis (Supporting Information). Further, **Figure 27, B** shows the height profile of a single, carboxylated SWNT prior to incubation with HRP. Section analysis confirmed a height of 1.8 nm, representative for this type of SWNT (Supporting Information). Upon examining carboxylated SWNTs incubated

with HRP (**Figure 27, C**), it was evident that enzyme attachment presumably occurred at the carboxylated sites along the axis of SWNTs. Section analysis (**Figure 27, D**) confirmed this additive effect of enzyme attachment. A similar trend, however, was noted for pristine SWNTs incubated with HRP. AFM of pristine SWNTs interacting with HRP displayed similar enzyme adsorption (Supporting Information). It may be that specific orientations between enzymes and SWNTs in solution promote or inhibit their degradation. Because pristine nanotubes are prone to bundle in solution, it may be that access is limited to the HRP active site. However, previous high-resolution TEM imaging shows exfoliation of larger bundles near the ends. These sites would then be suitable for enzymatic docking and subsequent degradation. Thus, a more probable scenario would be the docking of pristine SWNTs to an alternative hydrophobic site, further separated from the heme active site responsible for oxidation.

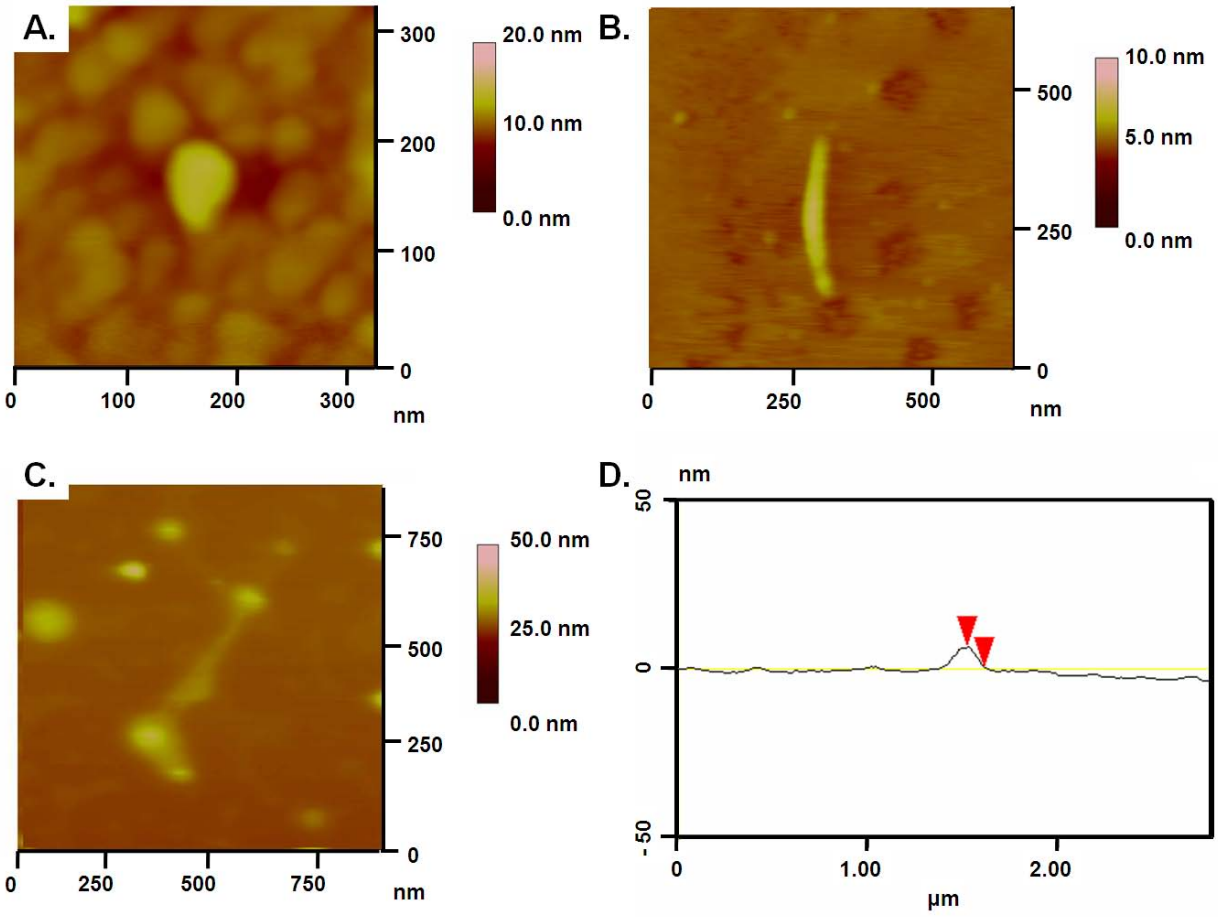

Figure 27. A) AFM image of single HRP unit under tapping mode imaging. B) AFM image of single, carboxylated SWNT. C) AFM image of carboxylated SWNT interacting with multiple HRP units. D) AFM section analysis of combined carboxylated SWNT and HRP showing a height of approximately 6.0 nm.

As further proof of proximity effects, carboxylated SWNTs were cast onto a quartz substrate and subjected to identical conditions involving HRP and H_2O_2. Thin-film UV-vis-NIR absorption spectroscopy data suggest that no significant degradation of the SWNT film occurred over a period of 10 days, presumably due to lack of mobility and spatial confinement of carboxylated SWNTs and adsorbed HRP (Supporting Information).

6.3.5 Molecular Modeling

Molecular modeling tested these theories regarding orientation effects between carboxylated and pristine nanotubes with HRP. Suggested previously,[195-197] there is a strong interaction between SWNTs and proteins due to the attractive forces between the carboxyl groups of SWNTs and positively charged domains of proteins. Such adsorption allows for the distance separation of the HRP active site to be diminished in relation to the carboxylated SWNT substrate. By bringing carboxylated SWNTs in proximity to the heme site forming Compound I, it is possible for the reactive species to oxidize and thus degrade SWNTs. It can then be assumed that because of the hydrophobic nature of pristine SWNTs, HRP is forced to align itself in such a way as to result in the increased proximal distance between the heme active site and SWNT substrate. Such a slight increase in distance will discourage the oxidation and thus the degradation of pristine SWNTs. To further understand the molecular interactions during the degradation of modified (carboxylated and hydroxylated) SWNTs by HRP, we identified the possible binding sites on the enzyme to accommodate SWNTs.[198,199] The generated modified and pristine SWNT models with the chirality (8,8), which are metallic SWNTs with 1.3 nm diameters, were docked to the HRP crystal structure (PDB ID: 1H5A, chain A). In each case, the resulting nine complexes were further analyzed to find the best docked conformation. For modified SWNTs with both

carboxyl and hydroxyl groups added at the end, 6 out of 9 docked conformations were predicted to bind to HRP in close proximity to the heme binding pocket (**Figure 28, A,C**). The carboxylated ends of the SWNT are oriented toward a positively charged arginine residue, Arg178, on HRP (**Figure 28, C**, Arg is colored in yellow). This may be important in stabilizing the binding of carboxylated/hydroxylated SWNTs with the protein. Analysis of the residues located within 5 Å distance from the docked modified SWNT revealed the presence of F68, N135, L138, A140, P141, F142, F143, T144, Q147, R178, F179, D182, N186, F187, S188, N189, and Q245. The involvement of most of these residues in the catalysis of oxidation reactions has been demonstrated previously.[200,201] In addition to this, some of these residues are also part of the catalytically active site of the enzyme.[201] In contrast, for pristine SWNTs, the most preferred interaction site (9 out of 9 conformations) was located at the distal end of the enzyme, opposite from its heme moiety (**Figure 28, B,D**). While the predicted interaction energies for the modified and pristine SWNTs were −15.1 kcal/mol (at the heme binding site) and −15.7 kcal/mol (at the distal end of the heme binding pocket), respectively (Supporting Information), the remoteness of the binding site for pristine SWNTs from the heme makes its catalytic oxidation unlikely. These predictions are in good agreement with the experimental results. Additional controls were performed to examine the effect of sidewall defects on HRP binding, the binding of bundled-pristine SWNTs to HRP, and a comparative inquiry of nanotube chirality where different helicities ((8,8) and (14,4) for metallic and semiconducting nanotubes, respectively) but identical diameter were studied. All results confirmed previous observations and can be found in the Supporting Information. Such data suggest that helicity has no apparent role over preferential enzymatic degradation. Most likely, diameter and especially surface functionalities are responsible for successful oxidation to occur.

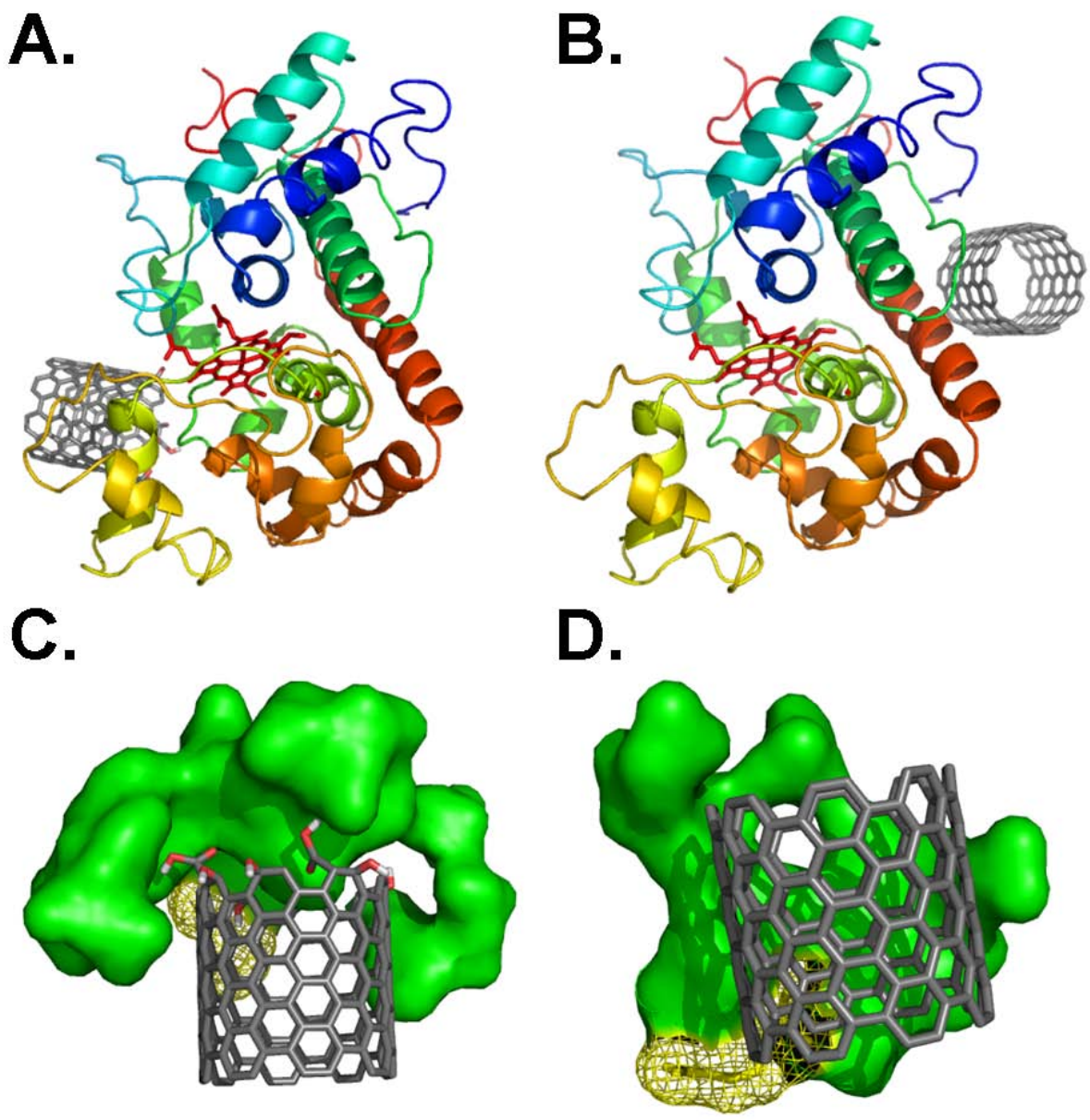

Figure 28. Binding of modified (carboxylated and hydroxylated) and pristine SWNT to horseradish peroxidase. Location of the most preferred binding site on HRP for (A) modified SWNT and (B) pristine SWNT. The corresponding 5 Å binding site residues from the (C) modified SWNT and (D) pristine SWNT to HRP for the predicted binding site locations shown in (A) and (B), respectively. SWNT is colored in gray and rendered in sticks. Residues that correspond to arginine are colored in yellow. The heme is rendered as sticks and colored in red and render as mesh.

6.4 CONCLUSIONS

Both pristine and carboxylated SWNTs were explored in terms of their ability to degrade in the presence of HRP. Moreover, varying conditions including temperature and concentrations of H_2O_2 were explored. Data suggest that strong adsorption of HRP to carboxylated sites facilitates the degradation of carboxylated SWNTs, while the hydrophobic nature of pristine SWNTs forces HRP to orient in a way that increases the distance between the heme active site and the SWNT surface, thus mitigating the enzyme's oxidative effects. Such data suggest heterolytic cleavage of H_2O_2 to form Compound I, as opposed to homolytic cleavage facilitated by hemin and $FeCl_3$. Use of either of the latter two species catalyzes the homolytic cleavage of H_2O_2, thus forming hydroxyl and hydroperoxyl radicals in a process known as Fenton's catalysis. Moreover, hydroxyl and hydroperoxyl radicals are able to diffuse in solution once formed, and oxidize both carboxylated and pristine SWNT substrates, causing their degradation. Further, the nature of the degradation products has been estimated by HPLC and LC–MS, and the formation of carbon dioxide was established by GC–MS. Future studies involving the preparative scale investigations of products formed during incomplete degradation could reveal their exact structures.

6.5 ACKNOWLEDGMENTS

This work was supported by AFOSR, Grant no. FA 9550-09-1-0478; NIOSH OH008282 and the 7th Framework Programme of the European Commission (NANOMMUNE).

6.6 SUPPORTING INFORMATION

Supporting information for Chapter 6.0 'Mechanistic Investigations of Horseradish Peroxidase-Catalyzed Degradation of Single-Walled Carbon Nanotubes' can be found in **Appendix E**. The data available includes Amplex Red controls with 80 μM (**Figure 59**) and 800 μM (**Figure 60**) H_2O_2 in H_2O, GC–MS control with H_2O (**Figure 61**), GC–MS of pristine SWNTs and hemin (**Figure 62**), GC–MS of pristine SWNTs and $FeCl_3$ (**Figure 63**), HPLC chromatograms of HRP-degraded SWNTs (**Figure 64**), *trans*-cinnamaldehyde (**Figure 65**), and mellitic acid (**Figure 66**), HPLC chromatogram of non-concentrated sample (**Figure 67**), HPLC chromatogram of HRP (**Figure 68**), section analysis of HRP (**Figure 69**), carboxylated SWNT (**Figure 70**), and carboxylated SWNT with HRP (**Figure 71**), AFM image of pristine SWNTs (**Figure 72**), section analysis of pristine SWNTs (**Figure 73**), AFM image of pristine SWNTs and HRP (**Figure 74**), section analysis of pristine SWNTs and HRP (**Figure 75**), UV-vis-NIR spectra of carboxylated SWNTs on fixed substrate (**Figure 76**), carboxylated SWNTs degraded by hemin (**Figure 77**), carboxylated SWNTs degraded by $FeCl_3$ (**Figure 78**), EDXA of products from pristine SWNTs degraded by hemin and H_2O_2 (**Figure 79, Figure 80**), intermolecular binding energies (**Table 3**), molecular modeling of HRP interaction with sidewall defects (**Figure 81**), interaction of HRP with bundled pristine SWNTs (**Figure 82**), and a comparative study of HRP docking with varying chirality SWNTs (**Figure 83**).

7.0 CONTRIBUTING ROLES IN ADDITIONAL PUBLICATIONS

The following abstracts are taken from publications in which I played a minor contributing role to the research. My contribution (and its significance), as well as the contributions of other authors are described in detail.

7.1 ELECTROCATALYTIC ACTIVITY OF NITROGEN-DOPED CARBON NANOTUBE CUPS

Citation: Y. Tang, B. L. Allen, D. R. Kauffman, and A. Star, *J. Am. Chem. Soc.* **2009**, *131*, 13200-13201.

Abstract

The electrochemical activity of stacked nitrogen-doped carbon nanotube cups (NCNCs) has been explored in comparison to commercial Pt-decorated carbon nanotubes. The nanocup catalyst has demonstrated comparable performance to that of Pt catalyst in oxygen reduction reaction. In addition to effectively catalyzing O_2 reduction, the NCNC electrodes have been used for H_2O_2 oxidation and consequently for glucose detection when NCNCs were functionalized with glucose oxidase (GOx). Creating the catalysts entirely free of precious metals is of great importance for low-cost fuel cells and biosensors.

For this published manuscript, my contribution consisted of synthesizing stacked NCNCs and separated NCNCs for use in electrochemical measurements. I further contributed electron microscopy (TEM) characterization of NCNCs. Yifan Tang, performed all electrochemical measurements, including detection of glucose with glucose oxidase. He further contributed by writing the manuscript and performing thermogravimetric analysis. Douglas Kauffman performed TEM characterization on Pt-decorated multiwalled carbon nanotubes, as well as x-ray photoelectron spectroscopy (XPS) measurements. All authors contributed to experimental discussion and data analysis.

7.2 UNDERSTANDING THE SENSOR RESPONSE OF METAL DECORATED CARBON NANOTUBES

Citation: D. R. Kauffman, D. C. Sorescu, D. P. Schofield, B. L. Allen, K. D. Jordan, and A. Star, *Nano Lett.* **2010**, *10*, 958-963.

Abstract

We have explored the room temperature response of metal nanoparticle decorated single-walled carbon nanotubes (NP-SWNTs) using a combination of electrical transport, optical spectroscopy, and electronic structure calculations. We have found that upon the electrochemical growth of Au NPs on SWNTs, there is a transfer of electron density from the SWNT to the NP species, and that adsorption of CO molecules on the NP surface is accompanied by transfer of electronic density back into the SWNT. Moreover, the electronic structure calculations indicate dramatic variations in the charge density at the NP-SWNT interface, which supports our previous observation that interfacial potential barriers dominate the electrical behavior of NP-SWNT systems.

For this published manuscript, my contribution consisted of performing Raman spectroscopy on SWNT samples (bare and gold nanoparticle modified). Analysis was performed in the radial breathing modes (RBM) regime (100 – 200 cm^{-1}) and the defect induced (D-band) and graphitic (G-band) regime (1000 – 1700 cm^{-1}). Douglas Kauffman contributed material functionalization, energy dispersive x-ray analysis (EDXA), XPS, SEM, absorbance spectroscopy, cyclic voltametry, and conductance vs. time measurements. Dan Sorescu and Dan Schofield performed all theoretical modeling calculations. All authors contributed to varying parts of the data analysis.

7.3 CARBON NANOTUBES DEGRADED BY NEUTROPHIL MYELOPEROXIDASE INDUCE LESS PULMONARY INFLAMMATION

Citation: V. E. Kagan, N. V. Konduru, W. Feng, B. L. Allen, J. Conroy, Y. Volkov, I. I. Vlasova, N. A. Belikova, N. Yanamala, A. Kapralov, Y. Y. Tyurina, J. Shi, E. R. Kisin, A. R. Murray, J. Franks, D. Stolz, P. Gou, J. Klein-Seetharaman, B. Fadeel, A. Star, and A. Shvedova, *Nature Nano.* **2010**, *5*, 354-359.

Abstract

We have shown previously that single-walled carbon nanotubes can be catalytically biodegraded over several weeks by the plant-derived enzyme, horseradish peroxidase. However, whether peroxidase intermediates generated inside human cells or biofluids are involved in the biodegradation of carbon nanotubes has not been explored. Here, we show that hypochlorite and reactive radical intermediates of the human neutrophil enzyme myeloperoxidase catalyze the biodegradation of single-walled carbon nanotubes in vitro, in neutrophils and to a lesser degree in macrophages. Molecular modeling suggests that interactions of basic amino acids of the enzyme with the carboxyls on the carbon nanotubes position the nanotubes near the catalytic site. Importantly, the biodegraded nanotubes do not generate an inflammatory response when aspirated into the lungs of mice. Our findings suggest that the extent to which carbon nanotubes are biodegraded may be a major determinant of the scale and severity of the associated inflammatory responses in exposed individuals.

For this published manuscript, my contribution consisted of performing absorbance and Raman spectroscopy, transmission electron microscopy, and atomic force microscopy. Utilizing these techniques, it was possible to evaluate the degree of degradation of single-walled carbon

nanotubes incubated with human myeloperoxidase. Cell-based experiments were performed by the members of Dr. Valerian Kagan's group of the Occupational and Environmental Health Department. Additional characterization, as well as animal studies, was performed by contributing authors. All authors participated in the design of experimental work and interpretation of the data (in their respective fields of research).

7.4 CARBON NANOTUBE SENSORS FOR EXHALED BREATH COMPONENTS

Citation: O. Kuzmych, B. L. Allen, and A. Star, *Nanotechnology* **2007**, *18*, 375502-1 – 375502-7.

Abstract

A new method for the detection of nitric oxide (NO) in gas phase is based on a combination of acidic gas scrubbing, oxidation, and conductivity measurements using a chemically functionalized carbon nanotube field-effect transistor (NTFET) device. Gas mixtures containing NO are passed through an Ascarite scrubber and then an oxidizing material (CrO_3) which converts NO into NO_2. The latter is delivered to the surface of the NTFET sensor coated with poly(ethylene imine) (PEI) polymer. Interaction of the gas with a chemically functionalized NTFET results in a conductivity change that is proportional to the NO gas concentration. The wide range of NO gas concentrations from about 2 ppb to 5 ppm was tested. A detection limit of NO has been measured as 5 ppb with a signal-to-noise ratio (S/N = 3) in inert atmosphere at a fixed relative humidity (RH = 30%). Cross-sensitivity to CO_2 and O_2 was measured in the gas mixture, modeling human breath conditions. Compared to using chemiluminescence, a state-of-the-art technique for monitoring NO concentrations, this method offers the advantages of low cost, compact size, and simplicity of set-up for monitoring NO concentrations while overcoming the limitations of cross-contaminants, possibly creating a foundation for enabling self-diagnostics and home care for asthma sufferers.

For this published manuscript, there was a combined effort of my former colleague, Oleksandr Kuzmych, and myself. Oleksandr contributed initial conductance measurements with bare and PEI – coated SWNT devices exposed to NO and converted NO (NO_2). He further

examined cross-sensitivity towards O_2, as well as relative humidity. My contribution to this work was investigating the cross-sensitivity towards CO_2 gas, and focusing on methods to mitigate its effect.

8.0 SUMMARY AND FUTURE WORK

8.1 SUMMARY OF WORK

In the preceding chapters, we have taken a multifaceted approach to the field of nanoscience, specifically in the realm of carbon-based nanomaterials. Not only did we develop new carbon-based hybrid materials, but also we have investigated the inherent toxicity of currently studied nanomaterials such as carbon nanotubes.

In Chapter 2.0, the synthesis of novel nitrogen-doped carbon nanotube cups (NCNCs) is discussed. By utilizing a nitrogen-containing precursor during chemical vapor deposition, it was possible to synthesize carbon fibers in "stacked cup" morphology. We then later discovered that these fibers could be broken down into component "cups" through simple mechanical grinding with a mortar and pestle. By the presence of a nitrogen-precursor, carbon fibers were inherently doped with varying nitrogen functionalities (predominantly located on the open-basal rim of each cup). These functionalities were probed through atomic force microscopy manipulation as well as bioconjugation with biotin and streptavidin-coated GNPs. Further complex measurements, such as force volume imaging, permitted a correlation of hydrogen bonding strength towards a given substrate (hydrophobic or hydrophilic).

In Chapter 3.0, we utilize the presence of nitrogen-functionalities located on the basal rim of nanocups for cross-linkage purposes. By the simple addition of 4% glutaraldehyde, we

demonstrated the ability to cross-link adjacent NCNCs to form hollow nanocapsules. Such capsules were characterized by a variety of methodologies including transmission electron microcopy and atomic force microscopy. Taking this a step further, we then sought to encapsulate nanoparticles for a proof-of-concept demonstration. Commercially-available GNPs were, indeed, encapsulated by their addition in a suspension of separated NCNCs prior to cross-linkage. As GNPs possess a surface plasmon resonance in the visible regime, we were able to track the encapsulation by the apparent red shifting of the resonance peak as a result of aggregation within the interior. Other methods of examination included AFM to verify internal encapsulation versus exterior adsorption. We further showed the general applicability of this approach by encapsulating quantum dots synthesized at the University of Pittsburgh by the Petoud Group.

In Chapter 4.0, we sought to possess structural control over the dimensions of formed nanocapsules from NCNCs to discriminate loading capacity. Based from previous research and with the assistance of an undergraduate student, Matthew B. Keddie, iron nanoparticles were synthesized using thermal decomposition reactions of an iron-containing precursor. Particle sizes were finitely controlled and correlated to fatty acid (capping ligand) chain length. Three monodispersed sizes were used for CVD growth of NCNC fibers. TEM results demonstrated that diameter distributions could be tailored by nanoparticle size. Furthermore, we demonstrated the control over segment length by varying the nitrogen-precursor concentration (1%, 5%, 9%). Segment lengths were shown to be proportional to nitrogen-doping. The resultant capsules (formed by cross-linkage) had loading capacities proportional to segment length and diameter.

In Chapters 5.0 and 6.0, we “switch gears” to focus on the inherent toxicity of nanomaterials. Specifically, we investigated the bioremediation of single-walled carbon

nanotubes using benign approaches. Prior to this work, it was known that because of the natural resiliency of carbon nanotubes, oxidation or degradation could only occur by thermal oxidation in air at high temperatures or harsh chemical treatment. Our study demonstrated the oxidation and degradation of SWNT by the addition of common enzyme known as horseradish peroxidase (HRP) and low localized concentrations of H_2O_2 (~40 μM). The first occurrence was at 4 °C resulting in degradation over the span of 12 weeks. In our second study, however, the degradation time was reduced to 10 days at room temperature. We also began to fundamentally investigate the mechanism of degradation using the enzymatic system. These studies demonstrated that carboxylated, hydrophilic SWNTs oxidized in the presence of HRP/H_2O_2, but pristine did not. It was believed that carboxylated SWNTs docked at a proximal binding site towards the active heme group in HRP, whereas pristine SWNTs docked at a distal site. Such a hypothesis was confirmed by theoretical modeling performed by Dr. Naveena Yanamala and Dr. Judith Klein-Seetharaman. Further experimentation was performed to examine the effect of the heme porphyrin and iron salt with SWNTs (carboxylated and pristine). Degradation was observed in all cases demonstrating that HRP heterolytically cleaved H_2O_2 to form Compound I and H_2O (increasing substrate selectivity), while heme porphyrin and iron salt homolytically cleaved H_2O_2 producing free radicals capable of non-specific oxidation.

Finally, Chapter 7.0 described contributing roles to other publications in a variety of nano-based research experiments including fundamental investigations of stacked carbon nanotube cups acting as a catalyst for oxygen reduction reactions, understanding the sensor response of metal-decorated single-walled carbon nanotubes, investigating human peroxidase enzymes, specifically myeloperoxidase, for the enzymatic degradation of carbon nanotubes, and finally the use of single-walled carbon nanotubes as a sensor platform for gas analyte detection.

8.2 FUTURE WORK

We believe each of these projects (materials synthesis and enzymatic bioremediation) contribute to the field of nanoscience and nanotechnology. However, such progress is a continuum, and work is never done. All of these projects, while important, constitute stepping stones in which to perform further studies.

For example, in the investigations of NCNCs as nanocapsules, subsequent experimentation can yield promising results. Thus far, we have attempted cross-linkage only using glutaraldehyde. This linkage is pH sensitive, and acid hydrolysis will result in the opening of nanocapsules. It is curious, however, what cross-linkers may be implemented in order to direct the specific opening of these capsules and the subsequent release of their inherent cargo. For instance, replacing the cross-linker with a disulfide containing molecule, it may be possible to have redox-mediated opening of such capsules. Of a more fundamental nature, one could analyze what phenomenological events occur within the interior of these capsules. Aggregation is obviously forced even in the presence of highly electrostatically repulsed particles such as GNPs. Upon capsule opening, do the interior interactions of the capsules irreversibly modify

their cargo? This, of course, can be tested by examining a variety of particles for encapsulation with varying surface functionalities. Small fluorescent molecules may additionally be used to examine the porosity of these multiwalled capsules. After adequate characterization, it may then be possible to perform application-based studies, such as the encapsulation of contrast agent for enhanced MRI platforms. Of important note, in lieu of successful applications, there still exists the possible toxicity of these nanomaterials.

In that essence, much room for research is still present for the study of bioremediation using enzymatic catalysis. As we have demonstrated, it is possible to oxidize carboxylated SWNTs using this approach. However, the question remains, "What are the fundamental properties that dictate the ability of peroxidase enzymes to degrade carboxylated SWNTs". If it is, indeed, the mere hydrophilic nature of carboxylated SWNTs to dock in proximity to the heme site of HRP, then simple non-covalent modification of pristine SWNTs through polymer wrapping or molecule attachment should facilitate the same degradation. There is, of course, the possibility that it is a more complex interaction that not only relies on hydrophilicity, but also perhaps the induced defects to the graphitic lattice or the potential surface charge on the SWNTs. There may also be a diameter or shape dependency to allow enzyme docking. All of these factors are open for investigation. Manipulation may even be explored as varying peroxidases are examined or their cofactors (active sites) modified to accommodate hydrophobic interactions over hydrophilic.

In my experience here, the pursuit of science has been an ongoing journey of imagination, innovation, stick-to-it-ness, and compromise. These words are so selected because as any scientist may attest, what one would expect to find is typically not the outcome. This is ever true in research.

APPENDIX A

SYNTHESIS, CHARACTERIZATION, AND MANIPULATION OF NITROGEN-DOPED CARBON NANOTUBE CUPS: SUPPORTING INFORMATION

This Appendix contains supporting information for Chapter 2.0 'Synthesis, Characterization, and Manipulation of Nitrogen-Doped Carbon Nanotube Cups'. It contains electron energy loss spectroscopy (EELS) of nitrogen-doped carbon nanotube cups (**Figure 29**) as well as AFM manipulation of unmodified nanocups (**Figure 30**), section analysis of GNP-decorated cups (**Figure 31**), 3D topographical AFM imaging of cups decorated with GNPs without biotinylation (**Figure 32**), AFM imaging of free GNPs (**Figure 33**), spring constant calculations, force volume plots **(Figure 34 and Figure 35**), adhesion force calculations and statistical data.

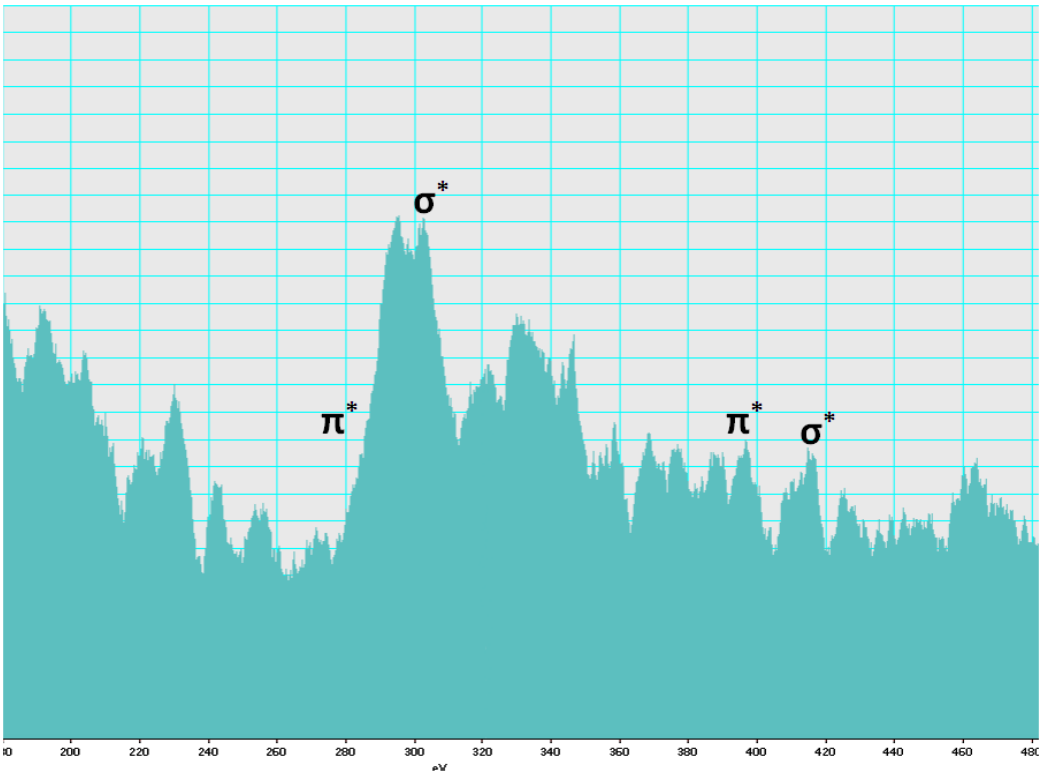

Figure 29. Electron Energy Loss Spectrum (EELS) of nitrogen-doped carbon nanotube cups. K-edges are seen for carbon at approximately 300 eV and 410 eV for nitrogen, according to reference 68.

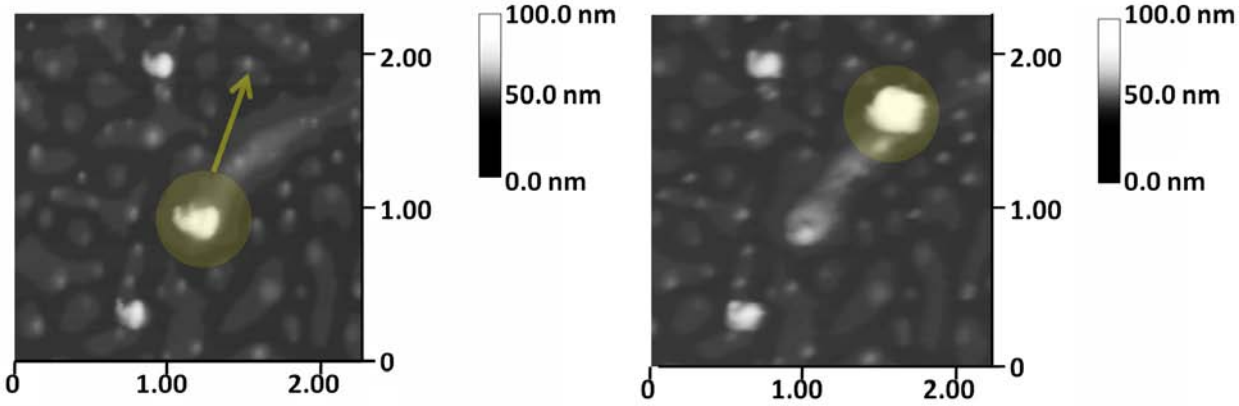

Figure 30. AFM manipulation of unmodified nanocups on freshly cleaved mica. Nanocups could be manipulated without noticeable destruction to the structure or substrate.

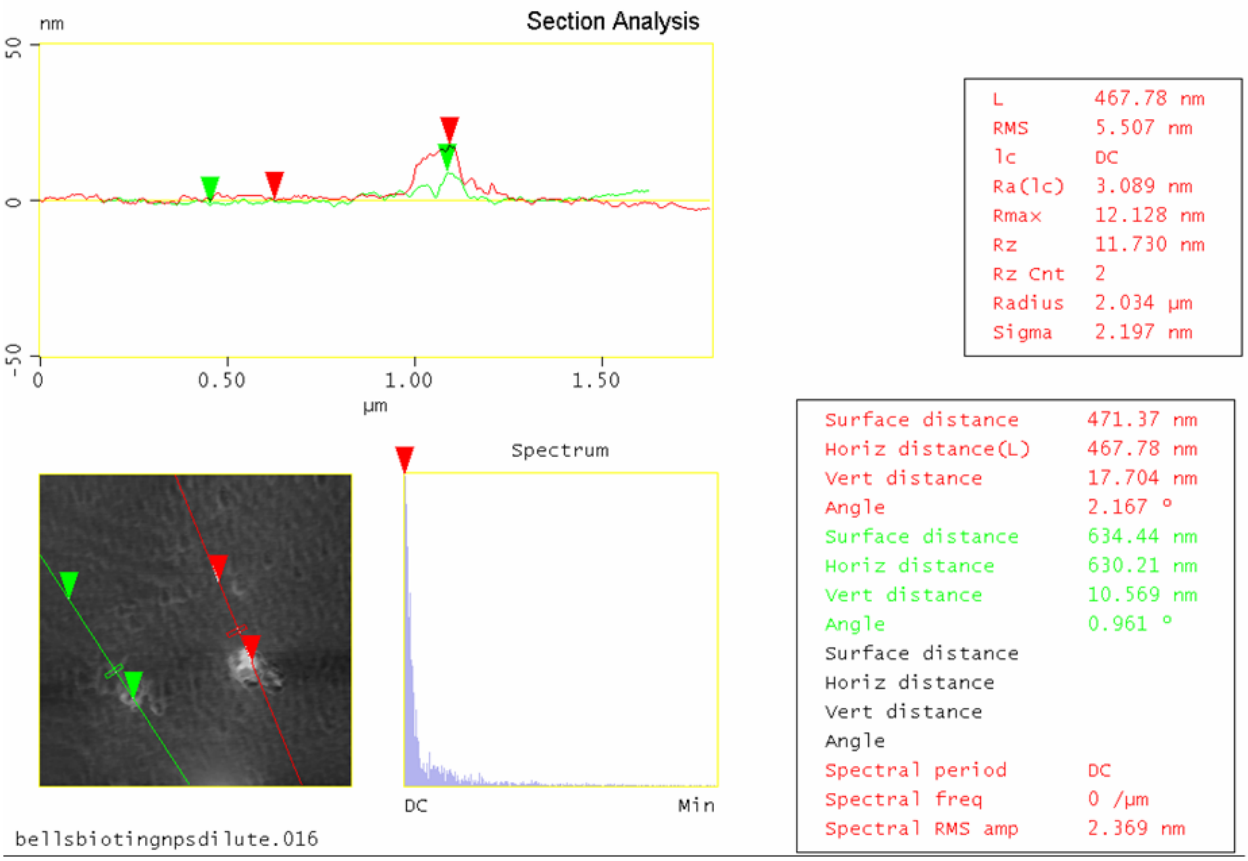

Figure 31. AFM section analysis of GNP-decorated nanocup: AFM analysis shows a height of approximately 18 nm for the GNP-decorated cup. Rough features in the cross section indicate the presence of smaller particles surrounding the cup.

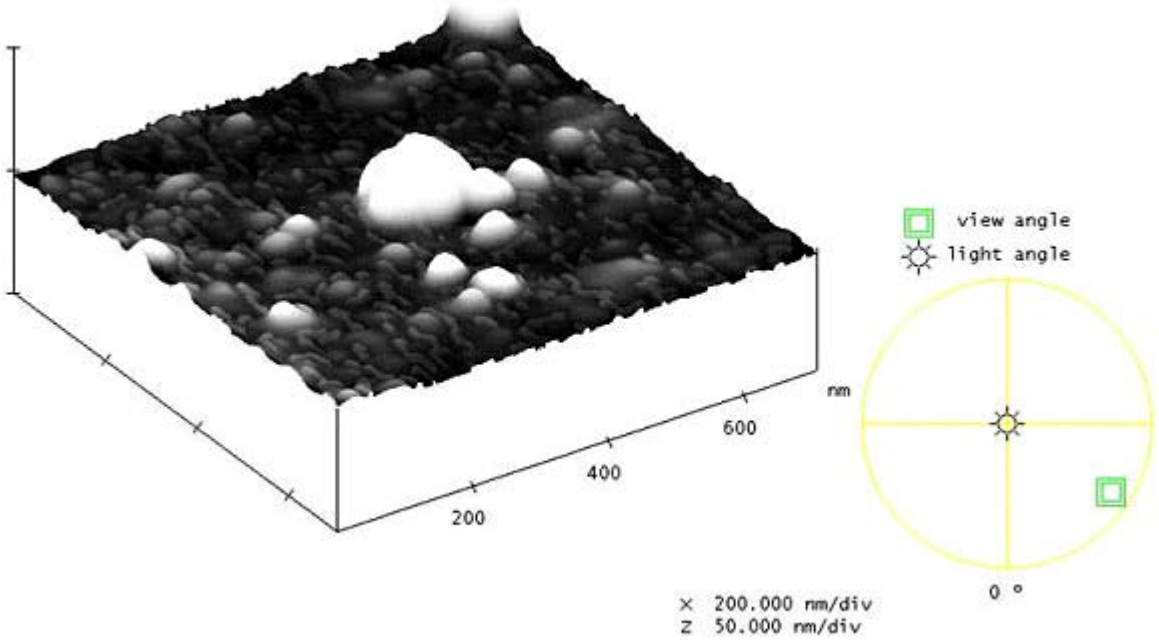

Figure 32. 3D topographical AFM image of nanocups decorated with GNPs without prior biotinylation: AFM images shows a single GNP decorating a nanocup after incubation. No biotinylation occurred attributing any attachment to hydrogen bonding between streptavidin on the GNP and nitrogen groups present in the cup.

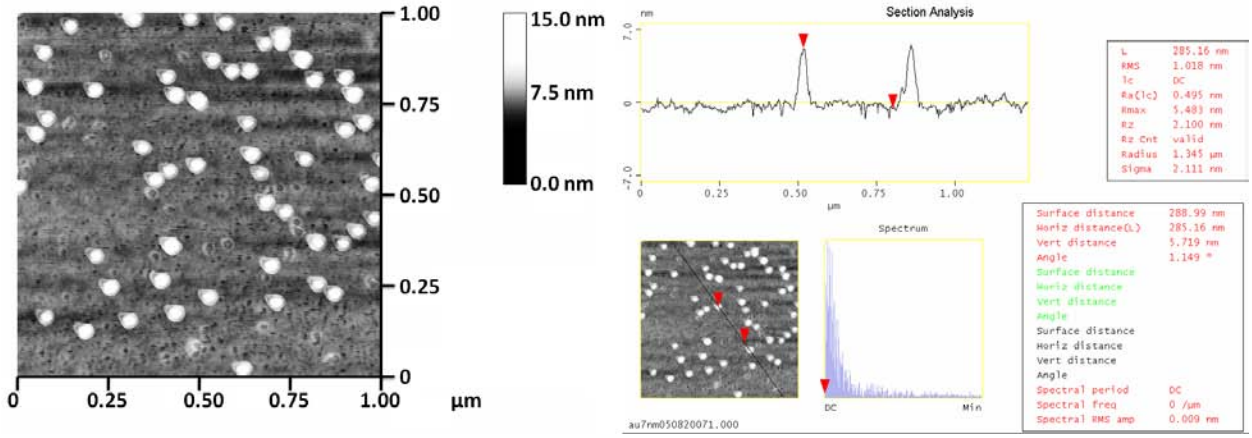

Figure 33. AFM image of gold nanoparticles (GNPs) on poly-L-lysine treated mica. (Left) Height image of GNPs. (Right) Section analysis of GNPs indicated an average height of 6-7 nm.

Spring Constant Calculations

The Reference Cantilever method (Veeco) was performed to calculate our contact probe spring constant. Reference probes were purchased from Veeco with a thermal tune calculated spring constant of 0.17431 N/m and length of 400 microns. It was important to select a reference cantilever such that the nominal spring constant of our contact probe was in the range of $0.3k_{ref} < k < 3k_{ref}$. Briefly, the reference cantilever was mounted on a sample disc using double-sided tape. The reference cantilever was aligned such that its long axis was aligned with the contact probe to be calibrated but in the opposite direction. The contact probe is then engaged on the bulk substrate of the reference cantilever. Ten deflection sensitivity measurements were made in ramp mode to get average deflection sensitivity, S_{hard}, of 246.2 nm/V. The contact probe was then withdrawn and realigned close to the end of the reference cantilever, before being engaged. Once again, ten deflection sensitivity measurements were made and averaged to a value of 327.7 nm/V, S_{ref}. Lastly, the offset of the contact probe to the reference probe tip was measured as 75.0 microns.

Using the following equation, we calculated our contact probe spring constant:

$k = k_{ref}\,[(S_{ref} / S_{hard}) - 1](L / L - \Delta L)^3$, where L is the reference probe length and ΔL is the offset.

Therefore, k = 0.107 N/m.

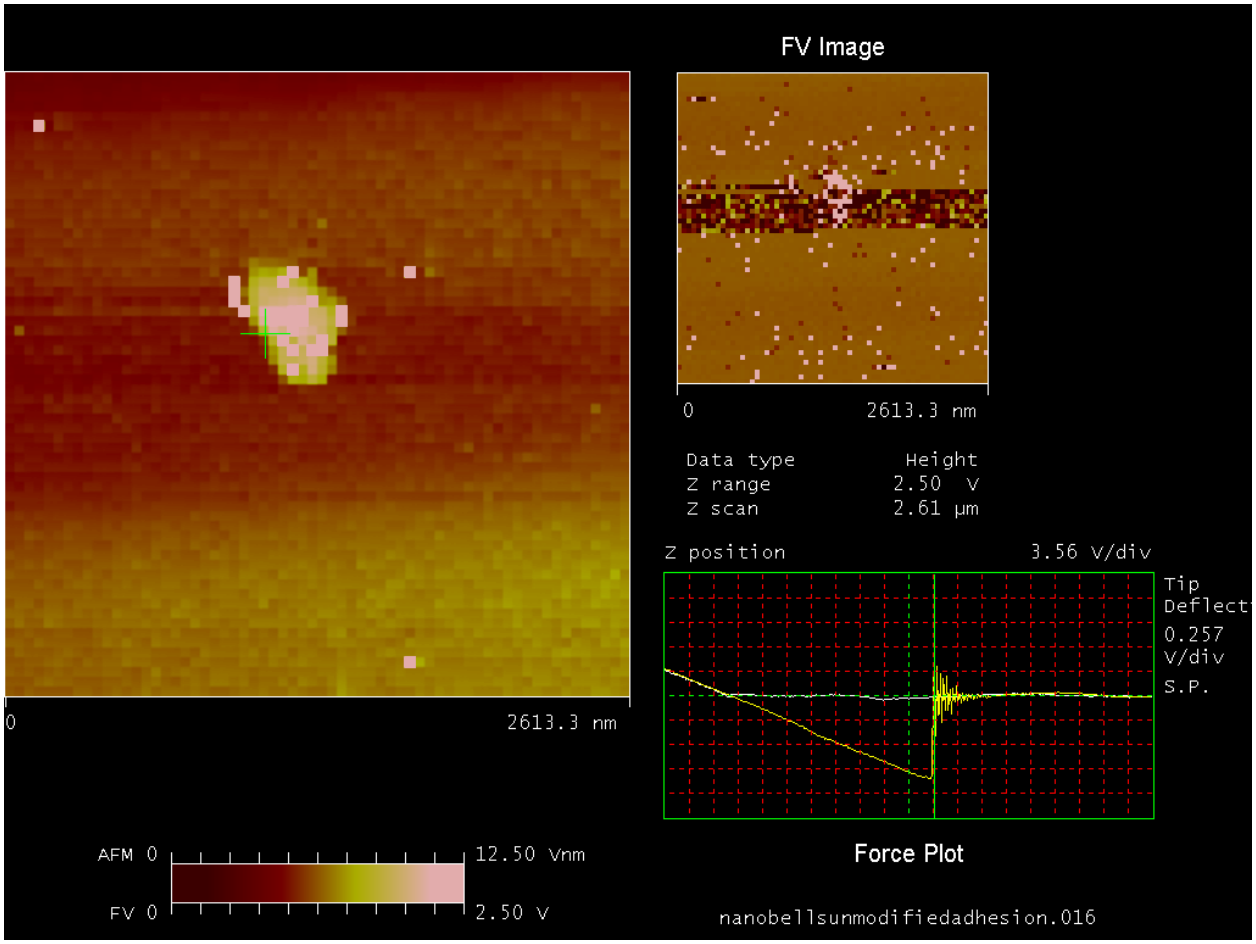

Figure 34. Force volume plot of an unmodified nanocup on a treated mica substrate.

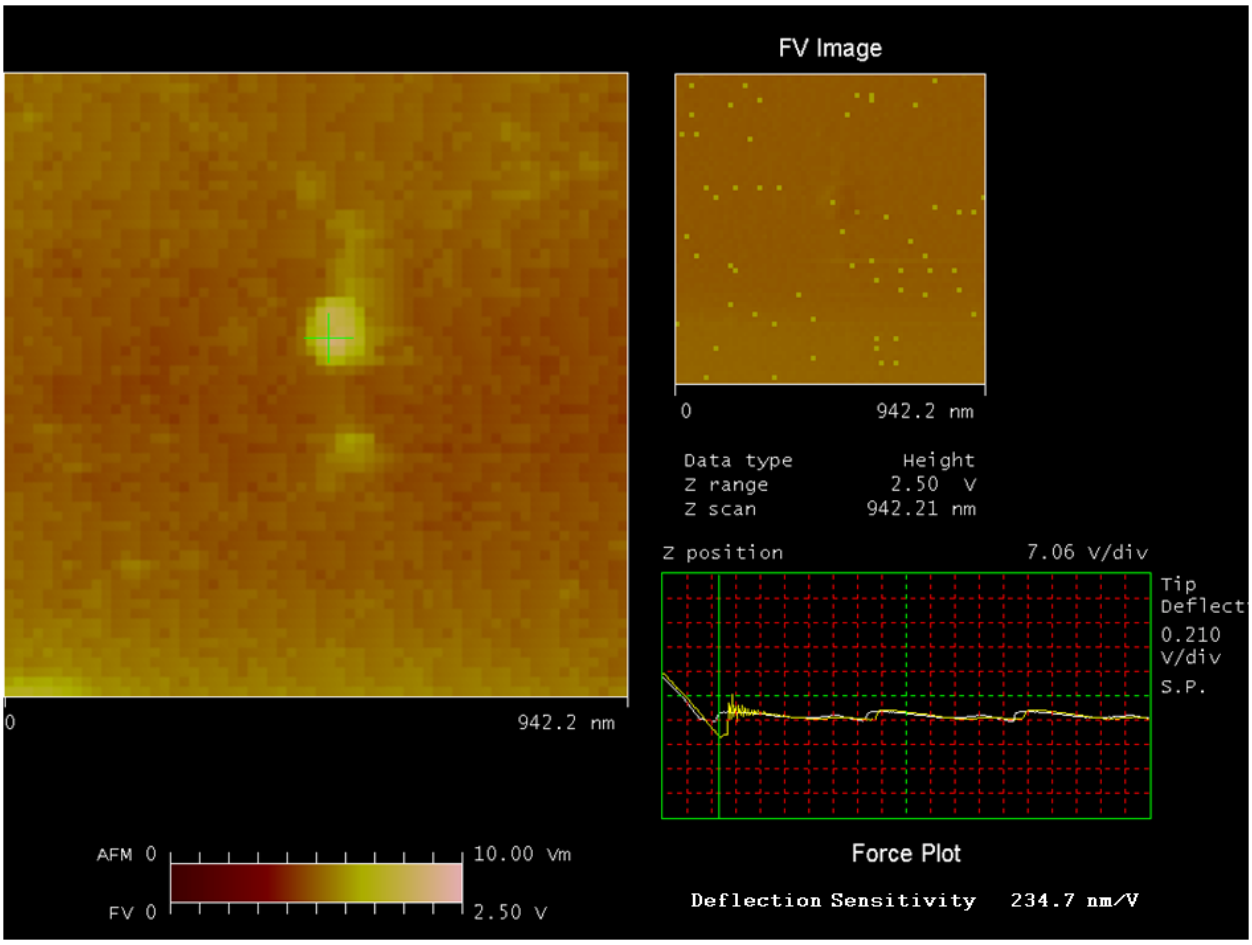

Figure 35. Force volume plot of GNP-decorated nanocup on a treated mica surface.

Adhesion Force Calculations

Given a spring constant, k, adhesion force is calculated at the set point (horizontal green line above) by the equation $F = k (\Delta Z)$, where ΔZ is the displacement of the contact probe.

ΔZ = [z-position (V/div)][# div][deflection sensitivity (nm/V)]

k = 0.107 (calculated above)

Statistical Data

Unmodified Nanobells	
Size (nm)	Force (nN)
15.737	902.1
18.368	864.5
20.032	345.6
22.783	582.6
23.129	610.8
27.995	816.7
32.869	454.8
37.533	657.8
41.785	770.6
48.927	939.7

Avg. Size	Avg. Force	Std. Dev
28.9158	694.52	198.0197

Nanobells and GNPs	
Size (nm)	Force (nN)
15.747	289.1
17.152	192.7
17.294	216.8
23.297	168.6
24.062	256.9
28.059	195.03
29.057	283.7
32.117	372.3
39.082	212.7
43.578	263.68

Avg. Size	Avg. Force	Std. Dev.
26.9445	245.151	60.5951

APPENDIX B

GRAPHITIC NANOCAPSULES: SUPPORTING INFORMATION

This Appendix contains supporting information for Chapter 3.0 ‘Graphitic Nanocapsules’. It contains UV/Vis spectra of separated and crosslinked NCNCs (**Figure 36**), section analysis of crosslinked NCNCs encapsulating GNPs (**Figure 37**), 3D AFM profile of separated NCNC and GNP **(Figure 38**), section analysis of separated NCNCs and GNPs (**Figure 39**), TEM imaging of crosslinked NCNCs followed by GNP incubation (**Figure 40**), AFM phase imaging of crosslinked NCNCs followed by GNP incubation (**Figure 41**), UV/Vis spectra of free GNPs and GNPs added after crosslinkage of NCNCs (**Figure 42**), TEM imaging of mismatched, crosslinked NCNCs with GNPs (**Figure 43**), TEM imaging of free GNPs with 4% glutaraldehyde (**Figure 44**), UV/Vis spectra of free GNPs and GNPs with 4% glutaraldehyde (**Figure 45**), UV/Vis spectra of free GNPs, encapsulated GNPs, and separated NCNCs with GNPs (**Figure 46**), TEM imaging showing particle migration (**Figure 47**), TEM imaging of non-encapsulated GNPs (**Figure 48**), and time-resolved emission and excitation spectra of ZnS:Tb nanoparticles (**Figure 49**).

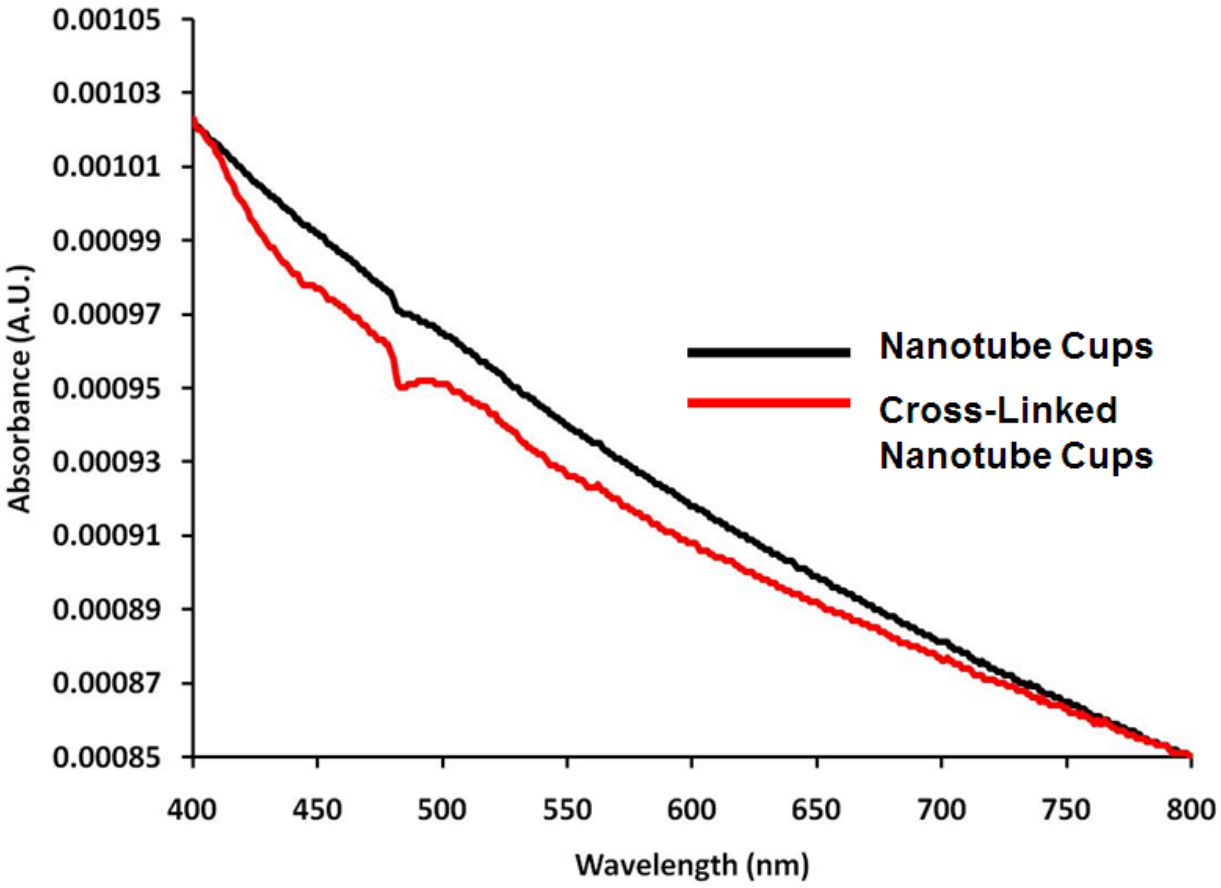

Figure 36. UV/Vis spectra of separated NCNCs (black) and crosslinked NCNCs (red).

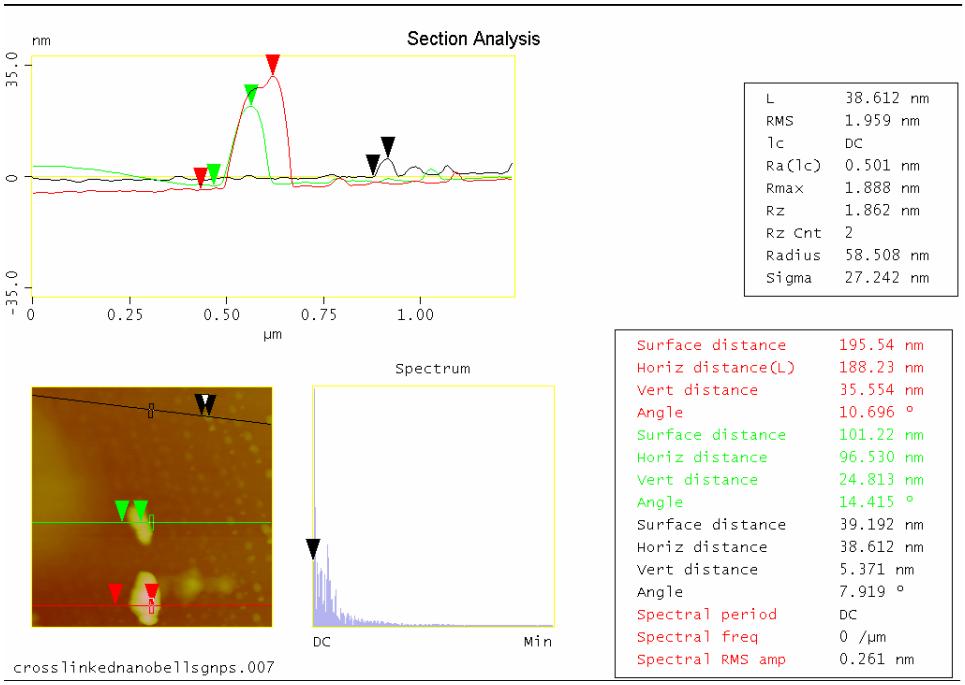

Figure 37. AFM section analysis of crosslinked NCNCs encapsulating GNPs. Non-encapsulated GNPs were found on the same sample and are indicated by a vertical distance of ~5 nm shown in black.

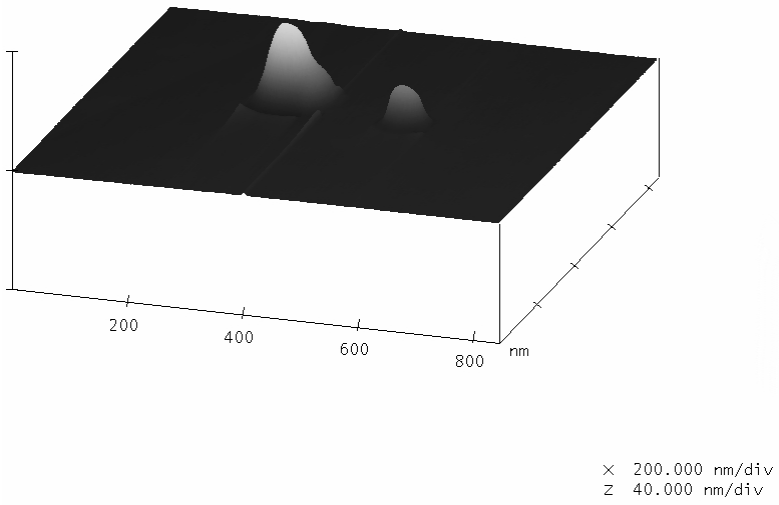

Figure 38. AFM 3D profile of a single separated NCNC and GNP. Imaging was performed prior to cross-linkage with 4% glutaraldehyde. As NCNCs hydrogen bond, the structure is fixated in an open-side down conformation against a poly-L-lysine treated-mica surface.

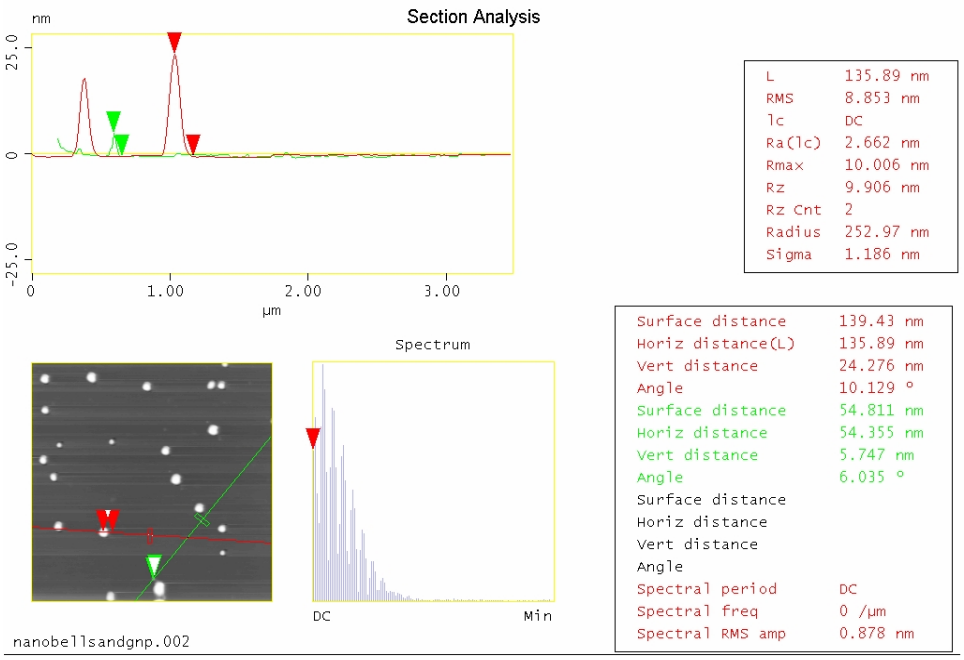

Figure 39. AFM section analysis of separated NCNCs and GNPs. As demonstrated, a single NCNC is shown as approximately 25 nm, while the GNP is measured at approximately 6 nm.

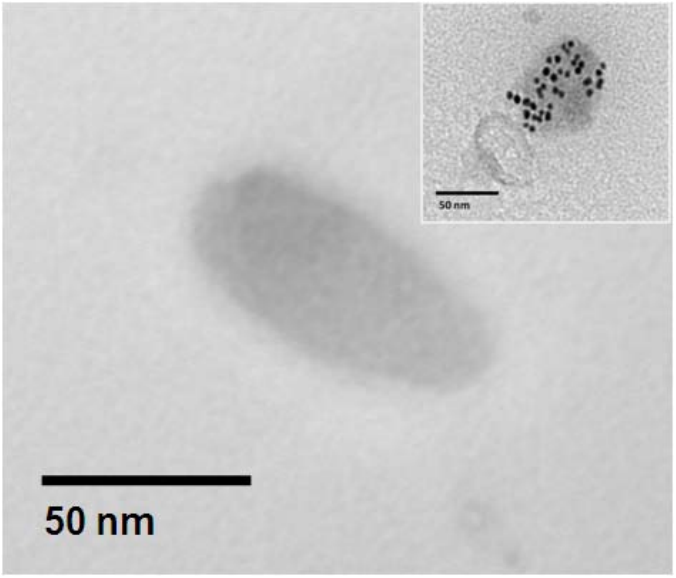

Figure 40. TEM image of NCNCs cross-linked, followed by incubation with commercially available GNPs. The majority of TEM fields demonstrated NCNCs with no confinement of GNPs. On rare, sporadic fields GNPs were observed as adsorbing to the exterior of NCNCs (inset).

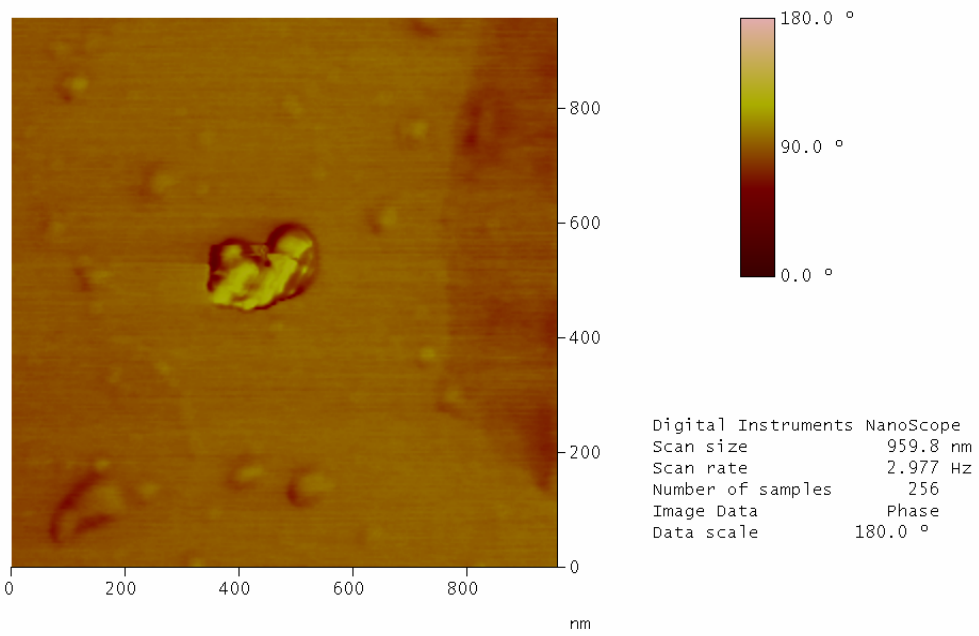

Figure 41. AFM phase image confirming the topology of NCNCs crosslinked followed by incubation with GNPs.

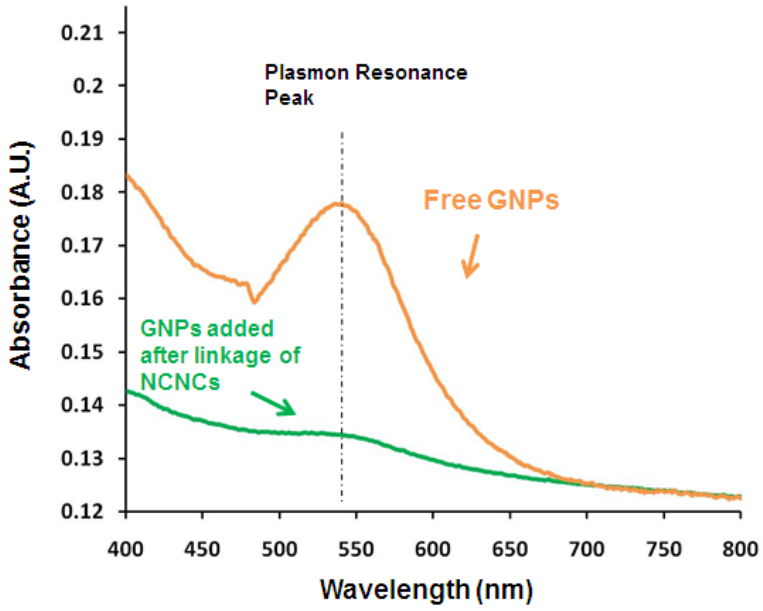

Figure 42. UV/Vis spectra of free GNPs and GNPs added after the crosslinkage of NCNCs. It is important to note that there is no shifting of the plasmon resonance peak of GNPs, indicating no encapsulation.

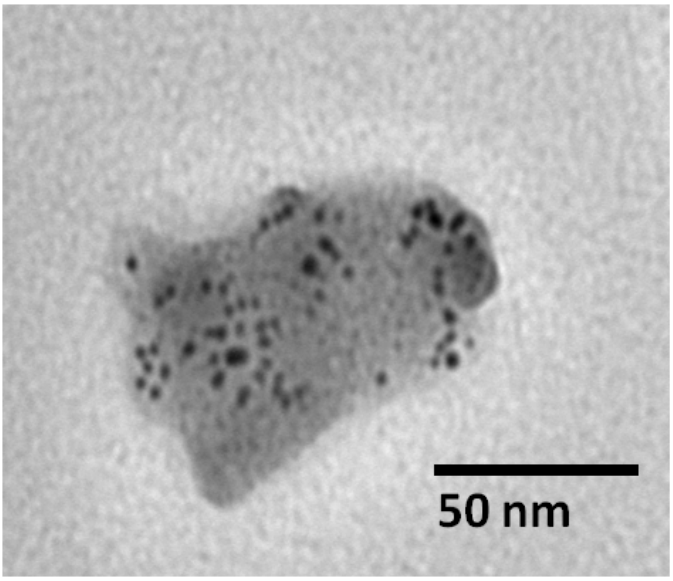

Figure 43. TEM image of multiple mis-matched diameter NCNCs crosslinked with GNPs.

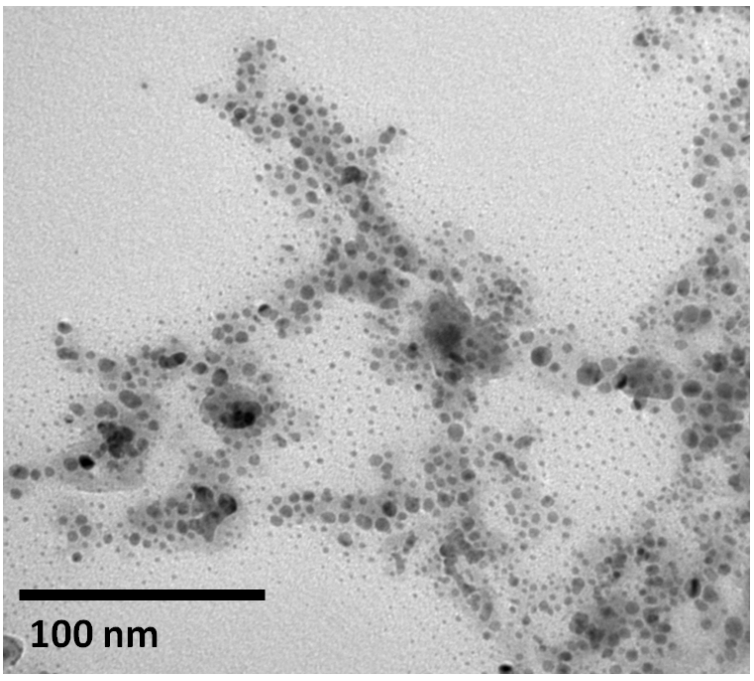

Figure 44. TEM image of GNPs (~5 nm mean diameter) incubated with 4% glutaraldehyde in EtOH.

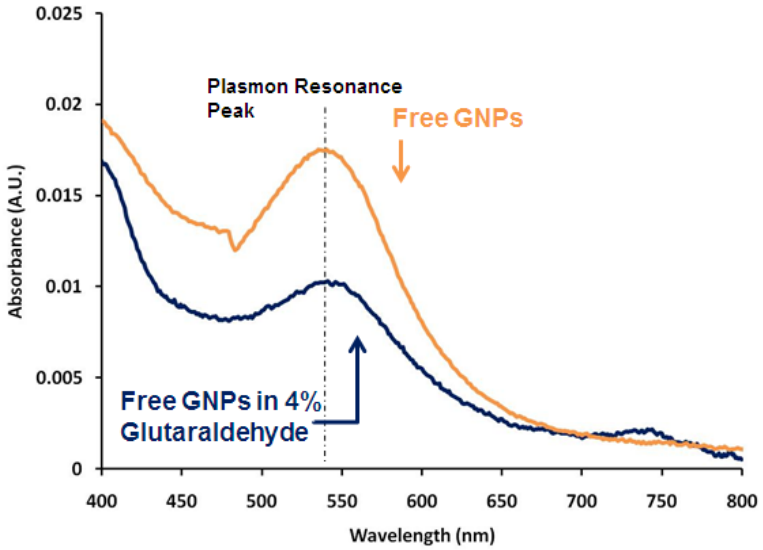

Figure 45. UV/Vis spectra of free GNPs and GNPs added to 4% glutaraldehyde in EtOH.

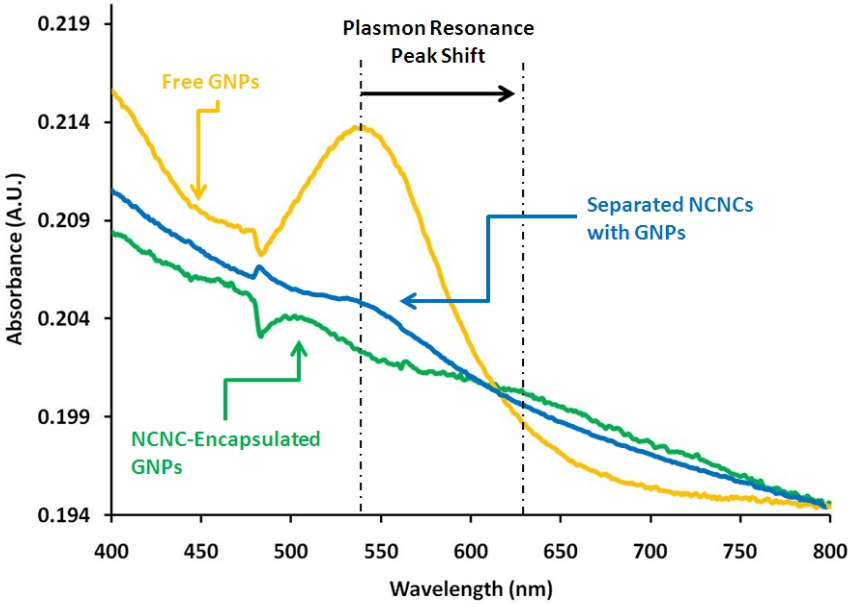

Figure 46. UV/Vis spectroscopic comparison of free GNPs, separated NCNCs incubated with GNPs prior to crosslinkage, and GNPs encapsulated by NCNCs after 4% glutaraldehyde addition. It is important to note that only the encapsulated GNPs demonstrate a plasmon resonance shift, due to spatial confinement of the particles. This is not the case for unlinked NCNs, allowing movement within the hollow cavity and back out.

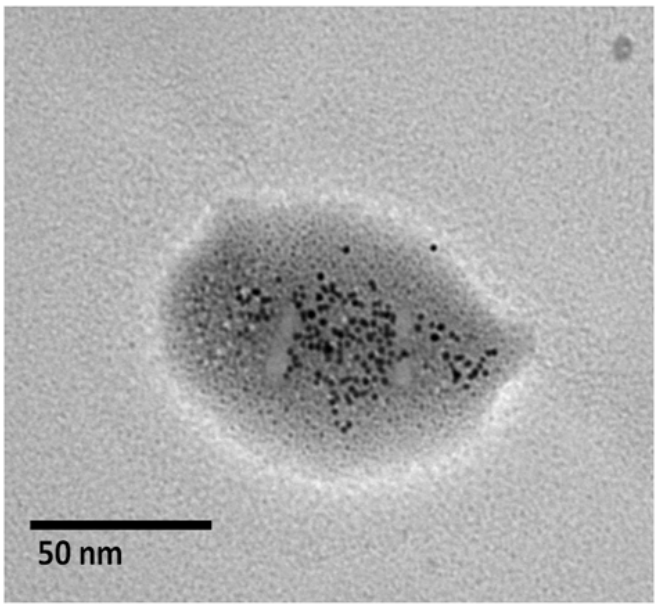

Figure 47. TEM image of another NCNC nanocapsule encapsulating GNPs, demonstrating migration within the interior cavity.

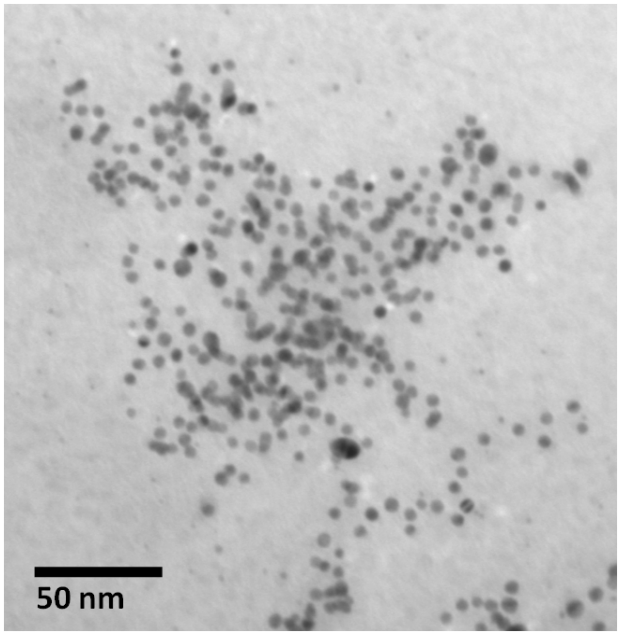

Figure 48. TEM image of non-encapsulated GNPs on the same TEM grid as shown above.

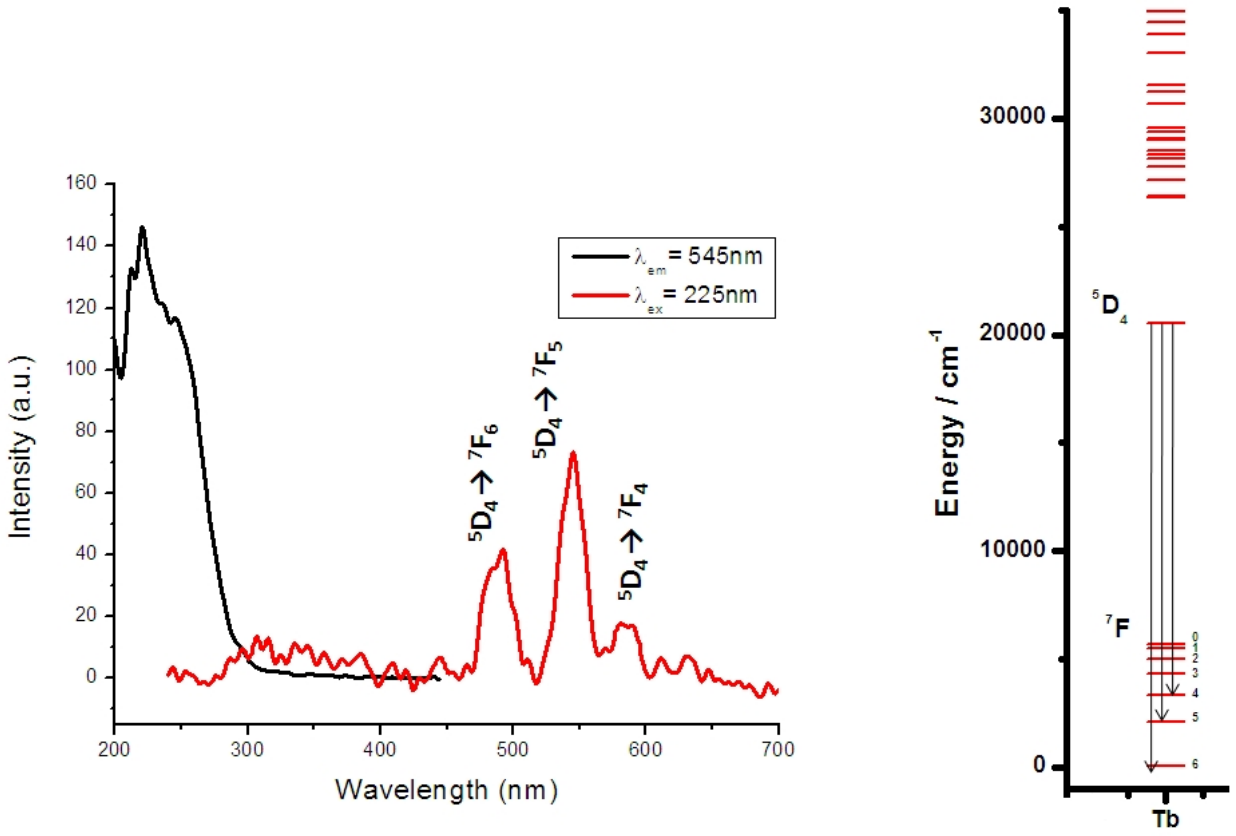

Figure 49. Time-resolved emission (red) and excitation (black) spectra of ZnS:Tb nanoparticles recorded with a delay after excitation flash of 0.5 msec. Emission spectrum was collected at an excitation wavelength of 225 nm, while excitation spectrum was collected upon Tb^{3+} - centered emission wavelength, 545 nm. An energy level diagram (right) shows emission pathways for respective transitions of Tb^{3+}.

APPENDIX C

CONTROLLING THE VOLUMETRIC PARAMETERS OF NITROGEN-DOPED CARBON NANOTUBE CUPS: SUPPORTING INFORMATION

This Appendix contains supporting information for Chapter 4.0 'Controlling the Volumetric Parameters of Nitrogen-Doped Carbon Nanotube Cups'. It contains AFM height profiles of synthesized FeNPs (**Figure 50**), DLS measurements of synthesized FeNPs (**Figure 51**), high-resolution TEM and EELS analysis of synthesized NCNCs (**Figure 52**), and low-resolution TEM image of encapsulated GNPs (**Figure 53**).

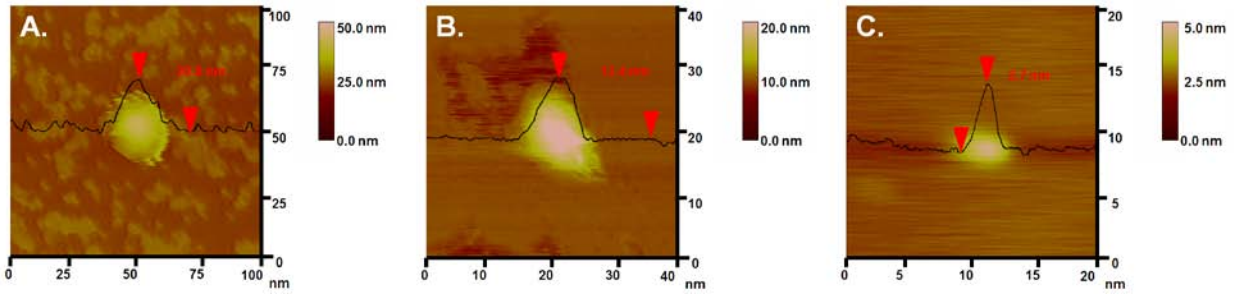

Figure 50. AFM height images of (A) octanoic acid-, (B) lauric acid-, and (C) oleic acid-capped FeNPs displaying height profiles of 20.8 nm, 12.4 nm, and 2.7 nm, respectively.

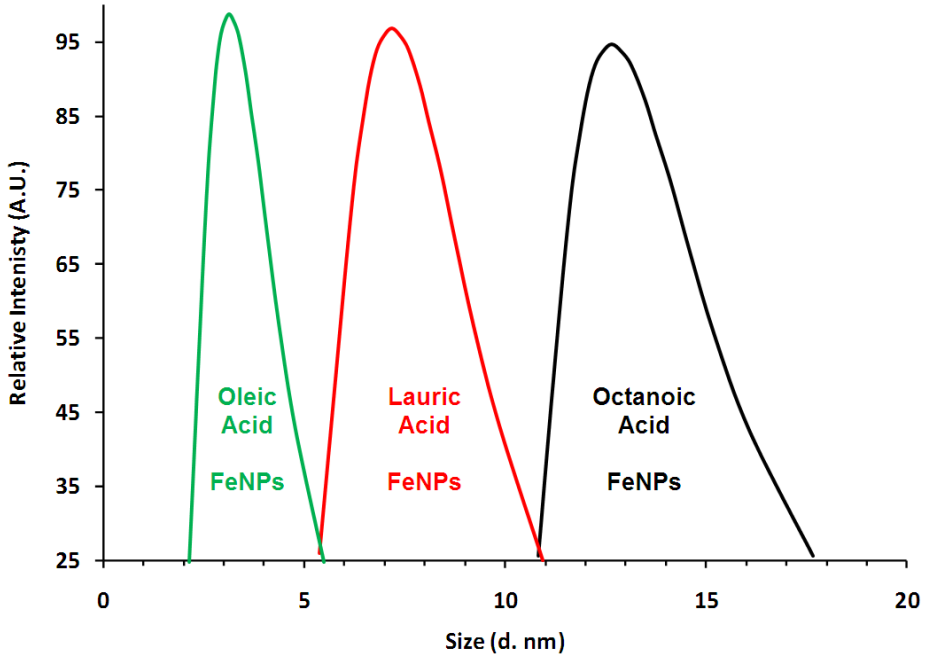

Figure 51. Dynamic light scattering (DLS) measurements of synthesized FeNPs of varying diameter distributions.

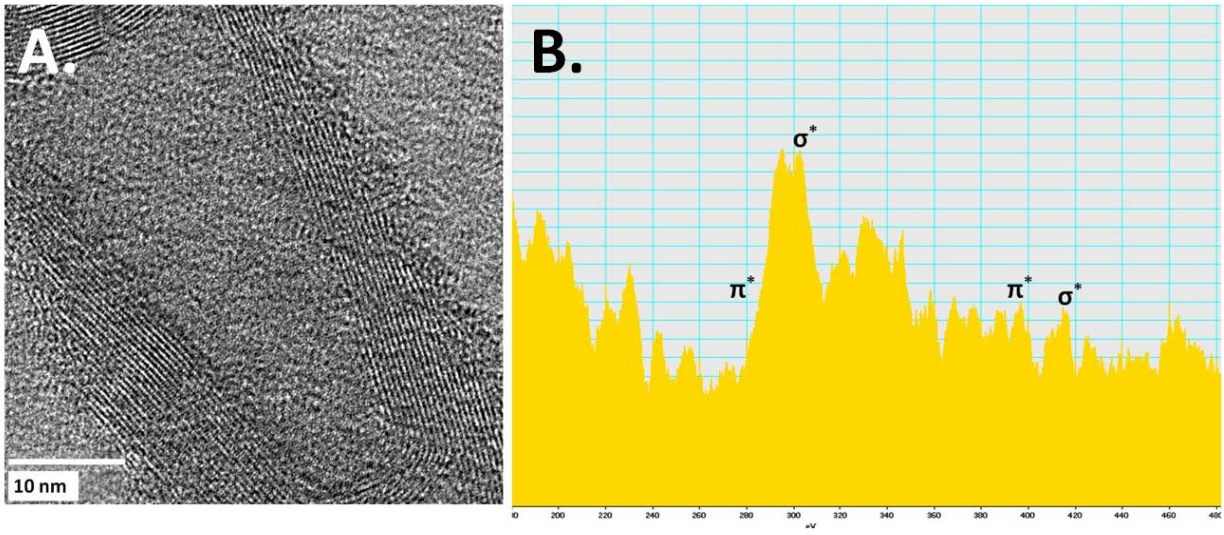

Figure 52. High resolution TEM micrograph of synthesized NCNC. Striations indicate lattice walls running in parallel to each other but diagonal to the longitudinal axis of the fiber. (b) Corresponding EELS analysis indicated the presence of 2-7% N as a result of nitrogen doping.

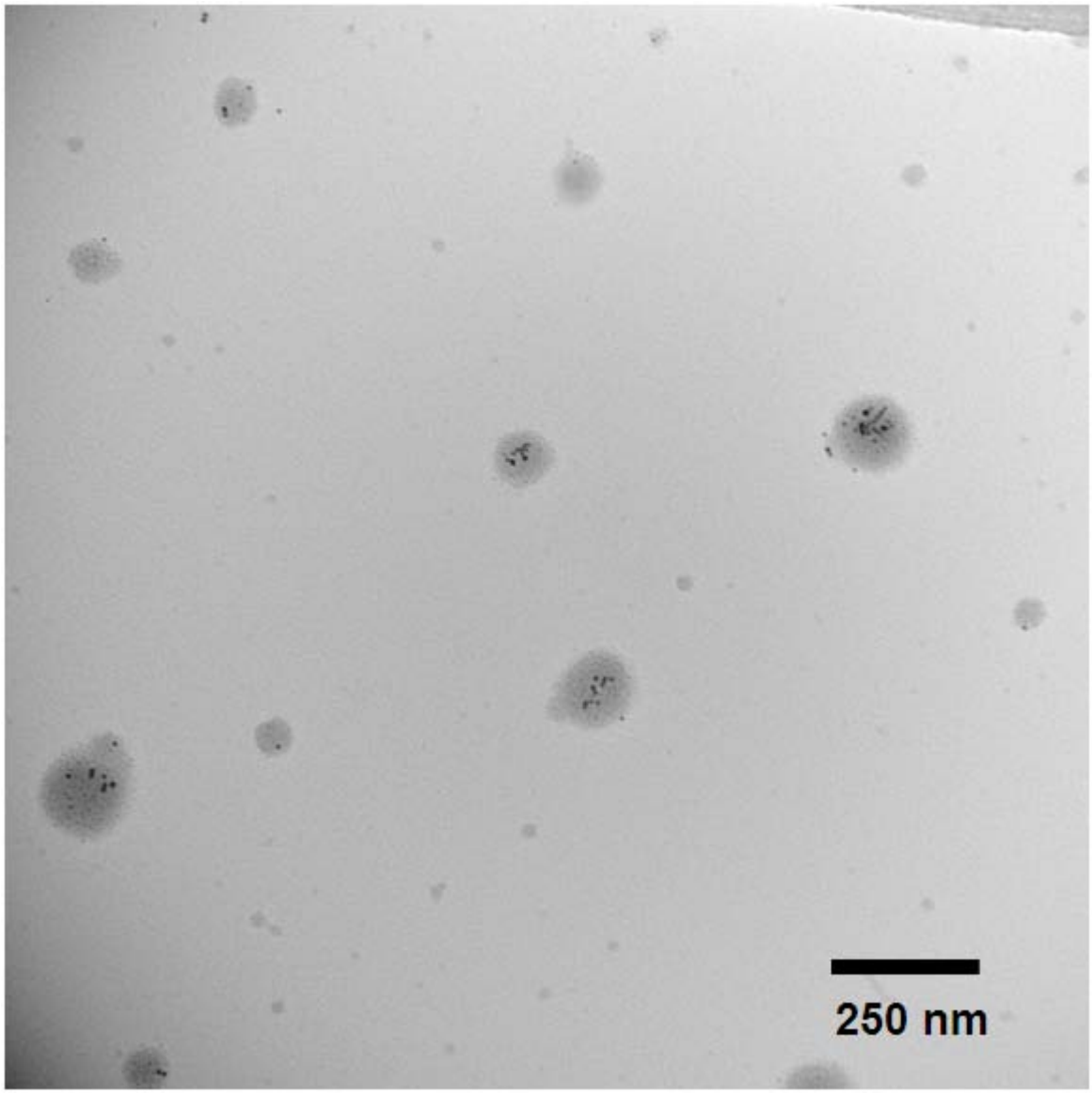

Figure 53. A typical TEM image depicting multiple nanocapsules containing gold nanoparticles (GNPs) prepared by cross-linking NCNCs from 5% NH_3.

APPENDIX D

BIODEGRADATION OF SINGLE-WALLED CARBON NANOTUBES THROUGH ENZYMATIC CATALYSIS: SUPPORTING INFORMATION

This Appendix contains supporting information for Chapter 5.0 'Biodegradation of Single-Walled Carbon Nanotubes through Enzymatic Catalysis'. It contains statistical data correlating nanotube length as a function of time (**Table 2**), TEM imaging of H_2O_2 (**Figure 54**) and HRP **(Figure 55**) controls, AFM imaging of carbon nanotubes prior to incubation (**Figure 56**) and after 8 weeks of incubation with HRP/H_2O_2 (**Figure 57**), EPR spectra (**Figure 58**), and EPR methodology.

Table 2. Statistical data table correlating nanotube length as a function of time. All samples were confirmed via TEM as salt concentration was too high for AFM imaging.

Carbon Solutions Single-Walled Carbon Nanotube Samples						
	t = 2 weeks	**t = 4 weeks**	**t = 8 weeks**	**t = 16 weeks**	**Control = CS and 80μM H_2O_2**	**Control = CS and HRP**
Length (nm)	317 425 478 480 497 519 551 600 632 639 663 678 683 741 794 821 844 869 883 937 962 967 989 1090 1110 1150 1350 1500 1690	284 343 351 360 398 468 484 502 531 576 593 639 648 705 757 818 835 907 986 996 1060 1070 1120 1150 1160 1160 1270 1310 1330 1350 1440 1480 1480	131 138 142 151 164 165 168 171 172 193 202 210 259 260 267 294 309 359 430 439	No measureable nanotube material found.	287 341 344 380 387 413 437 463 467 481 511 524 545 552 568 579 603 673 676 678 683 684 754 765 855 902 911 912 931 1090 1100 1250 1300 1350 1440 1570	526 544 643 819 917 927 929 945 977 992 992 1050 1080 1290 1470 1530 2280
Avg. Length (nm)	823	865	231	------	753	1054
Median	794	835	198	------	677	977
Range	1373	1196	308	------	1283	1754
Standard Dev.	325	376	94	------	340	418

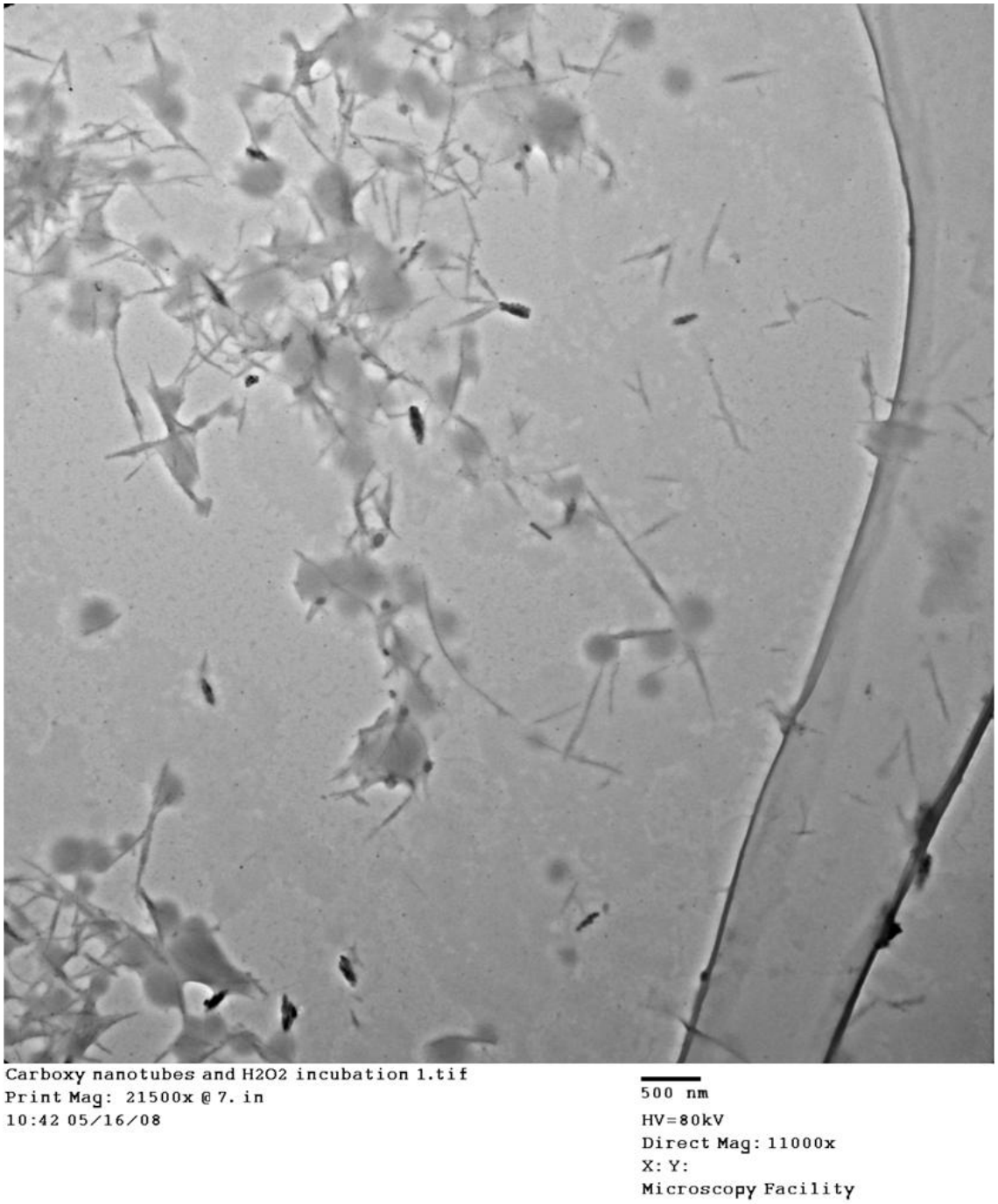

Figure 54. TEM Image of Carboxylated Nanotubes after 16 weeks incubation with 80 µM H_2O_2 as a control. No length decrease in the nanotube sample was found to be evident.

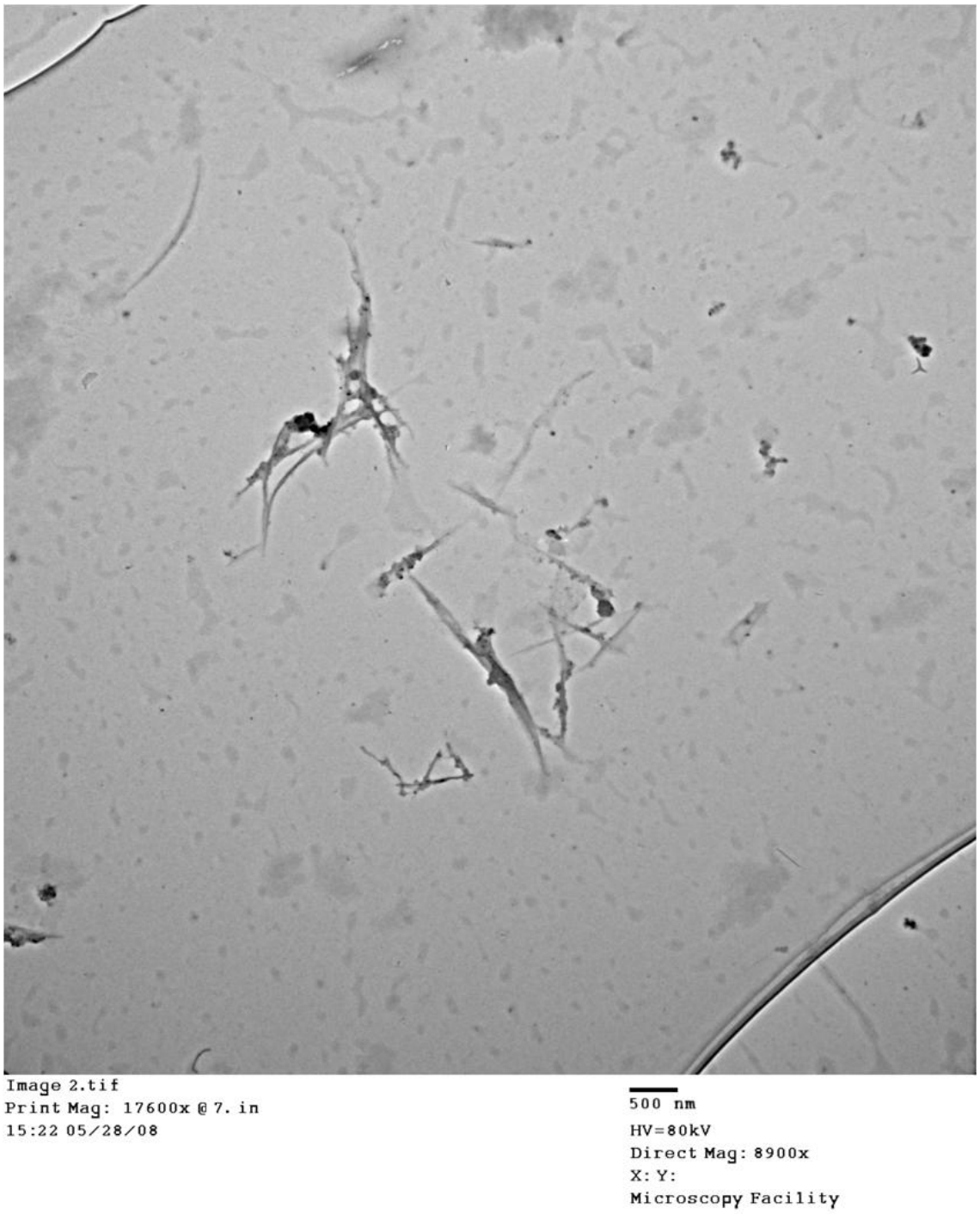

Figure 55. TEM Image of HRP-functionalized Carboxylated Nanotubes after 16 weeks. No length decrease in the nanotube sample was found to be evident.

Figure 56. Atomic force microscopy (AFM) of carboxylated nanotubes prior to incubation with HRP. Left panel displays height image; right panel displays phase image. Point-to-point measurements show nanotubes of approximately 400 nm in length.

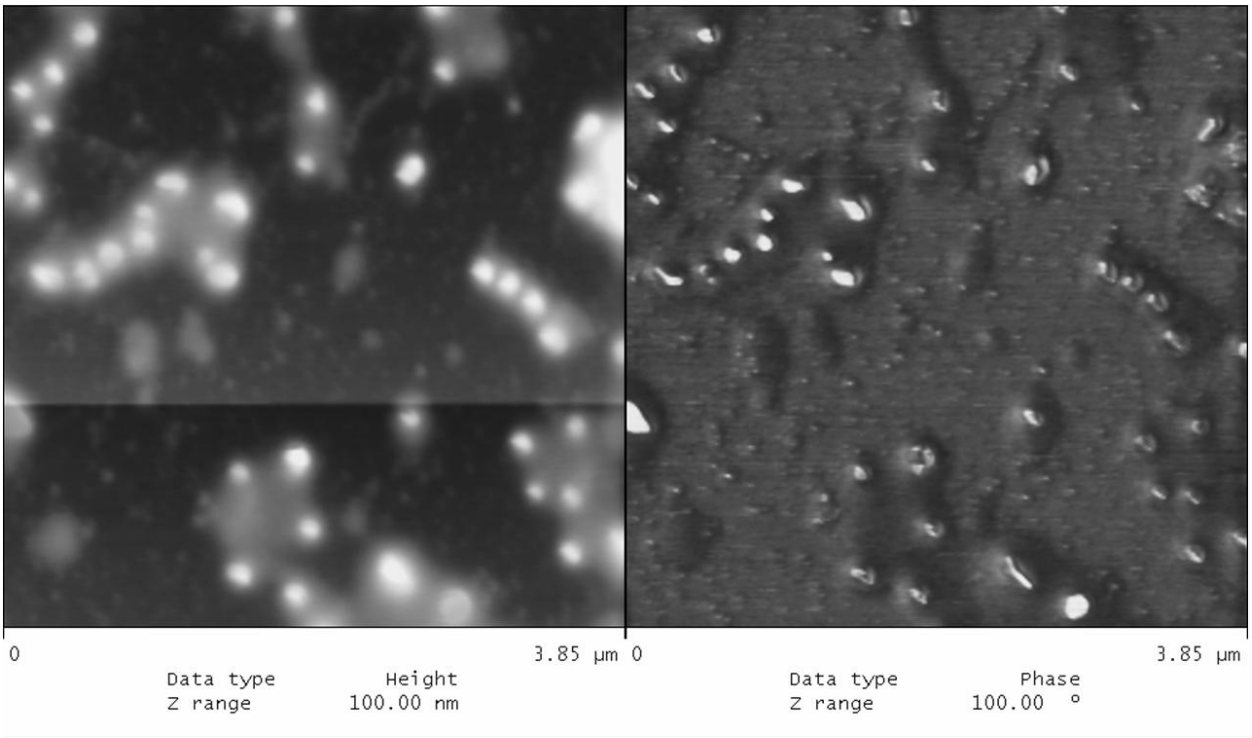

Figure 57. Atomic force microscopy (AFM) of carbon nanotubes after incubation with HRP and H_2O_2 for 8 weeks. Left panel displays height image; right panel displays phase image. As can be seen no noticeable nanotube material is imaged.

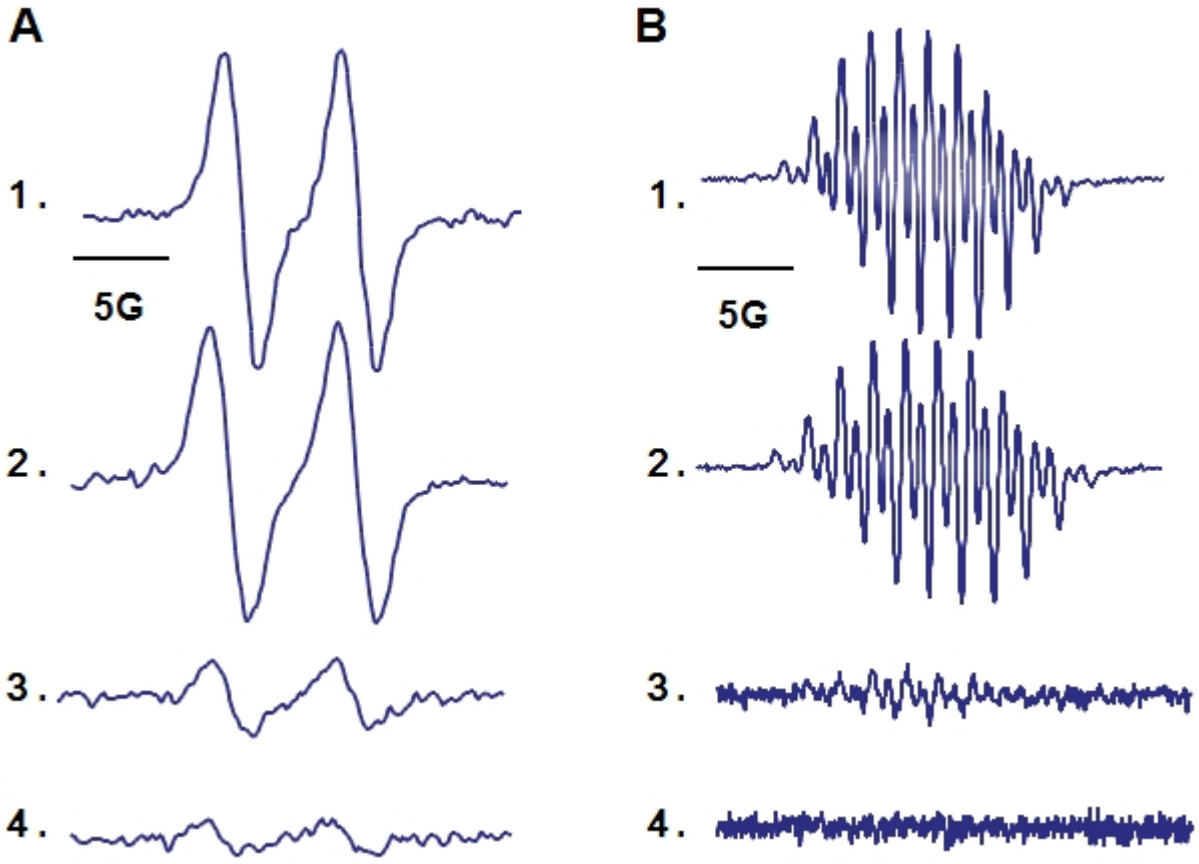

Figure 58. EPR spectra of radicals (A) and etoposide phenoxyl radicals (B) characterizing peroxidase activity of HRP in the presence and absence of single walled carbon nanotubes. 1) HRP and H_2O_2, 2) Nanotubes, HRP, and H_2O_2, 3) Nanotubes and HRP, 4) Nanotubes and H_2O_2.

EPR Discussion and Methodology

The activity of HRP in the presence of nanotubes was studied using two peroxidase substrates - ascorbate and etoposide. The typical doublet signal of the ascorbate radical with a hyperfine splitting constant of 1.7 G was detected upon incubation of HRP with ascorbate in the presence of H_2O_2 (**Figure 58, A**). Addition of nanotubes to the incubation mixture did not change the EPR signal of ascorbate radical. In the absence of HRP or H_2O_2, the magnitude of the signal was several-fold lower thus confirming that oxidation of ascorbate occurred mainly via the peroxidase reaction.

The addition of H_2O_2 to peroxidase in the presence of etoposide produced a characteristic EPR signal of etoposide phenoxyl radical (etoposide-$O^{\bullet}$) (**Figure 58, B**). Because the lifetime of etoposide phenoxyl radicals is on the order of several min at μM concentrations, we measured the steady-state EPR signals of etoposide-$O^{\bullet}$ in 10 min after addition of H_2O_2. The spectra were identical in the presence and in the absence of nanotubes (**Figure 58, B**, 1-2). In the absence of H_2O_2, the signal of etoposide-$O^{\bullet}$ was only barely detectable from the mixture of nanotubes and HRP; similarly the signal was undetectable in the absence of HRP.

Incubation conditions: HRP(0.35 mkM) was incubated with nanotubes (0.02 mg/ml) for 1 min at room temperature in PBS, then etoposide (200 mkM) or ascorbate (100 mkM) were added and the peroxidase reaction was initiated by H_2O_2 (80 μM). EPR spectra of ascorbate radicals were recorded 1 min after addition of H_2O_2, EPR spectra of etoposide phenoxyl radicals were recorded - 10 min after addition of H_2O_2.

EPR spectra were recorded on a JEOL REIX spectrometer with 100 kHz modulation (JEOL, Kyoto, Japan). Measurements were performed at room temperature in gas-permeable Teflon tubing (0.8 mm internal diameter, 0.013 mm thickness) obtained from Alpha Wire

Corporation (Elizabeth, NJ). The tubing was filled with 60 µl of sample, folded doubly, and placed in an open 3.0 mm internal diameter EPR quartz tube. Spectra of etoposide phenoxyl radicals were recorded at 3350 G, center field; 50 G, sweep width; 10 mW, microwave power; 0.5 G, field modulation; $2.5*10^2$, receiver gain; 0.03 s, time constant; and 2 min, scan time. EPR spectra of ascorbate radicals were recorded at 3350 G, center field; 10 G, sweep width; 10 mW, microwave power; 0.5 G, field modulation; 10^3, receiver gain; 0.1 s, time constant; 1 min, scan time.

APPENDIX E

MECHANISTIC INVESTIGATIONS OF HORSERADISH PEROXIDASE-CATALYZED DEGRADATION OF SINGLE-WALLED CARBON NANOTUBES: SUPPORTING INFORMATION

This Appendix contains supporting information for Chapter 6.0 'Mechanistic Investigations of Horseradish Peroxidase-Catalyzed Degradation of Single-Walled Carbon Nanotubes'. It contains Amplex Red controls with 80 μM (**Figure 59**) and 800 μM (**Figure 60**) H_2O_2 in H_2O, GC−MS control with H_2O (**Figure 61**), GC−MS of pristine SWNTs and hemin (**Figure 62**), GC−MS of pristine SWNTs and $FeCl_3$ (**Figure 63**), HPLC chromatograms of HRP-degraded SWNTs (**Figure 64**), *trans*-cinnamaldehyde (**Figure 65**), and mellitic acid (**Figure 66**), HPLC chromatogram of nonconcentrated sample (**Figure 67**), HPLC chromatogram of HRP (**Figure 68**), section analysis of HRP (**Figure 69**), carboxylated SWNT (**Figure 70**), and carboxylated SWNT with HRP (**Figure 71**), AFM image of pristine SWNTs (**Figure 72**), section analysis of pristine SWNTs (**Figure 73**), AFM image of pristine SWNTs and HRP (**Figure 74**), section analysis of pristine SWNTs and HRP (**Figure 75**), UV−vis−NIR spectra of carboxylated SWNTs on fixed substrate (**Figure 76**), carboxylated SWNTs degraded by hemin (**Figure 77**), carboxylated SWNTs degraded by $FeCl_3$ (**Figure 78**), EDXA of products from pristine SWNTs

degraded by hemin and H_2O_2 (**Figure 79, Figure 80**), intermolecular binding energies (**Table 3**), molecular modeling of HRP interaction with sidewall defects (**Figure 81**), interaction of HRP with bundled pristine SWNTs (**Figure 82**), and a comparative study of HRP docking with varying chirality SWNTs (**Figure 83**).

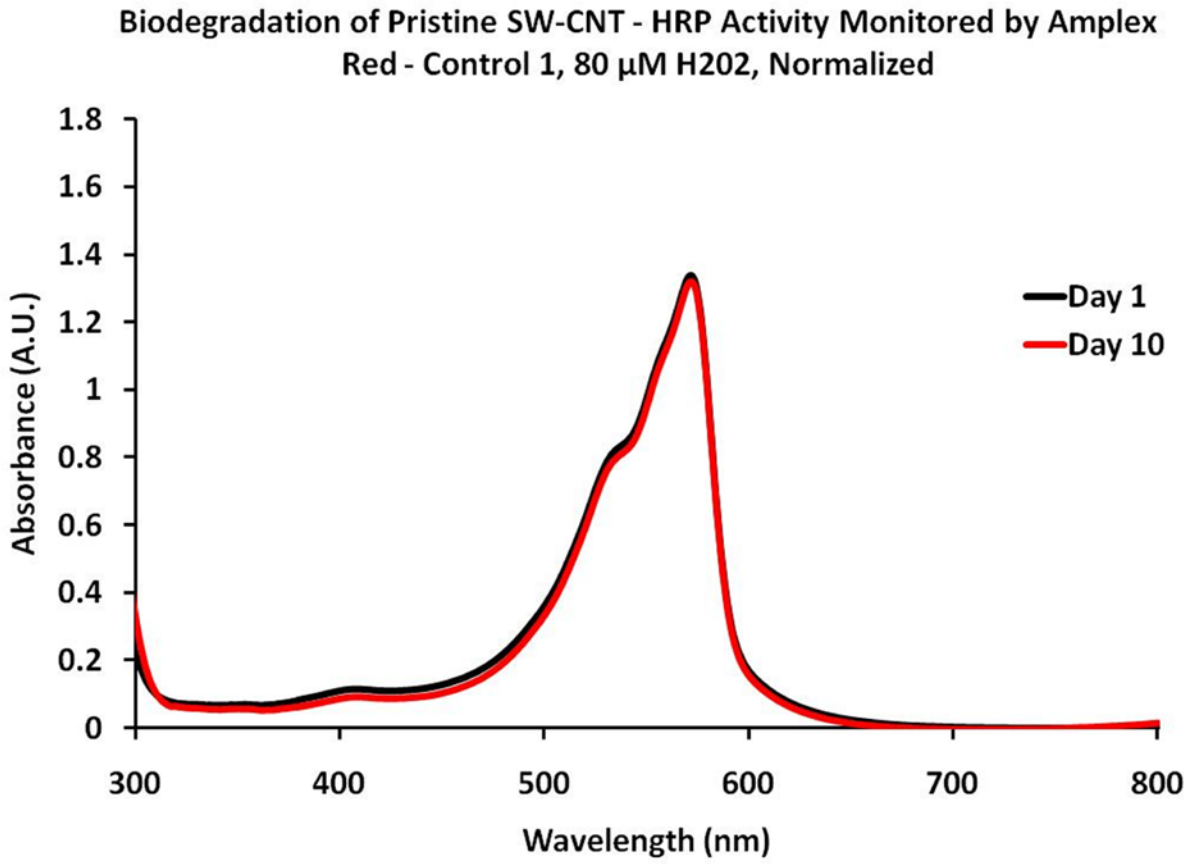

Figure 59. UV-Vis spectra of Amplex Red demonstrating HRP activity in the absence of pristine SWNTs. Absorbance measurements between Day 1 and Day 10 show no loss of activity of HRP when 80 µM H_2O_2 additions are made.

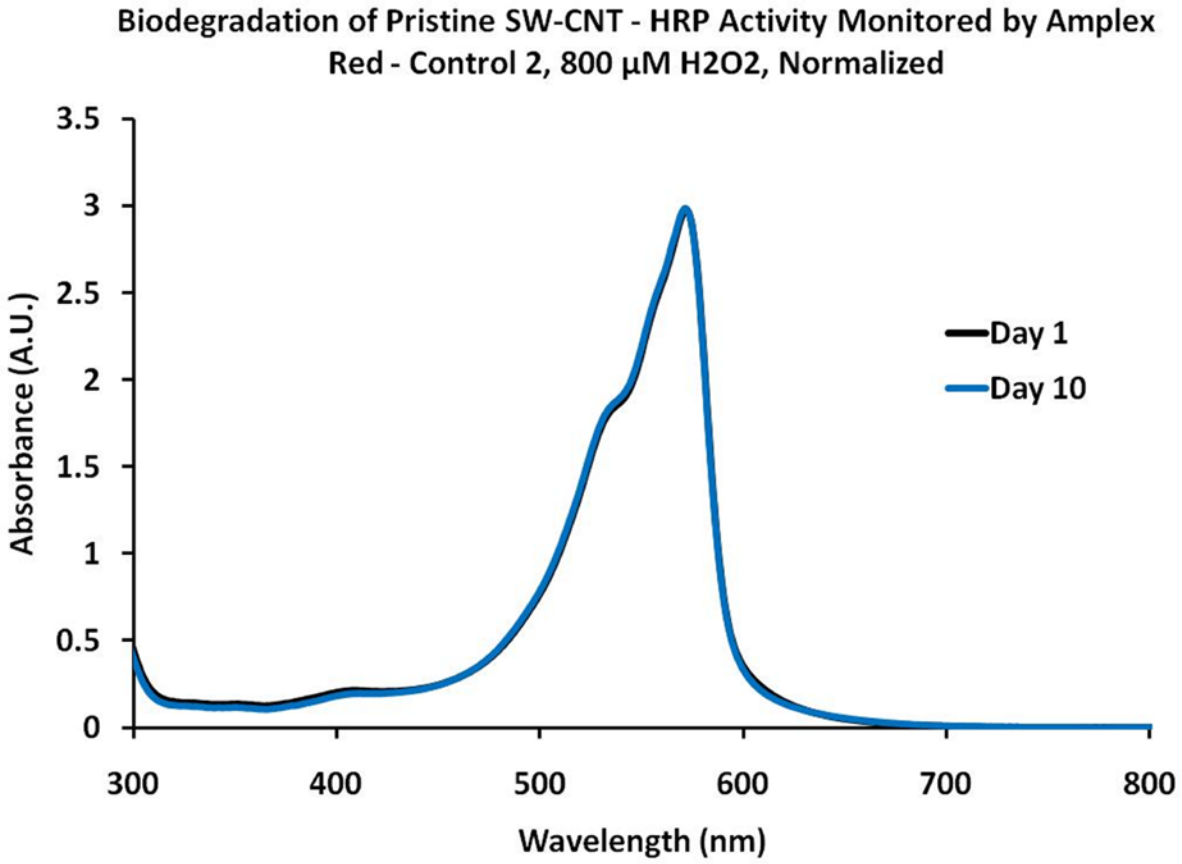

Figure 60. UV-Vis spectra of Amplex Red demonstrating HRP activity in the absence of pristine SWNTs. Absorbance measurements between Day 1 and Day 10 show no loss of activity of HRP when 800 µM additions are made.

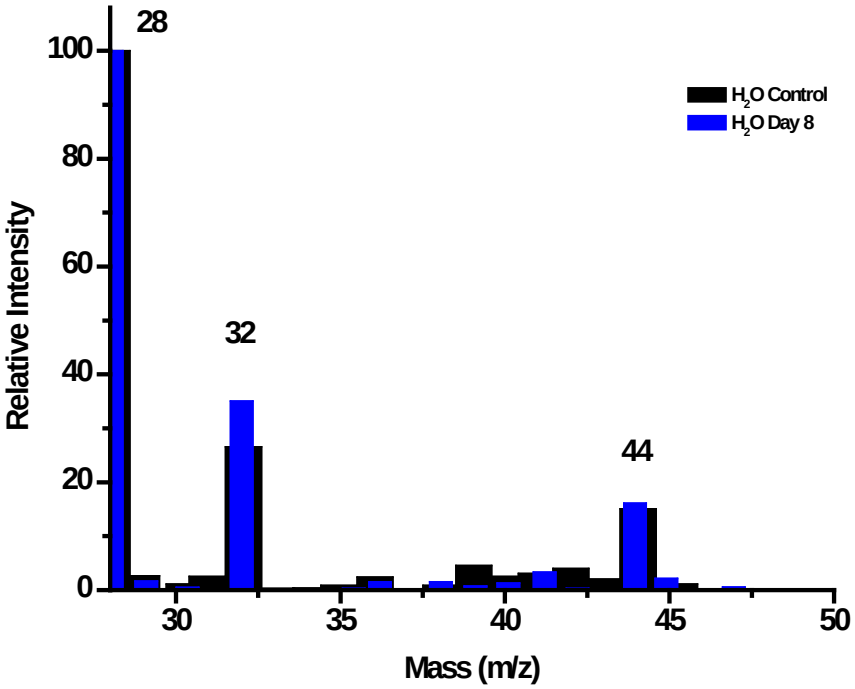

Figure 61. GC-MS spectra showing a 1% change in CO_2 abundance (44 m/z) in a control vial of H_2O with daily additions of 800 µM H_2O_2 (250 µL) after eight days. As expected, ambient CO_2 levels contribute little to increases in concentration.

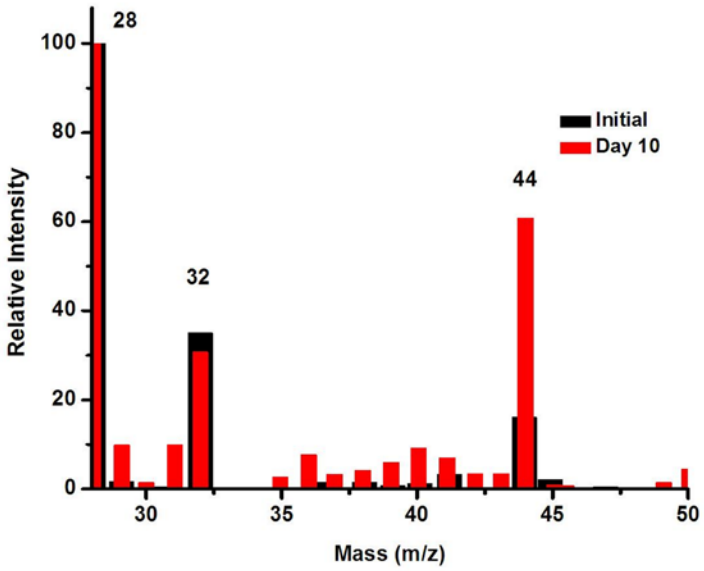

Figure 62. GC-MS spectra showing a 280% change in CO_2 abundance (44 m/z) in a vial of Pristine SWNTs incubated with hemin and with daily additions of 800 µM H_2O_2 (250 µL) after ten days.

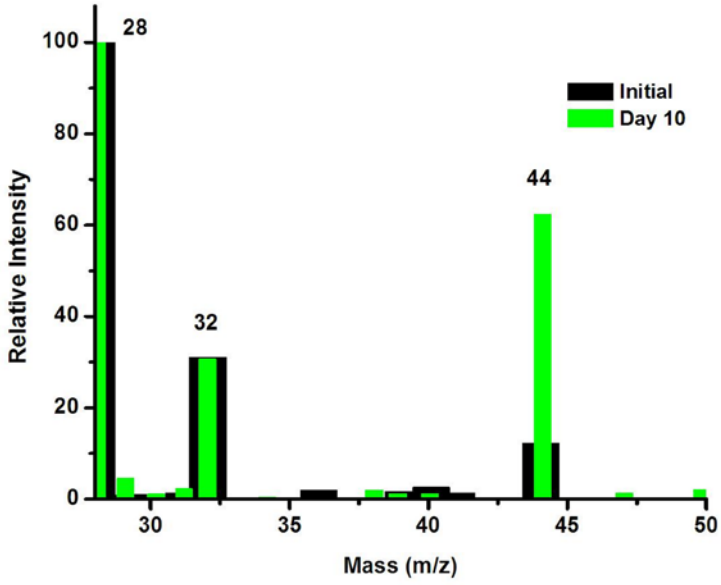

Figure 63. GC-MS spectra showing a 400% change in CO_2 abundance (44 m/z) in a vial of Pristine SWNTs incubated with $FeCl_3$ and with daily additions of 800 µM H_2O_2 (250 µL) after ten days.

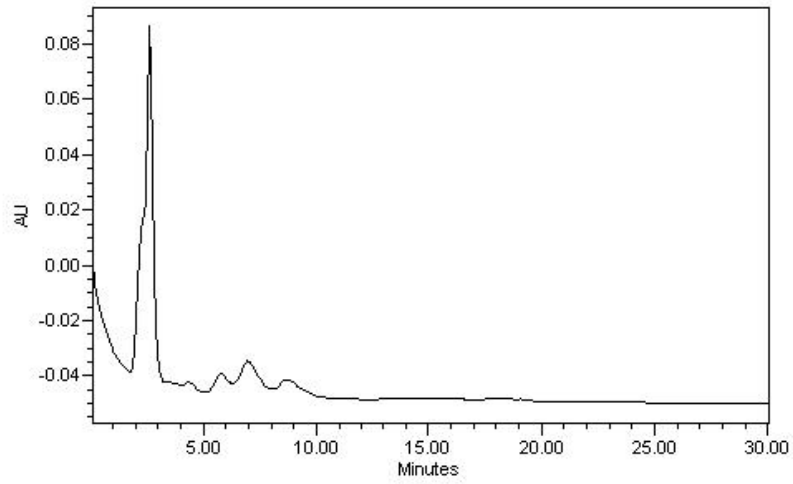

Figure 64. Resulting refractive index chromatogram from HPLC of HRP-degraded, carboxylated SWNTs after 8 days of incubation. The sample was suspended in pure methanol and injected with an isocratic mobile phase of 30:70 H_2O:MeCN using a *Waters Symmetry 300 C18* column to confirm previously obtained results. Elution peaks are present at times earlier than that previously shown, with the first analyte eluting at approximately 2.3 minutes.

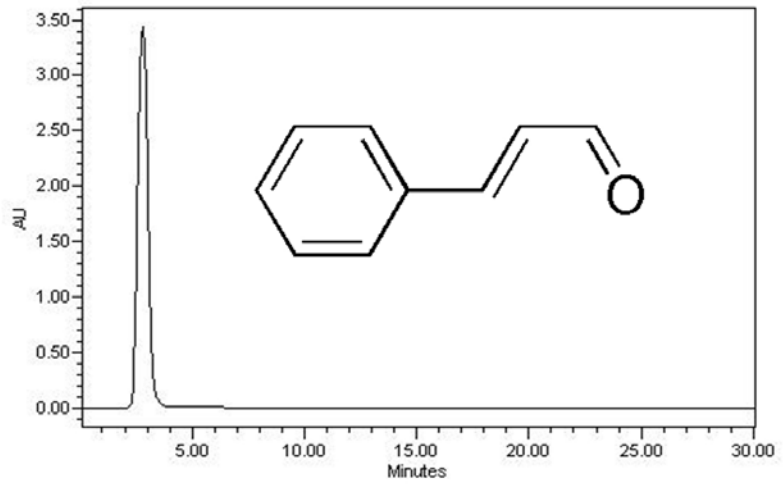

Figure 65. Resulting refractive index chromatogram from HPLC of trans-cinnamaldehyde. Pure trans-cinnamaldehyde was injected in pure methanol with elution from an isocratic mixture of H_2O:MeCN (30:70) utilizing a *Waters Symmetry 300 C18* column. A single elution peak is present at approximately 2.8 minutes, in correlation with observed elution peaks from HRP-degraded products.

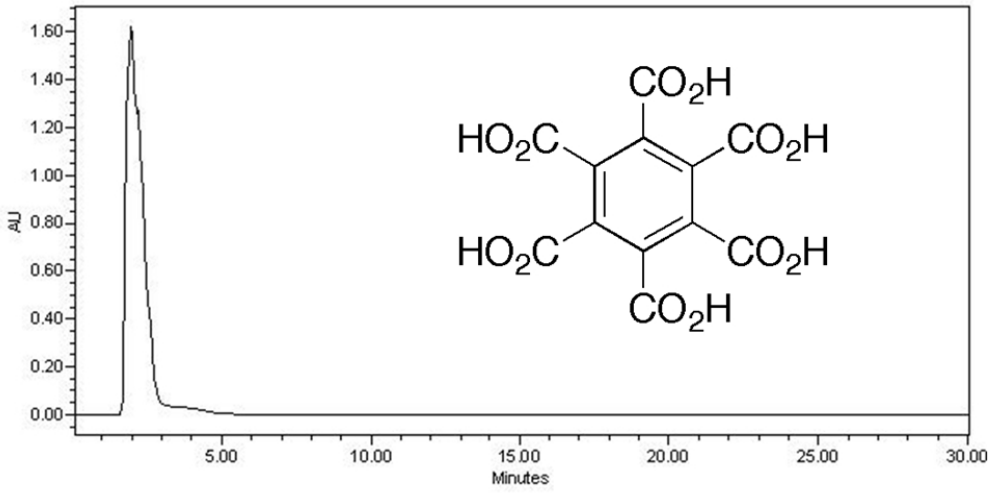

Figure 66. Resulting refractive index chromatogram from HPLC of mellitic acid. Pure mellitic acid was injected in pure methanol with elution from an isocratic 30:70 mixture of H_2O and MeCN utilizing a *Waters Symmetry 300 C18* column. Chromatogram displays single elution peak at approximately 2.3 minutes, in good agreement with peaks observed under the same conditions for HRP-degraded products.

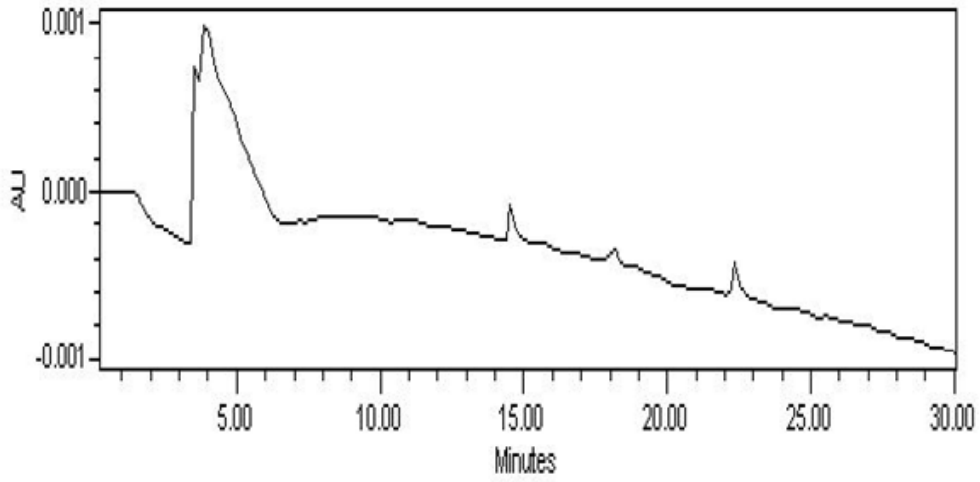

Figure 67. HRP-degraded SWNTs (carboxylated) after three days of incubation with 80 μM H_2O_2. Relatively low concentrations of non-cyclic carbon species are not observed due to their insufficient quantities. However, larger hydrophobic structures are noted at 15, 18, and 22.5 minutes. Analysis was performed using a *Nova C18 (Waters)* column.

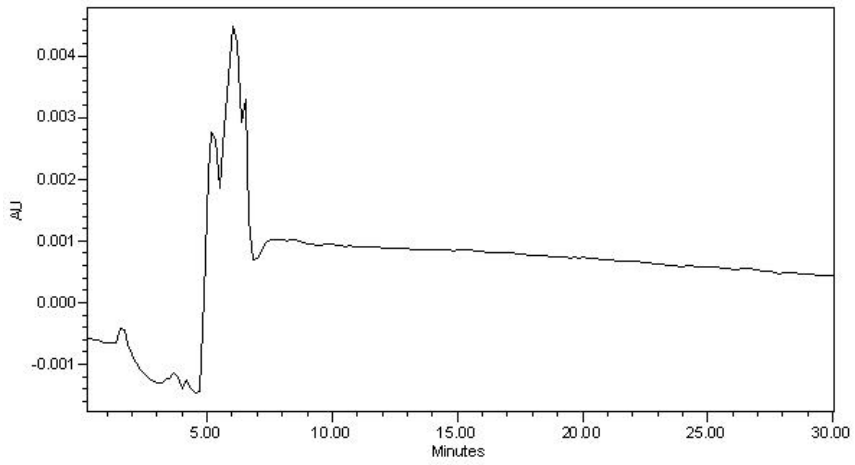

Figure 68. Chromatogram of HRP enzyme shows several peaks eluted from 5-6 minutes. No significant contributions from other species present are eluted past this time. Analysis was performed using a *Nova C18 (Waters)* column.

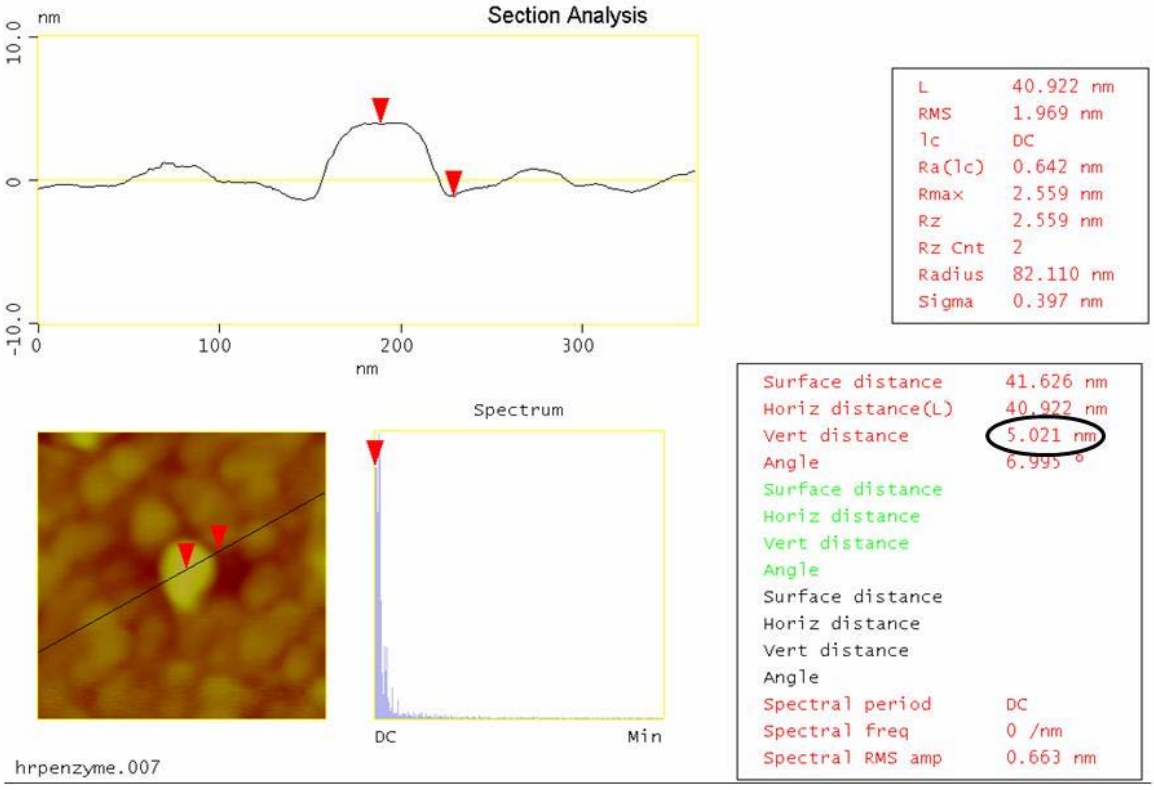

Figure 69. AFM section analysis image of single HRP unit showing a height of approximately 5.0 nm (circled in black).

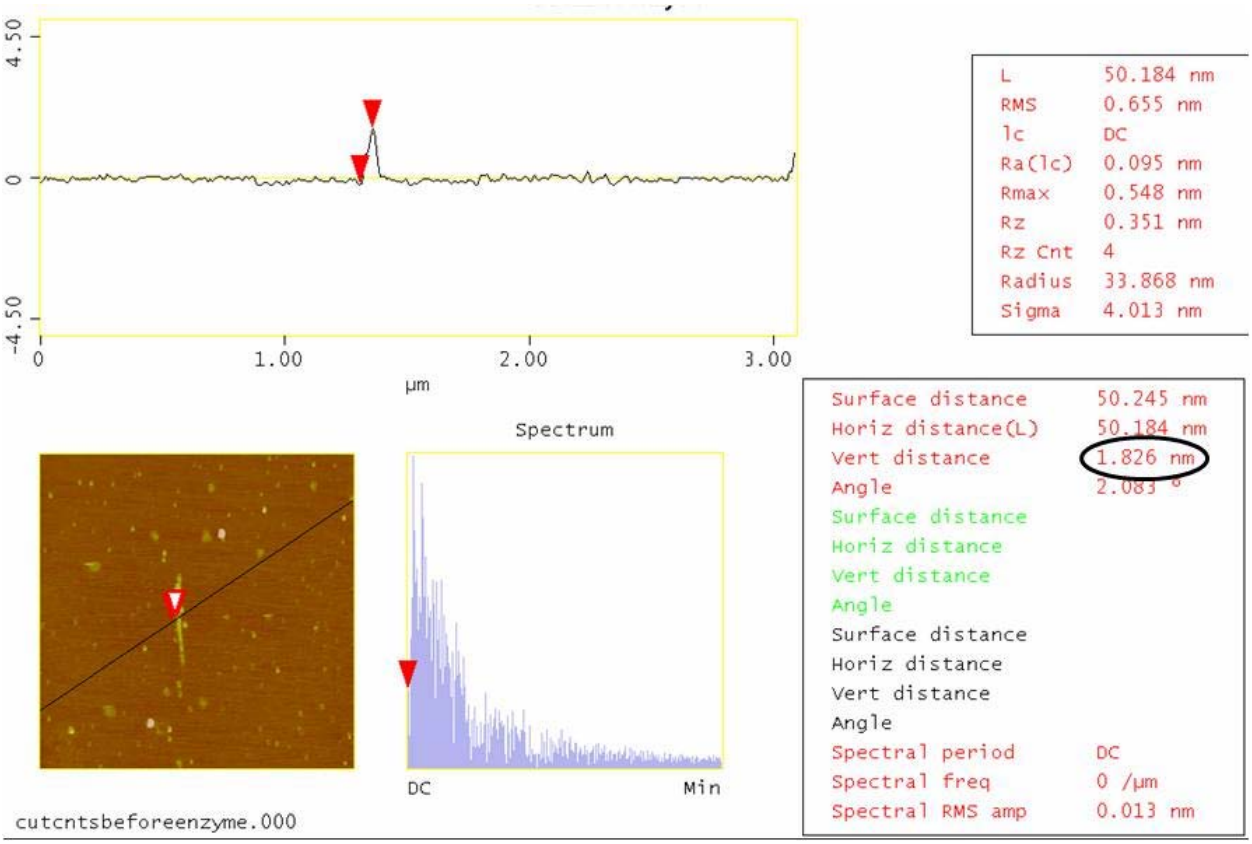

Figure 70. AFM section analysis image of single carboxylated SWNT showing a height of approximately 1.8 nm (circled in black).

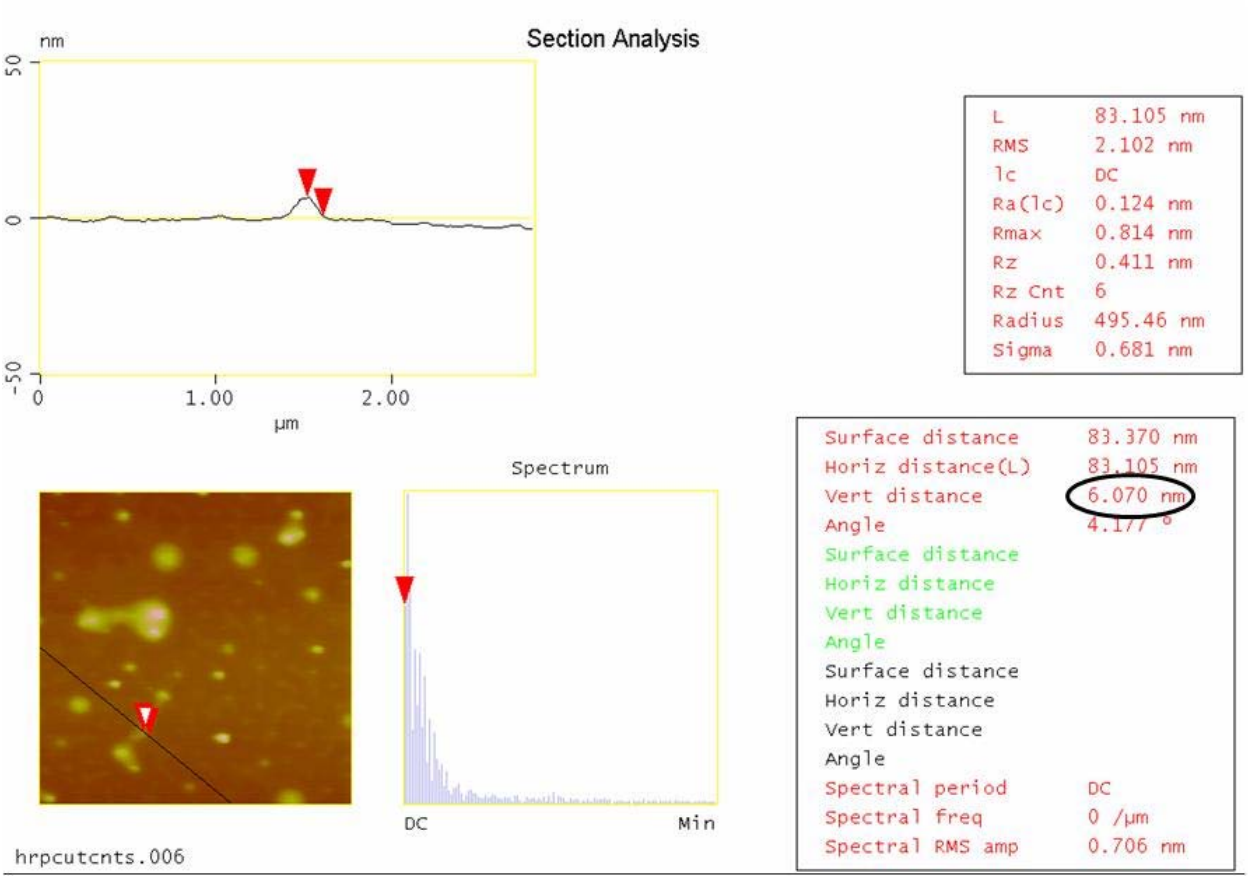

Figure 71. AFM section analysis image of combined carboxylated SWNT and HRP showing a height of approximately 6.0 nm (circled in black).

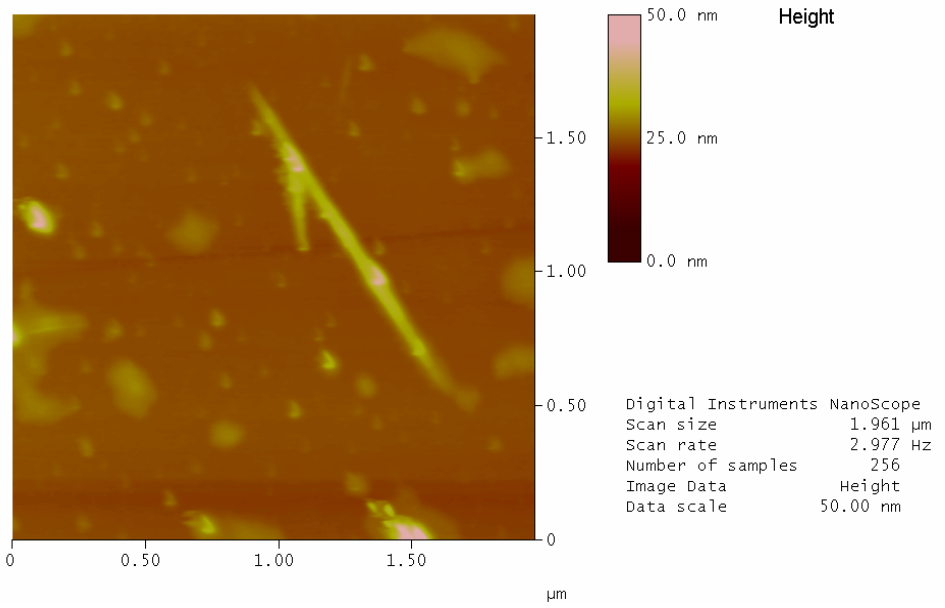

Figure 72. AFM height image of a bundle of pristine SWNTs. Particulate matter results from carbonaceous products and residual iron.

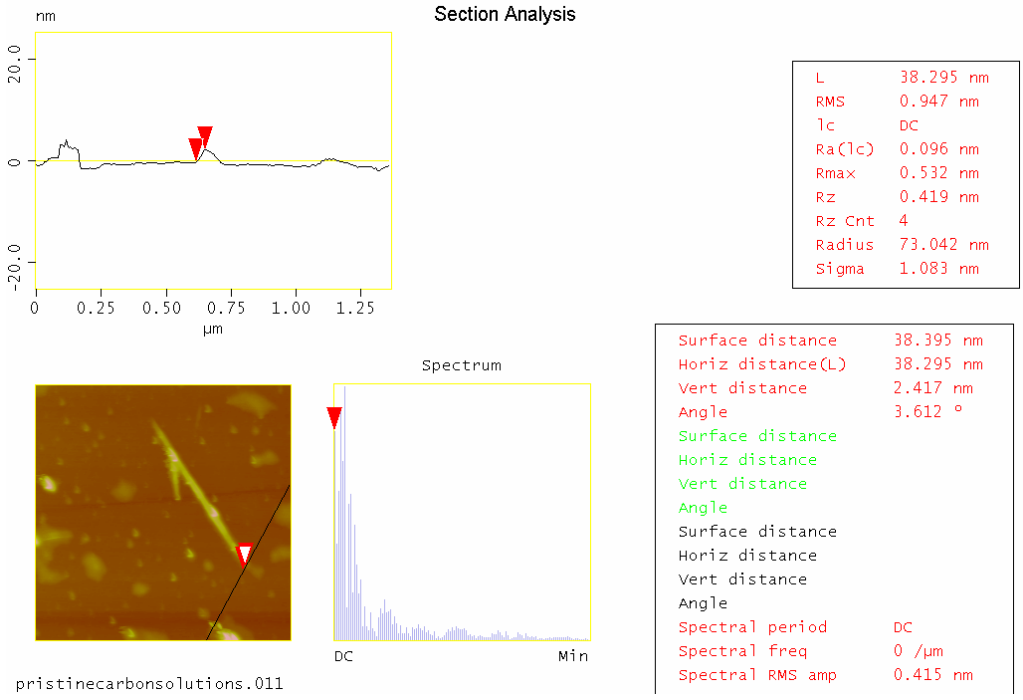

Figure 73. AFM sectional analysis image of a small bundle (~ 2) of pristine nanotubes exhibited a height of approximately 2 nm.

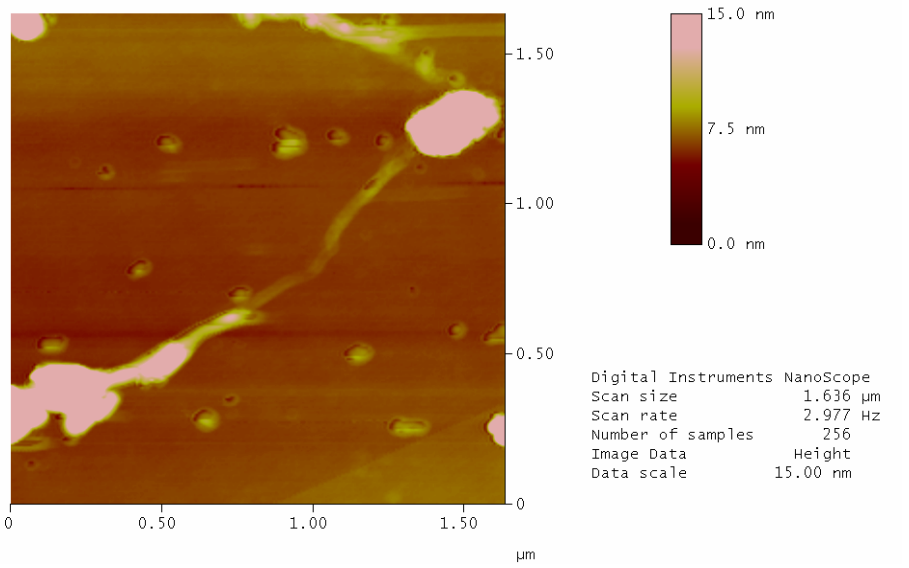

Figure 74. AFM height image of single pristine SWNT with HRP enzymes non-specifically bound along the tube length.

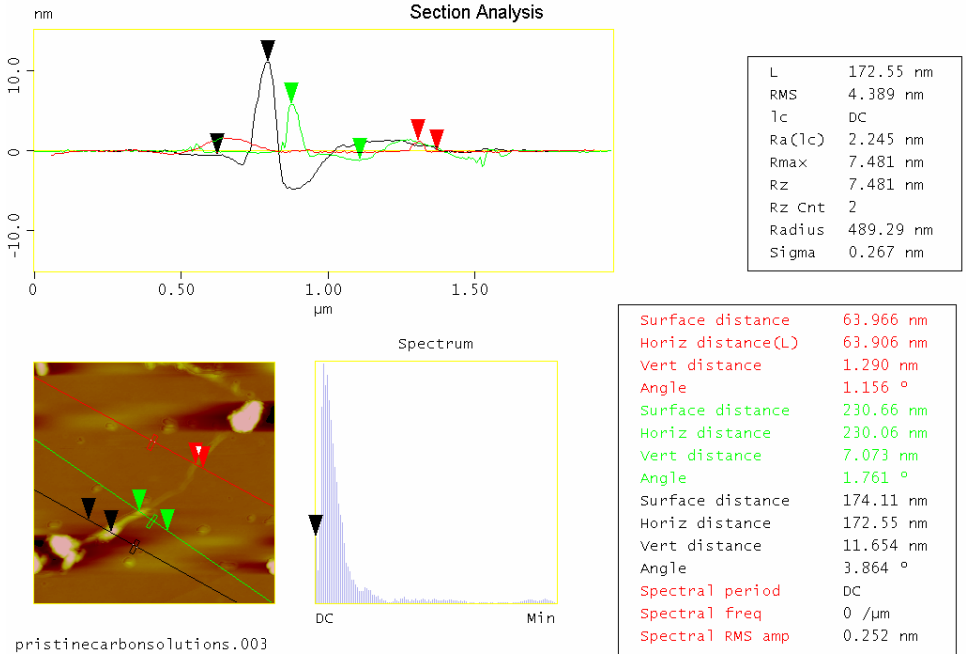

Figure 75. AFM section analysis image of HRP non-specifically bound to a single, pristine SWNT. Several units have attached as is evident by the bare nanotube height of approximately 2 nm (red), a single HRP unit attachment showing approximately 7 nm (green), and multiple units attached to the pristine SWNT (~12 nm, black).

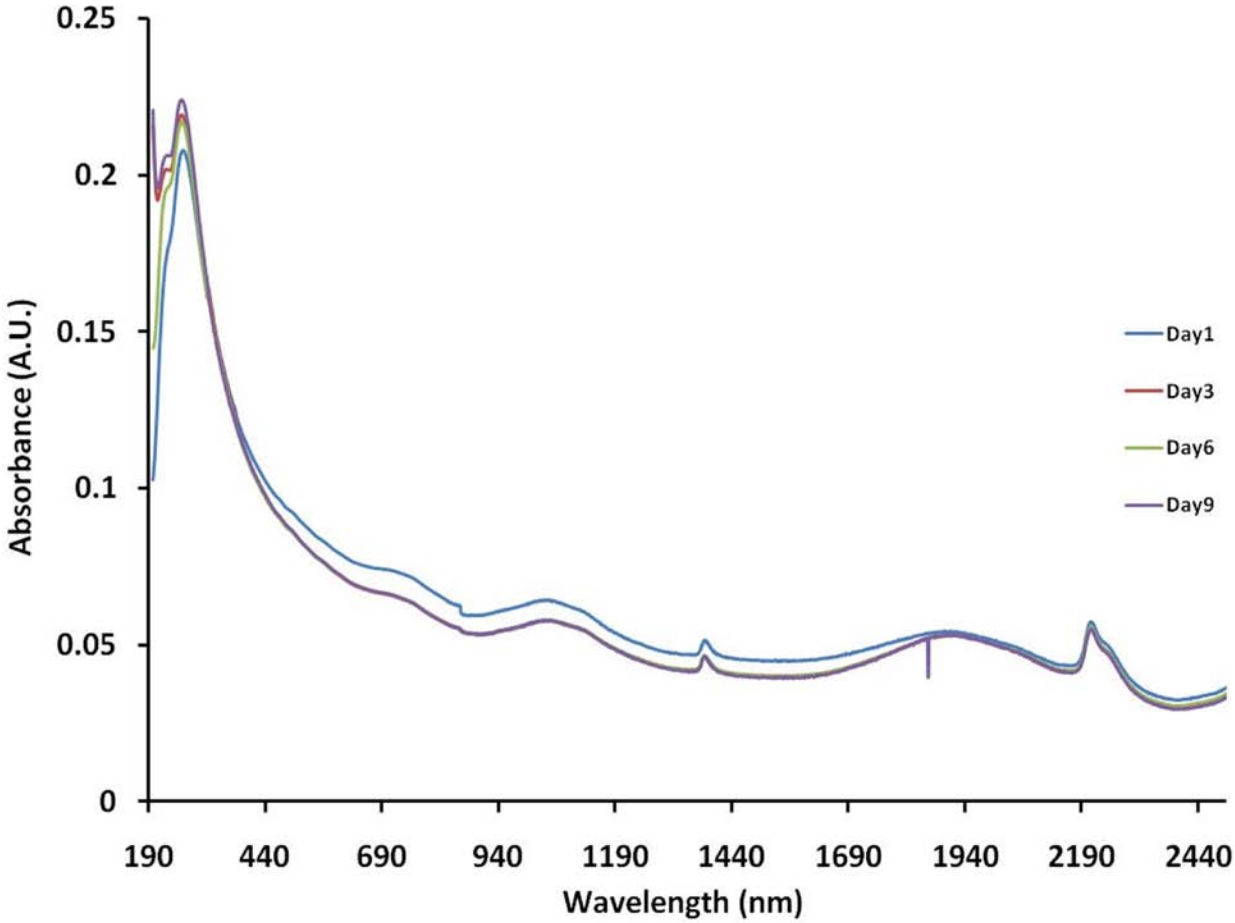

Figure 76. UV-Vis-NIR spectra of carboxylated SWNTs cast on quartz substrate by spray coating. Identical degradation conditions were performed over the course of ten days with HRP and 800 µM H_2O_2. No noticeable degradation as seen as all spectra features (S_1, S_2, M_1, and S_3) are observed between days 1 and 10.

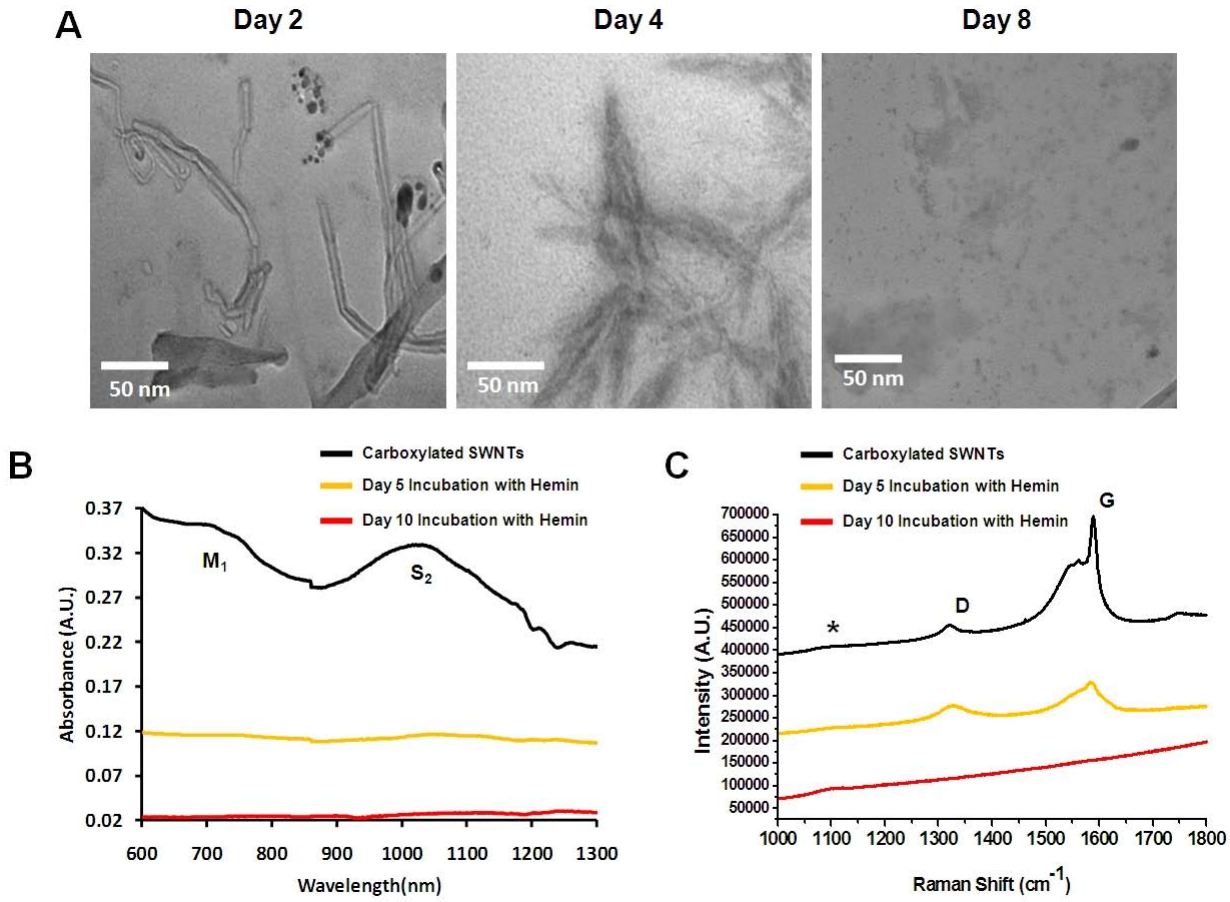

Figure 77. A) TEM micrograph confirming degradation of carboxylated SWNTs by hemin and H_2O_2. B) Vis-NIR spectra of carboxylated SWNTs (black), after 5 days of incubation with hemin and H_2O_2 (orange), and after 10 days of incubation with hemin and H_2O_2 (red). C) Raman spectra of carboxylated SWNTs (black), after 5 days of incubation (orange), and after 10 days of incubation (red) (asterisk indicates contribution from quartz substrate).

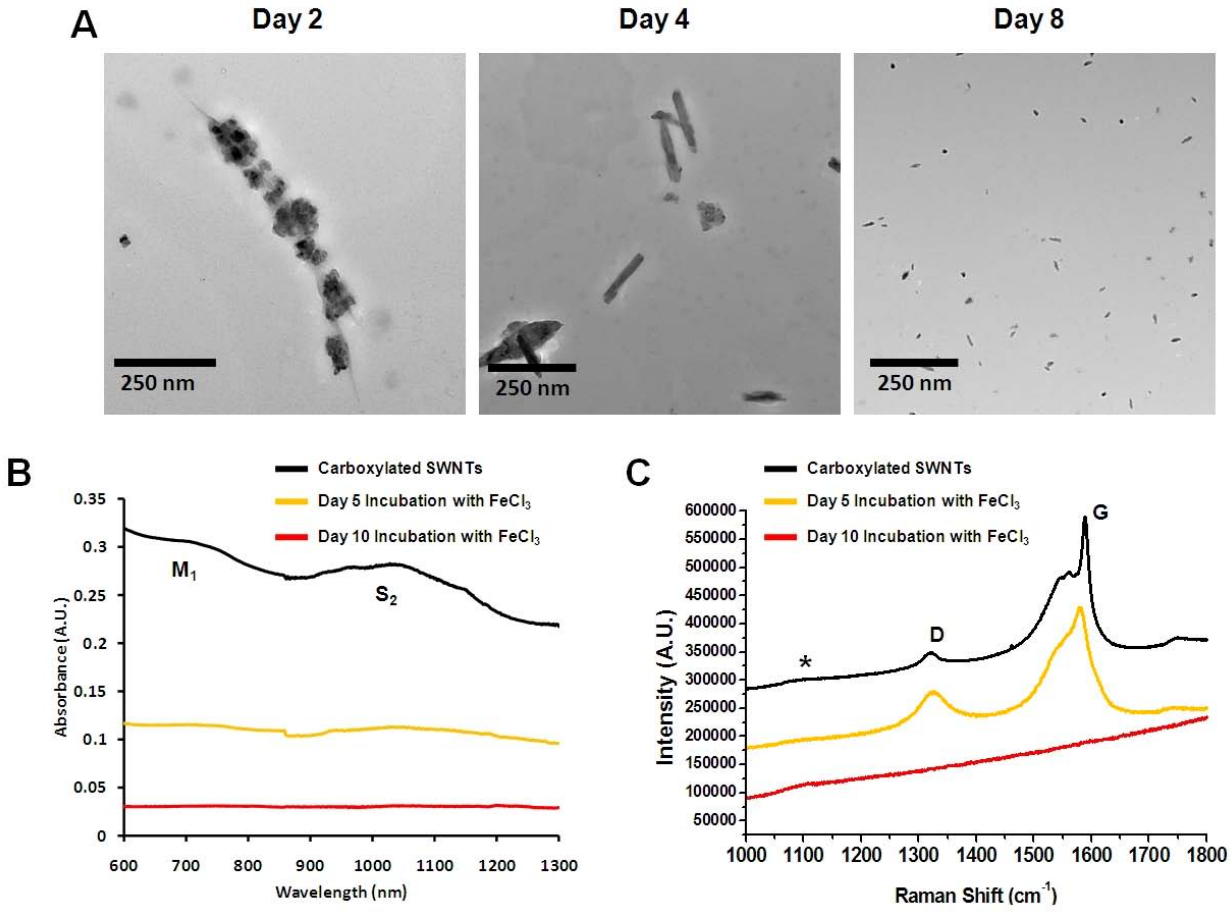

Figure 78. A) TEM micrograph confirming degradation of carboxylated SWNTs by $FeCl_3$ and H_2O_2. B) Vis-NIR spectra of carboxylated SWNTs (black), after 5 days of incubation with $FeCl_3$ and H_2O_2 (orange), and after 10 days of incubation with hemin and H_2O_2 (red). C) Raman spectra of carboxylated SWNTs (black), after 5 days of incubation (orange), and after 10 days of incubation (red) (asterisk indicates contribution from quartz substrate).

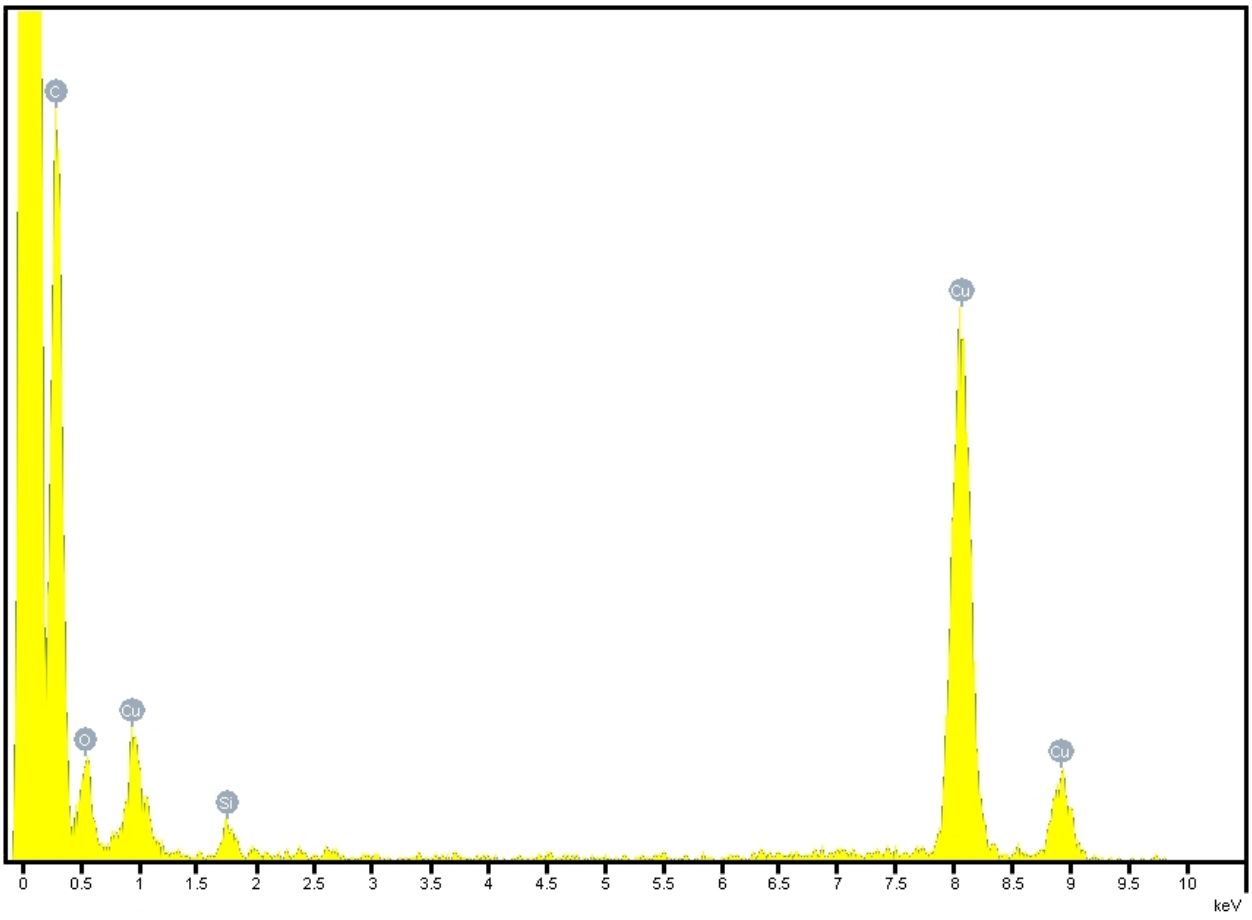

Figure 79. Energy dispersive x-ray analysis (EDXA) of products resulting from degradation of pristine SWNTs with hemin and 800 μM H_2O_2. The only observable peaks include those for carbon, oxygen, silicon, and copper. Copper and silicon contributions are from the TEM grid.

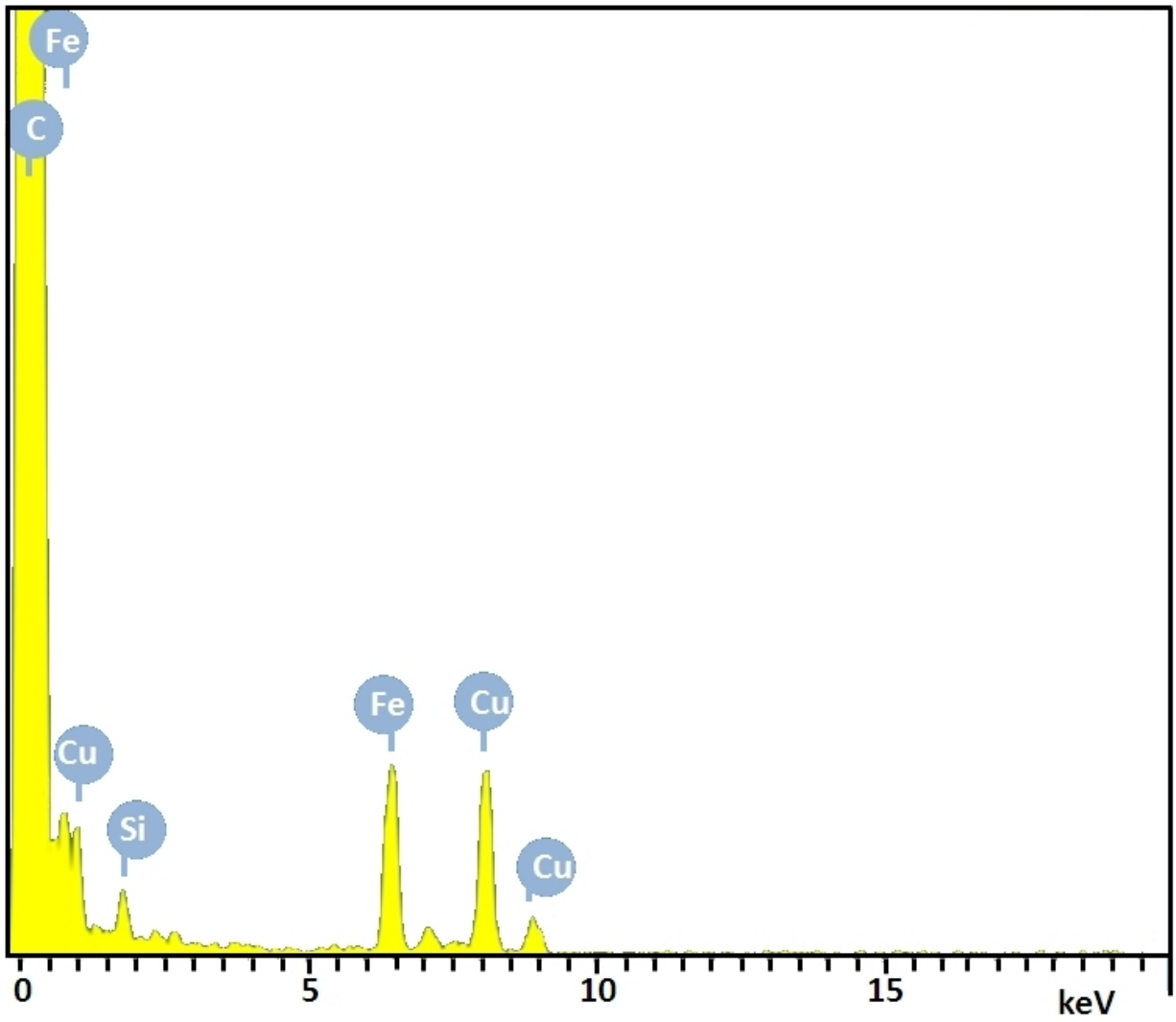

Figure 80. EDXA of residual metallic particles after degradation of pristine SWNTs with hemin and 800 µM H_2O_2. Observable peaks show large contributions for carbon and iron, in addition to background contributions from copper and silicon, a result of the TEM grid.

Table 3. Molecular docking of pristine and carboxylated SWNT to horseradish peroxidase. The 5Å binding pocket residues are listed. For ease of identification, we also provide a description of the most preferable binding site location. The interaction energies, followed by the number of conformations observed in each case in brackets, are also listed.

	Binding site location	Binding Energy (# of conformations)	5Å Residues
Carboxylated and Hydroxylated SWNT (8,8)	In proximity to the heme binding site	-15.1 (6/9)	F68, N135, L138, A140, P141, F142, F143, T144, Q147, R178, F179, D182, N186, F187, S188, N189, Q245
Carboxylated and Hydroxylated SWNT (8,8)	At the distal end of the heme pocket	-13.7 (3/9)	L2, P4, S116, W117, R118, P120, N275, V278, E279, D282, N286
Pristine SWNT (8,8)	At the distal end of the heme pocket	-15.7 (9/9)	L2, P4, S116, W117, R118, P120, N275, V278, E279, D282, N286

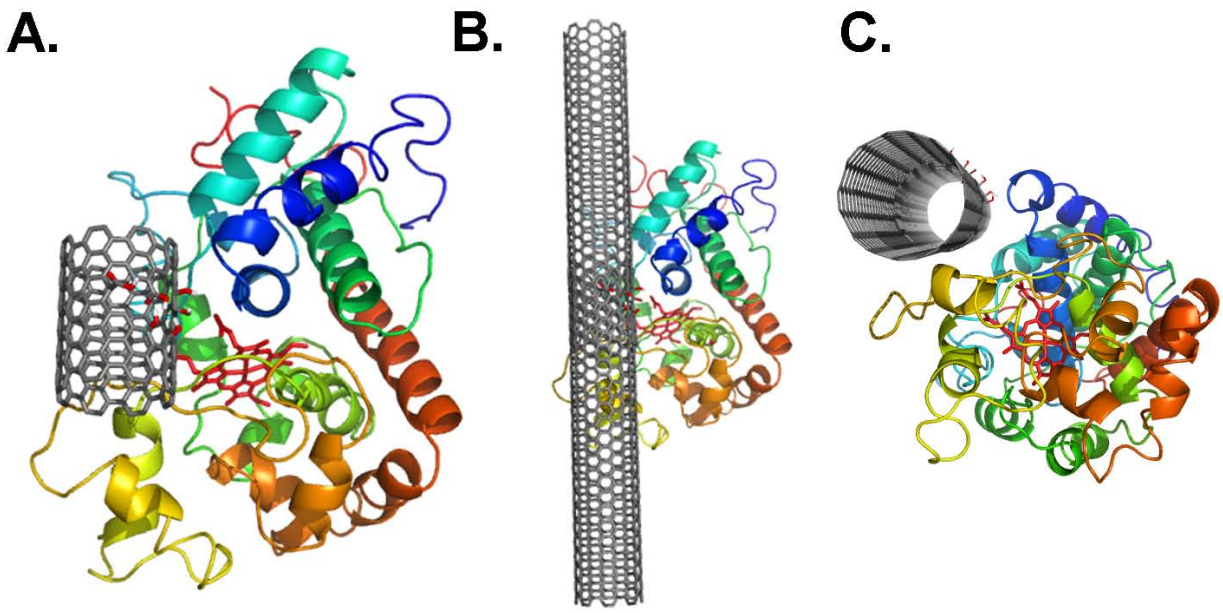

Figure 81. Molecular modeling of HRP to SWNT with (8,8) chirality carrying defects in the middle. A) The docked SWNT of length 1.5 nm is shown. B) The SWNT length has been extended to 10 nm to demonstrate the lack of steric hindrance in binding. C) Same as (B) but tilted by approximately 90°. The receptor HRP is rendered as cartoon and colored in gradient from N-C terminus representing blue to red. SWNT is colored in grey and represented as stick in both cases. Heme in (B) is rendered as sticks and colored in red. The lowest energy and best bound conformation (5/9) was also found in close proximity to the heme binding pocket. The conformation – which was slightly different from the one observed when the SWNT carried defects at the ends – is shown. The predicted binding pocket residues within 5 Å were S28, D29, P30, R31, R75, K174, L208, N214, S216, A217, and L218. The distance of the closest carboxyl group to the nearest atom of the heme is 8.1 Å in this case, where the defects are in the middle. This is similar to the respective distance of 7.6 Å for the end-carboxylated SWNT.

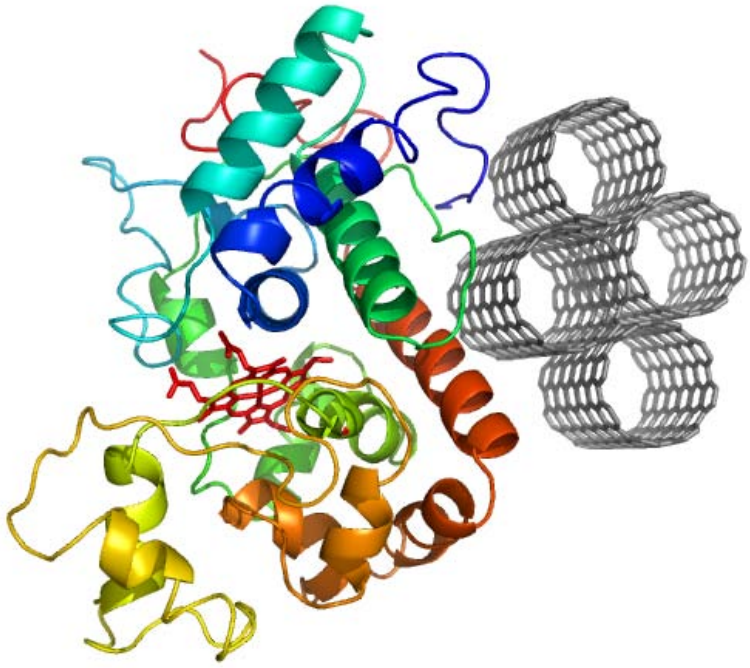

Figure 82. The model representing the binding of a pristine SWNT bundle to HRP. This model was generated using the bound conformation of a single pristine SWNT. The place where the pristine SWNT docks has sufficient space for additional SWNTs to be stuck to the one actually in contact with the protein. The binding model clearly indicates that the docking study with single pristine nanotube would also be relevant for bundles of multiple SWNT.

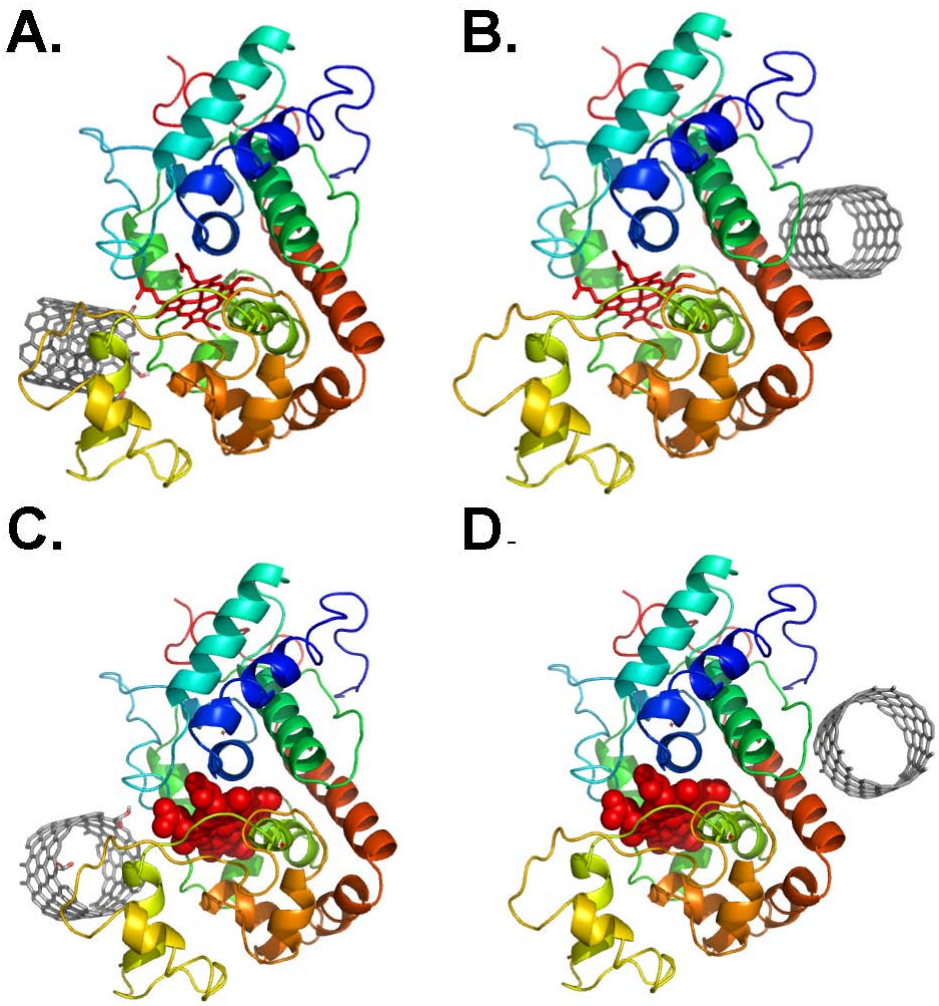

Figure 83. Binding of HRP to (A) carboxylated SWNT with (8,8) chirality, (B) non-carboxylated SWNT with (8,8) chirality, (C) carboxylated SWNT with (14,4) chirality, and (B) non-carboxylated SWNT with (14,4) chirality. The receptor HRP is rendered as cartoon and colored in gradient from N-C terminus representing blue to red. Heme and SWCNT are colored in red and grey, respectively and represented as stick structure in each case. Heme in (C) and (D) is rendered as spheres and colored in red. In the case of non-carboxylated SWNT all the conformations (9/9) were found to bind at the second binding site, located away from the heme binding pocket. SWNT with a defect/modification introduced at the ends, bound predominantly (6/9) in proximity to the heme binding site.

BIBLIOGRAPHY

(1) Kroto, H. W.; Heath, J. R.; O'Brien, S. C.; Curl, R. F.; Smalley, R. E. *Nature* **1985**, *318*, 162-163.

(2) Kauffman, D. R.; Star, A. *Angew. Chem. Int. Ed.* **2008**, *47*, 6550-6570.

(3) Allen, B. L.; Kichambare, P. D.; Star, A. *Adv. Mater.* **2007**, *19*, 1439-1451.

(4) Zanello, L. P.; Zhao, B.; Hu, H.; Haddon, R. C. *Nano Lett.* **2006**, *6*, 562-567.

(5) Iijima, S. *Nature* **1991**, *354*, 56-58.

(6) Iijima, S.; Ichihashi, T. *Nature* **1993**, *363*, 603-605.

(7) Bethune, D. S.; Klang, C. H.; de Vries, M. S.; Gormon, G.; Savoy, R.; Vazquez, J.; Beyers, R. *Nature* **1993**, *363*, 605-607.

(8) Odom, T. W.; Huang, J. –L.; Kim, P.; Lieber, C. M. *J. Phys. Chem. B* **2000**, *104*, 2794-2809.

(9) Dresselhaus, M. S.; Dresselhaus, G.; Eklund, P. C. *Science of Fullerenes and Carbon Nanotubes*; Academic: San Diego, 1996.

(10) Anantram, M. P.; Léonard, F. *Rep. Prog. Phys.* **2006**, *69*, 507-561.

(11) Guo, T.; Nikolaev, P.; Thess, A.; Colbert, D. T.; Smalley, R. E. *Chem. Phys. Lett.* **1995**, *243*, 49-54.

(12) Jose-Yacaman, M.; Miki-Yoshida, M.; Rendon, L.; Santiesteban, J. G. *Appl. Phys. Lett.* **1993**, *62*, 657-659.

(13) Nakazawa, S.; Yokomori, T.; Mizomoto, M. *Chem. Phys. Lett.* **2005**, *403*, 158-162.

(14) Zhang, Y. F.; Gamo, M. N.; Xiao, C. Y.; Ando, T. *Physica B* **2002**, *323*, 293-295.

(15) Chung, Y. –H.; Jou, S. *Mater. Chem. Phys.* **2005**, *92*, 256-259.

(16) Journet, C.; Berier, P. *Appl. Phys. A* **1998**, *67*, 1-9.

(17) Terrones, M. *Inter. Mater. Rev.* **2004**, *49*, 325-377.

(18) Guo, T.; Nikolaev, P.; Rinzler, A. G.; Tomànek, D.; Colbert, D. T.; Smalley, R. E. *J. Phys. Chem.* **1995**, *99*, 10694-10697.

(19) Thess, A.; Lee, R.; Nikolaev, P.; Dai, H.; Petit, P.; Robert, J.; Xu, C.; Lee, Y. H.; Kim, S. G.; Rinzler, A. G.; Colbert, D. T.; Scuseria, G. E.; Tomànek, D.; Fischer, J. E., Smalley, R. E. *Science* **1996**, *273*, 483-487.

(20) Qin, L. C.; Iijima, S. *Chem. Phys. Lett.* **1997**, *269*, 65-71.

(21) Chen, Y.; Sun, Z.; Li, Y. N.; Tay, B. K.; *Mater. Chem. Phys.* **2006**, *98*, 256-260.

(22) Li, Y. L.; Kinloch, I. A.; Shaffer, M. S. P.; Geng, J.; Johnson, B.; Windle, A. H. *Chem. Phys. Lett.* **2004**, *384*, 98-102.

(23) Colomer, J. –F.; Stephan, C.; Lefrant, S.; Van Tendeloo, G.; Willems, I.; Konya, Z.; Fonseca, A.; Laurent, C.; Nagy, J. B. *Chem. Phys. Lett.* **2000**, *317*, 83-89.

(24) Nasibulin, A. G.; Moisala, A.; Brown, D. P.; Jiang, H.; Kauppinen, E. I. *Chem. Phys. Lett.* **2005**, *402*, 227-232.

(25) Bondi, S. N.; Lackey, W. J.; Johnson, R. W.; Wang, X.; Wang, Z. L. *Carbon* **2006**, *44*, 1393-1403.

(26) Ivanov, V.; Nagy, J. B.; Lambin, Ph.; Lucas, A.; Zhang, X. B.; Zhang, X. F.; Bernaerts, D.; van Tendeloo, G.; Amelinckx, S.; van Landuyt, J. *Chem. Phys. Lett.* **1994**, *223*, 329-335.

(27) Suh, D. J.; Park, T. –J.; Kim, J. –H.; Kim, K. –L. *Chem. Mater.* **1997**, *9*, 1903-1905.

(28) Xu, C.; Zhu, J. *Nanotechnology* **2004**, *11*, 1671-1681.

(29) Schwarz, J. A.; Contescu, C.; Contescu, A., *Chem. Rev.* **1995**, *95*, 477-510.

(30) Nikolaev, P.; Bronikowski, M. J.; Bradley, R. K.; Rohmund, F.; Colbert, D. T.; Smith, K. A.; Smalley, R. E. *Chem. Phys. Lett.* **1999**, *313*, 91-97.

(31) Dai, H. *Acct. Chem. Res.* **2002**, *35*, 1035-1044.

(32) Donaldson, K.; Aitken, R.; Tran, L.; Stone, V.; Duffin, R.; Forrest, G.; Alexander, A., *Toxicol. Sci.* **2006**, *92*, 5-22.

(33) Mossman, B. T.; Churg, A., *Am. J. Respir. Crit. Care Med.* **1998**, *157*, 1666-1680.

(34) Donaldson, K.; Tran, C. L., *Mutat. Res.* **2004**, *553*, 5-9.

(35) Kane, A. B. Mechanisms of mineral fibre carcinogenesis, in *Mechanisms of fibre carcinogenesis*, (ed. Kane, A. B.; Boffetta, P.; Saracci, R.; Wilbourn, J. D.) 11-34 (IARC, Lyon, 1996).

(36) Takagi, A; Hirose, A.; Nishimura, T.; Fukumori, N.; Ogata, A.; Ohashi, N.; Kitajima, S.; Kanno, J., *J. Toxicol. Sci.* **2008**, *33*, 105-116.

(37) Kane, A. B.; Hurt, R. H., *Nature Nanotech.* **2008**, *3*, 378-379.

(38) Lacerda, L.; Ali-Boucetta, H.; Herrero, M. A.; Pastorin, G.; Bianco, A.; Prato, M.; Kostarelos, K., *Nanomedicine* **2008**, *3*, 149-161.

(39) Muller, J.; Delos, M.; Panin, N.; Rabolli, V.; Huaux, F.; Lison D., *Toxicol. Sci.* **2009**, *110*, 442-448.

(40) Muller, J.; Huaux, F.; Moreau, N.; Misson, P.; Heilier, J. –F.; Delos, M.; Arras, M.; Fonseca, A.; Nagy, J. B.; Lison, D., *Toxicol. Appl. Pharmacol.* **2005**, *207*, 221-231.

(41) Cui, D.; Tian, F.; Ozkan, C. S.; Wang, M.; Gao, H., *Toxicol. Lett.* **2005**, *155*, 73-85.

(42) Mitchell, L. A.; Gao, J.; Vander Wal, R.; Gigliotti, A.; Burchiel, S. W.; McDonald, J. D., *Toxicol. Sci.* **2007**, *100*, 203-214.

(43) Pulskamp, K.; Diabate, S.; Krug, H. F., *Toxicol. Lett.* **2007**, *168*, 58-74.

(44) Hussain, S. M.; Braydich-Stolle, L. K.; Schrand, A. M.; Murdock, R. C.; Yu, K. O.; Mattie, D. M.; Schlager, J. J.; Terrones, M., *Adv. Mater.* **2009**, *21*, 1-11.

(45) Sato, Y.; Yokoyama, A.; Shibata, K. –i.: Akimoto, Y.; Ogino, S. –i.; Nodasaka, Y.; Kohgo, T.; Tamura, K.; Akasaka, T.; Uo, M.; Motomiya, K.; Jeyadevan, B.; Ishiguro, M.; Hatakeyama, R.; Watari, F.; Tohji, K., *Mol. BioSyst.* **2005**, *1*, 176-182.

(46) Poland, C. A.; Duffin, R.; Kinloch, I.; Maynard, A.; Wallace, W. A. H.; Seaton, A.; Stone, V.; Brown, S.; MacNee, W.; Donalson, K., *Nature Nanotech.* **2008**, *3*, 423-428.

(47) Muller J.; Huaux, F.; Fonseca, A.; Nagy, J. B.; Moreau, N.; Delos, M.; Raymundo-Pinãéero, E.; Beãáguin, F.; Kirsch-Volders, M.; Fenoglio, I.; Fubini, B.; Lison, D., *Chem. Res. Toxicol.* **2008**, *21*, 1698-1705.

(48) Dujardin, E.; Ebbesen, T. W.; Krishnan, A.; Treacy, M. M. J., *Adv. Mater*. **1998**, *10*, 611-613.

(49) Kim, Y. A.; Hayashi, T.; Osawa, K.; Dresselhaus, M. S.; Endo, M., *Chem. Phys. Lett.* **2003**, *380*, 319-324.

(50) Kagan, V. E.; Tyurina, Y. Y.; Tyurin, V. A.; Konduru, N. V.; Potapovich, A. I.; Osipov, A. N.; Kisin, E. R.; Schwegler-Berry, D.; Mercer, R.; Castranova, V.; Shvedova, A. A., *Toxicol. Lett.* **2006**, *165*, 88-100.

(51) Walling, C. *Acc. Chem. Res.* **1975**, *8*, 125-131.

(52) Bottini, M.; Bruckner, S.; Nika, K.; Bottini, N.; Bellucci, S.; Magrini, A.; Bergamaschi, A.; Mustelin, T., *Toxicol. Lett.* **2006**, *160*, 121-126.

(53) Kroto, H. W.; Heath, J. R.; O'Brien, S. C.; Curl, R. F.; Smalley, R. E., *Nature* **1985**, *318*, 162-163.

(54) Iijima, S., *Nature* **1991**, *354*, 56-58

(55) Ugarte, D., *Nature* **1992**, *359*, 707-709.

(56) Krishman, A.; Dujardin, E.; Treacy, M. M. J.; Hugdahl, J.; Lynum, S.; Ebbesen, T. W., *Nature* **1997**, *388*, 451-454.

(57) Iijima, S.; Yudasaka, M.; Yamada, R.; Bandow, S.; Suenaga, K.; Kokai, F.; Takahashi, K., *Chem. Phys. Lett.* **1999**, *309*, 165-170.

(58) Zhang, G. Y.; Jiang, X.; Wang, E. G., *Appl. Phys. Lett.* **2004**, *84*, 2646-2648.

(59) Hasobe, T.; Fukuzumi, S.; Kamat, P. V., *Angew. Chem. Int. Ed.* **2006**, *45*, 755-759.

(60) Novoselov, K. S.; Jiang, D.; Schedin, F.; Booth, T. J.; Khotkevich, V. V.; Morozov, S. V.; Geim, A. K., *Proc. Nat. Acad. Sci.* **2005**, *102*, 10451-10453.

(61) Rao, C. N. R.; Cheetham, A. K., *J. Mater. Chem.* **2001**, *11*, 2887-2894.

(62) Lee, S.; Pérez-Luna, V. H., *Langmuir* **2007**, *23*, 5097-5099.

(63) Broz, P.; Driamov, S.; Ziegler, J.; Ben-Haim, N.; Marsch, S.; Meier, W.; Hunziker, P., *Nano Lett.* **2006**, *6*, 2349-2353.

(64) Leonhardt, A.; Mönch, I.; Meye, A.; Hampel, S.; Büchner, B., *Adv. Sci. Tech.* **2006**, *49*, 74-78.

(65) Meunier, V.; Krstić, P. S., *J. Chem. Phys.* **2008**, *128*, 041103-1 – 041103-4.

(66) Weda, P.; Trzebicka, B.; Dworak, A.; Tsvetanov, Ch. B., *Polymer* **2008**, *49*, 1467-1474.

(67) Ye, X.; Gu, X.; Gong, X. G.; Shing, T. K. M.; Liu, Z. –F., *Carbon* **2007**, *45*, 315-320.

(68) Bai, X. D.; Zhong, D.; Zhang, G. Y.; Ma, X. C.; Liu, S.; Wang, E. G.; Chen, Y.; Shaw, D. T., *Appl. Phys. Lett.* **2001**, *79*, 1552-1554.

(69) Zhong, D. Y.; Zhang, G. Y.; Liu, S.; Wang, E. G.; Wang, Q.; Li, H.; Huang, X. J., *Appl. Phys. Lett.* **2001**, *79*, 3500-3502.

(70) Ma, X.; Wang, E.; Zhou, W.; Jefferson, D. A.; Chen, J.; Deng, S.; Ningsheng, X.; Yuan, J., *Appl. Phys. Lett.* **1999**, *75*, 3105-3107.

(71) Ma, X.; Wang, E. G.; Tilley, R. D.; Jefferson, D. A.; Zhou, W., *Appl. Phys. Lett.* **2000**, *77*, 4136-4138.

(72) Endo, M.; Kim, K. A.; Hayashi, T.; Fukai, Y.; Oshida, K.; Terrones, M.; Yanagisawa, T.; Higaki, S.; Dresselhaus, M. S., *Appl. Phys. Lett.* **2002**, *80*, 1267-1269.

(73) Kim, C.; Kim, Y. J.; Kim, Y. A.; Yanagisawa, T.; Park, K. C.; Endo, M.; Dresselhaus, M. S., *J. Appl. Phys.* **2004**, *96*, 5903-5905.

(74) Endo, M.; Kim, Y. A.; Ezaka, M.; Osada, K.; Yanagisawa, T.; Hayashi, T.; Terrones, M.; Dresselhaus, M. S., *Nano Lett.* **2003**, *3*, 723-726.

(75) Zhao, G. L.; Bagayoko, D.; Wang, E. G., *Mod. Phys. Lett. B* **2003**, *17*, 375-382.

(76) Sun, H. -L.; Jia, J. –F.; Zhong, D.; Shen, Q. –T.; Sun, M.; Xue, Q. –K.; Wang, E. G., *Phys. Rev. B* **2002**, *66*, 085423-1 – 085423-5.

(77) Iijima, S.; Ichihashi, T.; Ando, Y., *Nature* **1992**, *356*, 776-778.

(78) Lin, M.; Ying Tan, J. P.; Boothroyd, C.; Loh, K. P.; Tok, E. S.; Foo, Y. –L., *Nano Lett.* **2007**, *7*, 2234-2238.

(79) Chen, L.; Cheung, C. L.; Ashby, P. D.; Lieber, C. M., *Nano Lett.* **2004**, *4*, 1725-1731.

(80) Decossas, S.; Mazen, F.; Baron, T.; Brémond, G.; Souifi, A., *Nanotech.* **2003**, *14*, 1272-1278.

(81) Dietzel, D.; Mönninghoff, T.; Jansen, L.; Fuchs, H.; Ritter, C.; Schwarz, U. D.; Schirmeisen, A., *J. Appl. Phys.* **2007**, *102*, 084306-1 – 084306-11.

(82) Muto, H.; Yamada, K.; Miyajima, K.; Mafuné, F., *J. Phys. Chem. C* **2007**, *111*, 17221-17226.

(83) Sumpter, B. G.; Meunier, V.; Romo-Herrera, J. M.; Cruz-Silva, E.; Cullen, D. A.; Terrones, H.; Smith, D. J.; Terrones, M., *ACS Nano* **2007**, *1*, 369-375.

(84) Panchakarla, L. S.; Govindaraj, A.; Rao, C. N. R., *ACS Nano* **2007**, *1*, 494-500.

(85) Wu, Y.; Hudson, J. S.; Lu, Q.; Moore, J. M.; Mount, A. S.; Rao, A. M.; Alexov, E.; Ke. P. C., *J. Phys. Chem. B* **2006**, *110*, 2475-2478.

(86) Willing, G. A.; Ibrahim, T. H.; Etzler, F. M.; Neuman, R. D., *J. Colloid Interface Sci.* **2000**, *226*, 185-188.

(87) Baughman, R. H.; Zakhidov, A. A.; de Heer, W. A., *Science* **2002**, *297*, 787-792.

(88) Smith, B. W.; Monthioux, M.; Luzzi, D. E., *Nature* **1998**, *396*, 323-324.

(89) Gaponik, N.; Radtchenko, I. L.; Gerstenberger, M. R.; Fedutik, Y. A.; Sukhorukov, G. B.; Rogach, A. L., *Nano Lett.* **2003**, *3*, 369-372.

(90) Shchukin, D. G.; Radtchenko, I. L.; Sukhorukov, G. B., *Mater. Lett.* **2002**, *57*, 1743-1747.

(91) Dujardin, E.; Ebbesen, T. W.; Hiura, H.; Tanigaki, K., *Science* **1994**, *265*, 1850-1852.

(92) Ugarte, D.; Châtelain, A.; de Heer, W. A., *Science* **1996**, *274*, 1897-1899.

(93) Seraphin, S.; Zhou, D.; Jiao, J.; Withers, J. C.; Loufty, R. *Nature* **1993**, *362*, 503.

(94) Mittal, J.; Monthioux, M.; Allouche, H.; Stephan, O., *Chem. Phys. Lett.* **2001**, *339*, 311-318.

(95) Lamprecht, A.; Saumet, J. –L.; Roux, J.; Benoit, J. –P., *Int. J. Pharm.* **2004**, *278*, 407-414.

(96) Broz, P.; Driamov, S.; Ziegler, J.; Ben-Haim, N.; Marsch, S.; Meier, W.; Hunziker, P., *Nano Lett.* **2006**, *6*, 2349-2353.

(97) Hampel, S. Kunze, D.; Haase, D.; Krämer, K.; Rauschenbach, M.; Ritschel, M.; Leonhardt, A.; Thomas, J.; Oswald, S.; Hoffmann, V.; Büchner, B., *Nanomedicine* **2008**, *3*, 175-182.

(98) Rigler, P.; Meier, W., *J. Am. Chem. Soc.* **2006**, *128*, 367-373.

(99) Zhong, D. Y.; Zhang, G. Y.; Liu, S.; Wang, E. G.; Wang, Q.; Li, H.; Huang, X. J., *Appl. Phys. Lett.* **2001**, *79*, 3500-3502.

(100) Shiraishi, M.; Takenobu, T.; Yamada, A.; Ata, M.; Kataura, H., *Chem. Phys. Lett.* **2002**, *358*, 213-218.

(101) Allen, B. L.; Kichamabare, P. D.; Star, A., *ACS Nano* **2008**, *2*, 1914-1920.

(102) Wei, H.; Li, B; Li, J.; Dong, S.; Wang, E., *Nanotechnology* **2008**, *19*, 095501-1 – 095501-5.

(103) Norman, Jr., T. J.; Grant, C. D.; Magana, D.; Zhang, J. Z.; Liu, J.; Cao, D.; Bridges, F.; Buuren, A. V., *J. Phys. Chem. B* **2002**, *106*, 7005-7012.

(104) Ajayan, P. M.; Iijima, S., *Nature* **1993**, *361*, 333-334.

(105) Pugh, T. L.; Heller, W., *J. Polym. Sci.* **1960**, *47*, 219-227.

(106) Storhoff, J. J.; Lazarides, A. A.; Mucic, R. C.; Mirkin, C. A.; Letsinger, R. L.; Schatz, G. C., *J. Am. Chem. Soc.* **2000**, *122*, 4640-4650.

(107) Li, L. S.; Pradhan, N.; Wang, Y.; Peng, X., *Nano Lett.* **2004**, *4*, 2261-2264.

(108) Chengelis, D. A.; Yingling, A. M.; Badger, P. D.; Shade, C. M.; Petoud, S., *J. Am. Chem. Soc.* **2005**, *127*, 16752-16753.

(109) Zhao, G. L.; Bagayoko, D.; Wang, E. G., *Mod. Phys. Lett. B* **2003**, *17*, 375-382.

(110) Saito, R.; Fujita, M.; Dresselhaus, G.; Dresselhaus, M. S., *Appl. Phys. Lett.* **1992**, *60*, 2204-2206.

(111) Stephan, O.; Ajayan, P. M.; Colliex, C.; Redlich, Ph.; Lambert, J. M.; Bernier, P.; Lefin, P., *Science* **1994**, *266*, 1683-1685.

(112) Terrones, M.; Ajayan, P. M.; Banhart, F.; Blasé, X.; Carroll, D. L.; Charlier, J. C.; Czerw, R.; Foley, B.; Grobert, N.; Kamalakaran, R.; Kohler-Redlich, P.; Rühle, M.; Seeger, T.; Terrones, H., *Appl. Phys. A: Mater. Sci. Process.* **2002**, *74*, 355-361.

(113) Ma, X.; Wang, E. G., *Appl. Phys. Lett.* **2001**, *78*, 978-980.

(114) Kurt, R.; Karimi, A., *ChemPhysChem* **2001**, *2*, 388-392.

(115) Ma, X.; Wang, E. G.; Tilley, R. D.; Jefferson, D. A.; Zhou, W., *Appl. Phys. Lett.* **2000**, *77*, 4136-4138.

(116) Tang, Y.; Allen, B. L.; Kauffman, D. R.; Star, A., *J. Am. Chem. Soc.* **2009**, *131*, 13200-13201.

(117) Allen, B. L.; Shade, C. M.; Yingling, A. M.; Petoud, S.; Star, A., *Adv. Mater.* **2009**, *21*, 4692-4695.

(118) Cheung, C. L.; Kurtz, A.; Park, H.; Lieber, C. M., *J. Phys. Chem. B* **2002**, *106*, 2429-2433.

(119) Wang, E.G., *J. Mater. Res.* **2006**, *21*, 2767-2773.

(120) Chun, H.; Hahm, M. G.; Homma, Y.; Meritz, R.; Kuramochi, K.; Menon, L.; Ci, L. Ajayan, P. M.; Jung, Y. J., *ACS Nano* **2009**, *3*, 1274-1278.

(121) Ma, Y.; Dong, M. –F.; Hempenius, M. A.; Möhwald, H.; Vancso, G. J., *Nat. Mater.* **2006**, *5*, 724-729.

(122) Kauffman, D. R.; Star, A., *Chem. Soc. Rev.* **2008**, *37*, 1197-1206.

(123) Kam, N. W. S.; Jessop, T. C.; Wender, P. A.; Dai, H., *J. Am. Chem. Soc.* **2004**, *126*, 6850-6851.

(124) Prato, M.; Kostarelos, K.; Bianco, A., *Acc. Chem. Res.* **2008**, *41*, 60-68.

(125) Kam, N. W. S.; O'Connell, M.; Wisdom, J. A.; Dai, H., *Nat. Acad. Sci.* **2005**, *102*, 11600-11605.

(126) Jia, G.; Wang, H.; Yan, L.; Wang, X.; Pei, R.; Yan, T.; Zhao, Y.; Guo, X., *Environ. Sci. Technol.* **2005**, *39*, 1378-1383.

(127) Magrez, A.; Kasas, S.; Salicio, V.; Pasquier, N.; Seo, J. W.; Celio, M.; Catsicas, S.; Schwaller, B.; Forró, L., *Nano Lett.* **2006**, *6*, 1121-1125.

(128) Jin, H.; Heller, D. A.; Strano, M. S., *Nano Lett.* **2008**, *8*, 1577-1585.

(129) Shvedova, A. A.; Kisin, E. R.; Mercer, R.; Murray, A. R.; Johnson, I. J.; Potapovich, A. I.; Tyurina, Y. Y.; Gorelik, O.; Arepalli, S.; Schwegler-Berry, D.; Hubbs, A. F.; Antonini, J.; Evans, D. E.; Ku, B. –K.; Ramsey, D.; Maynard, A.; Kagan, V. E.; Castranova, V.; Baron, P., *Amer. J. Physiol: Lung,* **2005**, *289*, L698-L708.

(130) Lacerda, L.; Bianco, A.; Prato, M.; Kostarelos, K., *Adv. Drug Delivery Rev.* **2006**, *58*, 1460-1470.

(131) Maynard, A. D.; Baron, P. A.; Foley, M.; Shvedova, A. A.; Kisin, E. R.; Castranova, V., *J. Toxicol. Environ. Health Part A* **2004**, *67*, 87-107.

(132) Heller, D. A.; Baik, S.; Eurell, T. E.; Strano, M. S., *Adv. Mater.* **2005**, *17*, 2793-2799.

(133) Shvedova, A. A.; Castranova, V.; Kisin, E. R.; Schwegler-Berry, D.; Murray, A.; Gandelsman, V. Z.; Maynard, A.; Baron, P., *J. Toxicol. Environ. Health Part A* **2003**, *66*, 1909-1926.

(134) Muller, J.; Huaux, F.; Moreau, N.; Misson, P.; Heilier, J. –F.; Delos, M.; Arras, M.; Fonseca, A.; Nagy, J. B.; Lison, D., *Tox. Appl. Pharm.* **2005**, *207*, 221-231.

(135) Ding, L.; Stilwell, J.; Zhang, T.; Elboudwarej, O.; Jiang, H.; Selegue, J. P.; Cooke, P. A.; Gray, J. W.; Chen, F. F., *Nano Lett.* **2005**, *5*, 2448-2464.

(136) Helland, A.; Wick, P.; Koehler, A.; Schmid, K.; Som, C., *Environ. Health Perspect.* **2007**, *115*, 1125-1131.

(137) Wei, Z.; Kondratenko, M.; Dao, L. H.; Perepichka, D. F., *J. Am. Chem. Soc.* **2006**, *128*, 3134-3135.

(138) Hunt, J. P.; Taube, H., *J. Am. Chem. Soc.* **1952**, *74*, 5999-6002.

(139) Basova, L. V.; Kurnikov, I. V.; Wang, L.; Ritov, V. B.; Belikova, N. A.; Vlasova, I. I.; Pacheco, A. A.; Winnica, D. E.; Peterson, J.; Bayir, H.; Waldeck, D. H.; Kagan, V. E., *Biochemistry* **2007**, *46*, 3423-3434.

(140) Goldman, R.; Bors, W.; Michel, C.; Day, B. W.; Kagan, V. E. *Environ. Nutrit. Inter.* **1997**, *1*, 97-118.

(141) Tyurina, Y. Y.; Kini, V.; Tyurin, A. A.; Vlasova, I. I.; Jiang, J.; Kapralov, A. A.; Belikova, N. A.; Yalowich, J. C.; Kurnikov, I. V.; Kagan, V. E. *Mol. Pharmacol.* **2006**, *70*, 706-717.

(142) Palwai, N. R.; Martyn, D. E.; Neves, L. F. F.; Tan, Y.; Resasco, D. E.; Harrison, R. G. *Nanotech.* **2007**, *18*, 235601.

(143) Asuri, P.; Bale, S. S.; Pangule, R. C.; Shah, D. A.; Kane, R. S.; Dordick, J. S. *Langmuir* **2007**, *23*, 12318-12321.

(144) Hayashi, Y.; Yamazaki, I., *J. Biol. Chem.* **1979**, *254*, 9101-9106.

(145) Filizola, M.; Loew, G. H., *J. Am. Chem. Soc.* **2000**, *122*, 18-25.

(146) Azevedo, A. M.; Martins, V. C.; Prazeres, D. M.; Vojinović, V.; Cabral, J. M.; Fonesca, L. P., *Biotechnol. Annu. Rev.* **2003**, *9*, 199-247.

(147) Shieh, Y. –T.; Liu, G. –L.; Wu, H. –H.; Lee, C. –C., *Carbon* **2007**, *45*, 1880-1890.

(148) Wengatz, I.; Schmid, R. D., *Anal. Lett.* **1992**, *25*, 1983-1997.

(149) White, C. T.; Mintmire, J. W., *J. Phys. Chem. B* **2005**, *109*, 52-65.

(151) Wu, W.; Wieckowski, S.; Pastorin, G.; Benincasa, M.; Klumpp, C.; Briand, J. –P.; Gennaro, R.; Prato, M.; Bianco, A., *Angew. Chem. Int. Ed.* **2005**, *44*, 6358-6362.

(152) Kam, N. W.; Liu, Z.; Dai, H., *J. Am. Chem. Soc.* **2005**, *127*, 12492-12493.

(153) Liu, Z.; Cai, W.; He, L.; Nakayama, N.; Chen, K.; Sun, X.; Chen, X.; Dai, H., *Nature Nanotech.* **2007**, *2*, 47-52.

(153) Kong, J.; Franklin, N.; Zhou, C.; Peng, S. S.; Cho, J. J.; Dai, H., *Science* **2000**, *287*, 622–625.

(154) Collins, P. G.; Bradley, K.; Ishigami, M.; Zettl, A., *Science* **2000**, *187*, 1801-1804.

(155) Ajayan, P. M.; Schadler, L. S.; Giannaris, C.; Rubio, A., *Adv. Mater.* **2000**, *12*, 750-753.

(156) Zhu, J.; Kim, J.; Peng, H.; Margrave, J. L.; Khabashesku, V. N.; Barrera, E. V., *Nano Lett.* **2003**, *3*, 1107-1113.

(157) Agüí, L.; Yáñez-Sedeño, P; Pingarró, J. M., *Anal. Chem. Acta* **2008**, *622*, 11-47.

(158) Bianco, A.; Kostarelos, K.; Prato, M., *Curr. Opin. Chem. Biol.* **2005**, *9*, 674-679.

(159) Kam, N. W. S.; Jessop, T. C.; Wender, P. A.; Dai, H., *J. Am. Chem. Soc.* **2004**, *126*, 6850-6851.

(160) Singh, R.; Pantarotto, D.; McCarthy, D.; Chaloin, O.; Hoebeke, J.; Partidos, C. D.; Briand, J. –P.; Prato, M.; Bianco, A.; Kostarelos, K., *J. Am. Chem. Soc.* **2005**, *127*, 4388-4396.

(161) Manna, S. K.; Sarkar, S.; Barr, J.; Wise, K.; Barrera, E. V.; Jejelowo, O.; Rice-Ficht, A. C.; Ramesh, G. T., *Nano Lett.* **2005**, *5*, 1676-1684.

(162) Lam, C.-W.; James, J. T.; McCluskey, R.; Arepalli, S.; Hunter, R. L., *Crit. Rev. Toxicol.* **2006**, *36*, 189– 217.

(163) Poland, C. A.; Duffin, R.; Kinloch, I.; Maynard, A.; Wallace, W. A. H.; Seaton, A.; Stone, V.; Brown, S.; MacNee, W.; Donaldson, K., *Nat. Nanotechnol.* **2008**, *3*, 423– 428.

(164) Kam, N. W. S.; O'Connell, M.; Wisdom, J. A.; Dai, H., *Proc. Natl. Acad. Sci. U.S.A.* **2005**, *102*, 11600– 11605.

(165) Pantarotto, D.; Partidos, C. D.; Graff, R.; Hoebeke, J.; Briand, J.-P.; Prato, M.; Bianco, A., *J. Am. Chem. Soc.* **2003**, *125*, 6160– 6164.

(166) Liu, Z.; Sun, X.; Nakayama-Ratchford, N.; Dai, H., *ACS Nano* **2007**, *1*, 50– 56.

(167) Allen, B. L.; Kichambare, P. D.; Gou, P.; Vlasova, I. I.; Kapralov, A. A.; Konduru, N.; Kagan, V. E.; Star, A., *Nano Lett.* **2008**, *8*, 3899– 3903.

(168) Filizola, M.; Loew, G. H., *J. Am. Chem. Soc.* **2000**, *122*, 18– 25.

(169) Hayashi, Y.; Yamazaki, I., *J. Biol. Chem.* **1979**, *254*, 9101– 9106.

(170) Schreiner, K. M.; Filley, T. R.; Blanchette, R. A.; Bowen, B. B.; Bolskar, R. D.; Hockaday, W. C.; Masiello, C. A.; Raebiger, J. W., *Environ. Sci. Technol.* **2009**, *43*, 3162– 3168.

(171) Journet, C.; Maser, W. K.; Bernier, P.; Loiseau, A.; Lamy de la Chapelle, M.; Lefrant, S.; Deniard, P.; Lee, R.; Fischer, J. E., *Nature* **1997**, *388*, 756– 758.

(172) Kauffman, D. R.; Kuzmych, O.; Star, A., *J. Phys. Chem. C* **2007**, *111*, 3539– 3543.

(173) DeLano, W. L. *The PyMOL Molecular Graphics System*; DeLano Scientific: Palo Alto, CA, **2002**.

(174) Trott, O.; Olson, A. J., *J. Comput. Chem.*,DOI: 10.1002/jcc21334.

(175) Yanamala, N.; Tirupula, K. C.; Klein-Seetharaman, J., *BMC Bioinf.* **2008**, *9*, S16.

(176) Magazanik, L. G.; Vyskocit, F. J., *Physiol.* **1975**, *249*, 285– 300.

(177) Hunt, J. P.; Taube, H., *J. Am. Chem. Soc.* **1952**, *74*, 5999– 6002.

(178) Hamon, M. A.; Itkis, M. E.; Niyogi, S.; Alvaraez, T.; Kuper, C.; Menon, M.; Haddon, R. C., *J. Am. Chem. Soc.* **2001**, *123*, 11292– 11293.

(179) Dresselhaus, M. S.; Dresselhaus, G.; Jorio, A.; Souza Filho, A. G.; Saito, R., *Carbon* **2002**, *40*, 2043– 2061.

(180) Gilabert, M. A.; Fenoll, L. G.; García-Molina, F.; Tudela, J.; García-Cánovas, F.; Rodríguez-López, J. N., *Biol. Chem.* **2004**, *385*, 795-800.

(181) Gorris, H. H.; Walt, D. R., *J. Am. Chem. Soc.* **2009**, *131*, 6277-6282.

(182) Walling, C., *Acc. Chem. Res.* **1975**, *8*, 125– 131.

(183) Yan, E. B.; Unthank, J. K.; Castillo-Melendez, M.; Miller, S. L.; Langford, S. J.; Walker, D. W., *J. Appl. Physiol.* **2005**, *98*, 2304– 2310.

(184) Nakamoto, K. *Coord. Chem. Rev.* **2002**, *226*, 153-165.

(185) Kosynkin, D. V.; Higginbotham, A. L.; Sinitskii, A.; Lomeda, J. R.; Dimiev, A.; Price, K. B.; Tour, J. M., *Nature* **2009**, *458*, 872– 876.

(186) Duque, J. G.; Pasquali, M.; Schmidt, H. K., *J. Am. Chem. Soc.* **2008**, *130*, 15340– 15347.

(187) Kuznetsova, A.; Popova, I.; Yates, J. T., Jr.; Bronikowski, M. J.; Huffman, C. B.; Liu, J.; Smalley, R. E.; Hwu, H. H.; Chen, J. G., *J. Am. Chem. Soc.* **2001**, *123*, 10699– 10704.

(188) Bamforth, S. M.; Singleton, I., *J. Chem. Techol. Biotechnol.* **2005**, *80*, 723-736.

(189) Kanaly, R. A.; Harayama, S., *J. Bacteriol.* **2000**, *182*, 2059– 2067.

(190) Hafner, J. H.; Cheung, C.-L.; Woolley, A. T.; Lieber, C. M., *Prog. Biophys. Mol. Biol.* **2001**, *77*, 73– 110.

(191) McAllister, C.; Karymov, M. A.; Kawano, Y.; Lushnikov, A. Y.; Mikheikin, A.; Uversky, V. N.; Lyubchenko, Y. L., *J. Mol. Biol.* **2005**, *354*, 1028– 1042.

(192) Singh, K. V.; Pandey, R. R.; Wang, X.; Lake, R.; Ozkan, C. S.; Wang, K.; Ozkan, M., *Carbon* **2006**, *44*, 1730– 1739.

(193) Sano, M.; Kamino, A.; Shinkai, S., *Angew. Chem., Int. Ed.* **2001**, *40*, 4661– 4663.

(194) Radmacher, M.; Tillamnn, R. W.; Fritz, M.; Gaub, H. E., *Science* **1992**, *257*, 1900– 1905.

(195) Kam, N. W. S.; Dai, H., *Phys. Status Solidi B* **2006**, *243*, 3561– 3566.

(196) Lee, Y.-M.; Kwon, O.-Y.; Yoon, Y.-J.; Ryu, K., *Biotechnol. Lett.* **2006**, *28*, 39– 43.

(197) Davis, J. J.; Coleman, K. S.; Azamian, B. R.; Bagshaw, C. B.; Green, M. L. H., *Chem.-Eur. J.* **2003**, *9*, 3732– 3739.

(198) Goodsell, D. S.; Morris, G. M.; Olson, A. J., *J. Mol. Recognit.* **1996**, *9*, 1– 5.

(199) Österberg, F.; Morris, G. M.; Sanner, M. F.; Olson, A. J.; Goodsell, D. S., *Proteins* **2002**, *46*, 34– 40.

(200) Das, P. K.; Caaveiro, J. M. M.; Luque, S.; Klibanov, A. M., *J. Am. Chem. Soc.* **2002**, *124*, 782– 787.

(201) Henrikson, A.; Schuller, D. J.; Meno, K.; Welinder, K. G.; Smith, A. T.; Gajhede, M., *Biochemistry* **1998**, *37*, 8054– 8060.